The effects of surface architecture and physics on bacterial biofilm growth

A thesis submitted to the Faculty of Science, Agriculture and Engineering for the Degree of Doctor of Philosophy in PhD in MECH (FT) 8090F programme

By

YUNYI CAO

School of Engineering,

Newcastle University,

Newcastle Upon Tyne, UK

January 2020

To my dear family and beloved friends who supported me on this journey

Abstract

Bacteria are ubiquitous in the environment and can adhere onto abiotic or biotic surfaces to form biofilms. These three-dimensional (3D) communities of sessile cells are encased in a matrix of extracellular polymeric substances (EPS). Bacterial biofilms can be detrimental to human health, causing infections and diseases. Notably, bacterial biofilms are robust structures and are difficult to treat via traditional antibiotic therapy. The EPS matrix acts as a barrier to agents trying to access the interior of the biofilm, subsequently triggering the development of antibiotic resistance, which has been shown for both *Staphylococcus epidermidis* and *Pseudomonas aeruginosa*. Physical strategies, in particular the use of rationally surface design, have gained interests and present us with an effective approach to prevent bacterial adherence and biofilm growth without the requirement for antimicrobials.

In this study, we aim to develop biomaterial surfaces via surface modifications that can control bacterial growth, as well as investigate the bacterial-material interactions on these surfaces. We firstly designed and fabricated nano-pillar structured surfaces via electron-beam lithography and polymer moulding technique. The results showed that rod-shaped *Pseudomonas aeruginosa* can align within the pillars if the space is comparable to the bacteria size; and the extended bacterial growth showed that fibrous network was formed and can help to connect isolated bacterial clusters within the pillars thereby aid in the continuous biofilm growth. Therefore, biomimetic hierarchical structured surfaces were fabricated based on the natural rose-petal via the same method of replicating nano-pillars. The key results showed that hierarchical structures are more effective in delaying biofilm growth of *Staphylococcus epidermidis* and *Pseudomonas aeruginosa* compared to the unitary structure. The nano-folds across the hemispherical micro-papillae restrict initial attachment of bacterial cells and delay the direct contacts of cells via cell alignment, and the hemispherical micro-papillae arrays isolate bacterial clusters and inhibit the formation of a fibrous network. Finally, we made two kinds of slippery surfaces via infusing the silicone oil. These slippery surfaces showed superior anti-wetting properties and exhibited excellent "self-cleaning" effects. Additionally, either slippery surface can prevent around 90% of bacterial biofilm growth of *Staphylococcus epidermidis* and *Pseudomonas aeruginosa* after 6 days, as compared with the unmodified control PDMS surfaces.

This study detailed investigated the different bacterial responses when making contacts with artificial biomaterial surfaces. Multiply imaging techniques such as fluorescent microscopy,

scanning electron microscopy and wettability analysis were adopted in this study, will instruct researchers to reveal the physic-chemical interactions of bacteria and materials. Particularly, the anti-biofilm surface design in this study will give insights to develop a more effective way for controlling robust biofilm growth, thereby paving a high way for preventing infection or fouling problems in either medical or industry contexts.

Acknowledgements

Throughout my PhD study in Newcastle University, I have had the opportunity to meet so many kind and wonderful people here, who supported me a lot either in my life or in my research.

Firstly, I would like to express my sincere gratitude to my supervisors Dr. Jinju Chen and Dr. Nicholas S Jakubovics. I met my main supervisor Dr. Jinju Chen when I was doing MSc study in Newcastle University, who motivated and inspired me to pursue a higher education level towards PhD. I would greatly thanks to her for providing me Research Excellence Academy PhD studentship to carry on my research in Newcastle. I would also greatly thanks to my secondary supervisor, Dr. Nicholas S Jakubovics, who provided me the lab space and his office door is always open to answer my questions. My deepest appreciation goes to both supervisors, for sharing great knowledge and expertise to make my research to go in the right directions. Without their patience, advice, and encouragement, I cannot finish my PhD and become an independent researcher.

A very special gratitude goes out to my colleague and great friend Dr. Saikat Jana. His valuable knowledge always can help my research to step forward. He spent so much time with me in the lab and has been so patient for useful discussions. He did not only give suggestion for experiment sections, but also teach me how to solve problems. His great personality also taught me to be a nice person to treat people and my own personal life. His encouragement can always make me to calm down and to be patient when meeting difficulties.

Another special gratitude goes out to the people in oral microbiology lab on the level 7 of dental school. Katya Kozhevnikova, Christopher Dowson, Jay Sangha, Nicola Griffiths and Dr. Nadia Rostami have been so helpful and always make my lab-work easier. A tremendous thank you goes to Dr. Nadia Rostami who invited me for her wedding ceremony and I have a great travelling adventure with Chris! Another special thanks to Katya who invited me for the great BBQ party, and it is such a good memory, which I cannot forget during my life!

I am grateful to have so many friends around the world and tremendous thank you goes to all of you. No matter of time difference, and wherever she stayed in New York or Shanghai,

my great friend Mona Zhou always picks up my call and helps me to overcome difficulties. I am so sorry to miss the wedding ceremony of “Xiaozhou Wang and Yang Zhang”, while as the witness of their love, I am so happy for them and grateful for their encouragement whenever I need them, especially inviting me for a great dinner.

Heartfelt thanks to the friends in the UK who make me stay in happy. Firstly, I want to thank my friends in Newcastle, my wonderful “alcohol friends” (Dr. Allen Wang and Hathaway Han) and “smoking friends” (Zhengguang Xiao, Dr. Chenyang Tang, Xiaolong Tan, Joey Zhou, Dr. Sam Charlton and Professor Hai Huang) always make me to relax. Special thanks to my “shopping & cooking & eating & travelling friends”, Xiaoyan Zhang, Rixia Zan, Wenjian Yang, Ma Luo (all the best wishes for you to finish PhD!) and Professor Huagui Zhang, who make my weekends colorful.

Above all, I would like to thank my family, especially my Dad, Mum, my sister and my brother in law, for their endless support on my PhD study mentally and financially. They give me the faith, motivation, and backup during my life, let me feel there is a strong pillar whenever I need.

Table of Contents

List of Figures

List of Tables

List of Abbreviations

ACA	advancing contact angle
AMPs	antimicrobial peptides
AMEs	antimicrobial enzymes
CA	contact angle
CL	contact line
CAH	contact-angle hysteresis
CCL	constant contact line
CCA	constant contact angle
CFU	colony forming units
CPD	critical point drying
CF	cystic fibrosis
cryo-EM	cryogenic electron microscopy
DLVO theory	Derjaguin–Landau–Verwey–Overbeek theory
EPS	extracellular polymeric substances
e-beam lithography	electron beam lithography
FFT	fast Fourier transforms
FIB	focused ion beam
ITO glasses	indium tin oxide glasses
LIS	lubricant-impregnated surfaces
MDR	multi-drug resistant
P. aeruginosa	*Pseudomonas aeruginosa*
PBS	Phosphate Buffered Saline
PDMS	polydimethylsiloxane
PMMA	polymethyl methacrylate

PTFE	polytetrafluoroethylene
QAC	quaternary ammonium compound
RCA	receding contact angle
S. epidermidis	*Staphylococcus epidermidis*
SLIPS	slippery liquid infused surfaces
SEM	scanning electron microscope
Si	silicon
S-PDMS	swollen polydimethylsiloxane
T4P	type IV pili
Ti	titanium
TSB	Trypticase Soy Broth
TIRF	total internal reflection fluorescence

Chapter 1
Introduction

1. INTRODUCTION

A biofilm is a sessile community of bacteria in a matrix of extracellular polymeric substances (EPS), which strongly colonizes on artificial surfaces when exposed to bulk fluid environments (Berne *et al.*, 2018). Biofilms can be useful in biotechnological processes such as bioremediation, biofertilizers, and in microbial fuel cells (Berne *et al.*, 2018). By contrast, biofouling caused by biofilms pose risks and have detrimental consequences for many diverse industries, including potable water treatment and transport, maritime shipping, aquaculture, food processing and biomedical devices (Berne *et al.*, 2018; Molino *et al.*, 2018). Especially certain biofilms can be detrimental to human health, causing infections and diseases (Mon *et al.*, 2017; Berne *et al.*, 2018). It has been estimated that up to 80% of bacterial infections in humans are biofilm associated, and biofilms are responsible for the majority of hospital-acquired infections. Biofilm associated infections are the fourth leading cause of death worldwide, within the U.S. about 2 million annual cases lead to more than $5 billion USD in added medical costs per annum (Bryers, 2008; Joo and Otto, 2012; Cao *et al.*, 2018). In the UK, about 300,000 people per annum in England suffer from hospital-acquired infections under NHS care and the costs also run into billions of pounds (Mantle and England, 2015). Hence, it is important to investigate techniques that can control biofilm growth on artificial surfaces and reduce the instances of infections.

Bacterial biofilms are robust structures and significant evidences have shown that bacteria living system can adapt and evolve with environments, by either altering gene expression to trigger biofilm formation, or communicating with surrounding bacteria to initiate coordinated activity (Howell *et al.*, 2018). Additionally, the EPS matrix protects biofilms from predators and showed recalcitrance against biocides, disinfectants, antibiotics, making biofilm removal difficult (Li *et al.*, 2013; Berne *et al.*, 2018). Notably, bacterial biofilms are difficult to treat via traditional antibiotic therapy (Mantle and England, 2015; Cao *et al.*, 2018; Chang *et al.*, 2018). Whenever an antibiotic is applied to a typical biofilm population, its efficacy in killing the bacteria is limited to the top layer of the biofilm, as the EPS matrix acts as a barrier to agents trying to access the interior of the biofilm (Tripathy *et al.*, 2017; Chang *et al.*, 2018). Therefore, antibiotics has the poor ability of penetrating and exerting the bactericidal effects throughout the biofilm, and can subsequently trigger the development of antibiotic resistance over prolonged periods of use (Tripathy *et al.*, 2017). Some bacteria (i.e. *Staphylococcus aureus*, *Escherichia coli* and *Pseudomonas aeruginosa*) have evolved into antibiotics-resistance "super-bug" to be better suited to thrive (Cao *et al.*, 2018; Howell

et al., 2018). The infections caused by antimicrobial-resistant bacteria or biofilms has resulted in 700,000 death every year from all across the world, and it may increase to 10 million by 2050 if the overuse of antibiotics is not stopped (Tripathy *et al.*, 2017).

To tackle detrimental biofilm growth on surfaces without uses of antibiotics, some methods have been proposed, which involved bio-inspired surface textures (Fadeeva *et al.*, 2011; Ivanova *et al.*, 2012; Diu *et al.*, 2014; Bhadra *et al.*, 2015; Cao *et al.*, 2018), surface grafting with poly(ethylene glycol) (PEG) or zwitterionic polymers (Cheng *et al.*, 2007; Cheng *et al.*, 2009), immobilization of antimicrobial agents (Li *et al.*, 2013) (i.e. peptide, silver particles or nitric oxide) and biofilm-dispersing enzymes (Howell *et al.*, 2018). Among these methods, physical strategies via using a rational surface design have shown the potential in delaying bacterial growth on the man-made surfaces. For example, surfaces with structures akin to lotus leaf can delay the bacterial growth on a solid surface, owing to the trapped air within the surface textures restrict the direct contacts of bacteria-materials (Truong *et al.*, 2012). Surface structures mimicking the shark skin blocked the biofilm development as its protruded features acted as a physical obstacle to hinder the cell-cell communications (Reddy *et al.*, 2011). Additionally, cicada or dragonfly-wing inspired nanostructured surfaces can mechanically kill bacterial cells upon contact thereby delaying the biofilm growth (Bhadra *et al.*, 2015; Cao *et al.*, 2018). Furthermore, slippery liquid infused surfaces (SLIPS) via immobilizing a lubricant layer have shown the effective controlling of various bacterial growth, owing to its superior slipperiness and the hindrance of bacteria-material contacts by the lubricant (Epstein *et al.*, 2012; Kovalenko *et al.*, 2017; Howell *et al.*, 2018).

The efficacy of these artificial surfaces to control bacterial biofilm growth is strongly dependent on the bacteria-material interactions which are determined by surface charge, hydrophobicity, roughness, structure/topography, bacterial surface and appendages are of particular importance (Berne *et al.*, 2018). Therefore, investigating the effects of surface physical properties on bacterial attachment, bacterial alignment, and biofilm growth may help us to design a more sustainable surface that can inhibit biofilm growth in the long-term.

Therefore, this study is proposed to investigate the effects of surface architecture or surface physics such as wettability of different biomimetic surfaces on bacterial biofilm growth. The growth of clinically relevant bacterial strains — either *Staphylococcus epidermidis* or *Pseudomonas aeruginosa* were evaluated on the designed artificial surfaces. The quantitative analysis of bacterial growth via fluorescent microscopy demonstrated the anti-

biofilm efficacy, as well as the cell distribution/alignment within certain surface architectures. Bacteria-material interactions can be further studied at a higher spatial resolution using scanning electron microscope (SEM). In this study, unitary nano-pillars, hieratical rose-petal, and slippery liquid infused surfaces were designed and fabricated; and their anti-biofilm efficacy were evaluated as compared with their corresponding control surfaces. The different bacterial growth mechanisms on different surfaces will potentially provide an effective strategy to inhibit or eliminate mature biofilms on surfaces in the long-term. In addition, the design of anti-bacteria/biofilm surfaces in this study have great potential applications in controlling infections or fouling problems in either medical or industry contexts.

1.1 Aim and Objectives

The primary aim of this study is to develop artificial surfaces that can inhibit biofilm growth and reveal how surface physics affect bacterial growth. More specifically, the objectives of the study include:

- To study and develop the anti-biofilm surfaces with a rational surface design
- To test the anti-biofilm efficacy of designed surface against clinical relevant bacterial strains
- To investigate the effects of surface physics (i.e. architecture, wettability) on bacterial attachment, or bacterial alignment, and biofilm growth
- To investigate and propose the anti-biofilm mechanisms of the designed surfaces
- To develop a more effective strategy to control or remove detrimental biofilm growth on artificial surfaces

1.2 Thesis Structure

In order to achieve the objectives of this study, the thesis is divided into seven chapters.

Chapter 1 gives a brief introduction regarding to the topic of this thesis, including the main aim and objectives, as well as illustrating the thesis structures.

Chapter 2 gives a detailed literature review about the bacterial biofilms, including its history,

the importance of controlling biofilm growth, biofilm formation and lifecycles, as well as the key factors (i.e. surface charge, hydrophobicity, roughness, structure/topography, bacterial surface and appendages) affecting initial bacterial attachment. In addition, the current development of antibacterial surfaces (either bactericidal or anti-fouling) were discussed in this chapter.

Chapter 3 summarizes the general methods and techniques used in this study. The main fabricating methods: electron-beam lithography and soft lithography technique were described. Following this, the main characterization techniques: wettability, fluorescent microscopy, and SEM analysis were described with sufficient details.

Chapter 4 investigates the bacterial attachment, cell alignment and biofilm formation of *P. aeruginosa* on the periodic nano-pillar surfaces that have different pillar spaces. We demonstrated that bacterial cells can align between nano-pillars to maximize their contact area with the surface, where the pillars act as topographical extensions of the substrate. Additionally, the formation of bacterial nanotubes may aid in cell-surface or cell-cell connections. Nano-pillars with smaller spaces help the further extension of bacterial nanotube networks. Such nanotube networks can possibly aid in the cell-cell communications, thereby promoting the further biofilm development.

Chapter 5 investigates the growth of *S. epidermidis* and *P. aeruginosa* on hierarchical rose-petal structured surfaces. We duplicated the natural structures on rose-petal surfaces via a simple UV-curable nano-casting technique. We demonstrated that hierarchical structures are more effective in delaying biofilm growth. The mechanisms are two-fold: 1) the nano-folds across the hemispherical micro-papillae restrict initial attachment of bacterial cells and delay the direct contacts of cells via cell alignment, and 2) the hemispherical micro-papillae arrays isolate bacterial clusters and inhibit the formation of a fibrous network.

Chapter 6 investigates the anti-wetting performances and growth of *S. epidermidis* and *P. aeruginosa* on two different slippery lubricant-infused surfaces. The non-toxic silicone oil was either impregnated into the porous surface nanostructures (referred as LIS) or diffused into the polydimethylsiloxane (PDMS) matrix (referred as S-PDMS). The slippery lubricant layers have extremely low contact angle hysteresis, thereby either slippery surface showed superior anti-wetting performances with water droplet which was bouncing off or transient

rolling after impacting the surface. Additionally, we demonstrated that these surfaces have "cleaning effects". Besides, "coffee-ring" effects were inhibited on either slippery surface after the droplet evaporation, and can be easily removed. Either slippery surface can prevent around 90% of bacterial biofilm growth after 6 days, as compared with the unmodified control PDMS surfaces. The dried biofilm stains can also be easy removed from slippery surfaces.

In **Chapter 7**, the key observations and findings of biofilm growth on different surfaces are summarized and discussed. In addition, the limitations regarding to the surface design, experimental work are demonstrated. Finally, the suggestions for future work are provided regarding to effectively controlling bacterial biofilm growth.

Chapter 2
Literature review

2.1 A brief history of biofilm

As early as 1684, the Dutch scientist Anthony van Leewenhoek firstly observed the biofilms with his simple but effective microscopes, describing the vast accumulations of microorganisms on teeth surfaces, which he called as "animalcules in the scurf" (Garrett *et al.*, 2008). A breakthrough in microbiology studies did not begin until the mid of 19th century; with the method of Robert Koch, bacteria were investigated in a single species planktonic (water-based) culture. This pure culture approach became the paradigm to grow and isolate bacteria as free-floating cells (in planktonic form) for many years and proved microorganisms were more complex than expectations (Thomas and Nakaishi, 2006). Until to 1940, H. Heukelekian and A. Heller noticed the “bottle effect” for marine microorganisms, which showed that the growth of bacteria was substantially enhanced when attaching to surfaces in the marine environment (Donlan, 2002). On the other hand, Claude ZoBell also observed similar results as the attached microbial communities on surfaces was greatly enhanced than in the surrounding medium (i.e. seawater) (Costerton, 1999). With these findings, microbiologists began to realize the appearance of biofilms. Nowadays, biofilms have received considerable attentions among the scientists as biofilm formation will significantly affect people’s daily life.

2.2 Importance of controlling biofilm growth

In natural environment, biofilms can be easily formed by a lot of species (e.g. fungi, algae, protozoa, and especially bacteria) and will occur in many environmental settings. Even lots of literatures have reported that biofilms can be beneficial in the field of bioremediation to remove contaminants, either to degrade hazardous substances/chemicals in soil (Peterson *et al.*, 2015), or purify the industrial wastewater (Garrett *et al.*, 2008). unfortunately, more attentions are paid into the negative effects owing to the unwanted biofilm growth. In industry, biofilms can cause contamination of food/drink, enhancement of metal corrosion, clogging etc. (Poulsen, 1999; Garrett *et al.*, 2008; Beech *et al.*, 2010; Dufour *et al.*, 2010). For example, biofilms present a serious hazard to the drinking supply owing to the possibility of water contaminated with pathogens. On the other hand, during processing environments, pathogenic microflora attached onto the food can also cross-contaminate and cause post-processing contaminations (Poulsen, 1999). In the petrochemical industry, biofilms may cause the blockage of oil pipelines and equipment failure, which decrease the production efficiency (Garrett *et al.*, 2008). In marine industry, biofilm can cause biofouling

problem on marine vessels, leading to the increased drag and energy loss, which may damage the hull structures and propulsion systems (Beech *et al.*, 2010).

From a public health perspective, diseases like dental caries, periodontitis, cystic fibrosis pneumonia, native valve endocarditis, chronic otitis media, bacterial prostatitis, musculoskeletal infections, biliary tract infection, meloidosis, osteomyelitis and bacterial prostatitis are all likely to be caused by biofilm-associated microorganisms (Chandki *et al.*, 2011). Besides, hospital-related infection (nosocomial infection) is periodically caused by biofilms, which is also a major cause of human infections (Dufour *et al.*, 2010). Indeed, a large number of nosocomial infections are associated with the colonization of pathogens and the subsequent biofilm formation onto the surfaces of biomedical devices, such as scalpels, respirators, catheters (central venous, urinary), prosthetic heart valves, and orthopedic devices (see Table 2.1). It has been reported that 87% of bloodstream infections are associated with intravascular devices, 80% of pneumonias are relevant to mechanical ventilation, and 95% of urinary tract infections are related to a urinary catheter (Dufour *et al.*, 2010). These biofilm-related infections are clinically important as the structure of biofilm protects the encased bacteria from the host immune responses and antibiotic treatment. Such a special characteristic allows the bacteria to persist for a long time in the human body. Thus, the request of effective strategy to inhibit biofilm formation and subsequently avoid infections is necessary.

Table 2. 1 Biofilms of indwelling medical devices (Dufour *et al.*, 2010).

Medical device	***Principle microorganisms***
Contact lens	*P. aeruginosa*, Gram-positive cocci
Denture	*Candida* spp.
Urinary catheter	*E. coli*, *Candida* spp., *E. faecalis*, *P. mirabilis*, *K. pneumoniae*
Central venous catheter	CoNS*, *S. aureus*
Mechanical heart valve	CoNS, *S. aureus*
Artificial hip prosthesis	CoNS, *S. aureus*, *Enterococcus* spp.
Voice prostheses	*C. albicans*, CoNS
Endotracheal tubes	Enteric Gram-negative species

* CoNS: coagulase-negative staphylococci (e.g. *S. epidermidis*).

2.3 Biofilm formation and lifecycles

Investigating the biofilm formation and lifecycle will be helpful to determine methods to disrupt the biofilm structure or prevent harmful biofilm formation on surfaces. The development of biofilm formation is a dynamic process governed by a number of chemical, physical and biological factors (Palmer and White, 1997; Garrett *et al.*, 2008), and briefly involves five stages (see Figure 2.1). In which case, we mainly focus on the bacterial adhesion and biofilm formation process as follows:

1. Development of a surface conditioning film
2. Movement of microorganisms into close proximity with the surface
3. Adhesion (reversible and irreversible adhesion of microbes to the conditioned surface)
4. Growth and division of the organisms with the colonization of the surface, micro-colony formation and biofilm formation; phenotype and genotype changes
5. Biofilm cell detachment/dispersal

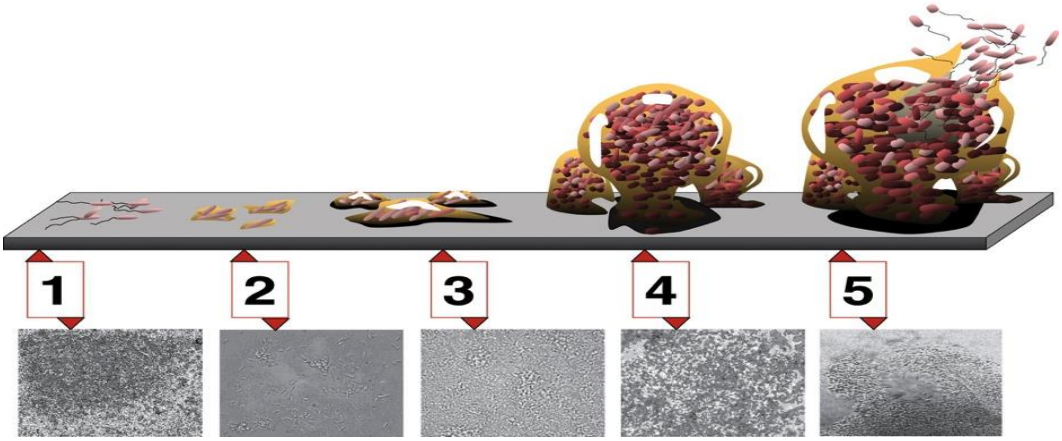

Figure 2. 1 The formation of biofilm (i.e. *Pseudomonas aeruginosa* biofilm in this case) with a five-stage process, each stage is corresponding to the five stages that mentioned above, which was taken from (Monroe, 2007).

The development of surface-conditioning films is considered as the initial step to form biofilms, which has been well reported (Garrett *et al.*, 2008; Lorite *et al.*, 2011; Kanematsu and Barry, 2015). The formation of conditioning films were firstly observed by Loeb *et al.* (Loeb and Neihof, 1975), where on the surfaces after few minutes of exposure to seawater, and they subsequently continued to grow for several hours. On the other hand, Mittelman (Mittelman, 1996) observed the effects of conditioning films on the bacterial attachment onto biomaterials, which mainly consisted of polysaccharides and proteinaceous from blood,

urine, tears, and saliva respiratory secretions. If there are sufficient nutrients, conditioning films will be formed with the adsorption of (macro) molecules or proteins onto surfaces, which alters the physicochemical properties of the substrate surface (e.g. surface charge, potential and tensions etc.). Particularly, the properties of the conditioning films proposed quite differently depending on the exposure environment of the substrate, thereby modifying substrates facilitating accessibility to microorganisms (Lorite *et al.*, 2011), and thus affects the initial bacterial attachment.

When moving into close proximity with the conditioned surface, planktonic bacterial cells attach onto the surface either by physical forces or by bacterial appendages like flagella (Garrett *et al.*, 2008). Initially, bacterial cells reach the surface by its motility or Brownian motion, and adheres reservedly. Elucidation of the mechanisms underlying bacterial adhesion can be explained by the classical Derjaguin–Landau–Verwey–Overbeek (DLVO) theory, with several physical forces contribute to this process, such as attractive van der Waals interactions and repulsive electrical double layer interactions (Hermansson, 1999). However, due to the weakness of bonds, if the attractive forces are smaller than repulsive forces, the bacterial cells will detach from the substrate surfaces (An *et al.*, 2000). In the following stage, bacterial cells use physical appendages (e.g. flagella, fimbriae and pili) or produce extracellular polymeric substances (EPS) to bridge the substrates, overcoming the physical repulsive forces of the electrical double layer (Garrett *et al.*, 2008; Hori and Matsumoto, 2010). After that, bacteria cells can anchor themselves and remain immobilized on the surfaces irreversibly. It is argued that the physical appendages consolidate the bacteria–surface bonds with stimulating chemical reactions such as oxidation and hydration by making contact with the bulk lattice of the conditioning layer (Kumar and Anand, 1998). Typically, evidences also have shown that hydrophobic/hydrophilic properties of interacting surfaces will significantly affect the bacterial adhesion processes, thereby taking into consideration of hydrophobic/hydrophilic interactions, which have been well explained by the thermodynamic approach and the extended DLVO theory (XDLVO) (Hori and Matsumoto, 2010).

Once the microbial cells have attached onto surfaces irreversibly, maturation of the biofilm begins to occur. Micro-colonies (i.e. bacterial clusters) are formed by the growth and division of the initial attached cells. This process involves the replication (binary division) of stationary cells, with the daughter cells spreading around from the attachment point to

form clusters (Garrett *et al.*, 2008). Progressively, micro-colonies enlarge and coalesce into a multi-layer of cells with a mushroom-like structure at the expense of the surrounding nutrients from the bulk fluid and the substrates (Dufour *et al.*, 2010). Typically, such a mushroom-like structure plays as the passages to help distribute nutrients to bacteria deep within a biofilm. At this stage, the contributions from physical and chemical factors end, and the biological processes begin to dominate. Proximity of cells within the micro-colony (or between micro-colonies) can provide an ideal environment for the creation of nutrient gradients, exchange of genes and quorum sensing, thereby affecting biofilm formation (Donlan, 2002).

The final stage of biofilm formation is known as dispersion, which is essential for the biofilm life cycle with the propagation of cells. It has been reported that enzymes are produced by the community itself, which then degrade the biofilm extracellular matrix, such as dispersin B and deoxyribonuclease, actively releasing the bacteria cells (Kaplan *et al.*, 2003; Izano *et al.*, 2008). Subsequently, these detached cells will spread and colonize onto new surfaces, following forming biofilms in the new environments.

The regulation of the molecular mechanisms during the different developmental stages of biofilm formation are quite different among various bacterial species, and also vary greatly depending on the environmental conditions for the same given species (Dufour *et al.*, 2010). However, biofilms possess a common characteristic, the biofilm matrix. Compared to the free-floating planktonic cells, the adherent cells in biofilms are frequently embedded within a self-secreted polymeric compounds, also called as the extracellular polymeric substance (EPS), which sticks them together (Flemming *et al.*, 2007). Depending on the species involved, biofilms may be composed of 75-90% EPS (by volume) and only 10–25% cells (by volume) (Costerton *et al.*, 1987). The components of EPS consist of polysaccharides, and a wide variety of proteins, glycolipids, glycoproteins, and in extracellular DNA (e-DNA) (Flemming *et al.*, 2007). The EPS is metaphorically called as the "house of the biofilm cells", which determines the immediate conditions of biofilm cells living in such a microenvironment (Flemming *et al.*, 2007). Also, the EPS is highly hydrated, which retains water and avoids desiccation of biofilms; and the EPS allows for sequestering of particulate and dissolves substances from the environment, providing nutrients for biofilm organisms (Flemming and Wingender, 2010). The EPS can also maintain the integrity of biofilm, which provides sufficient mechanical stability to keep a spatial arrangement for micro-consortia

over a prolonged period. This stability mainly comes from hydrophobic interactions, cross-linking by multivalent cations, and entanglements of the biopolymers. On the other hand, the EPS can also contribute to the antimicrobial resistance, which can play as a diffusion barrier, impeding the toxic substances such as disinfectants or antibiotics from reaching their targets (Donlan, 2002; Flemming *et al.*, 2007; Flemming and Wingender, 2010).

2.4 Factors affecting initial bacterial attachment

The colonization of bacterial cells onto surfaces involve a transition from a free living planktonic lifestyle in the bulk fluid environment to a sessile, surface-attached state (Berne *et al.*, 2018). Specifically, this process may have two different outcomes: (1) reversible adhesion, weakly attached bacterial cells detach from the surface and return to the planktonic bulk medium; (2): irreversible adhesion, the interaction of bacteria-surface is strengthened by cell appendages or production of adhesin molecules (Berne *et al.*, 2018). After this, the irreversibly attached cells can divide to grow and develop into a mature biofilm. Therefore, it is commonly accepted that the initial bacterial attachment with surface colonization is the key step to trigger biofilm growth on surfaces. For the initial bacterial attachment, we mainly considered two factors here: the solid surface and the bacterium itself.

2.4.1 Surface charge

Surface charge has long been known to affect the bacterial attachment onto material surfaces, and influence the subsequent biofilm formation. Most bacterial cells are negatively charged, hence generally a positively charged surface is more favorable for bacterial adhesion, and a negatively charged surface is more resistant to bacterial adhesion (Song *et al.*, 2015; Chen, 2016). Meanwhile, surfaces with certain cationic groups, such as cationic peptides, chitosan, quaternary ammonium, polyethylenimines and some antibiotics, have been reported to be antibacterial, which can also potentially kill the attached cells (Campoccia *et al.*, 2013; Song *et al.*, 2015; Chen, 2016). It was believed that modifying the surface charge to control bacterial adhesion may not work in a static system (Song *et al.*, 2015). This is because the dead cells may play as barriers which can reduce the surface charge, thereby may hinder the antibacterial efficiencies or even promote the bacterial attachment onto a positively charged surface (Song *et al.*, 2015). However, modifying the surface charge can be used in some oral applications as the shear forces (e.g. coming from the rising, brushing etc.) are expected to remove the dead cells from the dental materials (Song *et al.*, 2015).

2.4.2 Surface hydrophobicity

Surface hydrophobicity also plays an important role in bacterial attachment onto material surfaces and has been extensively investigated (Song *et al.*, 2015; Chen, 2016). The influences of surface hydrophobicity depends on the hydrophobicity of bacterial species, and the bacterial adhesion can be either promoted or inhibited (Quirynen and Bollen, 1995). For example, Mabboux *et al.* (Mabboux *et al.*, 2004) reported that the bacterial attachment of hydrophobic *S. sanguinis* onto the saliva-coated pure titanium grade 2 (cp-Ti) and Ti-6A-4V alloy was much higher compared to the hydrophilic *Streptococcus constellatus*. More contemporary researches showed that either superhydrophobic or superhydrophilic surfaces can inhibit the bacterial adhesion and biofilm formation. The main inspiration to design superhydrophobic surfaces came from the natural lotus leaf, which has a water contact angle above 150º. As indicated by the Cassie-Baxter model, for a patterned surface that reaches the Cassie state with an appropriate roughness, air can be trapped in the grooves between the surface features thereby preventing wetting (Chen, 2016). Thus, such superhydrophobic surfaces showed remarkable self-cleaning effects (Tang *et al.*, 2011). Adhesion of water drops that contact the superhydrophobic surfaces is so low that they can easily move and roll off the surface by sweeping of dusts, dirt and microorganisms (Ivanova *et al.*, 2012; Hasan and Chatterjee, 2015). A number of superhydrophobic surfaces have been designed based on these principles, such as silicone elastomer, TiO_2 nanotubes, poly(L-lactic acid) surface etc.(Zhang *et al.*, 2013). On the other hand, with the formation of a dense layer of water molecules, superhydrophilic surfaces possess as non-fouling that can weaken the cell-material interactions and therefore can reduce cell adhesion (Song *et al.*, 2015). This principle, which is well known as *water layer theory*, has been well applicable into designing various non-fouling surfaces. For example, zwitterionic polymers, which are superhydrophilic consisting of neutral molecules with a positive and a negative electrical charge in close proximity, can reduce the fouling caused by proteins or bacteria (Song *et al.*, 2015; Chen, 2016).

2.4.3 Surface roughness

Surface structure has been reported to have a significant influence on microbial colonization and biofilm formation. Generally, the surface structure can be characterized by the roughness (two-dimensional measurement based on the mean distance between peak and valley) and topography (three-dimensional measurement) (Song *et al.*, 2015). Both

experimental and computational modelling work have (Czarnecki and Warszyński, 1987; Bhattacharjee *et al.*, 1998; Scheuerman *et al.*, 1998; Taylor *et al.*, 1998; Ammar *et al.*, 2015) suggested that the increase of roughness (e.g. irregularities such as scratches and pores) on surfaces can promote the bacterial attachment as surface area is also increased, which may provide more favorable sites for colonization as well as a decrease in the energy barrier for bacteria to be deposited onto the material surface. For example, the experimental results of Taylor *et al.* (Taylor *et al.*, 1998) showed that the attachment of *S. epidermidis* and *P. aeruginosa* increased significantly on a rougher surface of poly (methyl methacrylate (PMMA), whose average roughness value (i.e. Ra) slightly increased from 0.04 μm to 1.24 μm. On the other hand, Taylor *et al.* (Taylor *et al.*, 1998) also suggested that there might exist an optimal Ra value for bacterial attachment in their experimental system as the attachment decreased when the roughness value Ra increased from 1.86 to 7.89 μm (Taylor *et al.*, 1998). In addition, it has also been well reported that bacterial attachment may be enhanced when the roughness is above a certain threshold (about 200 nm) (Tang *et al.*, 2009; Yoda *et al.*, 2014). However, Lorenzetti *et al.* (Lorenzetti *et al.*, 2015) reported that for the titanium-based substrates with roughness between 300-800 nm, the bacterial attachment of *E. coli* is reduced with the increase of roughness. Our previous work (Cao *et al*., 2018) also has found that the bacterial attachment is lower on nanostructured titanium surfaces (Ra ~195.0 ± 6.5 nm) as compared with a smoother polished titanium surface (Ra~ 13.2 ± 2.3 nm). This is because the conventional definition of roughness can only reflect unevenness in height (z) direction, which is expressed as the arithmetic average deviation of the surface valleys and peaks. Also, the conventional optical profilometry cannot predict surface roughness accurately owing to some samples may have poor light reflection; AFM measurement is also limited since the probe may only scan a small surface area (e.g. 10 μm^2). Therefore, surface roughness is limited to describe the three-dimensional features on the surfaces, especially the lateral dimensions in x, y directions as described by the surface topography. Surface topography may play the dominant role in bacterial attachment and biofilm formation especially at a micro or nanoscale, and will be demonstrated as follows.

2.4.4 Surface topography

The surface topography with specific patterns can modify hydrophobic properties of the surface, a crucial parameter for the initial bacterial attachment (Berne *et al.*, 2018). Also, it was believed that bacterial attachment strongly depends on the surface topography instead

of roughness at a micro or nanoscale (Xu and Siedlecki, 2014; Lorenzetti *et al.*, 2015). The scale of topography affects the retention of bacteria on the surface if the scale of topographic features (~microstructure or submicron-structure) is comparable to that of bacteria. The irregularity (e.g. crevices, trenches, grooves) is likely to enhance the overall surface area which bacterial cells can contact, thereby promotes bacterial adhesion (Palmer *et al.*, 2007; Seddiki *et al.*, 2014; Berne *et al.*, 2018). In addition to maximizing the contact area between the bacterial cells and surface, the specific cell patterning or alignment within the microstructures can reduce the shear experienced by attached cells (Renner and Weibel, 2011). It has been found that the model bacterial strains such as *Shewanella oneidensis* (Jeong *et al.*, 2013), *Pseudomonas aeruginosa* (Hochbaum and Aizenberg, 2010; Díaz *et al.*, 2011a; Lai, 2018), *E. coli* and *S. epidermidis* (Helbig *et al.*, 2016), preferentially attach into the recessed portions of micro-patterned surfaces (Figure 2.2a), thereby the attached bacterial cell exhibited the cell patterning behavior which aligned the designed micro-patterns on surfaces. For nano-patterned surfaces, lots of studies showed that the pathogens *P. aeruginosa*, *E. coli*, *S. aureus* and *S. epidermidis* experienced greatly impaired attachment if the surface nano-pattern is significantly smaller than the bacterial size (Helbig *et al.*, 2016; Hizal *et al.*, 2016; Lu *et al.*, 2016; Hizal *et al.*, 2017; Cao *et al.*, 2018). The scale of surface topography is too small for the bacterium to fit, it would reduce the contact area and the binding between the bacteria and the material surface, thereby leading to a much lower adhesive strength (Seddiki *et al.*, 2014). However, the effects of surface nano-patterns on bacterial attachment is still up for debate, and conflicting results have been reported owing to different experimental procedures (Figure 2.2 b) (Berne *et al.*, 2018; Cao *et al.*, 2018). For example, it has been found that nano-patterns cannot affect the attachment of *P. aeruginosa* or *E. coli*, while can significantly reduce the retention of the *Staphylococci* on surfaces (Ivanova *et al.*, 2011; Bagherifard *et al.*, 2015). The different cell responses were likely attributed to the different cell shape (rod-shape versus spherical-shape) (Ivanova *et al.*, 2011) and the composition of the cell envelope (Gram-negative versus Gram-positive) (Bagherifard *et al.*, 2015).

For a micro or nano-patterned surface, the scaling of surface topography would cause different bacterial responses depending on the different cell-material contacts, which also inspired researcher to design novel surface patterns to control the initial bacterial attachment, involving various techniques such as screen printing, soft lithography, nanoimprint lithography/embossing, laser ablation, three-dimensional printing and photo-patterning

(Chen, 2016). While these artificial man-made are fabricated by different materials, different methods, with different surface topography. Additionally, the tested bacterial strains are different and the experimental procedure (flow cell or static, different incubation time) also differ from study to study. With the increase of the studies on diverse material surfaces and bacterial systems, a clearer consensus on the effects of micro-structured or nanostructured surfaces on bacterial attachment may emerge.

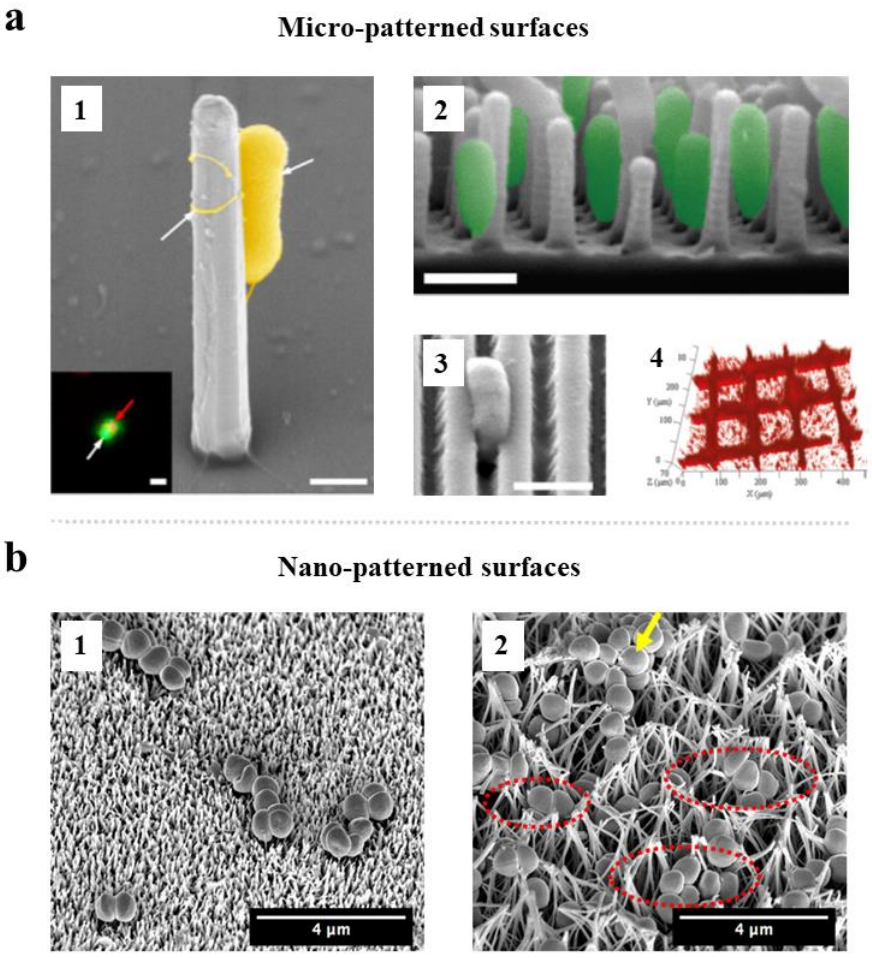

Figure 2. 2 Effects of surface topography on the bacterial attachment. **(a):** bacterial cells preferentially attach into the recessed portions of micro-patterned surfaces, showing as a1: *Shewanella oneidensis* preferentially attached and aligned along the length direction of an individual silicon nanowire (scanning electron microscope (SEM) image, scale bar 500 nm) (Jeong *et al.*, 2013); a2: *P. aeruginosa* cells aligned themselves along the length of the nano-pillars, normal to the surfaces, (the cross-sectional SEM image, scale bar 1 µm) (Hochbaum and Aizenberg, 2010); a3: SEM images of an aligned *P. aeruginosa* cell on nano-grating with the width of 350 nm (scale bar 1 µm) (Lai, 2018); a4: fluorescent three-dimensional view of bacterial clusters on a micro-patterned surface, showing bacteria prefer to attach into the valleys (Hou *et al.*, 2011). **(b1)** *S. epidermidis* cells settled on the top of spears resulting in point contacts; **(b2)** *S. epidermidis* settled inside the pocket-like nanostructures (outlines of selected pockets are marked by dashed red lines). The longer, intertwined nano-spears were also observed to provide colonization sites for bacteria (arrow) (Cao *et al.*, 2018).

2.4.5 Bacterial surface and appendages

Although the bacterial cell is usually negatively charged, the bacterial cell surface is highly heterogeneous and contains different exposed lipids, proteins, exopolysaccharides, non-fimbrial or fimbrial structures (Berne *et al.*, 2015). Therefore, the cell envelopes can exhibit different charges and hydrophobicity around the cell body, depending on the environmental pH and ionic strength (Figure 2.3) (Dufrêne *et al.*, 2013; Berne *et al.*, 2018). Notably, the hydrophobic components of the cell envelope, such as the polymeric brush layer, proteins and extracellular polysaccharides, can enhance the hydrophobic interactions of bacteria and surfaces at the microscale level (Berne *et al.*, 2018). These various biopolymers on cell surfaces may help bacterial cells to overcome the interfacial water, thereby can reach to surfaces closely (Figure 2.3 a). If the distance of bacteria to surface is approaching the nano-meter scale, the bacterial cell appendages (such as flagella, pili and curli) and the adhesin produced by bacteria can interact with the solid surfaces, thereby may promote the cell adhesion (Figure 2.3 b) (Berne *et al.*, 2018).

In addition to the swimming motility of bacterial flagella which can actively propel bacteria to the surface (Lemon *et al.*, 2007), the flagella can also help bacteria to anchor onto the surface irreversibly (McClaine and Ford, 2002; Conrad *et al.*, 2011; Berne *et al.*, 2018). For example, the presence of motile flagella was reported to aid in the surface wetting and mask the surface chemistry as the conditioning film for bacterial attachment (Friedlander *et al.*, 2013). By surface-bound spinning, flagella can help the repositioning of the cell body from a polar to a longitudinal attachment. As such, the longitudinal positioning may maximize the contact area between the bacterial cells and the surface, thereby enhance the cell attachment (Petrova and Sauer, 2012). In addition, bacterial flagella can provide substantial benefits for cell adhesion in topographical environments (Friedlander *et al.*, 2013). It has been found that the attachment of wild-type *E. coli* having the flagella was significantly increased on the microscale hummocks as compared with the flat surface, and flagella filaments aid in adhesion via accessing additional surface crevices (Friedlander *et al.*, 2013). Upon contact with the surface, bacteria may use their flagella to explore and access the additional surface topography, or to overcome unfavorable surface topographies, with forming a dense, fibrous network (Friedlander *et al.*, 2013). Furthermore, a recent study found that the flagella of *E. coli* cells can actively sense the material stiffness to see if attachment is favorable, thereby will reduce motility and initiate the colonization (Song *et al.*, 2017).

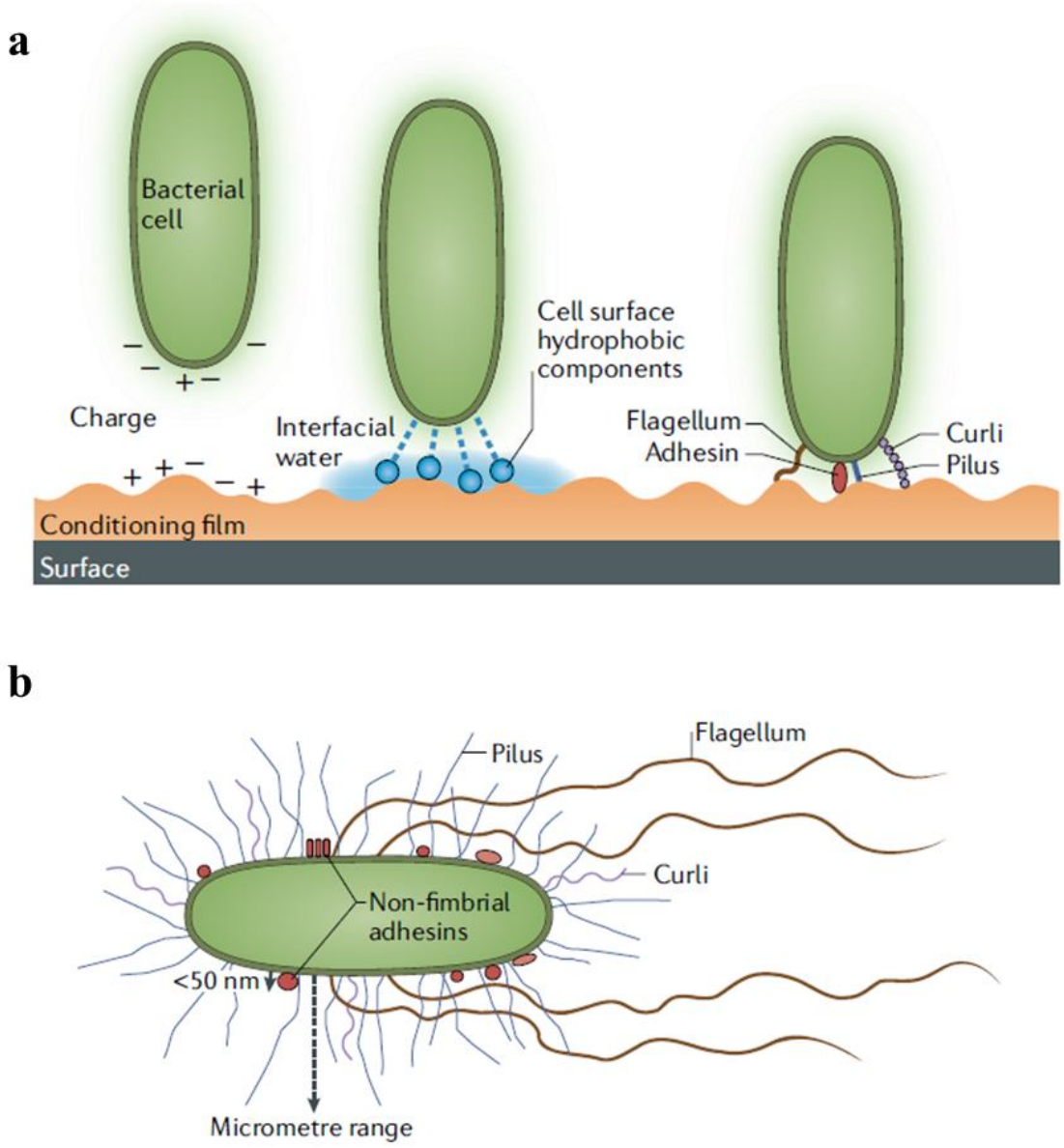

Figure 2. 3 (a): the interactions between the cell envelope and solid surface. Orange: the conditioning film; light blue: interfacial water; dark blue: hydrophobic components on the cell surface; **(b):** adhesins (red) and bacterial cell appendages (such as flagella (brown), pili (blue) and curli (purple)) on cell envelope.

In addition to flagella, other cell surface extensions such as fimbriae, curli and pili (Figure 2.3b), have been found to aid in the bacterial adhesion onto the solid surfaces (Berne *et al.*, 2018). Typically, the function of pili in different types of the various bacterial species have been well investigated in the first step of adhesion, for example, *E. coli* type I pili (Pratt and Kolter, 1998) and *P. aeruginosa* type IV pili (T4P) (Conrad *et al.*, 2011; Jin *et al.*, 2011). T4P can allow *P. aeruginosa* cells to rapidly explore microenvironments via horizontally oriented crawling and vertically oriented walking upon the surfaces (Conrad *et al.*, 2011).

The length of T4P can elongate via polymerization and retract by de-polymerization along the surfaces (Maier and Wong, 2015). There has some modelling work that study bacterial twitching in fluid flows, showing that number of pili and pili distribution angle, could be used to select the nature of bacterial twitching motility depending on the environmental conditions (Jayathilake *et al.*, 2019). When the pili adheres to an object during retraction, a large velocity of the slingshot motion is applied which enables bacteria to move and trigger downstream signaling in host cells, thereby can spread efficiently during biofilm formation (Jin *et al.*, 2011; Jayathilake *et al.*, 2019). In addition, when bacteria twitch on groove surfaces, they tend to accumulate around the downstream side of the groove walls (Jayathilake *et al.*, 2019).

2.5 Antibacterial surfaces

Biomaterial surface design is critical for controlling bacterial-material interactions, and various materials can be used like polymer (e.g. PDMS), ceramics (e.g. bio-glass), or metallic (e.g. titanium), depending on the actual applications (Chen, 2016). To eliminate or control the bacterial growth on the surfaces, it can be achieved by through inhibiting the bacterial attachment or growth, and by killing the attached bacterial cells. This yields the concept of 'antibacterial surface' (Hasan and Chatterjee, 2015), which are of mainly two kinds, 1): bactericidal or bacteria-killing surfaces, which can disrupt the cell on contact thereby causing the cell death, and 2): antifouling or bacteria-resistant surfaces, which are capable of resisting the extent of bacterial attachment thereby inhibiting an early-stage biofilm formation. Typically, designing antibacterial biomaterial surfaces can be either chemical-based or physical-based. For example, applying coatings or doing chemical surface modification of substrata (as are surface polymerization, functionalization, and derivatization) are generally considered to be a chemical approach, whereas, modification of the surface structure of a substrate can be considered a physical approach (Hasan *et al.*, 2013a).

2.5.1 Bactericidal surfaces

2.5.1.1 Chemical-based bactericidal surfaces

Antimicrobial agents might be the first one that come into mind when mentioning about killing bacteria, which are mainly of three kinds: oxidants (e.g. chlorine), biocides (e.g. metallic nanoparticles like silver) and antibiotics (e.g. tobramycin) (Hori and Matsumoto,

2010). Based on this, release-based bactericidal surfaces are designed by involving these antimicrobial agents, which are preloaded or embedded before being leached out to kill bacteria (Yu *et al.*, 2015). One of the typical examples is the silver nanoparticles (AgNPs), owing to their strong and broad-spectrum bactericidal characteristics (Shrivastava *et al.*, 2007; Knetsch and Koole, 2011; Prabhu and Poulose, 2012). By releasing Ag^{+} ions, it can damage the bacterial membrane as well as disrupt the function of bacterial enzymes or nucleic acid groups in the cellular protein and DNA, thereby killing the bacteria (Yu *et al.*, 2015). Other nanoparticles like photocatalytic TiO_2 with different crystal structures also have been reported to be bactericidal (Nel *et al.*, 2006; Lin *et al.*, 2014; Zhukova, 2015; Choi *et al.*, 2017). Owing to the photocatalytic activities under the UV-irradiation, the released TiO_2 nanoparticles can produce reactive oxygen species (ROS), which are strong oxidants that can damage the cell walls and membranes, with the consequent cell death (Zhukova, 2015). Other types of bactericidal surfaces that can release antibiotics or oxidants also have been reported and widely used to avoid the bacterial infections (Yu *et al.*, 2015). However, this approach is quite unsustainable due to the negative impacts on the environment. Another major concern is that the reservoir of leaching antimicrobial agent is subject to depletion over a period of time; and the gradually decreasing level of released agent can lead to the development of antimicrobial resistance (Lorenzetti *et al.*, 2015).

A more sustainable and environmentally friendly approach is to design the contact-based bactericidal surfaces, which are coated with contact-active antibacterial agents by either covalent conjugation or physical adsorption to kill the adhering bacteria (Yu *et al.*, 2015; Kaur and Liu, 2016). The most commonly reported contact-active antibacterial agents are some synthetic chemicals like quaternary ammonium compound (QAC) and polycations, or some natural biomolecules such as chitosan, antimicrobial peptides (AMPs) and antimicrobial enzymes (AMEs) (Yu *et al.*, 2015). Due to the positively charged quaternary ammonium groups and the long hydrophobic alkyl chains, QAC coatings have shown effective bactericidal activities against both Gram-negative and Gram-positive bacteria. The mechanism found in publications is that the ion exchange of Ca^{2+} and Mg^{2+} ions of the cytoplasmic membrane with QAC molecules, can cause the instability of the intracellular matrix of a bacterium (Yu *et al.*, 2015; Kaur and Liu, 2016). It was also believed that the hydrophobic tails can be interdigitated into the hydrophobic bacterial membrane over the entire surface area of a bacterium, resulting in the disturbance of the cytoplasmic membrane and the leakage of intracellular-fluids which consist of essential molecules (Yu *et al.*, 2015).

Quaternary ammonium silane of 3-(trimethoxysilyl)-propyldimethyloctadecyl ammonium chloride (QAS), which is considered as one typical QAC, can be easily immobilized via covalent bonds onto the surfaces with hydroxyl groups (such as cotton, silica particle, silicone rubber, titanium, and cellulose) (Yu *et al.*, 2015). Besides, other polymers with quaternary ammonium groups at their side chains have also been designed and fabricated as polymeric biocides, such as quaternized poly(4-vinyl-N-alkylpyridinium bromide) (PVP) and quaternized poly(2-(dimethylamino ethyl) methacrylate) (PDMAEMA) (Yu *et al.*, 2015).

Natural antibacterial agents like AMPs and AMEs also have been widely used, which can be immobilized onto surfaces via adsorption, layer-by-layer assembly or covalent bonding, to fabricate the bactericidal coatings (Yu *et al.*, 2015). AMPs are an integral part of the innate immune system with viricidal, fungicidal, tumoricidal and especially bactericidal properties (Hasan *et al.*, 2013a; Harding and Reynolds, 2014). Surfaces that coated with AMPs are thus inherently biocompatible and can impart antimicrobial activity derived from the cationic charged peptides (Harding and Reynolds, 2014). It has been reported that AMPs can be effectively bactericidal against various pathogenic bacterial strains, including *P. aeruginosa*, *Fusobacterium nucleatum*, *Fusobacterium nucleatum*, *S. aureus*, *S. gordonii*, and *Porphyromonas gingivalis* (Harding and Reynolds, 2014). For AMEs, they are also capable of killing bacteria and interfering with biofilm formation, and have been well reported. For example, proteolytic enzymes (e.g. subtilins) can hydrolyze bacterial proteins, and thereby damage the cells (Thallinger *et al.*, 2013). Polysaccharide-degrading enzymes (e.g. amylases and lysozymes) are also reported to be bactericidal against a variety of Gram-positive and Gram-negative bacteria (Thallinger *et al.*, 2013).

A new trend nowadays is incorporating different antibacterial agents into one system by combining of both release-based and contact-based mechanisms (Hasan *et al.*, 2013a; Yu *et al.*, 2015). For example, dual-functional bactericidal coatings with two distinct layered functional regions (i.e. a polyelectrolyte multilayer reservoir for the loading and release of bactericidal AgNPs and a SiO_2 NPs surface cap with immobilized QAS) have been developed (Hasan *et al.*, 2013a; Yu *et al.*, 2015). These dual-functional coatings showed very high initial bacteria-killing efficiency owing to the release of Ag^+ ions and retained significant antibacterial activity after the depletion of embedded Ag due to the immobilized QAS (Li *et al.*, 2006). Other dual-functional bactericidal coatings also have been reported, which included titanium-doped iron, silver-doped titanium, silver-doped silica films, silver-

doped phenyltriethoxysilane, silver-doped inorganic–organic hybrids and silver-doped HA coatings (Hasan *et al.*, 2013a).

2.5.1.2 Physical-based bactericidal surfaces

More contemporary approach with the production of nanostructured bactericidal surfaces by mimicking the surface topography of wings of cicada (Ivanova *et al.*, 2012; Hasan *et al.*, 2013b) or dragonfly (Ivanova *et al.*, 2013a; Mainwaring *et al.*, 2016), and gecko skin (Li *et al.*, 2016; Green *et al.*, 2017) has enjoyed increased interests from researchers. The main principle for these nanostructured bactericidal surfaces is that bacterial cell membranes may deform or mechanically rupture owing to the bacterial adhesion onto the nanostructures, or get stretching/compression in between the nanostructures, thereby causing the cell damages (Ivanova *et al.*, 2012; Pogodin *et al.*, 2013; Diu *et al.*, 2014; Xue *et al.*, 2015; Li, 2016; Li *et al.*, 2016).

Ivanova *et al.* (Ivanova *et al.*, 2012; Hasan *et al.*, 2013b) found that the naturally occurring high aspect ratio nanopillar-structures on the wing of *Psaltoda claripennis* cicada can kill the attached bacteria, including Gram-negative bacteria like *Branhamella catarrhalis*, *Escherichia coli*, and *Pseudomonas fluorescens*. Typically such a bactericidal activity was physically mechanical-based as the nanopilliars can potentially pierce the cell membrane thereby causing bacterial death, with no apparent influences arising from the chemistry of the surface (Ivanova *et al.*, 2012). In the following study, similar patterned surface features were also found on the dragonfly wings and have been reported to be bactericidal against both Gram-negative (*P. aeruginosa*) and Gram-positive (*Staphylococcus aureus*, *Bacilus subtilis*) bacteria, as well as yeast (Ivanova *et al.*, 2013a; Ivanova *et al.*, 2013b; Nowlin *et al.*, 2015; Mainwaring *et al.*, 2016). By mimicking the surface topography of dragonfly or wings of cicada, similar synthetic nanostructures, such as black silicon, titanium and polymers (e.g. poly (methyl methacrylate) (PMMA)) (Ivanova *et al.*, 2013a; Diu *et al.*, 2014; Bhadra *et al.*, 2015; Dickson *et al.*, 2015; Li, 2016; Sjöström *et al.*, 2016) have been produced. For example, high aspect-ratio nano-features similar to the dragonfly were fabricated on silicon by reactive-ion etching technique, and showed a mechanical-based bactericidal effect against Gram-negative (i.e. *Pseudomonas aeruginosa*) and Gram-positive (i.e. *Bacillus subtilis* and *Staphylococcus aureus*) bacteria (Ivanova *et al.*, 2013a). On the other hand, Bhadra *et al.* (Bhadra *et al.*, 2015) fabricated the antibacterial titanium nano-patterned arrays inspired by dragonfly wings via a simple hydrothermal etching process,

which can kill nearly 50% of *P. aeruginosa* and about 20% of *S. aureus* that adhered onto the nanostructured surface. In addition, by mimicking the cicada wings, Sjöström *et al.* (Sjöström *et al.*, 2016) fabricated the bactericidal nanospiked titanium surfaces via thermal oxidation, which can effectively kill the attached *E. coli*. The dimensions of these nanospikes depended on either the Ar flow rate or the annealing temperature during the oxidation process. Typically, the results also demonstrated that the close-packed, random-arranged nanospikes with pyramid shapes can be more effective to damage the bacterial cell walls (Sjöström *et al.*, 2016). Besides these, cicada-inspired nanopillars were fabricated on the PMMA surfaces by nanoimprint lithography, and exhibited the bactericidal activities against the attached *E. coli* (16%-141% higher dead fraction than the control). It also indicated that the closely spaced nanopillars with smaller diameters were more effective to kill the bacteria (Dickson *et al.*, 2015). Similar nano-patterns such as spear-like and pocket-like titanium nanowires were fabricated by Cao *et al.*(Cao et al., 2018) and tested against gram-positive *S. epidermidis*, and indicated that the bactericidal activities of these nanostructures were a result of the combined effects of the penetration and the stretching/compression from the nano-spears (Figure 2.4).

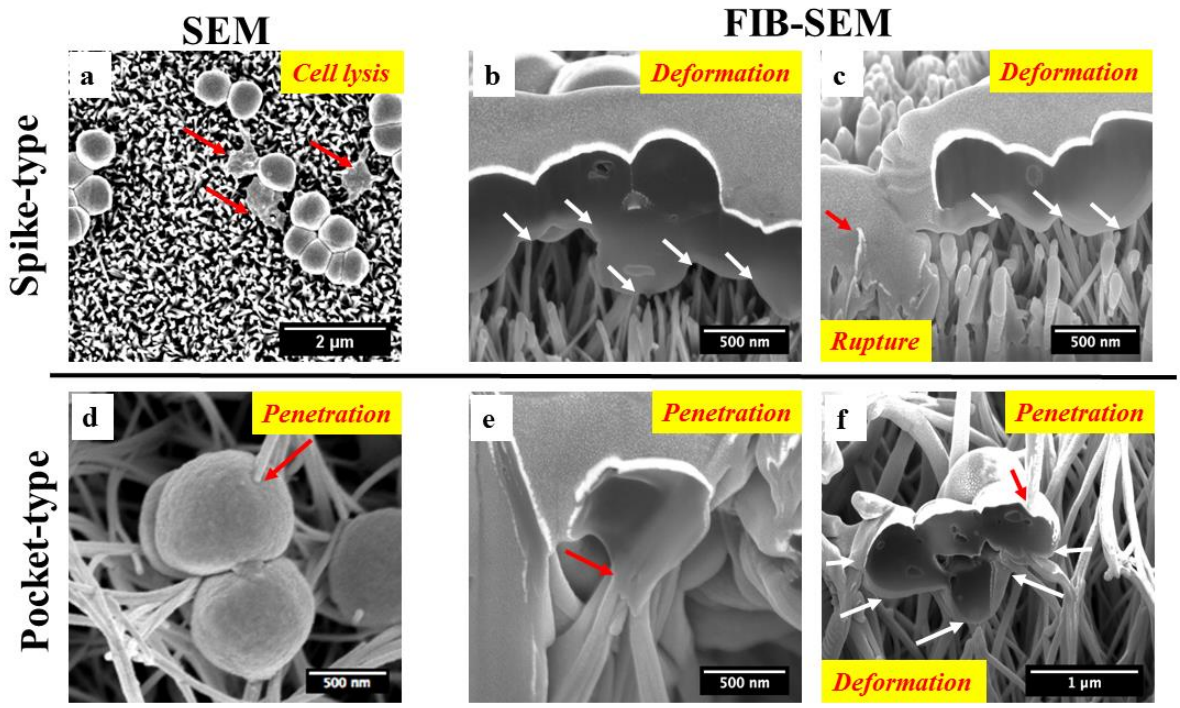

Figure 2. 4 Bactericidal activities of the spear-type and pocket-type surfaces after 2 hours' incubation. **(a)** SEM images showing morphology of *S. epidermidis* on the spear-type surface. Some bacteria were flattened indicating cell death (red arrows). **(b-c)** The interaction between *S. epidermidis* cell membrane and the nanostructured spear-type surface,

visualized by FIB-SEM. The sharp tips of nano-spears on surfaces resulted in the deformation of bacteria cell membranes (white arrows). The red arrows represent cell rupture and leakage of cytoplasm, which extended down into the nanostructure. (d) Representative SEM images showing S. epidermidis cell membrane directly penetrated by the longer nano-spears inside the pockets (red arrow). **(e-f):** The interaction between S. epidermidis cell membrane and the nano-spears of pocket-type, as visualized by FIB-SEM. The bactericidal activities of these nanostructures were a result of the combined effect of the penetration (red arrows) and the stretching/compression from the nano-spears (white arrows). [Adapted from our previous publication (Cao *et al.*, 2018)]

Another natural bactericidal surface is the gecko skin, which also have inspired researchers to produce the biomimetic material surfaces that can effectively kill the attached bacteria (Watson *et al.*, 2015; Li *et al.*, 2016; Green *et al.*, 2017). Watson *et al.* (Watson *et al.*, 2015) found that the gecko skins have the microstructures which typically consist of small hairs (also referred as spinules), from several hundred nanometers to several microns in length, and with a sub-micron spacing and a small radius of curvature from 10 to 20 nm. These patterned small hairs on the gecko skin was observed to be bactericidal and were capable of killing Gram-negative *P. gingivalis* that incubated up to a period of 7 days (Watson *et al.*, 2015). Following that, acrylic nanosurfaces have been produced to mimic these nanotipped hair-like structures on the gecko skin, and were reported to be bactericidal against *S. mutans* and *P. gingivalis* (Li *et al.*, 2016). It was indicated that the bactericidal efficiency strongly depends on the bacterial size and the surface topography and in general, dense nanostructures with high aspect ratios have proven to be more effective in inhibiting bacterial adhesion (Li *et al.*, 2016). Based on these findings, gecko micro/nanostructures have been bio-replicated using crystal grade polystyrene and prominent/popular natural biopolymers, including silk fibroin, chitosan, alginate and human hair keratin (Green *et al.*, 2017).

2.5.2 Anti-fouling surfaces

2.5.2.1 Chemical-based anti-fouling surfaces

Anti-fouling surfaces with chemical functions have been fabricated and well investigated (Hasan and Chatterjee, 2015; Yu *et al.*, 2015; Kaur and Liu, 2016). Some surfaces that modified with hydrophilic polymers or oligomers, have showed anti-fouling properties owing to the formation of a physical barrier known as a hydration layer in aqueous environments (Harding and Reynolds, 2014; Yu *et al.*, 2015). Such a hydration layer is formed as a result of hydrogen bonding between water molecules in the environment and

the functional groups on the material surface (Harding and Reynolds, 2014). With the formation of such a dense layer of water molecules, which is well known as *water layer theory*, surfaces can thus weaken the cell-material interactions and therefore reduces cell adhesion (Song *et al.*, 2015). It has also been well reported that the initial bacterial attachment is facilitated by a layer of adsorbed protein (Yu *et al.*, 2015). Thus, it is potential to resist the bacterial attachment if surfaces can prevent non-specific interactions with the biological environment, as well as the adsorption of proteins.

The anti-fouling hydrophilic materials have been well developed by using polymers or oligomers. One typical example involves the ethylene glycol (EG) repeat unit, such as oligo (ethylene glycol) (OEG) and poly (ethylene glycol) (PEG) (Chapman *et al.*, 2001; Ostuni *et al.*, 2001). It was found that the self-assembled monolayers (SAMs) of OEG-terminated alkanethiolates can be resistant to the initial bacterial attachment, with a reduction of 99.7% for both *Deleya marina* and *Staphylococcus epidermidis* (Ista *et al.*, 1996). Further studies reported that the increase of EG moieties can enhance the negative interfacial tension between the OEG SAMs and water, which therefore can promote the bacterial resistance (Ista and López, 2012). A series of EG-based substrates have been fabricated, either coated or covalently grafted with comb-like polymers with EG-containing side chains such as PHEMA or POEGMA, EG-containing linear polymers, EG-based hydrogels, or hyperbranched polymers, which can be potentially widely applicable into those ranging from the marine industry to biomedical devices (Yu *et al.*, 2015). Another intrinsically anti-fouling surfaces is PEG, either by self-assembled monolayers (SAMs) or to form a brush layer (Konradi *et al.*, 2012), which is capable of forming the hydration layer to resist nonspecific protein adsorption and thereby reduce the cell adhesion (Harding and Reynolds, 2014; Xu and Siedlecki, 2017). For example, titanium surfaces that coated with PEG (47 monomeric units) polylysine copolymer have been reported to reduce the adhesion of *Staphylococcus aureus* significantly by 89–93% (Harris *et al.*, 2004). Additionally, a PEG-grafted poly(urethane urea) (PUU) surface was also reported to be resistant to fibrinogen adsorption, and was able to repel both platelet adhesion/activation and bacterial adhesion/biofilm, with efficiencies of 87.2% and 97.3%, respectively (Xu and Siedlecki, 2017). It was also reported that different molecular weights of the PEG and the conformation of the polymer chains can influence the anti-fouling effectiveness (Harding and Reynolds, 2014).

Another material that commonly used for developing anti-fouling surfaces is zwitterionic polymers, which consist of an equimolar number of homogenously distributed anionic and cationic groups on their polymer chains (Yu *et al.*, 2015). Unlike the hydration layer that formed on the hydrophilic surfaces, which is maintained by weak hydrogen bonds, the hydration layer of zwitterionic polymers is more tightly bound via electrostatic interactions (Harding and Reynolds, 2014). The more tightly held the hydration layer, the more effective the material is at resisting a disruption in the protective surface barrier (Harding and Reynolds, 2014). Thus, zwitterionic polymers with balanced charge distribution along the surface can resist the nonspecific adhesion, thereby possessing more effective anti-fouling properties. Surfaces based on zwitterionic polymers have been developed, such as poly (sulfobetaine methacrylate) (PSBMA), poly (carboxybetaine methacrylate) (PCBMA) and etc., which can reduce the fouling caused by proteins or bacteria, and showed effective resistance toward the biofilm formation (Song *et al.*, 2015; Chen, 2016).

2.5.2.2 Surface topography based anti-fouling surfaces

Alternative strategy that design the anti-fouling surfaces is physical-based, by modifying the surface with special patterns at a micro or nano-scale. The different bacteria-material interactions thus depend on the shape, size, and pattern of surface structures, as well as the surface properties (Bos *et al.*, 1999; Goulter *et al.*, 2009; Seddiki *et al.*, 2014). Anti-fouling surfaces in nature like lotus leaf (Tang *et al.*, 2011; Truong *et al.*, 2012; Chung, 2015) and sharkskin (Chung *et al.*, 2007; Reddy *et al.*, 2011) exhibit nanostructures of varying patterns under a high resolution microscope and have inspired the development of various biomimetic surfaces. For example, inspired by lotus leaf, which is superhydrophobic with a water contact angle above 150º, anti-fouling titanium surfaces with TiO_2 nanotube arrays have been synthesized by electrochemical oxidation (Tang *et al.*, 2011). Such superhydrophobic TiO_2 nanotube arrays with a water contact angle of 156º are able to inhibit the adherence of *Staphylococcus aureus* due to the self-cleaning effect (Tang *et al.*, 2011). Adhesion of water drops that contact the superhydrophobic surfaces is so low that they can easily move and roll off the surface by sweeping of dusts, dirt and microorganisms (Ivanova *et al.*, 2012; Hasan and Chatterjee, 2015). More typical examples of such lotus-inspired superhydrophobic surfaces have been summarized in Table 2.2, as well as the key findings. Another typical example of anti-fouling surfaces was inspired by the natural sharkskin (Chung *et al.*, 2007; Reddy *et al.*, 2011). A micro-patterned topography, Sharklet AF^{TM}, has been designed on poly (dimethylsiloxane) (PDMS) and silicone elastomer by mimicking the

surface features on sharkskin, and has been demonstrated to have the ability to minimize the bacterial colonization and biofilm formation (e.g. *Staphylococcus aureus*, *Escherichia coli*) (Chung *et al.*, 2007; Reddy *et al.*, 2011). Such a Sharklet micro-pattern can also act as a physical obstacle to inhibit the migration of bacteria and presents as a promising means to block biofilm development (Figure 2.5).

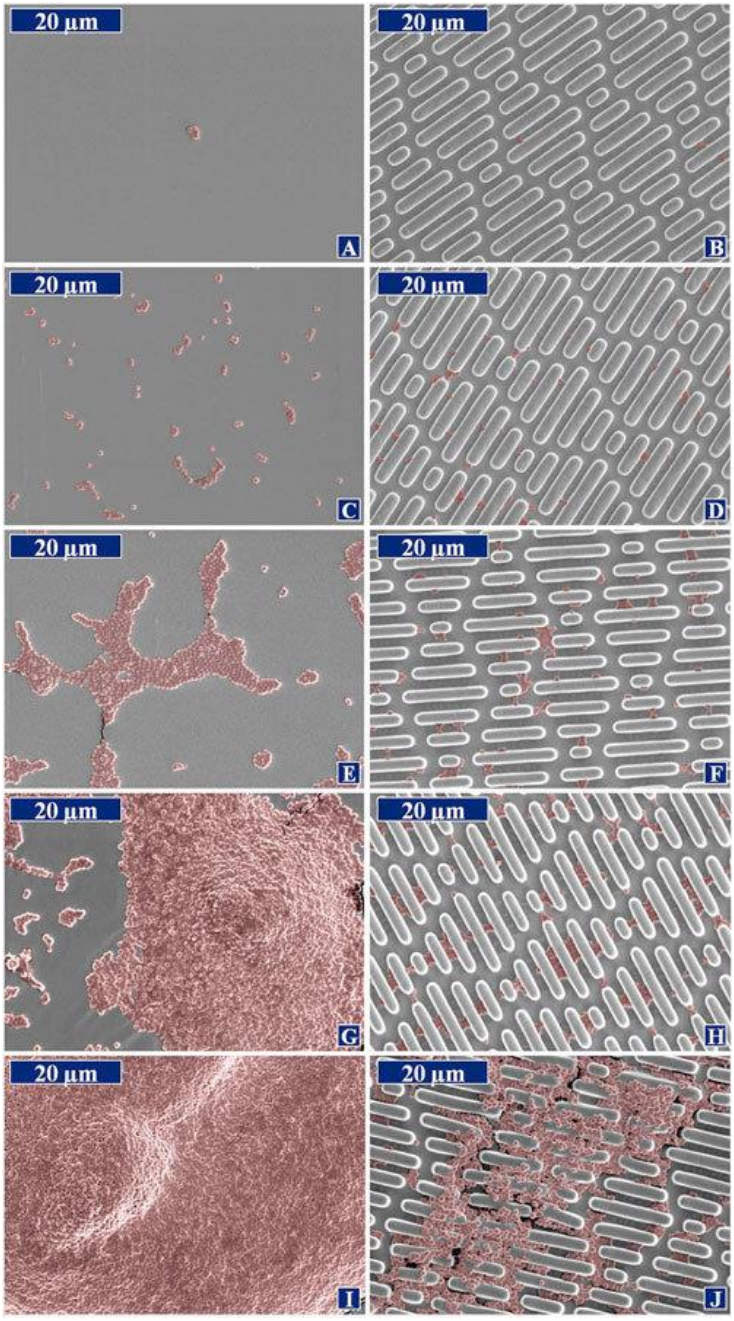

Figure 2. 5 Representative SEM images of *S. aureus* on PDMSe surfaces over the course of 21 days areas of bacteria highlighted with color to enhance contrast. On the left are smooth PDMSe surfaces and the right column shows Sharklet AF™ PDMSe surfaces. A and B day 0, C and D day 2, E and F day 7, G and H day 14, and I and J day 21. (Chung *et al.*, 2007)

Table 2. 2 Summary of the lotus leaf-inspired superhydrophobic surfaces and the key findings.

Bacterial species	**lotus-inspired superhydrophobic surfaces**	**Key findings**	**Ref.**
Escherichia coli (Gram negative, rod shape)	Silicone elastomer prepared by aerosol assisted chemical vapor deposition, with a water contact angles of 165°	Bacterial adhesion was reduced if comparing to an uncoated and a dip-coated elastomer hydrophobic glass after 1 h	(Crick *et al.*, 2011)
	Shrink-induced polystyrene (PS), polycarbonate (PC) and polyethylene (PE) surfaces, with a water contact angles of 150° averagely	2% of bacteria were attached, and only 0.1% of bacteria were remained after rinsing	(Freschauf *et al.*, 2012)
Pseudomonas aeruginosa (Gram negative, rod shape)	Laser ablated Ti surface, with a water contact angles of 166°	Nearly no bacterial adhesion after 18 h	(Fadeeva *et al.*, 2011)
	Fluorinated silica colloid surface, with a water contact angles of 167°	Reduced adhesion compared with the control samples after 1.5 h	(Privett *et al.*, 2011)
Staphylococcus aureus (Gram positive, sphere shape)	TiO_2 nanotubes by electrochemical oxidation, with a water contact angle of 156º	Less adhesion than on hydrophobic and hydrophilic surfaces after 2 h, scattered distribution, adhesion increased with time after 4 h	(Tang *et al.*, 2011)
	Fluorinated silica colloid surface, with a water contact angles of 167°	Reduced adhesion compared with the control samples after 1.5 h	(Privett *et al.*, 2011)
	Silicone elastomer prepared by aerosol assisted chemical vapor deposition, with a water contact angles of 165°	Bacterial adhesion was reduced if comparing to an uncoated and a dip-coated elastomer hydrophobic glass after 1 h	(Crick *et al.*, 2011)

In addition to biomimetic surfaces, other patterned surfaces with micro- or nanoscale features also have been reported to effectively resist the bacterial attachment and biofilm formation. The functions of such patterned surfaces strongly depend on the different contacts between bacteria and materials. For example, Lorenzetti *el al.* (Lorenzetti *et al.*, 2015) investigate the attachment of *E. coli* on the different Ti-based substrates, and the results showed that the nanostructured TiO_2 surface reduced nearly 50% bacterial attachment. The space between grooves (i.e. 400 nm) was much smaller compared to the size of *E. coli* (i.e. a rod of approximately 2 ×1 μm), thereby providing as the point-contacts and a much lower contact area, which potentially reduce the adhesive strength and thus resist the bacterial attachment. Nonetheless, surface contact area may not be the decisive factor for the bacterial attachment at a much smaller dimension, typically at the nanoscale. Feng *et al.* (Feng *et al.*, 2015) investigated the attachment of various bacterial species (i.e. *E. coli*, *L. monocytogenes*, *S. aureus*, *S. epidermidis*) on the anodic alumina surfaces with nanopores with diameters ranging from 15 to 100 nm. The results demonstrated that the much smaller pores can effectively reduce the attachment of all the tested bacteria, owing to the enhanced repulsive forces caused by the large surface areas originating from the high-density, small-diameter pores (Feng *et al.*, 2015). On the other hand, depending on the surface topography, bacteria cell can also be trapped and enclosed by the special designed walls, grooves, wells, pores, or the other geometric curves (Hasan and Chatterjee, 2015). Such patterned surfaces cannot hinder the initial attachment of bacterial cells, but can inhibit the further colonization due to lacking cell-cell commutations by separating the attached cells. For example, Kargar *et al.* (Kargar *et al.*, 2016) investigated the *P. aeruginosa* biofilm formation on the colloidal crystals with 450 or 1500 nm diameter. Even though the density of adhered bacteria on both was similar after 1 day, bacterial clusters after 2 days was much less developed on the 1500 nm spheres. It was indicated that the greater spacing between favorable sites can hinder the cell body contacts and cell communications, thus can delay the biofilm formation (Kargar *et al.*, 2016).

2.5.3 New trend of anti-bacterial slippery liquid-infused surfaces

Conventional antibacterial surfaces fabricated either via chemical functionalization or surface patterning (as described above), have shown promising to inhibit bacterial attachment and delay biofilm growth, while they still have some limitations such as lacking a sustainable anti-bacterial efficacy. The trapped air within the patterns on superhydrophobic surfaces is usually short-time and metastable, which can be displaced by bacterial flagella (Friedlander *et al.*, 2013; Friedlander *et al.*, 2015) or by complex fluids such as blood after several hours (Howell *et al.*, 2018). The self-assembled monolayers and tethered polymers created hydration layers with hydrogen bonds, while they can be easily broken up under various solution conditions (Chen *et al.*, 2010; Howell *et al.*, 2018). Additionally, the defects and damages on surfaces with patterns or functionalized molecular can negatively affect the anti-bacterial performances thereby resulting in their failure (Banerjee *et al.*, 2011). To overcome the limitations, it entails surfaces to have a more specific design (i.e. specific geometries, lengths, packing, or functional groups) to be more sustainable, or even combining together to have dual-functions. However, these methods are not general and cannot be widely applied, thereby may narrow the degrees of freedom for biomedical uses (Howell *et al.*, 2018).

Developing and designing more efficient antibacterial surface for real biomedical uses may lie in starting from these conventional approaches but thinking even further outside the box. Strikingly, the complex human body reveals its mostly fundamental feature -wetting interfaces, which commonly occurs everywhere: lungs, intestines, eyes, bones, joints are infused and lined with liquid; and these liquid interfaces can combat biological fouling (Howell *et al.*, 2018). Inspired by Nepenthes pitcher plants, Aizenberg *et al.* firstly introduced slippery liquid-infused surfaces (SLIPS) to combat the long-term biofouling and have shown greatly promising in medical settings (Wong *et al.*, 2011; Epstein *et al.*, 2012; Kim *et al.*, 2013; Howell *et al.*, 2014; Amini *et al.*, 2017; Kovalenko *et al.*, 2017; Howell *et al.*, 2018). Furthermore, researchers have used different fabrication processes to integrate different liquids into various artificial synthetic materials, such as ceramics, metals, polymer networks and gels, showing the superior slipperiness and the effective fouling resistance (Cao *et al.*, 2015; Wang *et al.*, 2016a; Wei *et al.*, 2016; Howell *et al.*, 2018; Keller *et al.*, 2019). Here, we discussed the fundamental design of SLIPS and many exciting developments of controlling biofilm growth emerging from this system.

2.5.3.1 Fundamental design of SLIPS

The design of thermodynamically stable SLIPS (Figure 2.6 a) has been well investigated and need to fulfill the following criteria: (1) the liquid A to be repelled and the wicked lubricant liquid B are largely immiscible; (2) the lubricant liquid B is nonreactive to the substrate surface and the tested liquid A; (3) the surface substrate is preferentially wetted by liquid B rather than liquid A; (4) the substrate surface is rough enough for a stable immobilization, or swelling in lubricant liquid B (Wong *et al.*, 2011; Epstein *et al.*, 2012; Li *et al.*, 2019). Stable configurations of droplets on SLIPS and the thermodynamic models have been proposed elsewhere and given a detailed instruction for the design (Smith *et al.*, 2013; Solomon *et al.*, 2016; Preston *et al.*, 2017). For example, Smith *et al.* (Smith *et al.*, 2013) considered twelve possible thermodynamic states depending on how the lubricant wets the surface texture in the presence of air and water. To achieve the most stable SLIPS, lubricants and solids with low surface energies were recommended; fluorocarbons (e.g. Krytox, FC-70), fatty alcohols (e.g. decanol), hydrocarbons, and silicone oils can be used for lubricants, and low-energy materials such as PTFE membranes or other materials (e.g. silicon, SU-8, aluminum) treated to be hydrophobic are preferred to be the surface substrates (Smith *et al.*, 2013; Solomon *et al.*, 2016). Additionally, the "cloaking effect" may occur owing to the low surface-energy lubricant spreads and forms a thin lubricant film around the impinging droplet (Smith *et al.*, 2013). This "cloaking effect" needs to be minimized for a long-term stability of SLIPS, since cloaking can cause lubricant drainage through entrainment in the water droplets after shedding from the surfaces (Smith *et al.*, 2013).

Thus far, there are two different methods (2D versus 3D lubricant infusion) widely adopted, to design stable SLIPS (Wei *et al.*, 2016; Amini *et al.*, 2017). The first method involves the 2D impregnation of lubricant into the chemically functionalized micro/nano-structures, preferentially facilitating the lubricant spreading and retention/blocking via van der Waals and capillary forces to form a stable immiscible over-layer (Figure 2.6 a) (Wong *et al.*, 2011; Epstein *et al.*, 2012; Solomon *et al.*, 2016; Amini *et al.*, 2017). Lots of textured substrates with chemistry functionalization have been utilized for the successful fabrications of SLIPS (Figure 2.6 b), including porous Teflon, nanoporous cellulose lauroyl ester (CLE), ordered polyacrylate, silicon nano-array, porous poly(butyl methacrylate-co-ethyleneglycol dimethacrylate), porous silicone nano-filament, and inverse colloidal monolayer (Rykaczewski *et al.*, 2013; Vogel *et al.*, 2013; Xiao *et al.*, 2013; Chen *et al.*, 2014; Wei *et al.*, 2014; Zhang *et al.*, 2014; Guo *et al.*, 2016; Wang *et al.*, 2016b; Meng *et al.*, 2018). The

second method involves the 3D encapsulation and adsorption of lubricant within the cross-linked polymer networks, forming an organogel-like surface (Howell *et al.*, 2014; MacCallum *et al.*, 2014; Solomon *et al.*, 2016; Amini *et al.*, 2017; Jiang *et al.*, 2017). This method makes the flat polymers swollen in the lubricant, and PDMS (substrate)/silicone oil (lubricant) were used most often (Howell *et al.*, 2014; MacCallum *et al.*, 2014; Amini *et al.*, 2017). The infusion lubricant depends on the initial thickness of PDMS, and by simply immersing the PDMS substrates in a silicone oil bath for several days, the fully infusion of the lubricant into the PDMS molecular structure can be achieved (Howell *et al.*, 2014). Silicone oil can also be infused into polyurethane catheter via this simple swollen process (MacCallum *et al.*, 2014). 3D SLIPS has recently proven to be a robust method with introducing self-replenishment capability (Howell *et al.*, 2018). For example, 3D self-replenishing SLIPS have been fabricated by molding or embedding channel networks into PDMS via 3D printing, thereby can supply continuous lubricant to the system and show a long-term stability (Howell *et al.*, 2014).

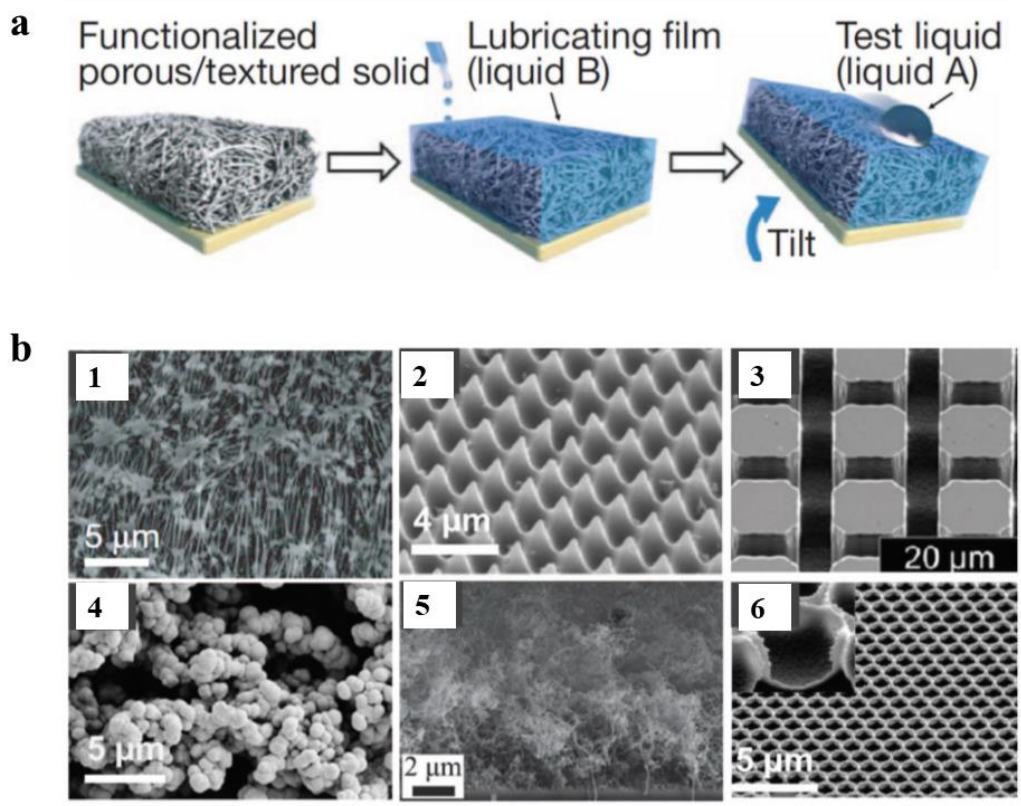

Figure 2. 6 (a): Scheme showing the fabrication of SLIPS, by infiltrating a functionalized porous/textured substrate with a lubricant liquid B, which is immiscible and repel tested liquid A (Wong *et al.*, 2011). **(b):** SEM images of representative textured porous substrates used for the fabrication of SLIPS: (1) porous Teflon, (2) Ordered polyacrylate, (3) Silicon nano-array, (4) porous poly(butyl methacrylate-co-ethyleneglycol dimethacrylate), (5) porous silicone nano-filament, (6) inverse colloidal monolayer. (Li *et al.*, 2019)

2.5.3.2 Antibacterial properties of SLIPS

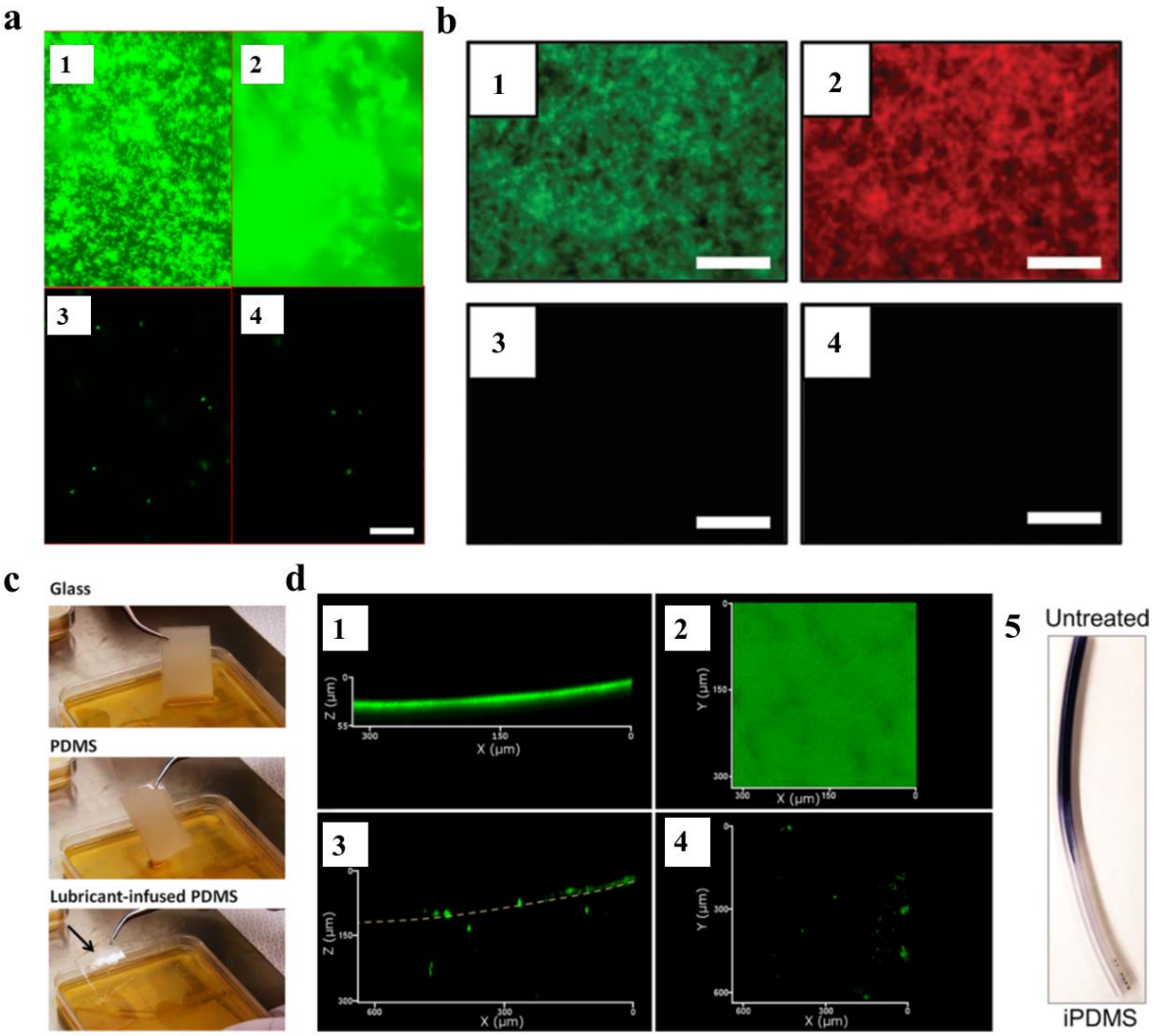

Figure 2.7 (a): Fluorescence imaging of *P. aeruginosa* biofilm grown on control polytetrafluoroethylene (PTFE) substrate (1-2) and SLIPS (3-4) surfaces after 1 day (1,3) and 7 days (2,4) growths in 10 mL⁄ min flow. Scale bar 30 µm. (Epstein *et al.*, 2012) **(b):** fluorescence microscopy images of bare glass and SLIPS substrates after incubation with *C. albicans* for 24 hours; Scale bars 200 µm. (Manna *et al.*, 2016) **(c):** Removal of glass, PDMS, and PDMS-based SLIPS from a solution of *S. aureus* after 48 hours. (Howell *et al.*, 2014) **(d):** confocal images of typical *P. aeruginosa* biofilms after 48 hours on untreated (1-2) and infused silicone tubing (3-4); and a typical photograph of CV-stained biofilms formed on the infused silicone tubing in the same conditions as 1-4; the lower half is infused and the top half is untreated. (MacCallum *et al.*, 2014)

Due to the liquid-like interface with superior slipperiness, various SLIPS have been tested against a variety of bacterial species, which has demonstrated that SLIPS can effectively repel live micro-organisms thereby inhibit biofilm formation (Howell *et al.*, 2018; Li *et al.*, 2019). Aizenberg *et al.* (Epstein *et al.*, 2012) firstly created 2D SLIPS via infiltrating perfluoropolyether liquids into a porous polytetrafluoroethylene (PTFE) substrate, and showed that SLIPS can significantly reduce the biofilm growth of *E. coli* (96.0% less) and *S. aureus* by (97.2% less) after 48 hours at low flow rates (10 mL/min). Additionally, *P. aeruginosa* biofilms were reduced by 96–99.6% after 1-7 days of growth under identical flow conditions (Figure 2.7 a) (Epstein *et al.*, 2012). By incorporation of triclosan (a model antimicrobial agent) into nano-porous decylamine-functionalized poly(ethyleneimine) (PEI)/ poly(2-vinyl-4,4-dimethylazlactone) (PVDMA) films prior to lubricant infusion, Manna *et al.* (Manna *et al.*, 2016) showed that active SLIPS can have dual-functions with repelling bacterial attachment and kill non-adherent pathogens via releasing antimicrobial agent (Figure 2.7 b). Besides, 3D swollen PDMS-based SLIPS also have shown its effective resistance to biofilm growth (Howell *et al.*, 2014; MacCallum *et al.*, 2014; Kovalenko *et al.*, 2017). For example, lubricant-infused PDMS can significantly inhibit *S. aureus* biofilms after 48 hours, as compared to the control PDMS and glass substrates (Figure 2.7 c) (Howell *et al.*, 2014). Additionally, by coating PDMS-based SLIPS onto polyurethane catheters, MacCallum *et al.* (MacCallum *et al.*, 2014) found that *P. aeruginosa* biofilms grown on the infused silicone tubing was poorly adhered even at very low shear rates, which can be easily removed (Figure 2.7 d).

Some antibacterial mechanisms of SLIPS have been proposed (Epstein *et al.*, 2012; MacCallum *et al.*, 2014; Howell *et al.*, 2018). One mechanism is that bacteria have a poor ability to anchor to the mobile lubricant interface (Epstein *et al.*, 2012). The lubricant oil layer is immiscible with the aqueous bacterial medium thereby can separate the direct contacts of bacteria and the solid surfaces. Thus bacteria is unlikely to penetrate the lubricant layer owing to the high surface tension of the interface (56.0 ±0.9 mN/m) (Epstein *et al.*, 2012). Another proposed mechanism is that SLIPS surface has superior droplet repellence due to extremely low contact angle hysteresis (<5°) (Wong *et al.*, 2011; Smith *et al.*, 2013; Daniel *et al.*, 2018). This important anti-wetting property can result in the ease removal of bacteria or biofilms under flow conditions (Howell *et al.*, 2014; MacCallum *et al.*, 2014; Kovalenko *et al.*, 2017; Howell *et al.*, 2018). Bacteria may mainly slide along the interface and an increased speed at the media-lubricating oil boundary may reduce the normal

adhesion forces that allow bacteria to colonize to the solid surfaces (MacCallum *et al.*, 2014). On the other hand, another possible mechanism is that the lubricant layer can smooth the surface roughness, and therefore impair the mechanical triggers for bacterial biofilm formation (MacCallum *et al.*, 2014).

Though SLIPS have shown effective resistance against bacterial attachment and biofilm growth, recent studies have reported that bacteria do attach onto SLIPS in some cases (Kovalenko *et al.*, 2017; Keller *et al.*, 2019). For example, the colony-forming unit counts showed that *E. coli* biofilms after 48 hours on silicone-oil-infused PDMS were comparable to the untreated PDMS, under dynamic conditions (Kovalenko *et al.*, 2017). One possible reason is that the lubricant oil layer is depleted by the orbital flow; and bacterial flagella may aid in the adhesion to infused surfaces while is still up to debate (Kovalenko *et al.*, 2017). Besides, Keller *et al.* (Keller *et al.*, 2019) found that Fluoropor-SLIPS with larger porosity cannot effectively inhibit *P. aeruginosa* biofilm growth after 7 days; bacteria can penetrate the lubricant layer and the lubricant oil within the larger pores is likely removed by shear forces under the flow conditions (Keller *et al.*, 2019). In addition, Li *et al.* (Li *et al.*, 2013) found that biofilm formation *of P. aeruginosa* on the SLIPS was strain dependent. Under a continuous flow condition, *P. aeruginosa* PA49 biofilm after 7 days on liquid-infused porous polymer surfaces was almost two times more than that on the control glass slide, while the biofilm growth of other *P. aeruginosa* stains (PA30, PA910 and PA14) were still significantly lower (Li *et al.*, 2013). Furthermore, by simulating a sneeze or cough, *E. coli* bacterial microdroplets via spraying was found to get pinned and more difficult to be removed from a silicone oil- infused PDMS surface than from a traditional textured superhydrophobic surface (Jiang *et al.*, 2017). This study indicated the potential transmission of bacteria through the microdroplet-contaminated surfaces; and the droplet size played an important role in the repellence on SLIPS, since a cloaking oil layer may form over the microdroplet thereby shielding its droplet motility (Jiang *et al.*, 2017).

Collectively, various SLIPS surfaces have demonstrated the capability to effectively inhibit bacterial attachment and biofilm formation, which has attracted intensive attention in recent years. However, the physics of interactions between bacteria and immiscible liquid–liquid interfaces needs to be further explored. For example, the stability of lubricant layer, the effective surface texture design, the role of bacterial appendages, or the droplet dynamics on SLIPS still need to be better addressed. Also, it is also important to investigate the diverse

bacterial strains, which may further improve understanding of the anti-bacterial mechanisms of SLIPS.

Chapter 3

General methodology and techniques

3.1 Electron beam lithography

Both photolithography and electron beam lithography (i.e. e-beam lithography) can transfer a pattern on a substrate (i.e. wafer). Photolithography is an optical means by using UV light to transfer a geometric pattern from a photomask to a light-sensitive photoresist on the substrate (Cirelli *et al.*, 2001). Photolithography has been widely used to fabricate micro-patterns, as its resolution is limited due to light diffraction (Chiu and Shaw, 1997). While e-beam lithography can have a better resolution especially for nano-fabrication as using electron beam to directly write the patterns (Mohammad *et al.*, 2012). In this study, we aimed to fabricate nano-pillars in a diameter of 500 nm, thereby e-beam lithography will be preferred and used.

E-beam lithography is one of the key fabrication techniques that allow us to make nanostructures onto different material surfaces. E-beam lithography originally developed in the late 1960s. A pattern generator and beam blanker was added to a scanning electron microscope (SEM), in order to control which areas of the viewing field are exposed (Rai-Choudhury, 1997; Altissimo, 2010). Nowadays, modern e-beam lithography system has been equipped with high brightness electron sources enabling a faster throughput. Furthermore, its high resolution mechanical stages can expose step-by-step large substrates under the relatively narrow field of focus of the electron beam (Mohammad *et al.*, 2012). It does not only allow to directly draw the customer patterns down to sub-10 nm dimensions, but is also capable of the high-volume nanoscale patterning techniques like deep ultraviolet (DUV) immersion lithography and extreme ultraviolet (EUV) lithography, as well as nano-imprint lithography through the formation of masks and templates (Mohammad *et al.*, 2012).

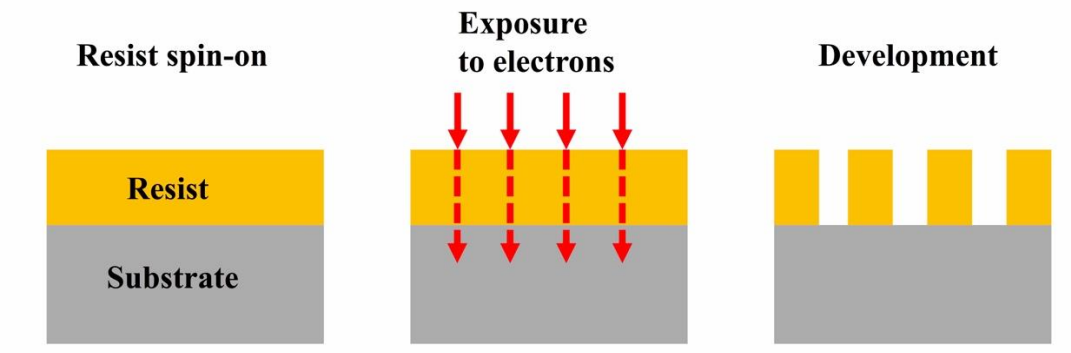

Figure 3. 1 A schematic of e-beam lithography fabrication processes to form a nano-pattern in a positive-tone resist layer (Mohammad *et al.*, 2012).

Generally, the working principle of e-beam lithography is similar to photolithography (Altissimo, 2010; Mohammad *et al.*, 2012). Figure 3.1 showed a typical schematic of e-beam lithography fabrication process to form a nano-pattern in a positive-tone resist layer. In principle, e-beam lithography is to apply a highly focused electron beam to write the custom patterns on a material surface, which is coated with an electron-sensitive film called a resist (McCord and Rooks, 2000). The solubility of this resist layer is modified by the energy deposited under the exposure of an electron beam, and the exposed resist areas will be removed after the immersion in a solvent. In this case, the designed customer patterns can develop on the resist layer and can be subsequently transferred to the substrate material via like etching process (Mohammad *et al.*, 2012).

E-beam lithography has been widely used to fabricate submicron- or nano-structures on surfaces, to investigate the anti-bacterial efficacy of surface patterns or the bacterial-material interactions (Hizal *et al.*, 2016). For example, Hizal *et al.* fabricated silicon (Si) nano-pillars with various pillar-to-pillar distances (200, 400, and 800 nm) by e-beam lithography and demonstrated their bactericidal efficacy against *S. aureus* and *S. epidermidis* (Hizal *et al.*, 2016). Doll *et al.* (Doll *et al.*, 2019) fabricated sub-100 nm Si nanopillars with a high aspect ratio and investigated bacterial interaction of *E. coli* on these nanostructures; *E. coli* cells attached onto the top of pillars showing as point contacts and the rod-shaped cells can align with the nanostructures to maximize their contact to the surface. Here, we also have used e-beam lithography to fabricate nanopillars on Si wafers, which will be further demonstrated in the method sections of Chapter 4 and Chapter 6.

3.2 Soft lithography technique

Though e-beam lithography has shown promising in the nanostructure creations on silicon wafers, its associated cost is very high and the fabrication process is time-consuming as shown as its main disadvantages (Pokroy *et al.*, 2009; Kim *et al.*, 2012; Lo *et al.*, 2012). Additionally, the access to the e-beam lithography is a common problem for many small research laboratories (Lo *et al.*, 2012). Notably, biology research (e.g. bacterial biofilms in this study) usually requires multiple samples to repeat several independent experimental works, thereby the associated costs will be very high if just using nanostructured silicon wafers. Therefore, we will introduce soft lithography technique via polymer molding, which

can simply replicate the surface structure and cost-effective for experimental work. Soft lithography technique can be used as a double casting method which create a mold from one single silicon template in an elastomeric polymer, polydimethylsiloxane (PDMS) (Pokroy *et al.*, 2009; Lo *et al.*, 2012). In other words, PDMS can be used as a secondary elastomeric mold instead of the final nanostructured material; and a final material like UV-curable epoxy resin can cast the replica from the PDMS mold (Figure 3.2) (Pokroy *et al.*, 2009). This simple molding-demolding process can successfully get the replicas from the first template, as have been demonstrated in elsewhere (Pokroy *et al.*, 2009; Hochbaum and Aizenberg, 2010; Kim *et al.*, 2012; Friedlander *et al.*, 2013).

To successfully dictate the success of mold releasing, one need to consider the material properties such as coefficient of thermal expansion and mechanical stabilities (Wolfe *et al.*, 2004; Lo *et al.*, 2012). Materials with large coefficients of thermal expansion can be distorted with the increase of temperature (Lo *et al.*, 2012). PDMS has a higher coefficient of thermal expansion (~310 ppm/°C) than silicon wafers (~3.2 ppm/°C), therefore the baking temperature for curing PDMS need to increase slowly to avoid the shrink/distortion or evaporation of polymers (Wolfe *et al.*, 2004; Lo *et al.*, 2012). On the other hand, a collapse of replicated surface features can be caused by the mechanical instabilities of polymers. For example, PDMS has a low tensile modulus (<2 MPa), which may cause shallow relief features of a mold to deform, buckle, or collapse if the replicated surface feature is smaller than 300 nm (Wolfe *et al.*, 2004). Using composite stamp method (i.e. *h*-PDMS) can have a high elastic modulus (4–10 MPa), which may overcome the limitations of conventional PDMS and can replicate surface features down to sub-100 nm (Odom *et al.*, 2002; Wolfe *et al.*, 2004; Lo *et al.*, 2012). Moreover, the replicated surface structures of polymers tend to deform upon release from the template owing to the surface energy (Odom et al., 2002). PDMS has a low surface free energy (~21.6 dyn/cm), and can be further lower to 12 dyn/cm via coating with a fluorosilane (Wolfe *et al.*, 2004), showing as a good candidate for moulding process.

By using PDMS as the secondary mould and UV-curable epoxy resin as the final casting material, Aizenberg *et al.* have fabricated various periodic nanostructure arrays in different dimensions, which can be used as model systems to investigate bacterial-material interactions (Pokroy *et al.*, 2009; Hochbaum and Aizenberg, 2010; Kim *et al.*, 2012; Friedlander *et al.*, 2013). Here, we also adopted the similar method to replicate the

nanopillars on silicon wafer or the surface structures on natural rose-petal, and more details have been further demonstrated in the method sections of Chapter 4 and Chapter 5.

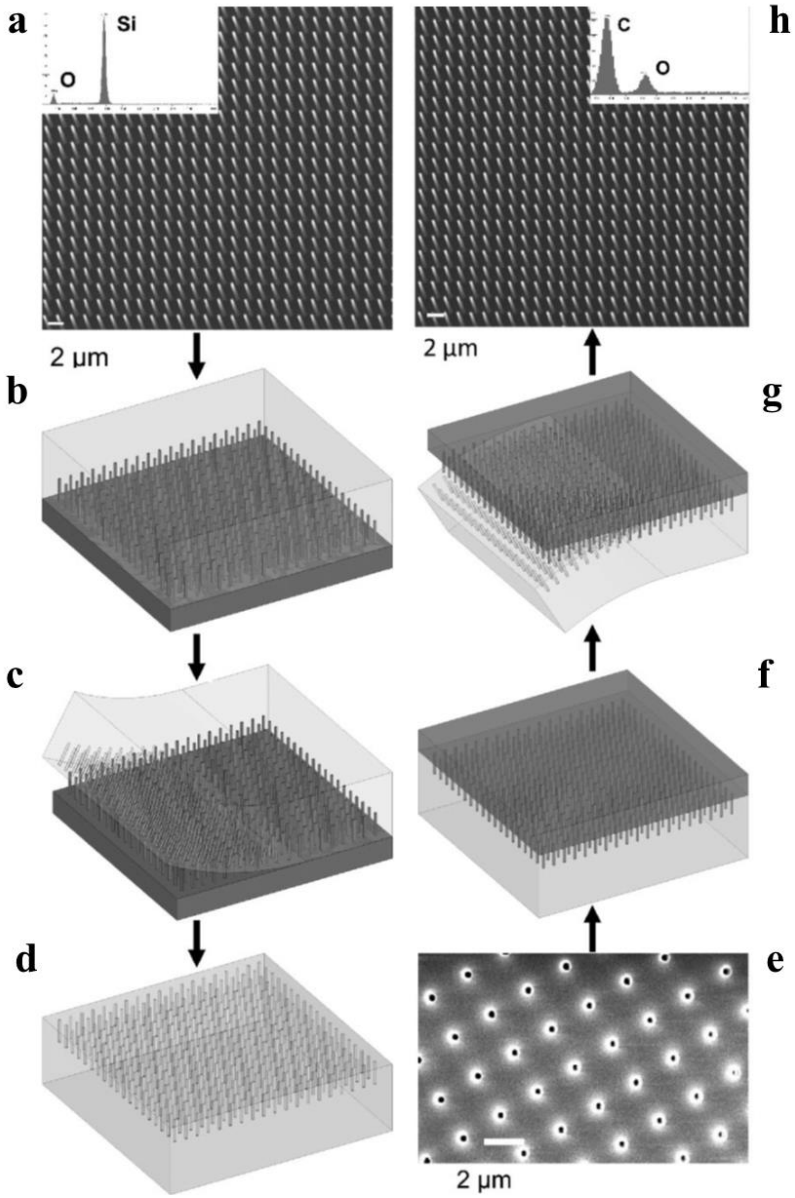

Figure 3. 2 Two-step polymer molding process for creating replicas of nanostructured surfaces (Pokroy *et al.*, 2009). **(a):** SEM image of an original nanostructure on a silicon master. **(b):** Liquid PDMS precursor is poured onto the master, treated with an anti-sticking agent, and cured. **(c):** The cured PDMS is peeled off from the Si substrate. **(d):** The negative PDMS mold, which contains the nanostructured holes corresponding to the positive nanostructures on Si substrate, and following to be treated with an anti-sticking agent. **(e)** SEM image of the negative PDMS mold. **(f):** Liquid precursor (i.e. UV-curable epoxy) is poured onto the negative PDMS mold and cured. **(g):** The PDMS mold is peeled from the cured positive replica. **(h):** SEM image of an exemplary nanostructured replica fabricated from epoxy resin. The replicated structure is geometrically indistinguishable from the master shown in (a).

3.3 Wettability analysis

Surface wettability has an important role in bacterial adhesion and biofilm growth, which have been detailed discussed in section 2.4.2 of Chapter 2. Additionally, surface wettability is an important parameter for the development of either superhydrophobic or SLIPS surfaces to control biofilm growth (Epstein *et al.*, 2012; Truong *et al.*, 2012; Zhang *et al.*, 2013; Cao *et al.*, 2015; Li *et al.*, 2019).

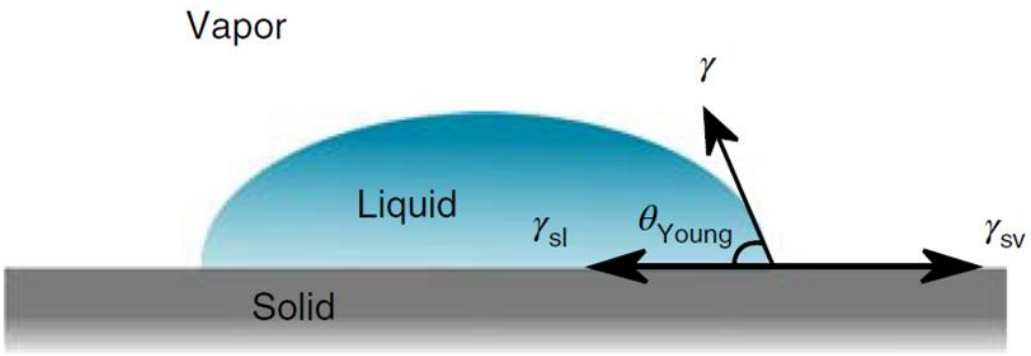

Figure 3. 3 A water droplet on an ideal solid surface. Young's contact angle (θ_{Young}) is determined by a balance of the horizontal projection of the surface tension of the water along the solid surface ($\gamma \cos\theta_{Young}$) and interfacial tensions γ_{sv} and γ_{sl} (Huhtamäki *et al.*, 2018).

Wetting is commonly characterized by the contact angle (CA), which is conventionally measured through the liquid side, and defined as the angle between the tangent to the solid surface and the liquid–vapor interface at the three-phase contact line (Figure 3.3) (Huhtamäki *et al.*, 2018). If assuming that a solid surface is atomically smooth, rigid, chemically homogeneous, insoluble, non-reactive and non-deformable by the liquid, the CA between liquid and an ideal solid surface has traditionally been determined by using the Young's equation as (Young, 1805; Zhang *et al.*, 2013):

$$\cos\theta_{Young} = \frac{\gamma_{sv}-\gamma_{sl}}{\gamma_{lv}} \qquad (1)$$

Where θ_{Young} is Young's contact angle, γ is the surface tension determined by the force per unit length of the interface; γ_{sv} represents the surface tension of the solid-vapor phase, γ_{sl} represents the solid-liquid phase, and γ_{lv} represents the liquid-vapor phase, respectively. Based on the Young's equation, a solid surface has a high surface energy γ_{sv} tends to have a low contact angle, and a low-energy surface has a high contact angle.

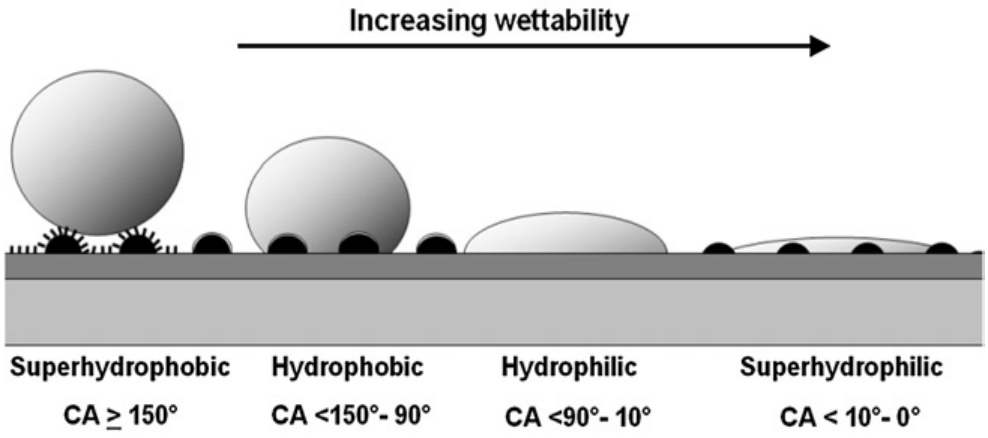

Figure 3. 4 Surfaces can be classified into as superhydrophobic, hydrophobic, hydrophilic and superhydrophilic, depending on the degree of water contact angle (Koch *et al.*, 2008).

The sessile/static drop contact angle measurement is commonly used for analyzing the surface wettability via a contact angle meter, allowing users to measure the contact angle visually (Uyama *et al.*, 1991; Decker *et al.*, 1999; Kwok and Neumann, 1999; Cao *et al.*, 2018; Huhtamäki *et al.*, 2018). By equipping with an optical subsystem and a backlight, the profile of a pure water droplet on a solid substrate can be captured. Depending on the measured CA of water droplets, surfaces can be generally classified into four categories as shown in Figure 3.4:

1. Superhydrophobic surfaces, with a CA >150º.
2. Hydrophobic surfaces, with a CA between 90º to 150º.
3. Hydrophilic surfaces, with a CA between 10º to 90º.
4. Superhydrophilic surfaces, with a CA <10º.

The sessile/static drop contact angle measurement assumes that the deposited sessile droplet is in a global energy minimum, thereby is in a stable state corresponding to the Young's contact angle (Huhtamäki *et al.*, 2018). However, the shape of sessile droplet on typical solid surfaces can be metastable, resulting in inconsistent measured results (Huhtamäki *et al.*, 2018). Therefore, this yields another important parameter for evaluating the surface wettability: contact-angle hysteresis (CAH), which is critical for evaluating the mobility of a drop on a surface, reflecting the activation energy required for movement of a droplet on a solid surface from one metastable state to another state (Gao and McCarthy, 2006). Notably, CAH can be defined as the difference between the advancing contact angle (ACA) the

receding contact angle (RCA), which are the highest and the lowest angle in the hysteresis range (Huhtamäki *et al.*, 2018). For example, a rain drop tends to fall down from a window if CAH is small, while the droplet can be pinned on surface if CAH is high (Eral and Oh, 2013); droplets on lotus leaf can easily move and roll along the surfaces owing to a low CAH (Marmur, 2004).

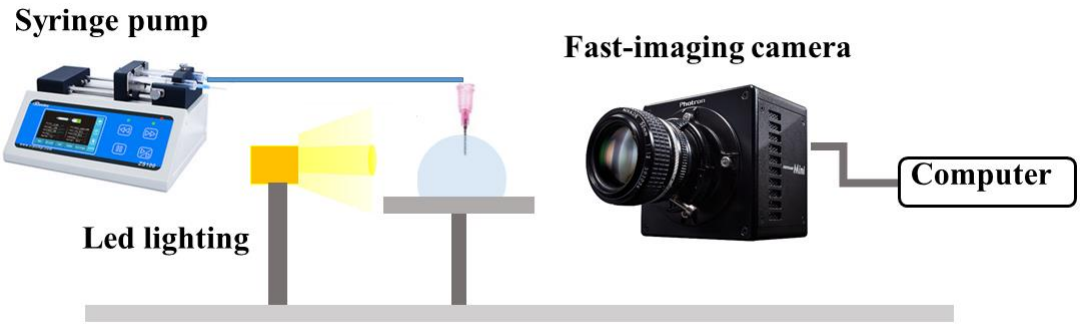

Figure 3. 5 Schematic of an in-house goniometer setup. The goniometer consists of a Led-light source, a dispensing system (a syringe pump connected to a needle by tubing), a sample stage, a fast-imaging camera to record videos and a computer for data storage and analysis.

An in-house goniometer (Figure 3.5) is set up in order to measure ACA and RCA by slowly increasing and decreasing the droplet volume of a needle using a syringe pump system. More details regarding to the set-up can be found in the nature protocol of Huhtamäki *et al.* (Huhtamäki *et al.*, 2018). Here, we choose a needle in a small width (needle gauge ~25) to avoid the distortion of water droplets. A 3-µl water droplet is initially dispensed by the syringe pump (dispensing rate~ 0.2 mL/min) and freely hangs on the needle tip. To make the droplet to contact with the tested sample surface, the sample stage is raised until the needle tip is embedded in the middle of water droplet (Figure 3.6 a). After this, a video can be recorded at 1000 fps and 7-µl of water droplet is dispensed at the same flow rate. The images of this video can be analyzed via ImageJ to determine the point of droplet base-line movement (Figure 3.6 b-c), and the CA values after that time are averaged to gain the ACA of the measurement. RCA can be measured using the same method with the syringe pump operating in a withdrawal mode at the same flow rate. At the point, video for the RCA is recorded when water is being slowly pumped from the surface, and the base-line receding point is determined by the captured images and analyzed in the same way as for the ACA (Figure d-f).

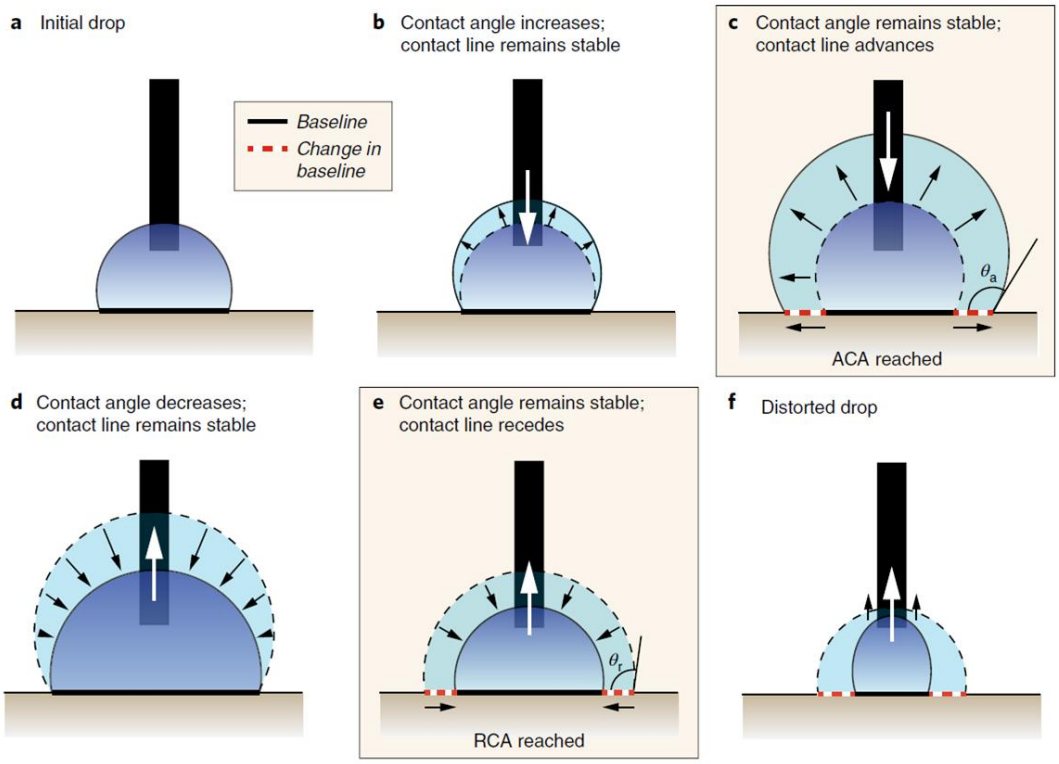

Figure 3. 6 Different stages of ACA and RCA measurement. **(a):** initially 3-µL droplet is deposited on the sample surface. **(b):** the droplet volume starting to increase while the ACA is not necessarily reached: the droplet shape changes, but the baseline (highlighted with a black line) remains as constant. (c): the ACA stage is reached, the baseline advances steadily as water is pumping, and the droplet volume increases from 3 to 10 µl while a video is recorded. **(d):** RCA measurement can start following the ACA measurement with pumping out the water. Initially the RCA is not yet necessarily reached; the droplet shape changes, and the baseline remains as constant. **(e):** RCA is reached, and the baseline recedes steadily as droplet volume is decreased from 10 to 3 µl while a video is recorded. **(f):** A droplet smaller than 3 µl becomes distorted by the needle and the data are not reliable. (Huhtamäki *et al.*, 2018)

Either static or dynamic drop contact angle measurement is an important approach for evaluating the surface wettability, thereby can give insights for the bacteria-material interactions. For example, static measurement with water droplets can determine the hydrophobicity or hydrophilicity of surfaces, as an indicator for Cassie or Wenzel states. Dynamic measurement for evaluating the CAH can evaluate the slipperiness of surfaces to determine the resistance for water droplets or even bacterial culture. Here, we also adopted the similar method to evaluate the wettability of rose-petal structured surfaces and slippery lubricant-infused surfaces, respectively, and more details have been further demonstrated in the method sections of Chapter 5 and Chapter 6.

3.4 Fluorescent image analysis

A standard practice for counting planktonic cells is measuring colony forming units (CFU) (Azeredo *et al.*, 2017). However, this is not straightforward for enumeration of bacteria in biofilms on patterned surfaces owing to difficulties of removing all cells from the surface and breaking up aggregates into single cells without killing them (Azeredo *et al.*, 2017; Cao *et al.*, 2018). Therefore, fluorescence microscopy and quantitative image analysis have been well employed to enumerate bacterial cells in biofilms and to assess their distributions on the surface.

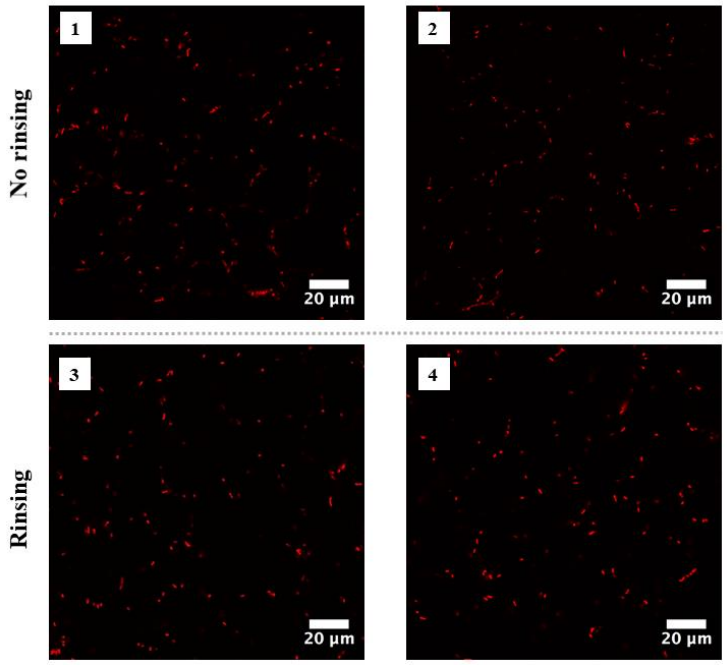

Figure 3. 7 A typical examples of fluorescent images of bacterial growth on rose-petal surfaces (see more details in chapter 5). For the samples named as "no rinsing", by using PBS, we diluted the bacterial culture three times, always immersed samples in the PBS in a 6-well plate; For the samples named as "rinsing", we pipetted our the bacterial culture and rinsed as usual with PBS three times, in a 6-well plate. Then we used Nikon A1 confocal microscopy with 40x water dipping lens to visualize the samples in the 6-well plates. As seen from the images, there was almost no difference of the cell distributions between "no rinsing" and "rinsing" samples.

Fluorescent microscopy is a useful base-line technique to provide quantitative assessments of bacterial surface coverage or biofilm biomass via cost-effective staining methods (Azeredo *et al.*, 2017). For example, the green-fluorescent nucleic acid stain SYTO-9 can be used to stain RNA and DNA in both live and dead Gram-positive and Gram-negative bacteria (Stiefel *et al.*, 2015), which yield a rapid procedure for quantitative analyses after

visualized by fluorescent microscopy. Additionally, based on the linear relation between the intensity of a pixel in biofilm images grabbed on the x–y plane and the corresponding number of cells in the z direction, which allows the calculation of the biofilm thickness and volume (Azeredo *et al.*, 2017). In this study, either short-term (e.g. 2 hours) or relative long-term (e.g. 1-2 days) bacterial growth are investigated. Therefore, for a consistence purpose, we do not aim to stain biofilm EPS and SYTO-9 was used to stain bacterial cells throughout the experimental work until specifically mentioned. In this study, 1.5 µl of SYTO-9 was added to 1 ml of Phosphate Buffered Saline (PBS, pH=7.4). After that, 150 µl of the staining solution was gently added to each substrate and plates were incubated for 15 minutes in the dark. Suspensions were then aspirated and the titanium substrates were transferred into a new well plate with ample PBS to fully immerse the sample.

Notably, after the bacterial attachment assay or biofilm formation assay, surfaces are usually gently rinsed three times with Phosphate Buffered Saline (PBS, pH=7.4) to remove loosely adhered bacteria. It is possible that the wash steps passing through the air-liquid interfaces may have selectively removed relatively weakly attached cells and affected the distribution of cells on surfaces (Busscher and van der Mei, 2006). Therefore, control experiments were performed where samples were never passed through an air-water interface and were imaged using a water immersion lens. The distribution of cells was very similar to those seen in washed samples (Figure 3.7), indicating that forces exerted during wash steps do not have a major impact on attached bacterial cells.

Here, all surfaces in this study were visualized using an Olympus BX61 upright fluorescent microscope with a 20x objective. For the bacterial attachment assay (2 hours), surface coverage was determined (see Figure 3.8) using 2D fluorescent images in a single focal plane (121.25 × 108.75 μm^2) from 5 random locations. For biofilms, z-stacks were performed through the thickness of biofilms from 5 random locations on the surfaces. The biomass in each field of view (430.00 × 324.38 μm^2) was determined using the COMSTAT2 plugin (Lyngby, Denmark) in ImageJ. Three independent experiments were performed for each surface type.

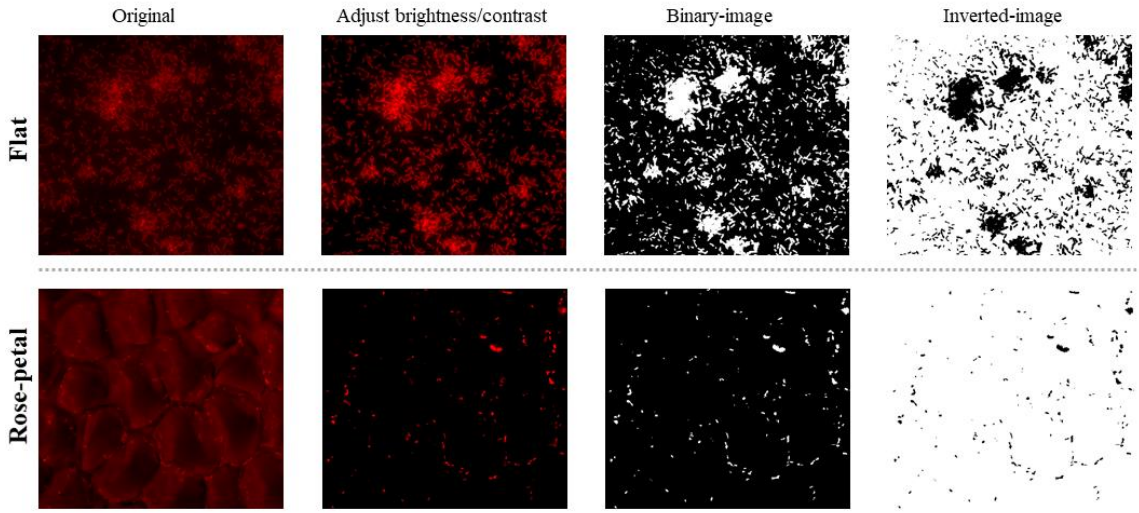

Figure 3. 8 A typical example of how the surface area covered by bacteria after 2 hours was determined (for rose-petal surfaces in Chapter 5). In order to detect the all bacterial cells within the fluorescent images, scale bars are not applied as they may cover the cells at the corners of images. These fluorescent images were all in the field of view of 121.25 × 108.75 μm^2), and were corresponding to Figure 5.4 a3-4 in Chapter 5 where have clear scale bars. The initial fluorescent images were adjusted for brightness and contrast by ImageJ, to remove noise without removing the signal from cells. Binary images were then made via manually setting the thresholds. Notably, the binary images were always compared with the adjusted fluorescent images, in order to detect all the edges of cells or clusters. After that, inverted images were made by ImageJ and analyzed by "analyze particles" function to determine the surface area.

3.5 Critical point drying and SEM analysis

A scanning electron microscope (SEM) is based on scanning the surface with a focused beam of electrons that can interact with specimen atoms. Secondary electrons emitted by specimen atoms can be detected by SEM, thereby can generate images of surface topography of specimen.

Owing to the large depth of field, SEM can provide a 3-D appearance or morphology of a specimen, which is useful for visualizing and investigating the sample structures (Azeredo *et al.*, 2017). Azeredo *et al.* (Azeredo *et al.*, 2017) summarized the following key advantages of SEM: (1) can visualize samples at a high resolution down to 50-100 nm and at a large field depth, (2) qualitative or quantitative data analysis in a 3-D manner; and (3) a wide range of magnifications for analyzing biofilm samples (20 x to 30,000 x).

Therefore, SEM have been widely adapted by researchers for visualizing bacteria and biofilms which provides high resolution of cell morphology, cell appendages, or EPS of biofilms (Fadeeva *et al.*, 2011; Hsu *et al.*, 2013; Ivanova *et al.*, 2013a; Bhadra *et al.*, 2015;

Kargar *et al.*, 2016; Mainwaring *et al.*, 2016; Cao *et al.*, 2018). By employing the SEM down to 1 μm, Hsu *et al.* investigated the different number and size of cellular appendages, which helped to understand the mechanisms of bacterial attachment in response to surface topography (Hsu *et al.*, 2013). Dawson *et al.* used SEM to visualize biofilm EPS down to 1 μm, and investigated the encapsulation of bacteria within the matrix (Dawson *et al.*, 2012). Also, by investigating the SEM images down to 200 nm, Ivanova *et al.* confirmed the bactericidal activities on black silicon arrays (Ivanova *et al.*, 2013a). Our previous work also adopted SEM down to 500 nm to investigate the bacterial cells on nanostructured titanium surfaces, which confirmed the cell penetration/deformations on these surfaces (Cao *et al.*, 2018). Therefore, SEM is an extremely useful tool for comparative analysis in bacterial biofilm research, especially when visualizing the bacterial growth on surfaces with nanotopography and evaluating the bacteria cell wall deformation or rupture (Ivanova *et al.*, 2012; Ivanova *et al.*, 2013a; Bhadra *et al.*, 2015; Cao *et al.*, 2018). Also, either qualitative or quantitative analysis of SEM images can be used to support the quantitative results from other imaging methods such as fluorescent microscopy, and has shown a high correlation (Di Bonaventura *et al.*, 2004; Di Bonaventura *et al.*, 2006; Hasan *et al.*, 2015; Li *et al.*, 2015; Azeredo *et al.*, 2017).

To prepare the biological samples such as bacterial biofilms, the living cells require chemical fixation (e.g. glutaraldehyde) to preserve and stabilize their structure. Additionally, samples need to be completely dry before the visualization, since the SEM chamber is at high vacuum. Owing to water has a high surface tension to air, air drying via evaporation can cause severe shrinkage, deformation or even collapse of bacterial biofilm structures as shown in our preliminary results in Figure 3.9. Therefore, critical point drying (CPD) has been suggested for drying bacterial biofilm samples which enables good imaging qualities (Figure 3.9) (Araujo *et al.*, 2003; Cao *et al.*, 2018). It has been well known that there has a critical point of temperature and pressure, where liquid and vapor can co-exist; and CPD is relying on this physical principle. The water in samples can be replaced with liquid CO_2 whose critical temperature and pressure (~35°C and~1,200 psi) is just above ambient. After increasing the temperature to above the critical temperature, the liquid CO_2 changes to vapor without change of density, thereby will not affect the structures by distorting morphology coming from the surface tension effects. Since liquid CO_2 has a poor ability to be miscible with water, an intermediate fluid such as ethanol is required, which can be miscible with both water and liquid CO_2.

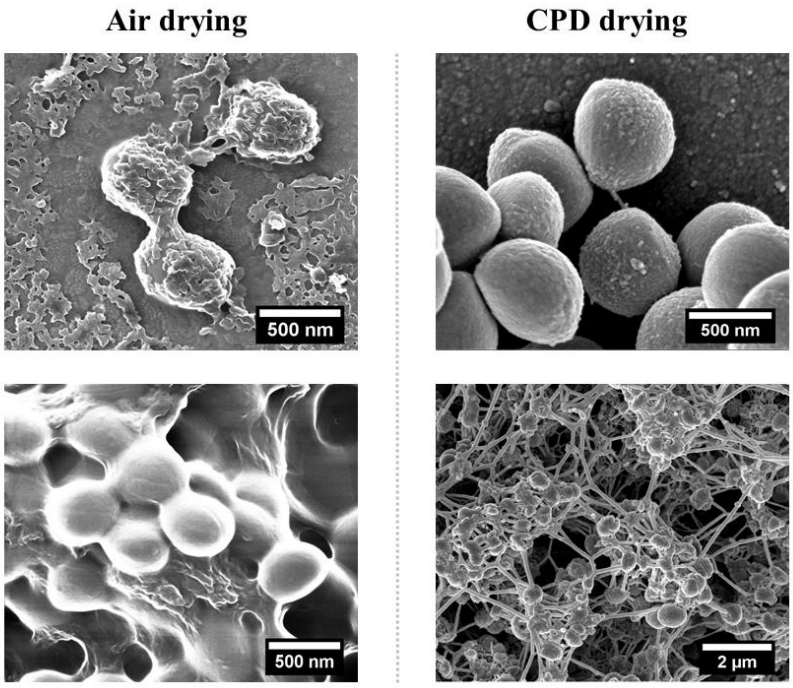

Figure 3. 9 Our preliminary results showing the SEM images of air drying versus CPD drying. The *S. epidermidis* bacterial cells collapsed and biofilm structures get distortion/shrinkage after air drying; while the bacterial cells and biofilms after CPD, clearly showed the cell morphology and the fibrous networks within the biofilms.

Here, we used CPD and SEM analysis for the samples in Chapter 4 and 5, in which case the following protocol was used throughout this study. Surfaces (with bacteria or biofilms) were washed three times with PBS and fixed in 2% glutaraldehyde with 3M Sorenson's phosphate buffer, overnight at 4°C. Then they were dehydrated through a series of ethanol solutions of 25% (v/v), 50%, 75%, and 100% for 5 minutes each. We noticed that the samples made by epoxy got shrinkage if immersing in the pure ethanol too long, possibly owing to the organic molecules got dissolved. Therefore, we quickly put the samples into the chamber of Leica EM CPD300 and start the dehydration without delays. Notably, the speed for "CO_2 in", "exchange" and "gas out" were set as "slow", which can further avoid disturbing cell morphologies. The dried surfaces (with bacteria or biofilms) were sputter-coated with 16 nm platinum to increase the surface conductivity, enabling higher resolution imaging by the SEM (FEI Helios NanoLab 600 DualBeam system). SEM was operated at an acceleration voltage of 5 KV, which allowed to get good magnifications without damaging the surfaces.

Chapter 4

Bacterial nanotubes mediate the bacterial growth on the periodic Nano-pillars

4.1 INTRODUCTIONS

Bacterial cells colonize onto surfaces and form biofilms, which are embedded in extracellular polymeric substances (EPS) (Kargar *et al.*, 2016; Cao *et al.*, 2018). The unique structure of biofilms protect bacteria from the surrounding environments, conferring an extreme capacity for persistence against phagocytosis, oxidative stresses, nutrient/oxygen restriction, metabolic waste accumulation, interspecies competitions, and conventional antimicrobial agents (Moradali *et al.*, 2017). Bacterial biofilms can trigger persistent human infections and have dramatically affected healthcare industries (Hochbaum and Aizenberg, 2010; Song and Ren, 2014). Specifically, *Pseudomonas aeruginosa* (i.e. *P. aeruginosa*) is an opportunistic pathogen and is one of the top three causes of opportunistic human infections (Stover *et al.*, 2000), causing nosocomial infections in the catheter lines, or the lungs of cystic fibrosis (CF) patients (Stover *et al.*, 2000; Moradali *et al.*, 2017). The major challenge to treat the infections of *P. aeruginosa* is that the extraordinary capacity of *P. aeruginosa* to form biofilms render antibiotic treatments inefficient thereby promoting chronic infectious diseases (Rasamiravaka *et al.*, 2015). Additionally, owing to its intrinsic resistance to antibiotics and disinfectants, *P. aeruginosa* has been identified as one of the notoriously multi-drug resistant (MDR) bacteria (Smith and Coast, 2013; Moradali *et al.*, 2017). Therefore, it is important to develop biomaterials that can control biofilm growth thereby reduce infections. Particularly, surface modification with physically creating rational surface topographies have gained great attentions, which have shown to inhibit bacterial attachment and biofilm growth without the use of antimicrobials (Song *et al.*, 2015; Sjöström *et al.*, 2016; Xu *et al.*, 2017; Cao *et al.*, 2018). Also, a comprehensive understanding of the bacteria-material interaction on surface topography may pave ways for a more effective strategy to resist biofilm growth.

Bacteria encounter surfaces are extremely diverse, and surface patterning is an important determinant of bacterial attachment. Bacterial adhesion is favored on recessed portions of patterned surfaces, and bacteria tend to attach preferentially to patterns in the micro or nanometer range rather than to smooth surfaces (Berne *et al.*, 2018). Jeong *et al.* (Jeong *et al.*, 2013) showed that *Shewanella oneidensis* can recognize nanoscale structures and attach preferentially with alignment along the length direction of nanowires. Hochbaum *et al.* (Hochbaum and Aizenberg, 2010) found that *P. aeruginosa* (strain PA14) tended to maximum their contact area with the surface, showing as a spontaneous cell alignment between the periodic nano-pillars with a gradient of post pitch (2.2, 0.9 and 0.7 μm). Similar

observations were also reported. For example, *P. aeruginosa* was found to align within subcellular-nanogratings (Lai, 2018). *Escherichia coli* preferred to orientate towards surface line patterns (Gu *et al.*, 2016), and *Pseudomonas fluorescens* were trapped preferentially in the surface trenches (Díaz *et al.*, 2011b). As such, topographical features with the micro-meter or submicro-meter length scales (i.e., comparable with the length scale of the bacteria themselves) can influence the arrangement of adhered cells during the early stage of biofilm development (Hochbaum and Aizenberg, 2010; Díaz *et al.*, 2011a; Hsu *et al.*, 2013). However, its underlying mechanism is still up to debate (Hochbaum and Aizenberg, 2010; Friedlander *et al.*, 2013; Gu *et al.*, 2016; Lai, 2018), which hinders the development of an overarching understanding of bacterial-material interactions.

In this chapter, the alignment, attachment of bacteria and biofilm growth are investigated on nano-pillars with systematic variations in dimensions. *P. aeruginosa* PAO1-mCherry were incubated with surfaces for either 2 hours and 24 hours, and characterizing them by using fluorescent microscopy and scanning electron microscopy (SEM). By using bacterial mutants (PAO1 *Δflim* and *ΔpilA*), we show here that cell alignment of the initial attachment (~2 hours) is a general phenomenon within these bacterial strains. Additionally, the bacterial nanotubes were observed via high-resolution SEM which may promote cell-cell communications. The biofilm growth after 24 hours showed that well-developed nanotube networks which connect cell clusters isolated by the pillars. This chapter suggests that bacterial nanotubes may provide an additional, structural function in the biofilm formation.

4.2 METERIALS AND METHODS

4.2.1 Design and fabrication of surface substrates with nano-pillars

In this study, the mask of nano-pillar patterns was initially designed by Klayout Editor (https://www.klayout.de/) software. A schematic of the nano-pillar arrays was shown in Figure 4.1 a. The silicon (i.e. Si) substrate which was used for e-beam lithography was in the dimension of 25 mm × 25 mm (Figure 4.1 b). The whole Si substrate was diced into four chips at the end, and each contained the different nano-pillar patterns as fabricated (Figure 4.2c). The configuration of the patterns was designed to create pillars with same dimension and varied pitch, as shown in Table 4.1.

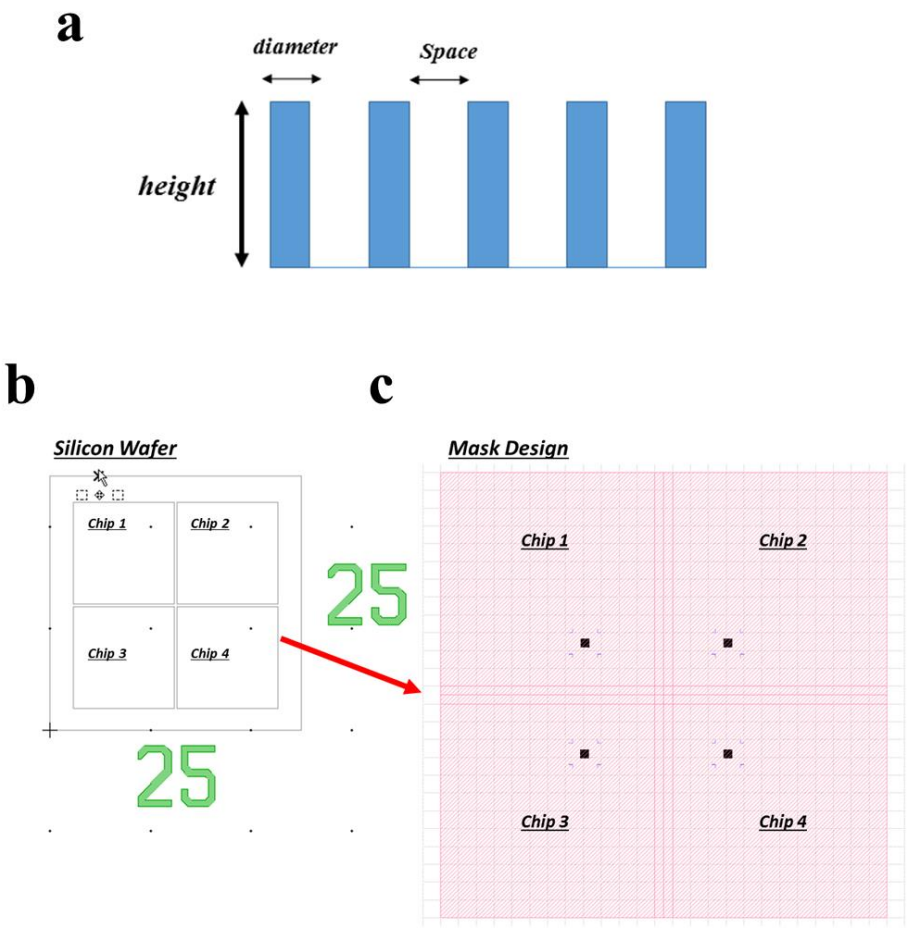

Figure 4. 1 The overview of the nano-pillar patterns as fabricated on silicon wafer and the pattern design in this study. **(a)** A schematic of the nano-pillars on silicon; **(b)** the dimension of the silicon wafer used in this study; **(c)** the mask design in this study.

Table 4. 1 The different nano-pillars with different spaces as fabricated in this study.

	Diameter (nm)	**Space (nm)**	**Height (nm)**
Chip 1	500	500	2000
Chip 2	500	1000	2000
Chip 3	500	2000	2000
Chip 4	500	5000	2000

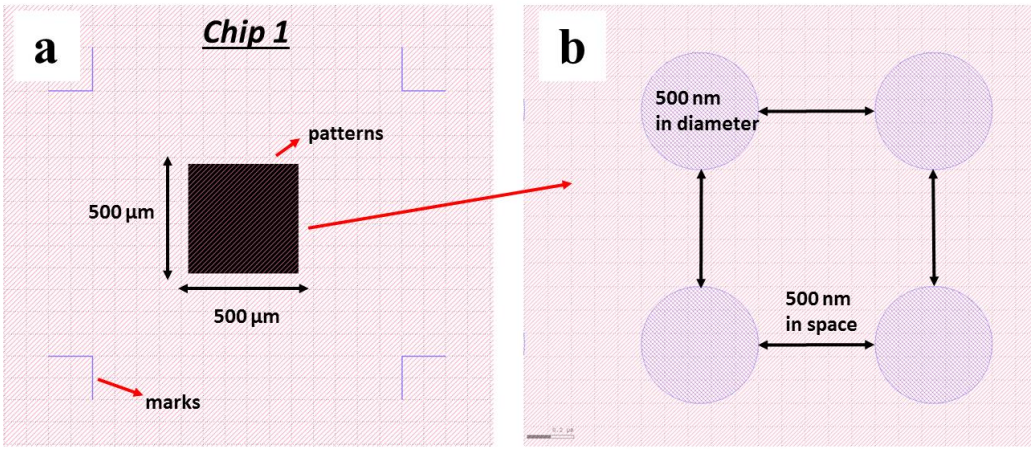

Figure 4. 2 The typical pattern design of nano-pillars on the chip 1 in this study, which contains the nano-pillars in the diameter of 500 nm, and with the space (i.e. edge to edge of nano-pillars) of 500 nm.

Figure 4.2 showed the typical pattern design of nano-pillars on the chip 1 in this study. All the nano-pillars have a diameter of 500 nm, and the space of adjacent pillars (i.e. edge to edge of nano-pillars) is set to 500 nm (Figure 4.2b). Hereafter, the nano-pillars on Si wafer were fabricated in INEX (Newcastle University, UK). It was reported that the exposure time of e-beam lithography is strongly dependent on the exposure area and the density of patterns (Parker *et al.*, 2000). If the exposure area is larger, then the exposure time is longer; and if the designed pattern is denser, then the exposure time is also longer (Parker *et al.*, 2000). In addition, it was reported that e-beam lithography cannot be used for high-volume manufacturing owing to its limited throughput (Parker *et al.*, 2000). Typically for a smaller exposure area, the e-beam writing will be much slower compared to the photolithography, as the smaller field of electron beam writing (<mm^2 for electron beam vs >40 mm^2 for an optical mask projection scanner) is required to scan more exposure fields to generate the final patterns (Parker *et al.*, 2000). In this case, for such a dense pattern with closed pillar-space on the chip 1 in this study, the exposure time of the e-beam lithography can be over a week if patterns cover an area of 10 × 10 mm^2, which leads to very high manufacture cost. Therefore, the exposure area with patterns (e.g. pillars in the diameter of 500 nm, and with the space of 500 nm) were reduced to an area of 500 × 500 μm^2 in this study, and the exposure time of e-beam lithography was significantly reduced to 16h 44mins. For the other chips in this study, the patterns of nano-pillars with the different spaces were also designed on an area of 500 × 500 μm^2 (Figure 4.1c). The pillars on other chips were less dense compared to chip 1, thereby resulting in a shorter exposure time, which are 7h 20mins for

chip 2, 2h 40mins for chip 3 and 33 mins for chip 4, respectively. On the other hand, four L-shaped marks were designed at four corners of the designed patterns as shown in Figure 4.2a, which was used for the recognition purpose in order to easily distinguish the patterned area on the chip for the further experiments. These L-shaped marks were applied and fabricated via e-beam lithography on the all chips in this study.

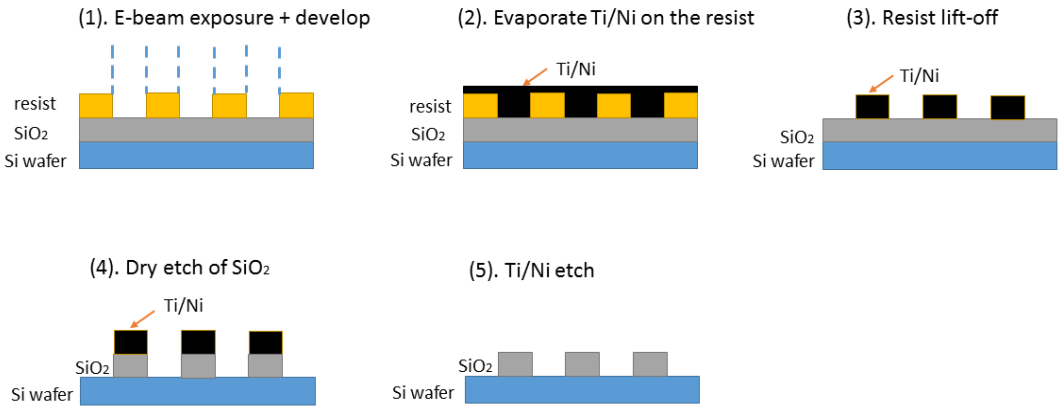

Figure 4. 3 A schematic of the silicon substrate with arrays of pillars that fabricated using e-beam lithography and the dry etch process in this study. Typically, 2 µm of SiO_2 will be deposited by plasma chemical vapor deposition (PCVD) on the silicon wafer before the fabrication. (1): e-beam lithography enables to write the patterns in the resist layer and develop. (2): The Ti/Ni will be evaporated by sputtering on the resist layer. (3): The resist and the unwanted deposited metal will lift-off. (4): Dry etch of the SiO_2 to form the 2 µm-height pillars. (5): The deposited Ti/Ni will be etched off.

Based on the 2D patterns designed by Klayout Editor (https://www.klayout.de/), e-beam lithography was used to fabricate the nano-pillar arrays on Si substrates, following the dry etch process as shown in Figure 4.3, which was also described elsewhere (Pokroy *et al.*, 2009; Kim *et al.*, 2011; Kim *et al.*, 2012). Then the Si nano-pillars arrays (Figure 4.4a) were treated with an anti-sticking agent (tridecafluoro-1, 1, 2, 2-tetrahydrooctyl)-trichlorosilane (Gelest Inc.) by exposure in a desiccator under vacuum for 30 mins (Figure 4.4b).

To get the negative replicas from the Si substrates, a mixture of PDMS solution was prepared using SYLGARD 184 Elastomer Kit (Dow Corning Corporation, Midland, MI) with a base-to-curing agent ratio of 10:1 (wt/wt). The pre-polymer solution was thoroughly mixed and degassed under vacuum for 30 mins to eliminate all air bubbles. Then, the mixture was poured over the Si substrates in a Petri dish, cured at 70 °C for 2 hours (Figure 4.4c). After cooling at room temperature, the negative PDMS mould was gently peeled off from the substrate (Figure 4.4d).

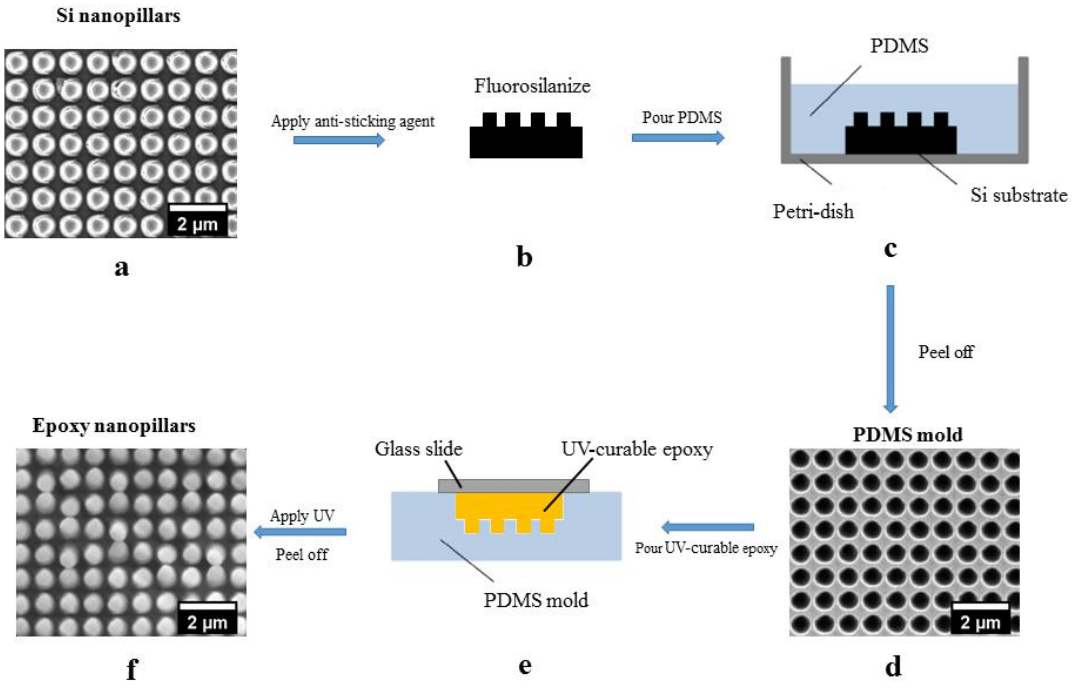

Figure 4. 4 A schematic of the double moulding procedure for creating epoxy replicas of nano-pillars.

To get the final replicas of the nano-pillars on Si substrates, UV-curable epoxy (OG 142-87, Epoxy Technology, Inc.) was poured onto the negative PDMS mould fabricated above, and air bubbles were removed by a plastic disposable pipette. The poured UV-curable epoxy was covered with a pre-cleaned glass slide, and cured at ~100 mW at 365 nm, for 20–25 minutes under a UV-lamp (Figure 4.4e). After cooling to room temperature, the cured epoxy was demolded by bending the PDMS mould (Figure 4.4f). The epoxy replicas can be stored for about a month at room temperature without noticeable deformation (Kim *et al.*, 2012).

4.2.2 Bacterial culture and biofilm formation of *P. aeruginosa*

P. aeruginosa PAO1-mCherry is used in this study, which is a biofilm-forming bacterial strain that has been widely used (McFarland *et al.*, 2015; Weigert *et al.*, 2017). PAO1-mcherry is the derivative of *P. aeruginosa* PAO1-N (Nottingham subline) (Sidorenko *et al.*, 2017), which was engineered via chromosomal insertion (attTn7::ptac-mcherry) to constitutively express fluorescent proteins. PAO1-mCherry cells were taken from the frozen stock that kindly shared by Dr. James Brown (Nottingham University, UK), streaked and grown for 1 day (24 hours) at 37℃ on Trypticase Soy Agar plates in an incubator. Single colony was picked and inoculated into 20 mL Trypticase Soy Broth (TSB) and grown for

another 24 hours overnight in a shaking incubator at 37℃ and 180 rpm. Then, the bacterial culture was poured into the 50 ml centrifuge tube, and bacteria was separated by centrifuge with 3,500 rpm for 15 minutes at 4℃ (Sigma 3K 10, rotor 11133). Subsequently bacterial stock was made with 50% glycerol and stored in the fridge at -80℃. This stock is used for all the experiments in this study.

For the bacterial attachment and biofilm formation, PAO1-mCherry cells were routinely cultured in Trypticase Soy Broth (TSB) (Melford Laboratories Ltd, UK), in a shaker at 180 rpm, 37℃ for 16 hours and then diluted to OD_{600}= 0.01 in 100x diluted TSB with a spectrophotometer (Biochrom Libra S11, Biochrom Ltd., Cambridge, UK). Prior to seeding, the epoxy nano-pillar substrates were added to a 12-well culture plate. For bacteria attachment assay, 3 ml of the diluted bacterial culture was incubated with substrates in 12-well culture plates for 2 hours at 37℃ and then removed for visualization. To examine the effect of nano-pillars on the biofilm formation by surviving bacteria, 3 ml of diluted bacterial suspension was added to each sample, and incubated for 24 hours at 37℃. In this study, at least three independent experiments have been performed for each substrate type.

4.2.3 Fluorescent microscope analysis

The substrates were removed from the wells with sterile forceps and gently rinsed three times with Phosphate Buffered Saline (PBS, pH=7.4) to remove non-adherent or loosely adhered bacteria. The samples were then put onto the glass slide covering with the coverslips, and visualized by Olympus BX61 upright fluorescent microscope with a 20x lens. The area of periodic nano-pillars was initially focused by using the bright-field channel.

The attachment and alignment of bacterial cells on nano-pillars after 2 hours' incubation was visualized by acquiring the 2D fluorescent images with the channel of Texas Red under the focal plane. The area of 121.25 × 108.75 μm^2 was selected from the 2D fluorescent images and analyzed by an in-house made MATLAB code. The alignment of bacterial cells was categorized as Parallel (0-30º), Diagonal (30-60º) or Perpendicular (60-90º), according to the smallest angle difference between the cell and horizontal axis of nano-pillar pattern (defined as 0º). On the other hand, the surface coverage of bacteria on nano-pillars was determined by calculating the surface area of bacteria cells with ImageJ. For the biofilms formed after 24 hours, z-stacks were performed through the thickness of biofilm from

random locations on the surface. The biomass under each field of view (430.00 × 324.38 μm^2) was determined by COMSTAT2 plugin (Lyngby, Denmark) in ImageJ.

4.2.4 Scanning electron microscope analysis

In this study, the visualization of bacterial attachment and biofilm formation on the epoxy nano-pillar substrates with the Dual Beam FIB system (Hitachi SU-70 FEG SEM, Durham University, UK) was carried out as the following steps. The samples were washed with PBS and fixed in 2% glutaraldehyde in 3M Sorenson's phosphate buffer overnight at 4℃. The samples were transferred into a new plate and dehydrated through a series of ethanol solutions of 25% (v/v), 50%, 75%, and 100%, followed by critical point drying as explained in Chapter 3. Then the samples were sputter-coated with 16 nm platinum coating using a Cressington 328 ultra-high quality coater to improve the imaging quality in the Dual Beam system, following the visualization of SEM. The beam voltage and current were set to 5 kV and 0.34 nA, respectively.

4.2.5 Statistical analysis

Data were represented by mean values with standard errors. The statistical differences among different samples were determined by Student's t-test assuming unequal variations. And $p < 0.05$ was considered statistically significant in this study, as indicated by the symbols in the representative figures.

4.3 RESULTS AND DISCUSSION

4.3.1 Nano-pillars with a space of 500 nm collapsed

When engineering a functional surface bearing pillars with a specific high aspect ratio, the stability of the expected structures need to be considered. Several factors can lead to the collapse of vertical-standing pillars on a surface: gravity, adhesion force between the pillars and the base surface, and adhesion between the pillars themselves (Pokroy *et al.*, 2009; Jiang *et al.*, 2014). Here, we successfully got the replicas of nano-pillars with the spaces of 5 μm, 2 μm and 1 μm. It was reported that the lateral collapse is not unusual when pitch between pillar is relatively small, in which case a gentle pillar bending during demoulding can lead to neighboring pillars sticked to each other (Chandra and Yang, 2010). Similar

observations were also found here. For example, the tips of the adjacent nano-pillars (space ~500 nm) bended laterally and adhered to the neighboring pillars (Figure 4.5), which renders these pillars unusable. In this case, this study only chose nano-pillars with the spaces of 5 μm, 2 μm and 1 μm to conduct the following experimental work.

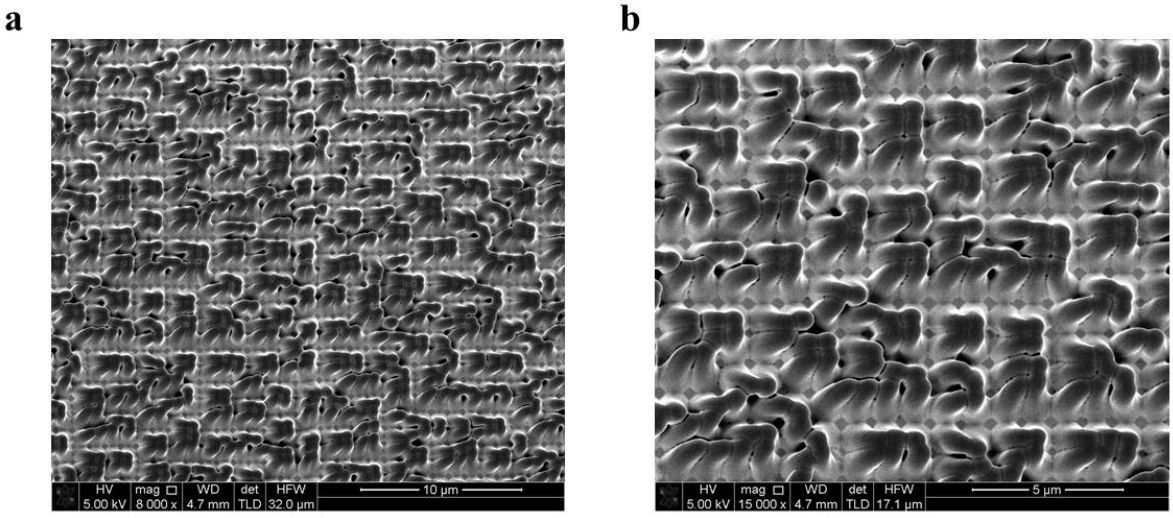

Figure 4. 5 Lateral collapse was found on the nano-pillars with the space of 500 nm. **(a):** the SEM image of collapsed nano-pillars was taken at a magnification of 8000 x; **(b):** the SEM image was taken at a higher magnification of 15,000 x.

4.3.2 Bacterial attachment, alignment and interactions with nano-pillars after 2 hours

P. aeruginosa PAO1-mCherry, a rod-shaped bacterium, was grown for 2 hours on the periodic nano-pillars with varying spaces (~5 μm, 2 μm and 1 μm). All the nano-pillars had a diameter of about 500 nm, a height of 2 μm, and periodically arranged in an array with square symmetry. We found that the initial attachment of *P. aeruginosa* exhibited preferences in the cell alignment and is sensitive to the spaces between pillars, as shown in the fluorescent microscopy images and the corresponding fast Fourier transforms (FFT) images (Figure 4.6a-b). For the nano-pillars with the space of 5 μm which is much larger than the cell dimensions, the bacterial attachment to the surface is random without preferred orientation. The Fourier Transform decomposes an image into its sine and cosine components. In the FFT images, each point represents a particular frequency contained in the spatial domain image. Therefore, the FFT images as shown in Figure 4.6b, contain the peaks associated with the spatial frequencies of bacteria within the nano-pillars. The FFT images of 5 μm-space showed no orientational order, akin to the attachment on the flat

surface, which has only faint central spot without showing positional ordering peaks (Figure 4.6b). Surprisingly, if the space of nano-pillars decreases further to 1 μm which approaches the dimensions of *P. aeruginosa*, bacteria preferred to align parallel or perpendicular to nano-pillars (Figure 4.6d). The corresponding FFT image (Figure 4.6b) also showed the transition when the nano-pillar pitch decreases. The faint central spot of FFT extended towards the [10] and [01] ordering peaks when the pillar spaces decrease, indicating the preferential cell orientation and alignment on the surfaces. The SEM images (Figure 4.6c) also confirmed the different bacterial alignment with the decreasing of nano-pillar spaces. Typically, the SEM image (Figure 4.6e) showed the interface between a flat region (right) and the periodic nano-pillars (left) with the space of 1 μm. It is evident that the bacteria changed from random orientation to preferred orientations according to the pillars. Therefore, we hypothesized that the preferential orientation/alignment behavior of cells when attaching onto nano-pillars were attributed to the different pillar-spaces, and nano-pillars with smaller spaces would have a more significant effect.

An in-house made MATLAB code (see 4.6 Appendix) was used to quantify the cell orientation/alignment of *P. aeruginosa* on the periodic nano-pillars. Attached bacterial cells were categorized as "Parallel (0-30º)", "Diagonal (30-60º)" or "Perpendicular (60-90º)", according to the smallest angle difference between the cell and horizontal axis of nano-pillar pattern which is defined as 0º (Figure 4.7a). It was found that the spacing of nano-pillars has profound effects on the different cell orientation/alignment as we hypothesized. For the nano-pillar with 5 μm-spacing, the cell orientation exhibited a near-uniform distribution of attachment angles (Figure 4.7) ($p > 0.05$), which is similar to the angle distribution as found on flat surface. If the space of nano-pillars decreased to 2 μm, more cells orientated as "Perpendicular (60-90º)" (41.58 ± 5.75% of the total attached cells) and "Perpendicular (60-90º)" (36.56 ± 5.30%), as compared with "Diagonal (30-60º)" (21.86 ± 5.36%) ($p < 0.05$). While if the space of nano-pillars decreased further to 1 μm, most cells orientated as "Parallel (0-30º)" (40.42 ± 8.36%) or "Perpendicular (60-90º)" (44.37 ± 8.76%) ($p < 0.05$), which is consistent with the fluorescent microscopy images as shown in Figure 4.6d. The quantification above confirmed that the periodic nano-pillars with smaller spaces have profound effects on the cell orientation/alignment when attaching onto the nano-pillar surfaces.

In addition to the effects on cell orientation/alignment of *P. aeruginosa*, the periodic nano-

pillars were also found inhibitory to the initial bacterial attachment. By assessing the fluorescent microscope images as shown in Figure 4.6a, the nano-pillar space is positively correlated with the initial bacterial attachment (Figure 4.7b, $r > 0.98$ for all surfaces, Pearson correlation analysis). Also, the total attachment of *P. aeruginosa* cells on flat and nano-pillar surfaces was found to be ranked in the order: flat surface > 5 μm-spacing > 2 μm-spacing > 1 μm-spacing. Additionally, all the nano-pillar surfaces harbored less surface area covered by bacteria, as compared with the flat surface (p <0.05). On the other hand, both 2 μm-spacing and 1 μm-spacing nano-pillar surfaces have less attached bacterial cells as compared with 5 μm-spacing one (p < 0.05). While the attached cells on 2 μm-spacing and 1 μm-spacing nano-pillar surfaces are not significant (p =0.13).

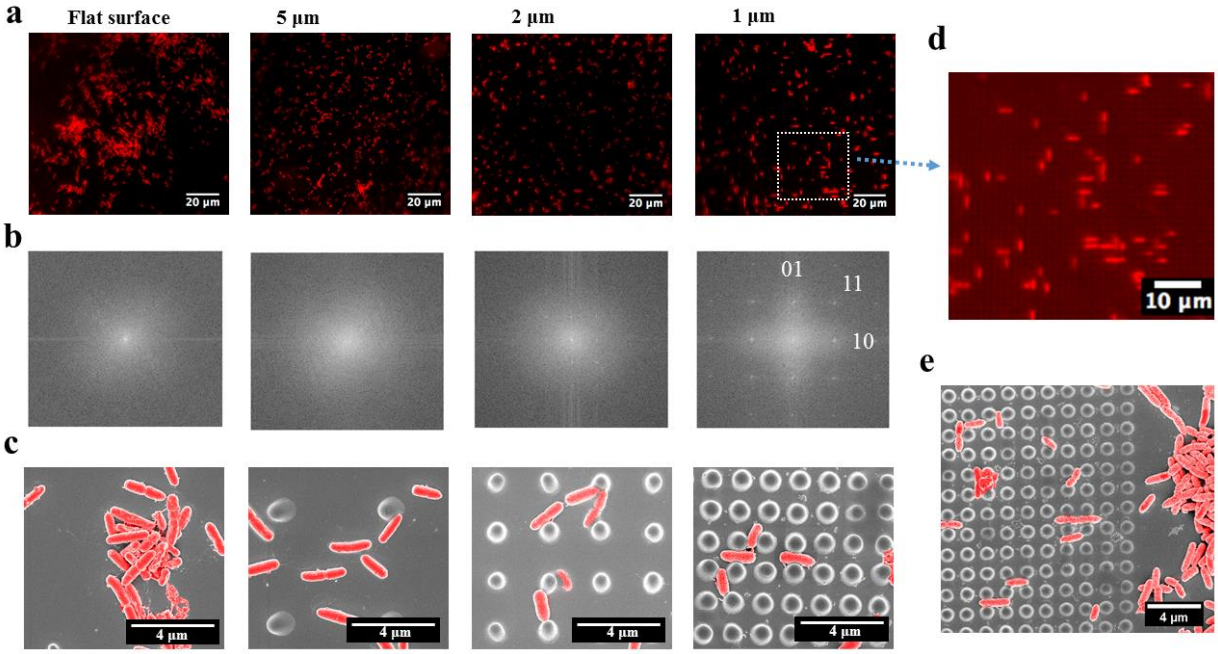

Figure 4. 6 The orientation/alignment of *P. aeruginosa* PAO1-mCherry cells on periodic nano-pillars after the initial attachment (~2 hours). **(a):** Fluorescent microscopy images of orientated cells on flat and nano-pillar patterned (~5 μm, 2 μm and 1 μm-spacing) surfaces. **(b):** The corresponding FFT images indicated the different ordering of cells. **(c):** The corresponding SEM images also showed the different bacterial alignment with the decreasing of nano-pillar spaces. **(d):** Bacteria attached parallel or perpendicular to nano-pillars with the space of 1 μm. **(e):** And this transition is apparent as shown in the SEM image.

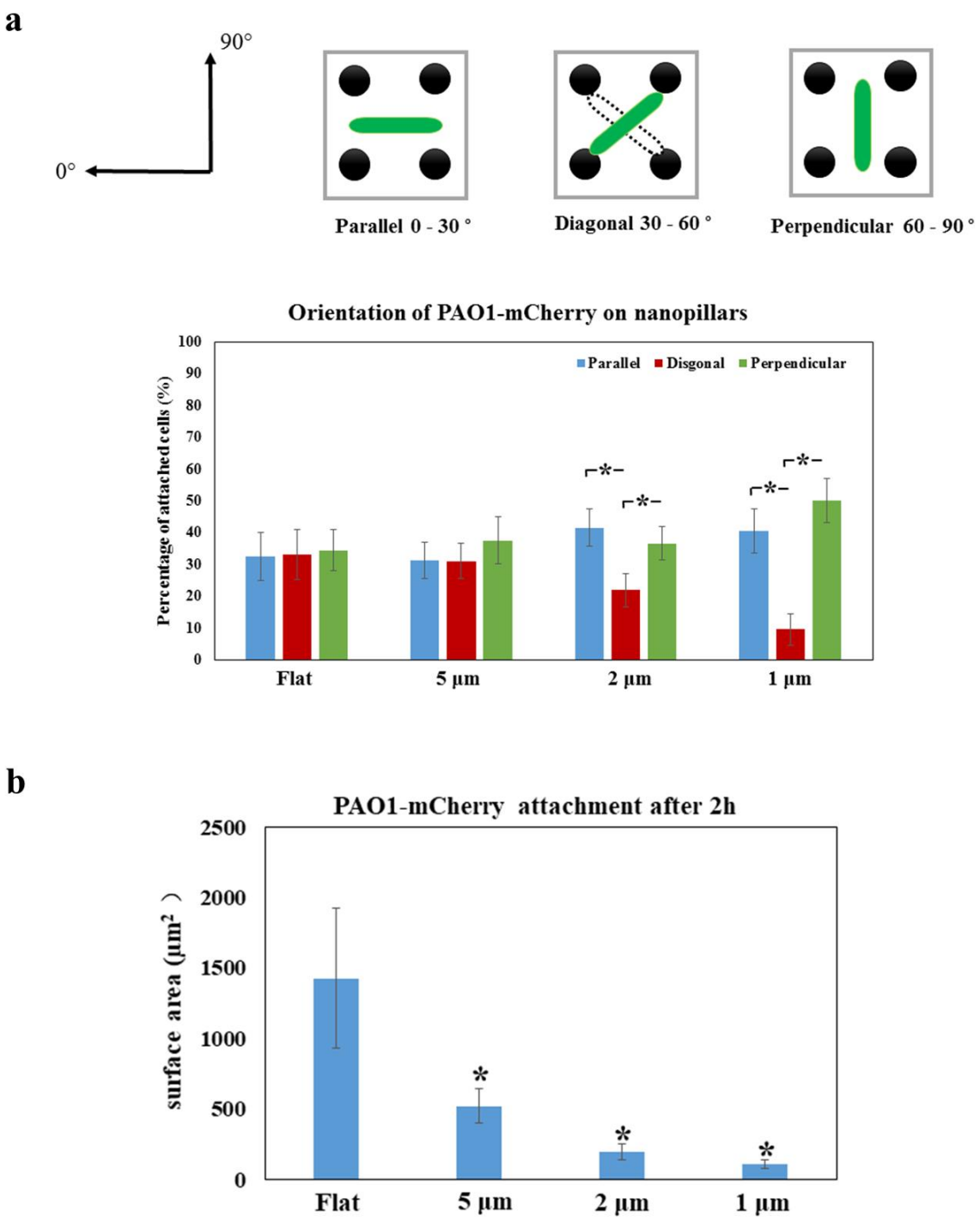

Figure 4. 7 (a): Distribution of *P. aeruginosa* PAO1-mCherry cell orientation/alignment on flat and nano-pillar patterned (~5 µm, 2 µm and 1 µm-spacing) surfaces after 2 hours' incubation, *statistically significant difference (p<0.05). **(b):** Surface area covered by bacteria in the field of view for each surface after 2 hours' incubation. *statistically significant difference as compared with flat surface (p<0.05). Values in (a-b) are mean ± standard deviation of three independent experiments.

To understand the interactions between the cell and pillars, we used SEM at a higher magnification to visualize the interaction of *P. aeruginosa* with surfaces (Figure 4.8 a-b). In addition, the measured diameter and length of *P. aeruginosa* cells were 0.54± 0.10 μm and 1.37 ± 0.81 μm based on analyzing SEM images (n=20). It is noted that most bacterial cells prefer to colonize between nano-pillars (Figure 4.6c &4.8a), which is attributed that these areas can provide more colonization sites as compared with the top of nano-pillars (Lorenzetti *et al.*, 2015; Cao *et al.*, 2018). For 5 μm-spacing nano-pillar surface, since the spacing between pillars is much larger than the bacterial size (0.54± 0.10 μm in diameter, 1.37 ± 0.81 μm in length), up to 2-10 bacterial cells can potentially deposit between pillars (Figure 4.6c &4.8a). Also, 23.14 ± 10.18% of the attached cells (based on 10 SEM images with a total of 314 cells number) can contact the sidewalls of nano-pillars (Figure 4.8 a1-2). When the nano-pillars space decreased to 2 μm which is near to the length of *P. aeruginosa*, up to 1-2 bacterial cells can potentially lie within the nano-pillars (Figure 4.6c &4.8a). Longer cells were able to contact two pillars (Figure 4.8 a3), and two bacterial cells can squeeze between the pillars as shown in Figure 4.8 a4. On the other hand, 88.66 ± 11.34% of attached cells (based on 10 SEM images with a total of 98 cells) can contact the sidewalls of nano-pillars on the 2 μm-spacing nano-pillar surfaces. In addition, if the pillar spacing further decreased to 1 μm which is closer to the diameter of *P. aeruginosa*, it showed the extreme case (Figure 4.8 a5-6) where 98.82 ± 1.18% cells squeezed between the pillars (based on 10 SEM images with a total of 76 cells), as the space only allowed up to one bacteria sit between nano-pillars thereby affecting cell alignment. With the decreasing of pillar spacing, it leads to less colonization sites for bacterial cells to attach in between pillars, which can inhibit the initial bacterial attachment as previously reported (Lorenzetti *et al.*, 2015; Cao *et al.*, 2018). While bacteria tend to maximize their contact area with the surface textures, where the nano-pillars act as topographical extensions of the substrate. Therefore, cells preferentially make contacts with nano-pillars, which led to the preferable alignment as shown in Figure 4.6-4.7. This also possibly explained why the attached cells on 2 μm-spacing and 1 μm-spacing nano-pillar surfaces are reduced.

4.3.3 Bacterial nanotubes aid in the cell-cell connections on nano-pillars after 2 hours

We further explored the high-resolution SEM images (Figure 4.8) and surprisingly, tubular structures (hereafter referred to as 'nanotubes') that project from the cell surface at different positions were plainly visible. These bacterial nanotubes were measured to be several micrometer in length and about 20-100 nm in diameter, consistent with the dimensions as previously reported (Dubey and Ben-Yehuda, 2011). Strikingly, we observed that "root-like" extending nanotubes projected from the single cell surface and elongated away to a distance of a few microns, which can bridge the sidewalls of nano-pillars (Figure 4.8, red arrows). Whilst we noticed that extending nanotubes can encounter and interconnect distal cells (Figure 4.8, yellow arrows), and even these ''long-distance'' intercellular nanotubes can occasionally make contacts with the nano-pillars (Figure 4.8 a4&b1, yellow arrows). Also, ''short-distance'' intercellular nanotubes (~ 1μm in length) were visible between the cells lying in proximity (Figure 4.8, dashed yellow arrows), and connected the neighboring cells together. Notably, long extending or intercellular nanotubes frequently exhibited both bright and dark regions, which may be attributed to the different focal positions under the SEM. The nanotubes originated from cell surfaces at a higher focal position, the emergence sites were usually brighter (Figure 4.8, red and yellow arrows), akin to the thickness of short intercellular nanotubes (Figure 4.8, dashed yellow arrows). While the long nanotubes in the dark regions (Figure 4.8, green arrows) looked as if they were thinner than the short intercellular ones. To improve the imaging quality of nanotube networks under the SEM, we used indium tin oxide (ITO) coated glass substrates and the identical culture conditions. With the good conductivity of ITO-glasses, we enabled to view the nanotubes without coating the bacteria (Figure 4.9). The complex nanotube networks were still visible, exhibiting with a uniform thickness of around 20 nm for all nanotube types (Figure 4.9). This confirmed that the coating thickness and the different focal planes contributed to the dissimilar nanotube morphology within nano-pillars. On ITO-glasses, even an isolated cell far away from its neighbors still produced nanotubes radially (Figure 4.9 a). By contrast, intercellular nanotubes that emerged between neighboring cells, showed as either long or short ones similar to the cells within nano-pillars (Figure 4.9 b-c). The observations above indicated that the development of nanotube networks is prevalent when bacteria grow on a solid surface, and may mediate the cell attachment.

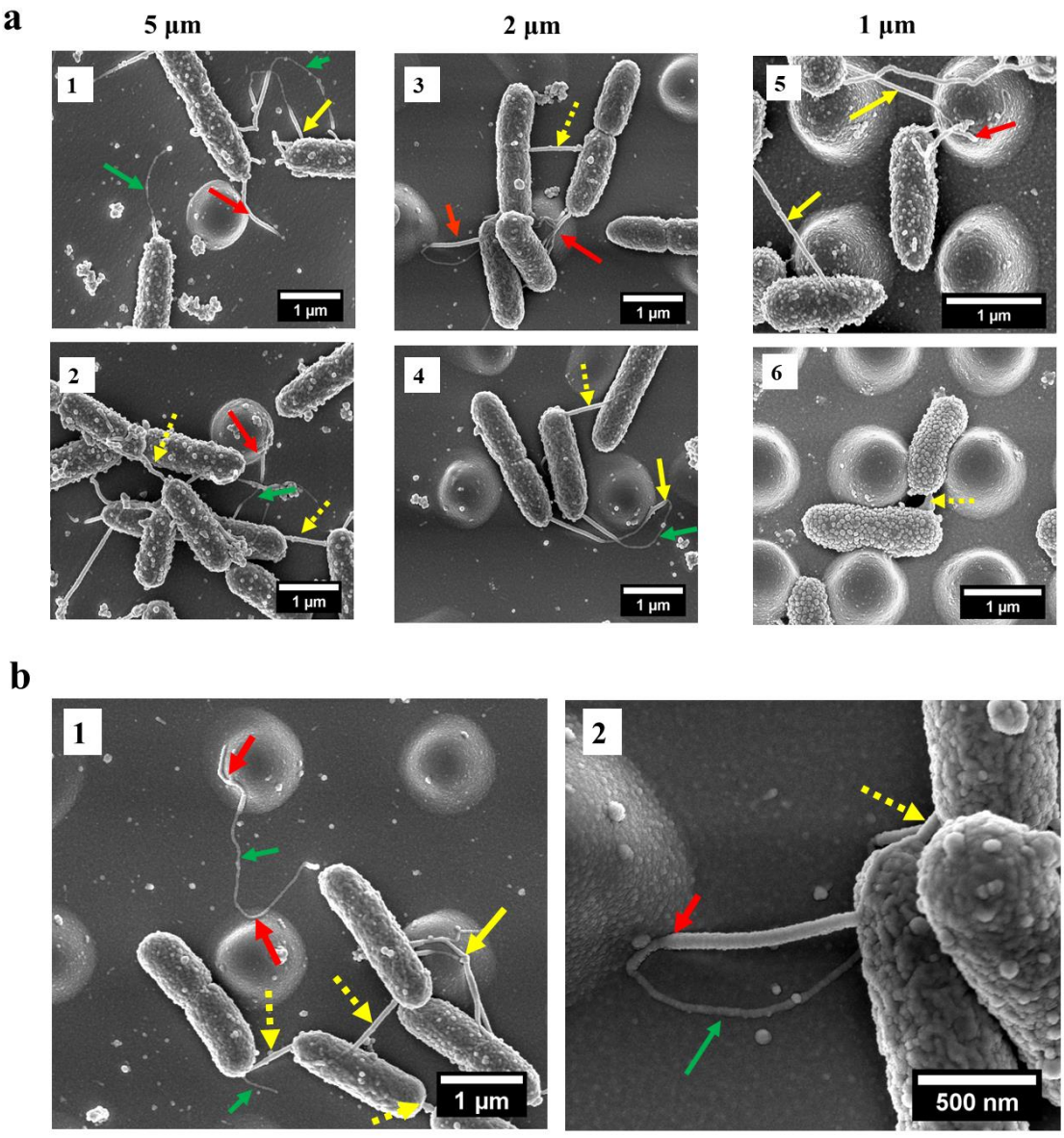

Figure 4. 8 Adherence of *P. aeruginosa* PAO1-mCherry on different surfaces after 2 hours' incubation. Red arrows: extending nanotube webs bridging the sidewalls of nano-pillars; yellow arrows: long intercellular nanotubes bridging the neighboring cells, which can also occasionally the nano-pillars; dashed yellow arrows: short intercellular nanotubes bridging the closely neighboring cells. Green arrows: nanotubes exhibiting dark appearances.

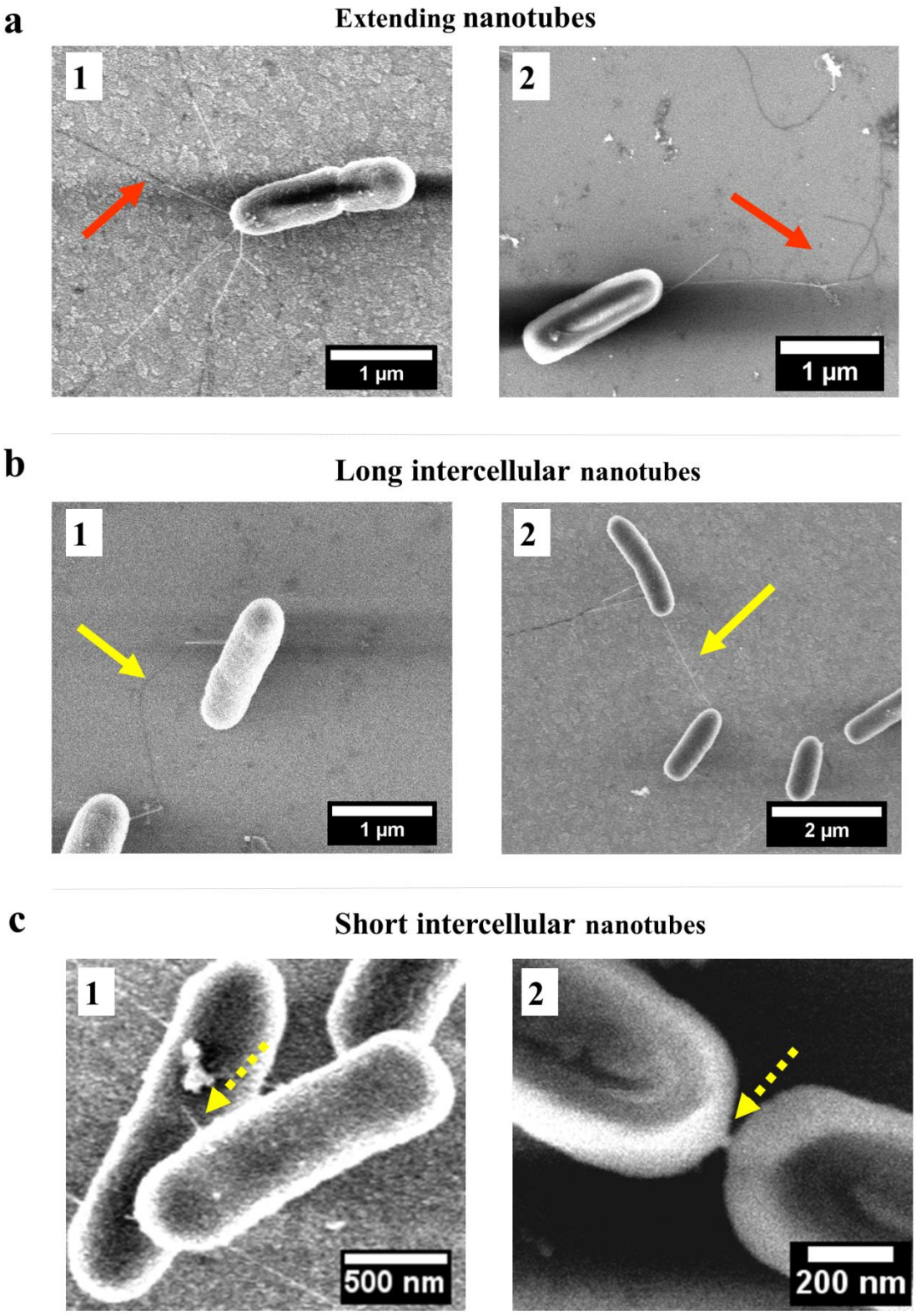

Figure 4. 9 Adherence of *P. aeruginosa* PAO1-mCherry on ITO glass substrates after 2 hours' incubation. Red arrows indicated extending nanotubes emerged from the single cell; yellow arrows indicated the long intercellular nanotubes for connecting neighboring cells; dashed yellow arrows indicated the short intercellular nanotubes when cells were residing close by.

The transition from reversible to irreversible adhesion of *P. aeruginosa* involves the cell repositioning to a longitudinal position via cell appendages like flagella or pili, as cells that are bound by their pole are capable of spinning along their axis or crawling to maximum the contact area between the cells and the surface (Berne *et al.*, 2018). To investigate that if these nanotubes were either flagella or pili and if they are involved into the cell alignment within the nano-pillars, mutants lacking the necessary genes to synthesize either flagella or pili (PAO1 *Δflim* and *ΔpilA*, kindly shared by Prof. Matthew Parsek, University of Washington) were used. *Δflim* bacteria do not possess flagella and show impaired swimming and swarming motilities thereby lacking cell spinning. *ΔpilA* mutant exhibited a major deficit in twitching motility thereby cannot walk or crawl over the surfaces (Conrad *et al.*, 2011; Bruzaud *et al.*, 2015). We grew these bacterial mutants on the nano-pillars with the spacing of 1 μm for 2 hours with identical culture conditions to those used for the wild type *P. aeruginosa* PAO1-mCherry. As shown in Figure 4.10 a, the cell alignment of either PAO1 *Δflim* or *ΔpilA* is similar to the wild type, and cell attachment showed as parallel or perpendicular within pillars. This indicates that the appendage knockouts (i.e. flagella and pili) have little effect on the cell alignment behavior within nano-pillars. Notably, the nanotubes were also evident on bacterial mutants (Figure 4.10 b), ruling out the possibility that these nanotubes are flagella or pili. Our investigations above indicated that the cell alignment maybe a general phenomenon, occurring in examples of wild-type bacteria and in the absence of flagella or pili.

Overall, the investigation above clearly showed that the surface topography at the micro- and nanoscale which is comparable to the bacterial size, can affect bacterial alignment and attachment. It is likely that cells try to maximize contact area with the surface topography, presumably to achieve a stronger and more stable attachment, which results in a specific alignment behavior of the attached cells. By using the nano-gratings with width varying from 100 to 500 nm, the cell alignment and physical isolation of entrenched *P. aeruginosa* bacterial cells were evident, and similar alignments were shown for its mutant strains (*ΔfliM*, *ΔpilA* and *ΔpilAfliM*) (Lai, 2018). Hochbaum *et al.* (Hochbaum and Aizenberg, 2010) also found that cells align between the periodic nano-pillars with a gradient of post pitch (2.2, 0.9 and 0.7 μm), occurred for other bacteria such as gram-positive *Bacillus subtilis*, gram-negative *P. aeruginosa* and *Escherichia coli*, as well as the mutant strains lacking of flagella or pili. These investigations in the literatures were consistent with the finding in this study. Also, the occurrence of nanotubes in the same manner suggested that the cell alignment is

related to interactions with the cell surfaces or biofilm components closely associated with the cell wall. Here, we did not show the direct evidence that nanotubes mediate the cell alignment within the nano-pillars. While it is plausible that either extending or intercellular nanotube networks can greatly increase the cell surface areas and enhance its ability to sense surrounding environment (Baidya *et al.*, 2018). Additionally, our high-resolution SEM images give the evidences showing that nanotubes can aid in cell-cell connections after the bacterial growth on surfaces even over a short time (2 hours).

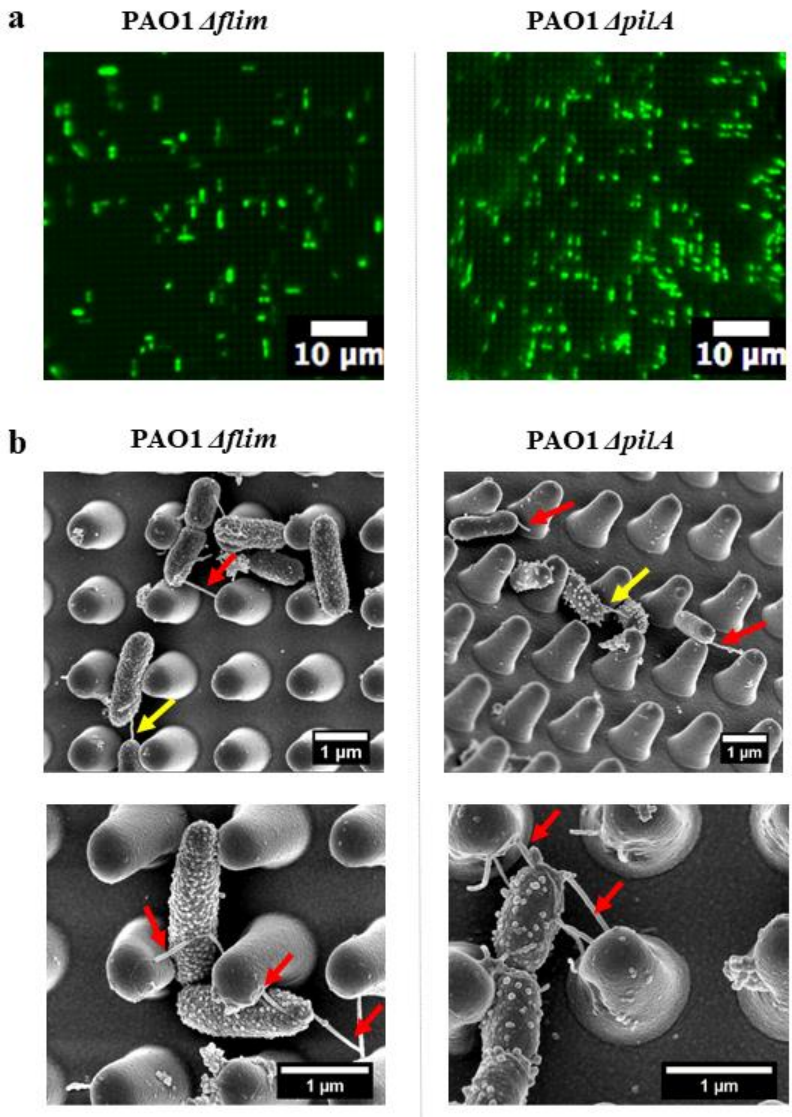

Figure 4. 10 The bacterial attachment (2 hours) of PAO1 *Δflim* and *ΔpilA* within nano-pillars. **(a):** The fluorescence microscopy images of PAO1 *Δflim* and *ΔpilA* showed that cell orientation is persistent even in strains lacking the appendages typically used for surface attachment. All cells were labeled with SYTO™9 green fluorescent nucleic acid stain. **(b):** The SEM images of PAO1 *Δflim* and *ΔpilA* showed the nanotubes. Red arrows indicated extending nanotubes bridging the sidewalls of nano-pillars. And yellow arrows indicated intercellular nanotubes bridging the neighboring cells.

4.3.4 The growth of *P. aeruginosa* biofilm is aided via bacterial nanotubes on periodic nano-pillars after 24 hours

By using fluorescent microscopy and SEM (Figure 4.11 a-b), we investigated *P. aeruginosa* growth on periodic nano-pillars after 24 hours. Firstly, we evaluated that if nano-pillars may also delay the biofilm growth. The total biomass on the flat surface was found to be almost 1.5 times, twice and 1.8 times more than that on nano-pillar surfaces (5 µm-spacing, 2 µm-spacing and 1 µm-spacing, respectively) (see Figure 4.11c). The flat surface harbored more *P. aeruginosa* biofilm clusters shown as a 3D structure with well-connected nanotube filament network as shown in the SEM images (Figure 4.11 b1-2). Smaller biofilm clusters with the nanotube networks were also found between the nano-pillars on the 5 µm-spacing structure (Figure 4.11 b3). In addition, small aggregates comprising around 7 cells were found near the pillar, which had connected each other via the nanotube filament network. Similar observations were also found on the 2 µm-spacing structure (Figure 4.11 b5-6 & 12c) and the biomass is significantly lower than that on 5 µm-spacing structure (Figure 4.11c, $p < 0.05$). Surprisingly, we observed that bacterial cells filled into the 1 µm-spacing structure and started forming biofilm clusters at the top layer of nano-pillars (Figure 4.11 b7-8). The biomass on this surface (15.77±4.26 $\mu m^3/ \mu m^2$) was higher than that on 2 µm-spacing structure (14.99±2.66 $\mu m^3/ \mu m^2$) even they are not significant (Figure 4.11c, p =0.61). Notably, the presence of a dense and much more complex web of nanotube filament network surrounding the cells was observed on this surface (Figure 4.11b8 & 12d). Similar to the adherence of *P. aeruginosa* within nano-pillars after 2 hours (Figure 4.8), extending nanotubes after 24 hours bridged the sidewalls of nano-pillars (Figure 4.11, red arrows) and some intercellular nanotubes bridged the neighboring cells (Figure 4.11, yellow arrows). Surprisingly, some nanotubes can reach up to 10 µm (or even longer) via migrating across the nano-pillars (Figure 4.11b &Figure 4.12), even there was no bacterial cells setting onto the pillars; and these long nanotubes can connect the isolated cells really far away. It seemed likely the observed nanotube filament networks further developed over time and facilitated cells to connect each other with forming either bacterial aggregates or clusters.

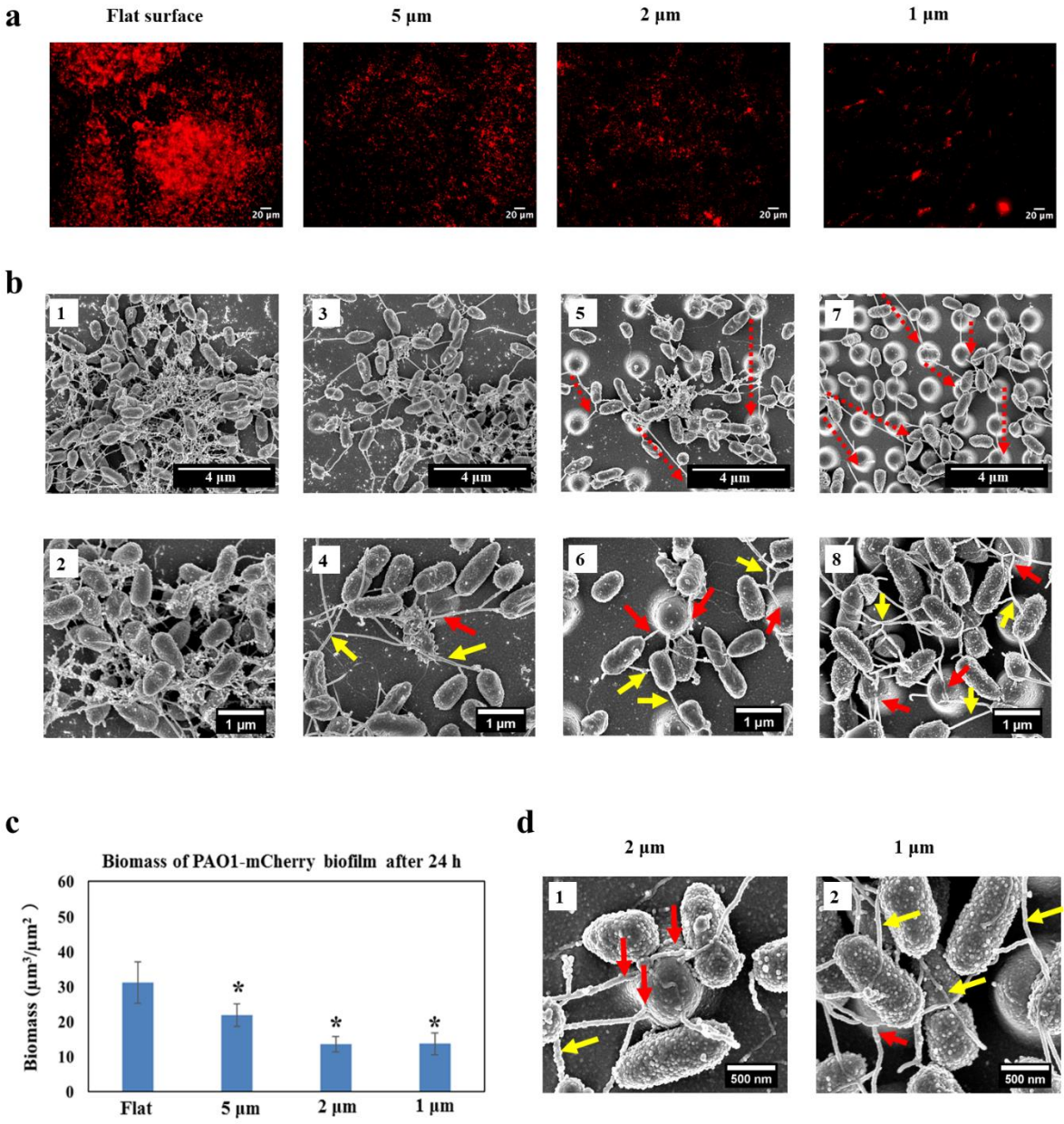

Figure 4. 11 (a) Early stage *P. aeruginosa* PAO1-mCherry biofilms grown on different surfaces over a period of 24 hours. Representative fluorescent images shown as maximum intensity projections through the thickness of the biofilms. **(b)** SEM images of *P. aeruginosa* PAO1-mCherry 24h-biofilms visualized at the magnification of 25000×. The dashed red arrows indicated the migration of nano-tubes. The red arrows indicated the nanotubes contacted the pillars and yellow arrows indicated the intercellular nanotubes for connecting neighboring cells; **(c)** Biomass volume per area on the nano-pillar substrates. *statistically significant difference as compared with flat surface ($p < 0.05$). Values are mean ± standard deviation of three independent experiments. **(d):** SEM images of *P. aeruginosa* PAO1-mCherry 24h-biofilms visualized at the magnification of 50000× on 2µm-spacing and 1µm-spacing nano-pillars. The red arrows indicated the nanotubes contacted the pillars and yellow arrows indicated the intercellular nanotubes for connecting neighboring cells.

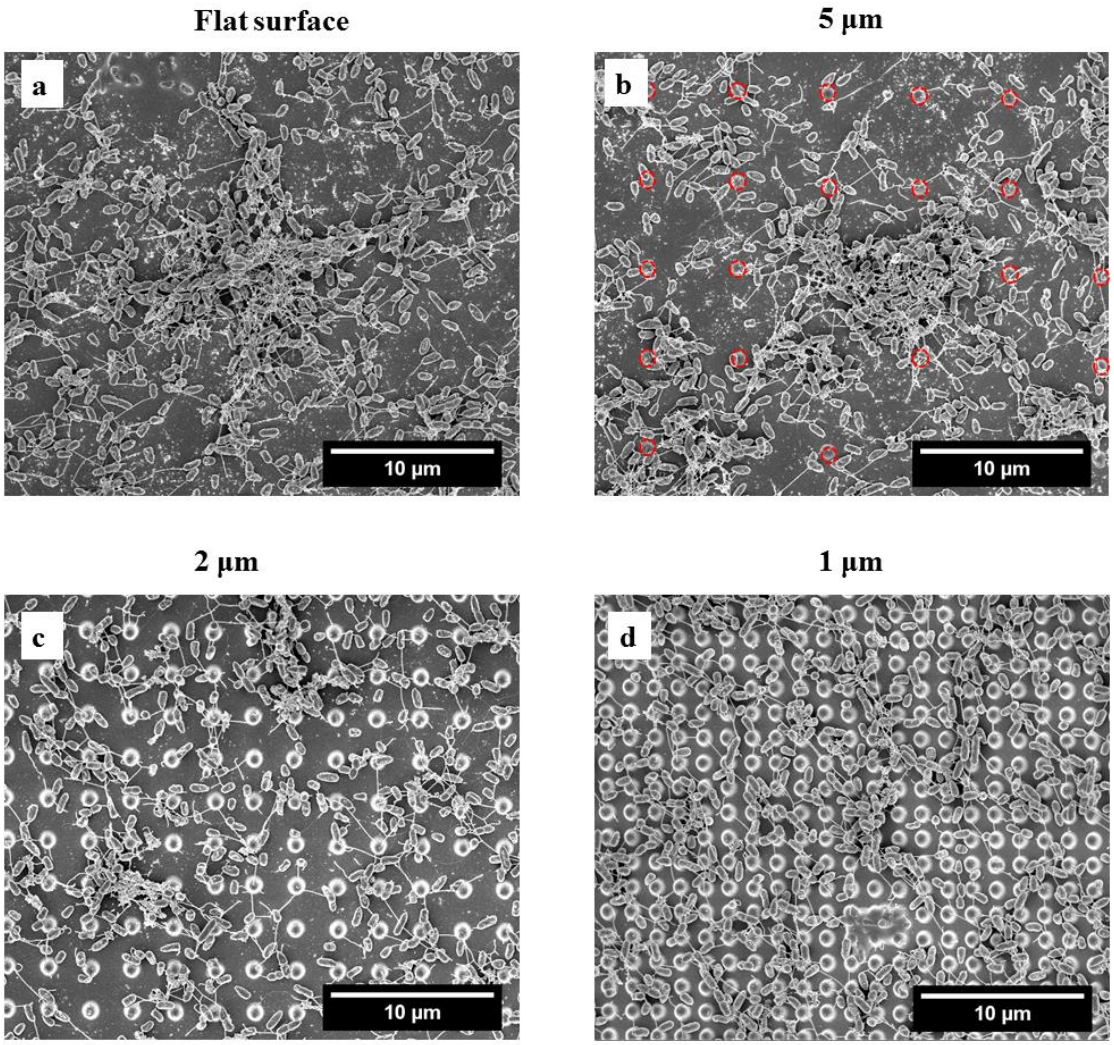

Figure 4. 12 SEM images of *P. aeruginosa* PAO1-mCherry 24h-biofilms visualized at the magnification of 8000×. The red circles in image 2 indicated the nano-pillars.

We herein set out to characterize the biofilm growth on the periodic nano-pillar surfaces over time. The first interesting observation is that, despite the different spaces of nano-pillars, *P. aeruginosa* still progresses through the typical early stage of biofilm development with developing bacterial aggregates or clusters (Figure 4.12), although the biomass on nano-pillar surfaces was lower than that on the flat surface (Figure 4.11c). At this stage, cells didn't exhibit any preferential orientation behavior as cells start to form aggregates or clusters, involving a much more complicated dynamic process. We observed that a preliminary biofilm cluster with a 3D structure formed between the nano-pillars with 5 µm space (Figure 4.11 b3 & Figure 4.12b), with the morphology which was akin to that on the flat surface (Figure 4.12a). By contrast, on 2 µm-spacing or 1 µm-spacing nano-pillars, *P.*

aeruginosa developed smaller and more heterogeneous bacterial clusters on recessed portions of patterned surfaces, possibly because nano-pillars isolated the bacterial cells or aggregates (Figure 4.12 c-d). One way to inhibit early-stage biofilm is employing a specific surface topography to hinder cell body contacts (Kargar *et al.*, 2016). Here, it has also demonstrated that the periodic pillars with a smaller pitch led to a lower attachment. In which case, bacterial cells were supposed to be separated by the nano-pillars. However, the isolation effects cannot be sustainable overtime since multiply bacterial cells can easily deposit between nano-pillars as shown in Figure 4.11 b5-8. For nano-pillars with 1 µm and 2 µm spacing, bacteria cells covered the pillar gaps and formed multi-layered bacterial clusters either around or on the top the nano-pillars (Figure 4.12 c-d). Additionally, the accumulated cells can either mask the surface chemistry or smooth the surface topography, and serve as a conditioning film to provide nutrients and adhesion receptors for subsequent bacterial attachment (Cao *et al.*, 2018). Collectively, nano-pillars can delay the biofilm growth owing to the isolation of cells within the structure, while may not be effective overtime with forming small biofilm clusters.

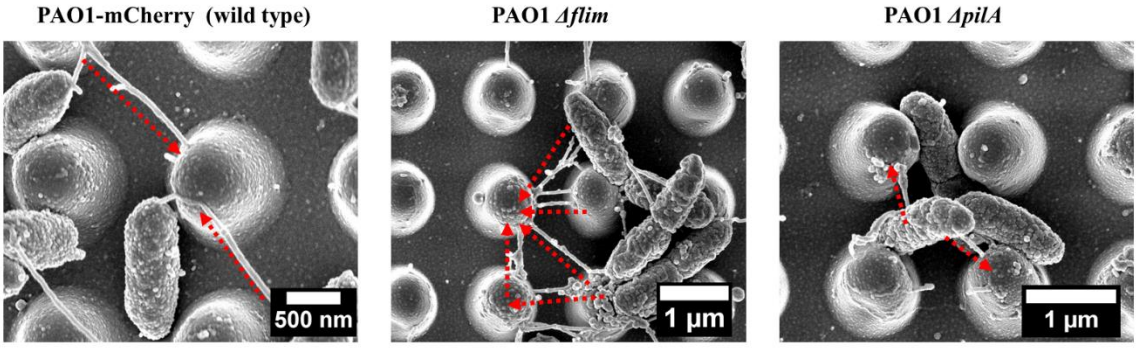

Figure 4. 13 SEM images of the nanotube networks of *P. aeruginosa* PAO1-mCherry, PAO1 *Δflim* and PAO1 *ΔpilA* after 24 hours. The red arrows indicate the nanotube connect the neighboring nano-pillars to form web-like networks.

The second interesting observation is that the 1 µm-spacing nano-pillars are not effective in delaying biofilm growth as compared with the 2 µm-spacing nano-pillars after 24 hours (Figure 4.11 c), even if it can inhibit the initial bacterial attachment. Therefore, there seems another separate effect, which mediate the bacterial growth on nano-pillars. We noticed that biofilm clusters developed within the confined spaces, while some separated bacterial cells or aggregates were connected together via the nanotube networks. Also, a more complex

network was observed with the decreasing of nano-pillar spaces (Figure 4.11b & 4.12d). Notably, the nanotube networks are still visible for the bacterial mutants (PAO1 *Δflim* and *ΔpilA*) after 24 hours, which showed the similar morphology to the ones of wild-type images (Figure 4.13). Unlike the nanotubes which only contact the sidewalls of nano-pillars after 2 hours, the nanotubes of either wild-type or mutant ones after 24 hours elongated a web-like network via migrating over nano-pillars (Figure 4.13, red arrows). It is likely that these nanotubes can explore the local geometry with binding onto the nano-pillars, and increase the cell surface area, which help to connect other neighboring or distal cells. To better characterize the nanotube networks without the shielding of cell clusters, we allowed bacteria to attach within nano-pillars after 2 hours. After washing with PBS to remove loosely attached cells, we supplied the new TSB and further grew for 24 hours (Figure 4.14). Strikingly, we observed the elongation of nanotube networks, which connected the nano-pillars one by one. Within the nano-pillars of 2 μm space, the nanotubes can continuously connect around 4-10 pillars (Figure 4.14 a). By contrast, the nanotubes continuously connected around 20-30 pillars within the nano-pillars of 1 μm space (Figure 4.14 b). This indicated that nano-pillars with smaller spaces help the connections between nanotubes. Here, we speculated that the nano-pillars play as the nodes within the nanotube networks for their extension and elongation. Nano-pillars of 1 μm space have more pillars within the same projected area and smaller spaces; and these extended surface topographies can aid in the continuously spread of nanotubes along the nano-pillars. Therefore, the nano-pillars with the spacing of 1 μm cannot effectively isolate the cell clusters, as the nano-pillars can be easily overcome by the nanotubes, which connected the bacterial aggregates far away. Here, the separated bacterial cells or aggregates can possibly communicate via the connected nanotube networks instead of direct cell body contacts, thereby promoting the further biofilm development. This speculation is consistent with the observations showing the increased biofilm growth and more complex nanotube networks on 1 μm-spacing nano-pillars.

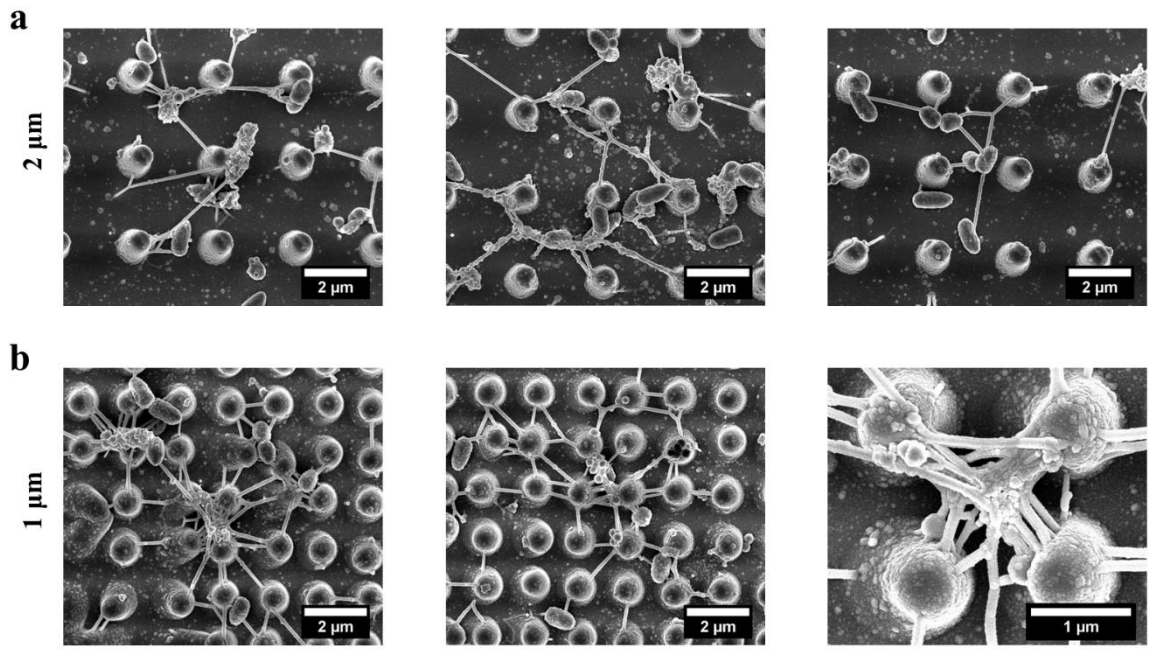

Figure 4. 14 SEM images of the nanotube networks of the attached *P. aeruginosa* PAO1-mCherry cells (after 2 hours) with the further incubation after 24 hours **(a)**: within the nano-pillars of 2 µm space; **(b)**: within the nano-pillars of 1 µm space.

Bacterial nanotubes or nanotube networks have been found within various bacterial species, suggesting that their existences are widespread in nature. For example, nanotubes of *B. subtilis* cells were formed within several minutes after bacteria grow on a solid surface, which exhibit as both intercellular tubes and extending tubes (Dubey *et al.*, 2016). In addition, Cryo-EM analysis showed that nanotubes directly emanate from the cytoplasmic cell membrane, consisting of chains of consecutive constricted segments harboring a continuous lumen (Dubey *et al.*, 2016; Baidya *et al.*, 2018). Also, these nanotube networks can serve as a route for exchange of cellular molecules within and between species (Dubey and Ben-Yehuda, 2011). Extracellular nanotube-like networks were also implicated in long-range extracellular electron transport in *Geobacter sulfurreducens*, *Shewanella oneidensis* MR-1, *Pelotomaculum thermopropionicum* and *Methanothermobacter thermoautotrophicus* (Reguera *et al.*, 2005; Malvankar and Lovley, 2012; Maruthupandy *et al.*, 2015; Steidl *et al.*, 2016; Sure *et al.*, 2016). Additionally, the nanotube-like networks of *S. oneidensis* MR-1 has been found to be extensions of the outer membrane which are associated with outer membrane vesicles, structures ubiquitous in Gram-negative bacteria, rather than pilin-based structures as previously thought (Pirbadian *et al.*, 2014). Similarly, nanotube networks produced by *Myxococcus xanthus* indicated to be in the form of outer membrane vesicle chains, which connect cells spatially and transfer outer membrane proteins in a contact-

dependent manner, thereby promote the biofilm growth (Remis *et al.*, 2014). Even the observations of nanotubes within various bacteria have been reported, little is known about the mechanism of nanotube formation. A gene implicated in nanotube formation of *B. subtilis* is *ymdB*, encoding a calcineurin-like phosphodiesterase, and *ymdB* mutants exhibited a great deficiency in nanotube production (Dubey *et al.*, 2016; Baidya *et al.*, 2018). *YmdB* can repress the expression of motility genes and induce the genes of biofilm formation, hence controlling the switch from a motile to a multicellular sessile life style (Baidya *et al.*, 2018). Additionally, recent studies revealed that the export apparatus of *B. subtilis* or *E. coli* flagella, designated CORE, can communally serve for the generations of both flagella and nanotubes (Bhattacharya *et al.*, 2019; Pal *et al.*, 2019). Mutants lacking CORE genes don't produce nanotube networks and is deficient in the associated intercellular molecular trafficking (Bhattacharya *et al.*, 2019). Clearly, the mechanism of nanotube formation is still unclear and up to debate. However, it is likely that the formation of nanotube networks might be a preceding stage in the development of a biofilm. Bacterial nanotubes provide the foundation for unhampered intercellular molecular flow via bridging the cells (Baidya *et al.*, 2018). Various SEM images of bacterial biofilms have indicated the potential existences of bacterial nanotubes as prominent bridges between cells (Takahashi *et al.*, 2015; Baidya *et al.*, 2018).

Some preliminary studies on possible nanotube synthesized by *S. epidermidis* was also carried out, which was provided in Appendix. Our preliminary SEM images of *S. epidermidis* also showed the prevalent occurrences of nanotubes on different surfaces (see Appendix, Figure S4.1-4.4). For example, the high-resolution SEM images of *S. epidermidis* cells (~ after 2 hours) on ITO-glasses indicated the bacterial nanotubes for bridging neighboring cells (Figure S4.1). *S. epidermidis* cells (~ after 2 hours) on epoxy surfaces also showed similar bacterial nanotube morphology and there occasionally had some extending nanotubes around the cell body (Figure S4.2). Notably, the FIB-SEM image of *S. epidermidis* cells (~ after 2 hours) on titanium surfaces showed the cross-section of cells that connected each other via nanotubes, which may emanate from the cell membrane (Figure S4.3). Gram-positive *S. epidermidis* does not have flagella or pili, while these tube-like structures were still visible (see Appendix, Figure S4.1-4.4). Though researchers considered these nanotubes as bacteria fibrils (Takahashi *et al.*, 2015), it contrasted our observations of the extending tubes within biofilm growth (see Appendix, Figure S4.4). However, mature bacterial biofilms are complex and heterogeneous structures, and especially the substantial

mass of EPS may shield the nanotubes, thereby precludes deciphering the nature of these connections.

4.4 CONCLUSIONS

In this chapter, the bacterial attachment, cell alignment and biofilm formation of clinically relevant strain *P. aeruginosa* were investigated on the periodic nano-pillar surfaces. Over the short time (~2 hours), bacterial cells showed lower attachment on the nano-pillar surfaces owing to cells preferentially attached into the confined spaces of nano-pillars. Specially, it showed bacteria are more likely to align parallel or perpendicular to nano-pillars with 1 μm pitch. The bacterial nanotubes were evident, where the extending nanotubes can contact the pillars and intercellular ones can connect the cells. By using the bacterial mutants (*Δflim* and *ΔpilA*) lacking flagella or pili, we further demonstrated that such cell alignment behavior within nano-pillars is a general phenomenon, possibly owing to cells tend to maximize their contact area with the surface, where the pillars act as topographical extensions of the substrate. Additionally, nanotubes also occurred in the bacteria mutants, indicating that the formation of bacterial nanotubes are prevalent to aid in cell-surface or cell-cell connections.

Smaller bacterial clusters were formed in between nano-pillars after 24 hours, and was likely to be isolated by the nano-pillars. Therefore, the bacterial growth of *P. aeruginosa* after 24 hours was delayed on periodic nano-pillars, with showing the lower biofilm biomass as compared with the flat surfaces. However, the 1 μm-spacing nano-pillars, which showed the lowest bacterial attachment after 2 hours is not effective in delaying biofilm growth after 24 hours. Nano-pillars with smaller spacing help the extension and elongation of bacterial nanotube networks. Therefore, nano-pillars of 1 μm space can be easily overcome by the nanotubes which connected the isolated bacterial aggregates far away; and such nanotube networks can possibly aid in the cell-cell communications, thereby promoting the further biofilm development.

“Bacterial nanotubes” was found to mediate the bacterial growth on periodic nano-pillars in this study. Similar observations have also been reported recently with showing the different morphologies if comparing with the cell appendages like flagella or pili (Dubey and Ben-Yehuda, 2011; Pirbadian *et al.*, 2015; Baidya *et al.*, 2018; Bhattacharya *et al.*, 2019; Pal *et al.*, 2019). By using bacterial mutants (*Δflim* and *ΔpilA*), we ruled out the effects of the appendage knockouts on the nanotube formation. However, the further characterization of the composition of *P. aeruginosa* bacterial nanotubes may need the sophisticated techniques

like Cryo-EM and total internal reflection fluorescence (TIRF) with super-resolution structured illumination microscopy (SIM) (Dubey *et al.*, 2016).

In the next chapter, hierarchical surface structures were fabricated via getting the imprints of natural rose-petal surfaces, since this chapter have demonstrated the unitary nano-pillars cannot effectively control biofilm growth. In addition, the anti-biofilm mechanism of the artificial rose-petal structured surfaces will be compared with the nano-pillars.

4.5 Appendix

Appendix 1

The Matlab code for determining the bacterial orientation within nano-pillars:

```
clear all; close all; clc
Ar_thresh=50;

I = imread('18.png');
figure(1)
imshow(I)
background = imopen(I,strel('disk',2));
figure
surf(double(background(1:8:end,1:8:end))),zlim([0 255]);
set(gca,'ydir','reverse');
I2 = I - background;
imshow(I2)
I3 = imadjust(I2);
imshow(I3);
bw = imbinarize(I,0.3);%creates a binary image
bw = bwareaopen(bw,10);%Remove Objects in Image Containing Fewer Than 8 Pixels
figure(2)
imshow(bw);
measurements = regionprops(bw, 'Orientation', 'MajorAxisLength', 'Centroid', 'Area');
q  = find([measurements.Area]>Ar_thresh);
measurements(q)=[];

allAngles = -[measurements.Orientation]
hold on;
for k = 1 : length(measurements)
   fprintf('For blob #%d, the angle = %.4f\n', k, allAngles(k));
   xCenter = measurements(k).Centroid(1);
   yCenter = measurements(k).Centroid(2);
   % Plot centroids.
   plot(xCenter, yCenter, 'r*', 'MarkerSize', 4, 'LineWidth', 1);
   % Determine endpoints
   axisRadius = measurements(k).MajorAxisLength / 2;
   x1 = xCenter + axisRadius * cosd(allAngles(k));
   x2 = xCenter - axisRadius * cosd(allAngles(k));
   y1 = yCenter + axisRadius * sind(allAngles(k));
   y2 = yCenter - axisRadius * sind(allAngles(k));
   fprintf('x1 = %.2f, y1 = %.2f, x2 = %.2f, y2 = %.2f\n\n', x1, y1, x2, y2);
   plot([x1, x2], [y1, y2], 'r-', 'LineWidth', 2);

end
z1=sum(allAngles>=-30 & allAngles<30);
z2=sum(allAngles>=-60 & allAngles<-30);
z3=sum(allAngles>=30 & allAngles<60);
z4=sum(allAngles>=60 & allAngles<=90);
```

```
z5=sum(allAngles<-60 & allAngles>=-
90);%z1=parallel,z2&z3=disgonal,z4&z5=perpendicular
z6=deg2rad(allAngles)+pi/2;

a1=z1;
a2=z2+z3;
a3=z4+z5;
```

Appendix 2

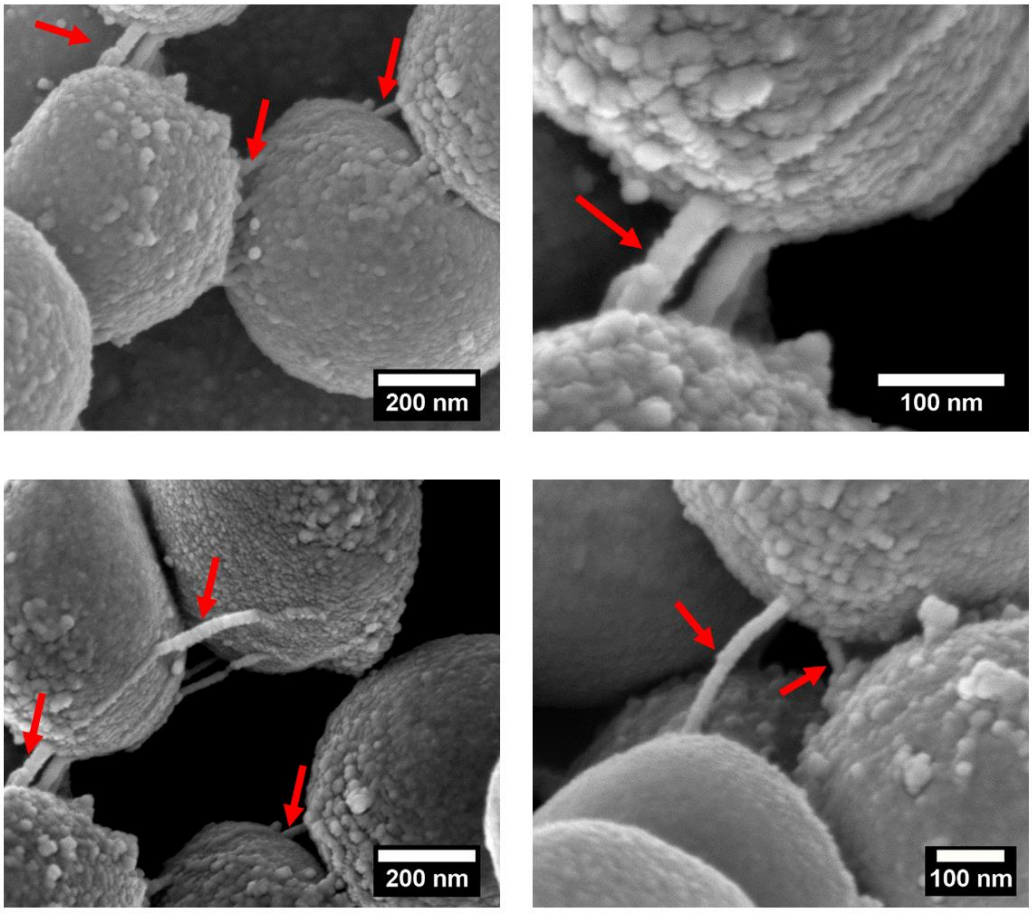

Figure S4. 1 SEM images of *S. epidermidis* cells on ITO-glasses after 2 hours' incubation. Red arrows indicated the bacterial nanotubes for bridging cells.

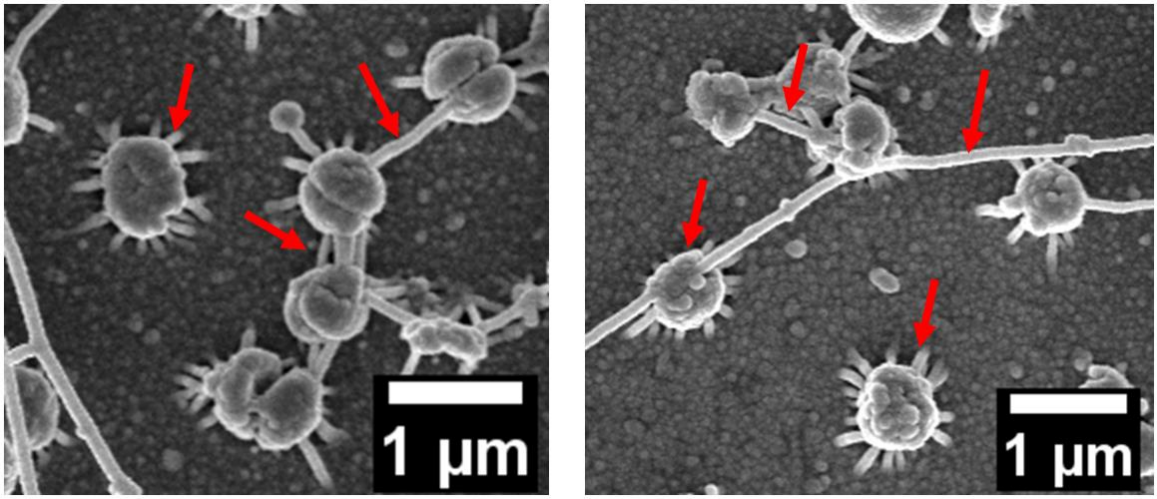

Figure S4. 2 SEM images of *S. epidermidis* cells on epoxy surfaces after 2 hours' incubation. Red arrows indicated the extending or internal bacterial nanotubes for bridging cells.

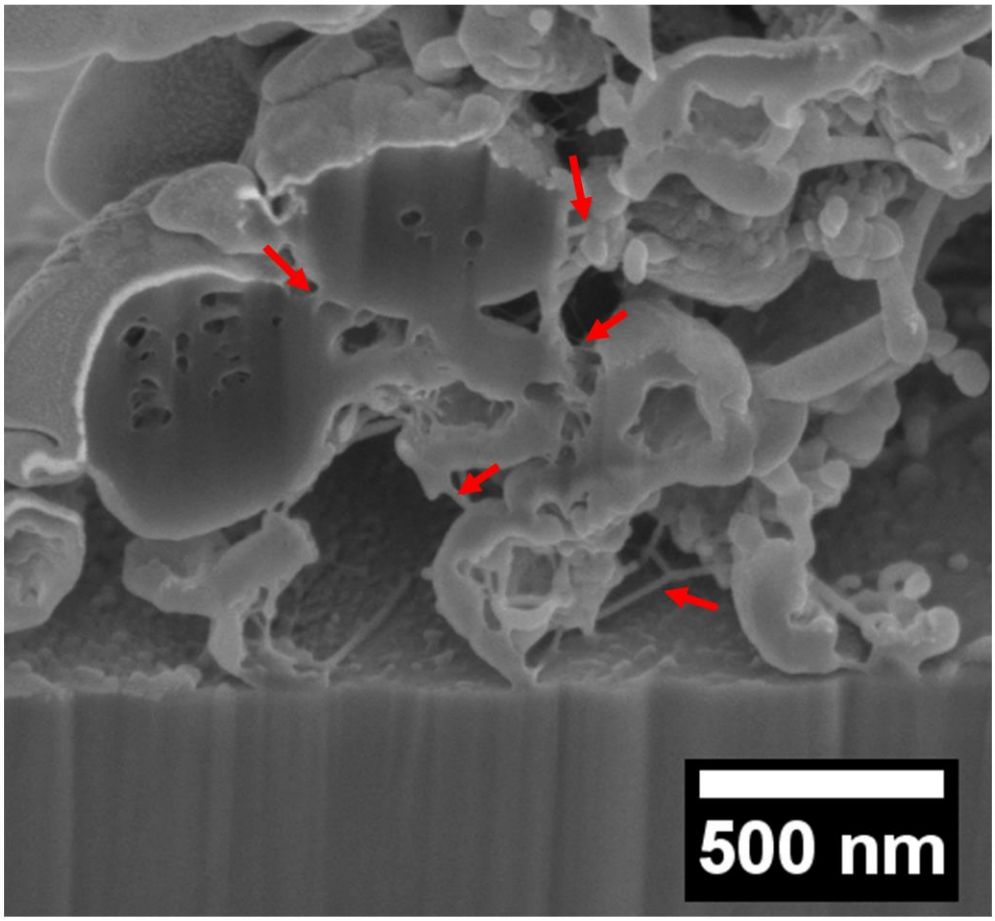

Figure S4. 3 FIB-SEM image of *S. epidermidis* cells on titanium surfaces after 2 hours' incubation. Red arrows indicated the bacterial nanotubes for bridging cells.

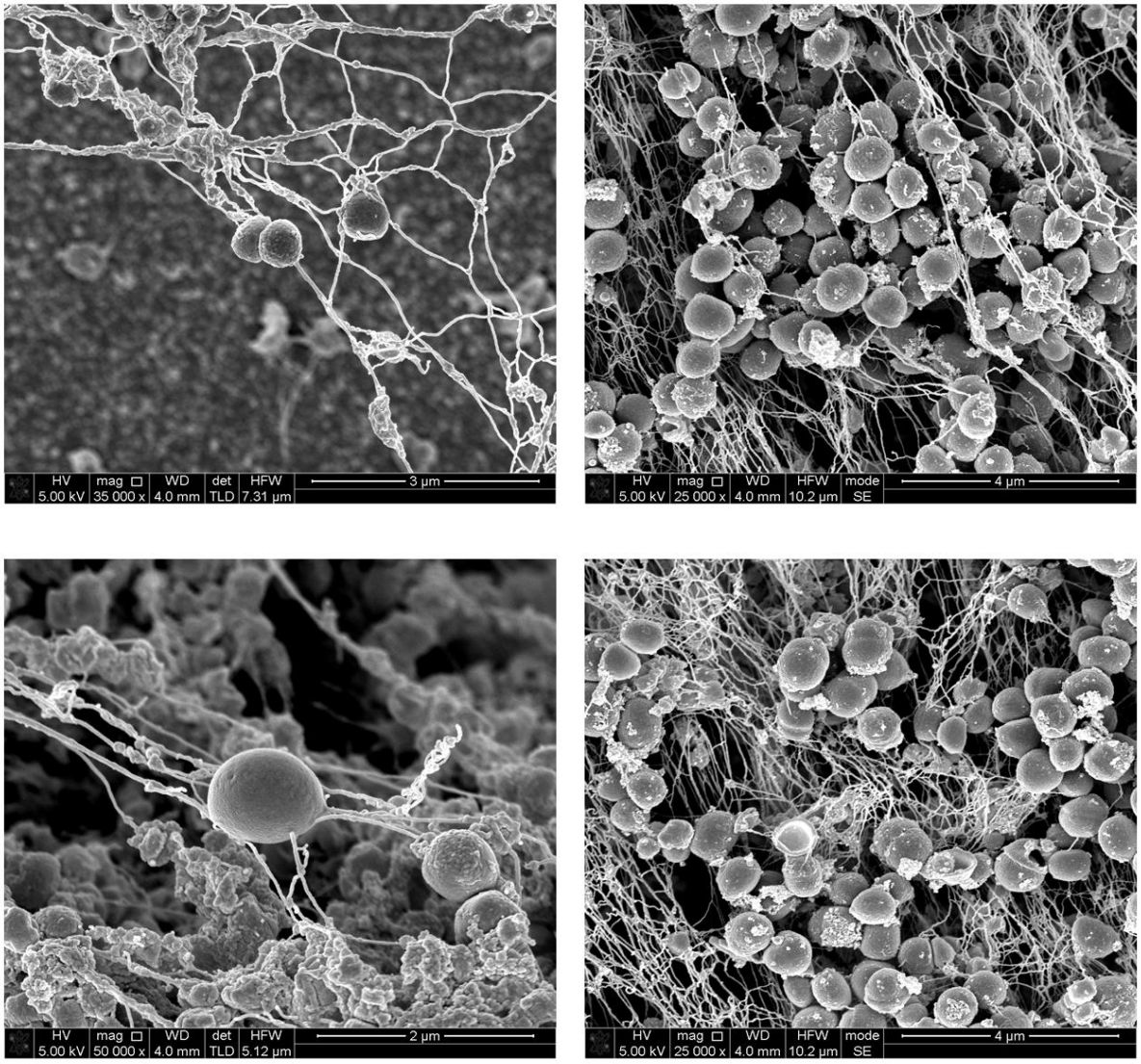

Figure S4. 4 SEM images of *S. epidermidis* biofilms on titanium surfaces after 6 days.

Chapter 5

Hierarchical rose-petal surfaces delay the early-stage bacterial biofilm growth

5.1 INTRODUCTION

Natural surfaces with micro/nano topographical patterns have inspired researchers to design artificial biomimetic surfaces to control biofilm growth. For example, lotus leaf has hierarchical structures such as micro-papillae (measuring ~3-11 μm diameter) that are randomly covered by nano-tubules (~100 nm diameter) (Saison *et al.*, 2008; Koch *et al.*, 2009). Water droplets on these surfaces cannot penetrate the air pockets formed within the hierarchical structures (i.e. Cassie state) (Saison *et al.*, 2008; Koch *et al.*, 2009). As a result, the lotus leaf is found to exhibit superhydrophobicity with a contact angle (CA) >150° and a low contact angle hysteresis (CAH) (i.e. <10°), which results in the easy rolling off of water droplets (i.e. self-cleaning effects) (Koch *et al.*, 2009; Liu and Choi, 2013; Watson *et al.*, 2017). However, it is challenging to reproduce the hierarchical structures on lotus leaf in the laboratory (Odom *et al.*, 2002; Wolfe *et al.*, 2004; Kumar *et al.*, 2018). Using lotus leaf as a template, it has only been possible to fabricate unitary structures based on the micro-papillae; the nano-tubules are too small for this approach (Crick *et al.*, 2011; Fadeeva *et al.*, 2011; Ma *et al.*, 2011; Tang *et al.*, 2011; Truong *et al.*, 2012; Zhang *et al.*, 2013). Hierarchical structures similar to the lotus leaf can be generated using chemical processes, but these are not exactly the same structures as found on natural lotus leaves (Bhushan *et al.*, 2009; Lee and Kim, 2009; Dai *et al.*, 2013; Kim *et al.*, 2013). Nevertheless, lotus leaf-inspired superhydrophobic surfaces (unitary structure or hierarchical structures) can mitigate biofouling by a range of bacteria including *Staphylococcus aureus*, *S. epidermidis*, *P. aeruginosa* and *Planococcus maritimus*, since the trapped air restricts the direct contacts between the solid surfaces and micro-organisms (Ma *et al.*, 2011; Tang *et al.*, 2011; Truong *et al.*, 2012). The anti-fouling efficacy strongly depends on the lifetime of non-wetting (Cassie) state. The wetting transition (Cassie to Wenzel state) can occur within 1-4 hours in submerged environments, with a significant decrease in CA and increase in CAH (Truong *et al.*, 2012; Friedlander *et al.*, 2013). Bacteria can also accelerate such transitions, for example by flagella-mediated motility (Friedlander *et al.*, 2013). Therefore, it is commonly accepted that surface topography features such as size, pitch or height play a primary role in delaying bacterial attachment or biofilm growth and that wettability (CA and CAH) is less important, especially when surfaces get fully wetted (Ma *et al.*, 2011; Friedlander *et al.*, 2013; Lorenzetti *et al.*, 2015; Cao *et al.*, 2018).

Different surface topographies on many other natural surfaces including rice leaves (Bixler *et al.*, 2014), shark-skin (Chung *et al.*, 2007; Reddy *et al.*, 2011; Dundar Arisoy *et al.*, 2018),

gecko-skin (Watson *et al.*, 2015; Li *et al.*, 2016; Green *et al.*, 2017), cicada wings (Ivanova *et al.*, 2012; Diu *et al.*, 2014; Cao *et al.*, 2018), or dragonfly wings (Bhadra *et al.*, 2015; Bandara *et al.*, 2017) have also been demonstrated to have anti-biofilm properties to different levels. Topographical features larger than bacterial cells, such as the microstructures in Sharklet AF^{TM}, constrain bacterial deposition to recessed regions and delay biofilm formation (Chung *et al.*, 2007). Topographies close in size to bacteria can lead to alignment of rod-shaped bacterial cells between the surface features and retard biofilm formation, possibly by blocking cell-cell communications (Hochbaum and Aizenberg, 2010; Díaz *et al.*, 2011a; Hsu *et al.*, 2013; Lai, 2018). By contrast, features such as tightly-spaced nano-spears that are smaller than bacterial cells can delay surface attachment without necessarily restricting biofilm formation to a great extent (Friedlander *et al.*, 2013; Cao *et al.*, 2018). Previous investigations have reported that rose petals have hierarchical structures with micro-papillae (~20 μm diameter) and nano-sized cuticular folds (~730 nm width) (Feng *et al.*, 2008; Dou *et al.*, 2015). Such hierarchical structures make the rose-petal surface superhydrophobic even allowing it to exert a high adhesive force on droplets (Feng *et al.*, 2008). A few studies examined the dynamics of water droplets and efficacy of the structured surfaces in preventing bacterial growth (Feng *et al.*, 2008; Dou *et al.*, 2015). However, the mechanism responsible for the inhibition of bacterial growth by the rose-petal structures is not well-understood. There was also a lack of study about how such structures may affect bacteria alignment and biofilm formation.

This chapter focuses on investigating bacterial attachment and early-stage biofilm formation on biomimetic rose-petal surfaces. The imprints of rose-petal hierarchical structures were fabricated via nano-casting technique. The wettability of rose-petal replicas was accessed by the static/dynamic contact angle measurement and droplet evaporation tests. By using fluorescent microscopy and scanning electron microscope (SEM), growth of two clinically relevant biofilm-forming strains *S. epidermidis* and *P. aeruginosa* were evaluated on the rose-petal-structured and flat surfaces. In addition, by comparing the growth of *P. aeruginosa* on the model unitary nano-pillar structures in chapter 4, we demonstrated the efficacy of hierarchical structures in delaying biofilm growth.

5.2 MATERIALS AND METHODS

5.2.1 Surface fabrication

One piece of fresh rose petal (Figure 5.1 a) was attached to a glass slide (1 cm ×1 cm) via a double-sided adhesive tape (Figure 5.1b). A mixture of Poly(dimethylsiloxane) (PDMS) and its curing agent was prepared from SYLGARD 184 Elastomer Kit (Dow Corning Corporation, Midland, MI) with a ratio of 10:1 (wt/wt). The solution was thoroughly mixed and degassed in a vacuum chamber for 30 minutes to eliminate air bubbles. The mixture was poured over the glass slide with rose petals in a Petri dish (Figure 5.1c), and cured at room temperature for 48 hours. After curing, the PDMS mould was gently peeled off which left a negative imprint of the structures on the petal (Figure 5.1d). UV-curable epoxy (OG 142-87, Epoxy Technology, Inc.) was poured onto the negative imprint of the PDMS mould and was gently covered with a pre-cleaned glass slide (1 cm ×1 cm) as a substrate. The UV-curable epoxy was cured under a UV-lamp, with the luminous intensity of 100 mW/cm^2 and the wavelength of 365 nm, for 20–25 minutes until fully cured (Figure 5.1e). After cooling to room temperature, the cured epoxy was demoulded by bending the PDMS mould (Figure 5.1f).

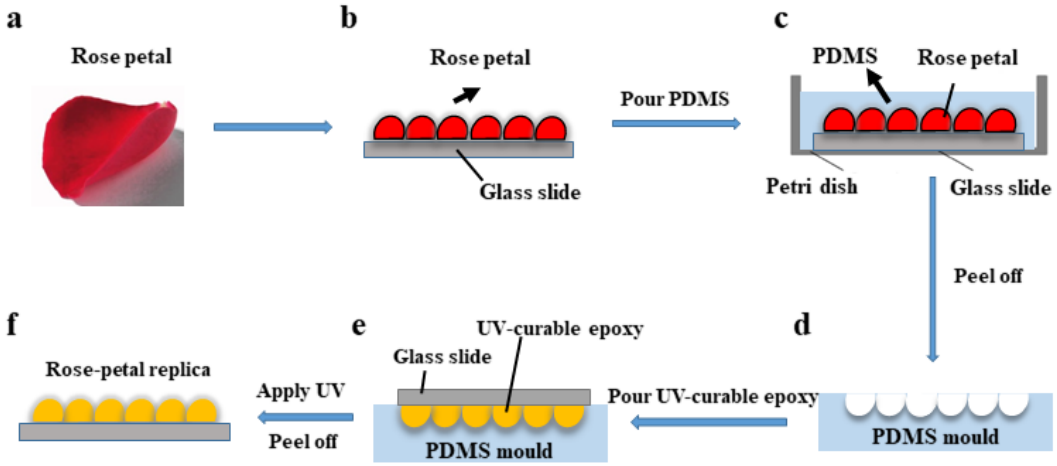

Figure 5. 1 Schematic of the fabrication method to obtain rose-petal replicas.

5.2.2 Characterization of rose-petal structured surfaces

The replicas of rose-petal surfaces were imaged using a scanning electron microscope (SEM). FEI Helios NanoLab 600 DualBeam system was operated at an acceleration voltage of 5 KV, which allowed to get good magnifications, while will not damage the surfaces. We also measured the contact angles (CA) on flat and rose-petal-structured epoxy surfaces by

placing a sessile drop of 3 µl deionized water (i.e. DI water), and evaluated by a CAM 100 optical contact angle meter (KSV Instruments Ltd., Finland). To characterize the evaporation dynamics, a 3 µl DI water droplet was placed on either of the surfaces, and their intensity projections were captured every 300 seconds by the optical contact angle meter. The droplet edges were extracted by an in-house Matlab code (see 5.5 Appendix) and plotted in a single image to visualize the droplet transitions overtime. An in-house goniometer (Gart *et al.*, 2015; Huhtamäki *et al.*, 2018) was set-up to measure the advancing contact angles on flat and rose-petal surfaces using a syringe-pump system (needle gauge ~25, water droplet volume ~10 µl, dispensing rate~ 0.2 ml/minute). Receding contact angles were also measured using the same method with the syringe pump operating in withdrawal mode. All the measurements were repeated for three instances and the images were processed using ImageJ. Results are presented as the mean contact angles with standard deviations.

5.2.3 Bacteria culture, attachment and biofilm growth

Biofilm-forming strains of *S. epidermidis* FH8 and *P. aeruginosa* PAO1-mCherry were used in this study (Shields *et al.*, 2013; McFarland *et al.*, 2015; Weigert *et al.*, 2017). *S. epidermidis* FH8 was isolated from a chronic rhinosinusitis patient at the Freeman Hospital, Newcastle Upon Tyne (Shields *et al.*, 2013). PAO1-mCherry is the derivative of *P. aeruginosa* PAO1-N (Nottingham subline) (Sidorenko *et al.*, 2017), which was engineered via chromosomal insertion (attTn7::ptac-mcherry) to constitutively express a red fluorescent protein mCherry. *S. epidermidis* FH8 and *P. aeruginosa* PAO1-mCherry were routinely cultured in Tryptic Soy Broth (TSB, Melford Laboratories Ltd, UK), in an incubating shaker at 180 rpm, 37℃ for 16 hours and then used for experiments.

The optical density of *S. epidermidis* FH8 was measured by a spectrophotometer (Biochrom Libra S11, Biochrom Ltd., Cambridge, UK) and diluted to OD_{600}= 0.30 with fresh TSB medium. 3 ml of the diluted bacterial culture was incubated with flat and rose-petal structured surfaces in 12-well culture plates for 2 hours at 37℃ and then removed for visualization. To monitor the early-stage biofilm formation, we cultured *Staphylococcus epidermidis* FH8 on flat/rose-petal surfaces for up to 2 days. *P. aeruginosa* PAO1-mCherry colonizes surfaces rapidly. Therefore, to avoid overloading the system, different culture conditions were selected for *P. aeruginosa* with a lower bacterial inoculum (OD_{600}= 0.01) and incubation in 100x diluted TSB for 2 hours (bacterial attachment assay) or 24 hours (biofilm formation assay). This method enabled biofilm growth to be visualized on the different surfaces without shielding the initial surface structure.

5.2.4 Fluorescent Microscope Analysis

After the bacterial attachment assay or biofilm formation assay, surfaces were gently rinsed three times with Phosphate Buffered Saline (PBS, pH=7.4) to remove loosely adhered bacteria. Surfaces incubated with PAO1-mCherry were directly visualized by fluorescent microscopy after washing. For *S. epidermidis* FH8, the adherent bacteria or biofilms were stained with SYTO®9 (Invitrogen, Life Technologies, Carlsbad, CA, USA) following the standardized methods. All surfaces were visualized using an Olympus BX61 upright fluorescent microscope with a 20x objective. For the bacterial attachment assay (2 hours), surfaces were examined by acquiring 2D fluorescent images in a single focal plane (121.25 × 108.75 μm^2). For biofilms, z-stacks were performed through the thickness of biofilms from 5 random locations on the surfaces. The biomass in each field of view (430.00 × 324.38 μm^2) was determined using the COMSTAT2 plugin (Lyngby, Denmark) in ImageJ. Three independent experiments were performed for each surface type.

5.2.5 SEM Analysis

Surfaces (with bacteria or biofilms) were washed three times with PBS and fixed in 2% glutaraldehyde with 3M Sorenson's phosphate buffer, overnight at 4°C. Then they were dehydrated through a series of ethanol solutions of 25% (v/v), 50%, 75%, and 100%, followed by critical point drying (Leica EM CPD300) as described in Chapter 3. The dried surfaces (with bacteria or biofilms) were sputter-coated with 16 nm platinum to increase the surface conductivity, enabling higher resolution imaging by the SEM.

5.2.6 Statistical Analysis

Data are represented as mean values with standard error. Student's t-test assuming unequal variations was applied and $*p < 0.05$ was considered statistically significant in this study.

5.3 RESULTS AND DISCUSSION

5.3.1 Characterization of surface topography and wettability of rose-petal replicas

SEM imaging of the UV-epoxy rose-petal replicas (Figure 5.2 a1) revealed the existence of periodic arrays of hemispherical micro-papillae in the diameter of 23 ±3 μm , similar to the microstructures on natural rose petals (~ 20 μm) (Feng *et al.*, 2008; Dou *et al.*, 2015). The magnified SEM images in Figure 5.2 a2 shows the existence of cuticular folds were found at the top of micro-papillae, closely mirroring the hierarchical topographies of the natural

rose petal. The width of each fold was measured to be in the range of 700 ±100 nm, similar to the size as previously reported (~ 730 nm) (Feng *et al.*, 2008; Dou *et al.*, 2015) and the gap between each fold was measured to be 500 ±150 nm (Figure 5.2 a3). Collectively, the rose-petal replicas exhibit as hierarchical structures with micro-papillae and nano-folds in two different scales.

The static water contact angle (CA) on the flat surface was measured to be 60.5º ±6.5º (Figure 5.2b), indicating that the cured flat epoxy surface was intrinsically hydrophilic. For the rose-petal replicas, the CA value on surfaces was measured to be 130.8º ±4.3º (Figure 5.2 b), indicating that the hierarchical structures had enhanced the surface hydrophobicity significantly. The water droplets stayed pinned on rose-petal structured surfaces under different tilt angles ranging from 30 -180° (Figure 5.2c), implying that there exist highly adhesive interactions between the drops and the structured surfaces (Feng *et al.*, 2008; Dou *et al.*, 2015). Contact angle hysteresis (CAH) measurement which is an indicator of slipperiness (water-repellence), were conducted by using the dynamic CA method (by increasing or decreasing the volumes of water droplets using a needle (MacCallum *et al.*, 2014)). CAH (also defined as the difference between the advancing and receding angle of a water droplet) of the rose-petal structured surfaces (91.0° ±4.9°) was measured to be significantly higher than that of the flat surfaces (44.8° ±4.3°), as shown in Figure 5.2b. This indicates the presence of a large number of pinning points on rose-petal structured surfaces, which cause the adhesion of liquid droplets.

We also evaluated the evaporation dynamics of water droplets on these two surfaces (Figure 5.2 d & 5.3), as CAH has been attributed to be the main factor affecting drop evaporation (Chuang *et al.*, 2014). Figure 5.2 e-f shows the evolution of CA and contact radius of a water droplet during the evaporation process. For the flat surface, the evaporation started with the constant contact line (CCL) mode up to 900s (Figure 5.2 f): the CA decreased, while the contact radius remained constant. After that, the CA decreased to its receding CA (i.e. 37.6° ± 4.5° in this study), and contact line started to recede. The CA remained almost constant ranging from 900-1500s (Figure 5.2 e), indicating that this is the constant contact angle (CCA) mode during this period of time. At the end of evaporation (1500-1800s), both CA and contact radius decreased (i.e. mixed mode) as shown in Figure 5.2f. This observation was consistent with the normal evaporation process which was reported on smooth hydrophilic surfaces (Khedir *et al.*, 2011). By contrast, rose-petal structured surfaces exhibited mostly as CCL mode over time (Figure 5.2d &f & 5.3) due to its higher CAH. The

CA of rose-petal surfaces require more time to decrease to its receding CA (i.e. 37.2° ± 4.3° in this study). Therefore, the contact line is pinned and contact radius keeps constant during the evaporation.

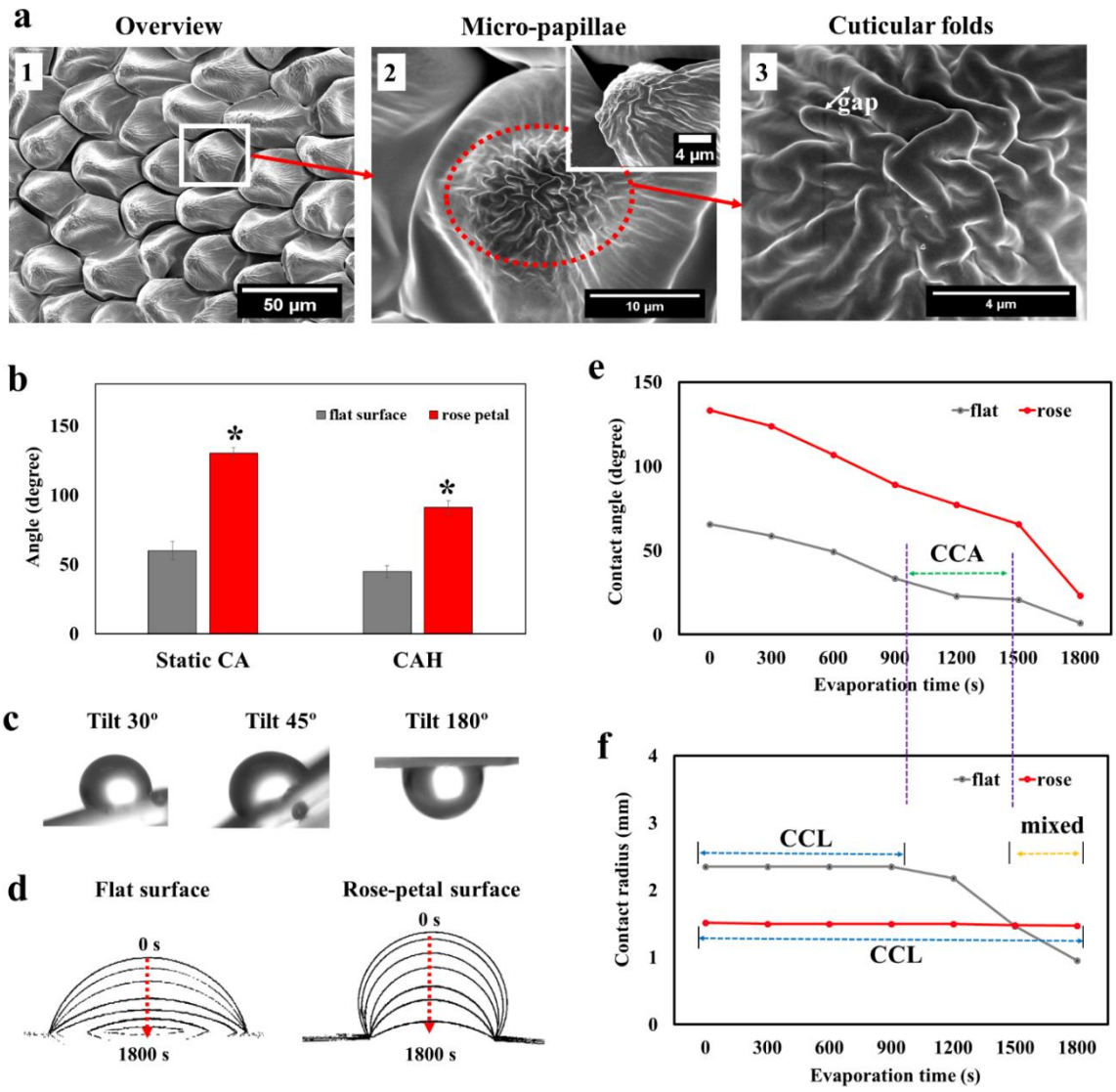

Figure 5. 2 (a) SEM images of the rose-petal replicas made by UV-epoxy. (a1) an overview of the hierarchical structures on surface, taken at 1000x. (a2) A typical SEM image taken at 8000x showing the hemispherical micro-papillae with cuticular folds, and the inset was taken at 20° tilt with the magnification of 12000x. (a3) The magnified SEM image taken at 25000x showing the detailed cuticular nano-folds. **(b)** Static water contact angle (CA) and contact angle hysteresis (CAH) measurements on flat and rose-petal structured surfaces. Values are mean ± standard deviation of three independent experiments. **(c)** Digital images of 3 µl water droplets on the rose-petal structured surfaces under different tilt angles. **(d)** A typical example of the edges of 3 µl water droplets, when evaporated on the flat and rose-petal structured surfaces overtime. The outside of droplet edge was extracted at the time of 0 s, and the time interval between each edge was 300 s. **(e-f)** A representative evolution of contact angle (e) and contact radius (f) of water droplets (3 µl) evaporating on flat and rose-petal structured surfaces.

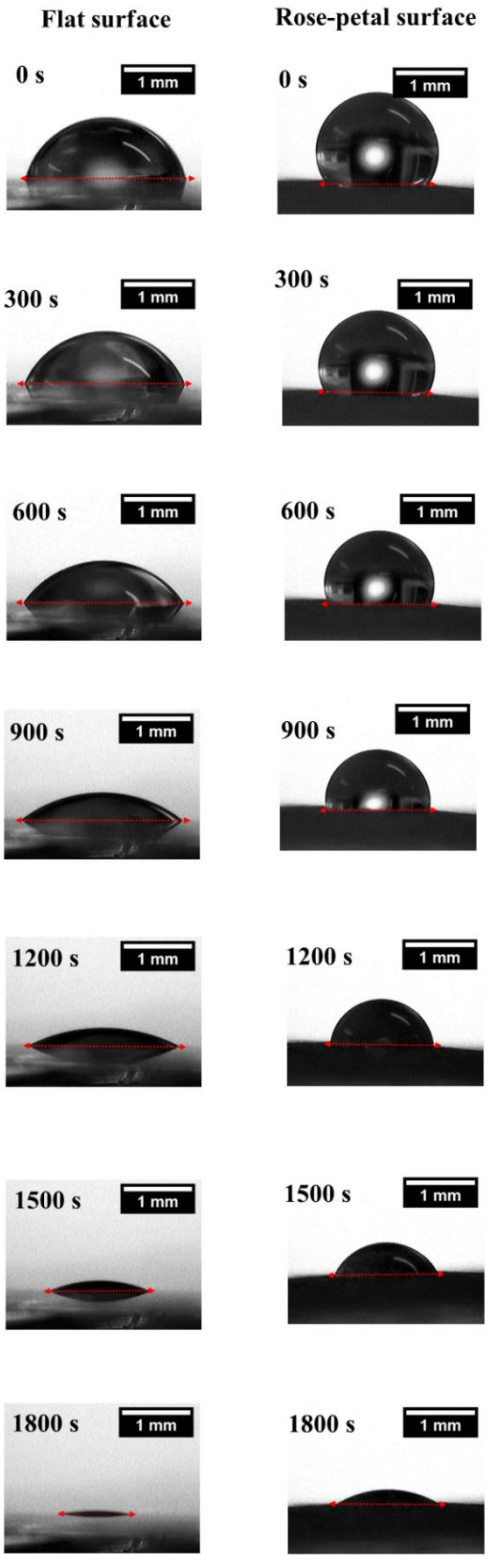

Figure 5. 3 A typical example of the digital images of 3 µl water droplets as a function of evaporation time when placed over the flat and rose-petal structured surfaces.

The evaporation process on rose-petal replicas didn't agree with the normal observations of hydrophobic surfaces, which is dominated by CCA mode as previously reported (Khedir *et al.*, 2011; Chuang *et al.*, 2014). The normal hydrophobic or superhydrophobic surface like lotus leaf allows air to remain inside the texture (i.e. Cassie state), thereby have a low CAH. This results in the evaporation process follows as CCA mode with the easy receding of contact line (Khedir *et al.*, 2011). However, it is believed that there have the coexistence of air pockets and water–solid contacts on rose-petal surface. This results in Cassie and Wenzel states coexist on rose-petal-like surfaces (also known as Cassie-Baxter impregnating wetting state (Feng *et al.*, 2008; Dou *et al.*, 2015)). Therefore, the rose-petal surface is hydrophobic but have a high CAH (Kulinich and Farzaneh, 2009). This special wetting state is attributed to the hierarchical micro- (i.e. arrays of papillae) and nanostructures (i.e. cuticular folds) on rose-petal surfaces. The relatively large and periodic arrays of papillae can exert a capillary force that facilitates the penetration of water into papillae valleys (Shin *et al.*, 2016). However, the water cannot enter into the nanoscale structures (i.e. cuticular folds) at the top where tapped air pockets exist. This kind of special wetting state on the rose-petal surfaces is also termed as the "petal effect" and has been well investigated by researchers (Feng *et al.*, 2008; Dou *et al.*, 2015; Shin *et al.*, 2016).

5.3.2 Bacterial adherence is delayed by the rose-petal structured surfaces

We initially assessed the attachment of two common human pathogens, *S. epidermidis* (spherical-shape) and *P. aeruginosa* (rod-shape) on the different surfaces after 2 hours. The distribution of fluorescence signals (green for *S. epidermidis* and red for *P. aeruginosa*) was relatively uniform on the flat surfaces, indicating that the bacterial cells had attached uniformly across the surface (Figure 5.4 a1&3). However, in the case of rose-petal structured surfaces, the fluorescent patches of *S. epidermidis* or *P. aeruginosa* were sparsely scattered, and large areas without fluorescent signal were observed. This indicated that cells were only able to attach to specific regions on the rose-petal structure (Figure 5.4 a2&4). Figure 5.4b shows that the surface area covered by *S. epidermidis* and *P. aeruginosa* on rose-petal structured surface, which was significantly lower (86.1± 6.2% less and 85.9 ±3.2% less, respectively) in comparison to the area covered by bacteria on flat surfaces. Overall, the observations indicate that the rose-petal structures have the ability to inhibit the initial bacterial attachment.

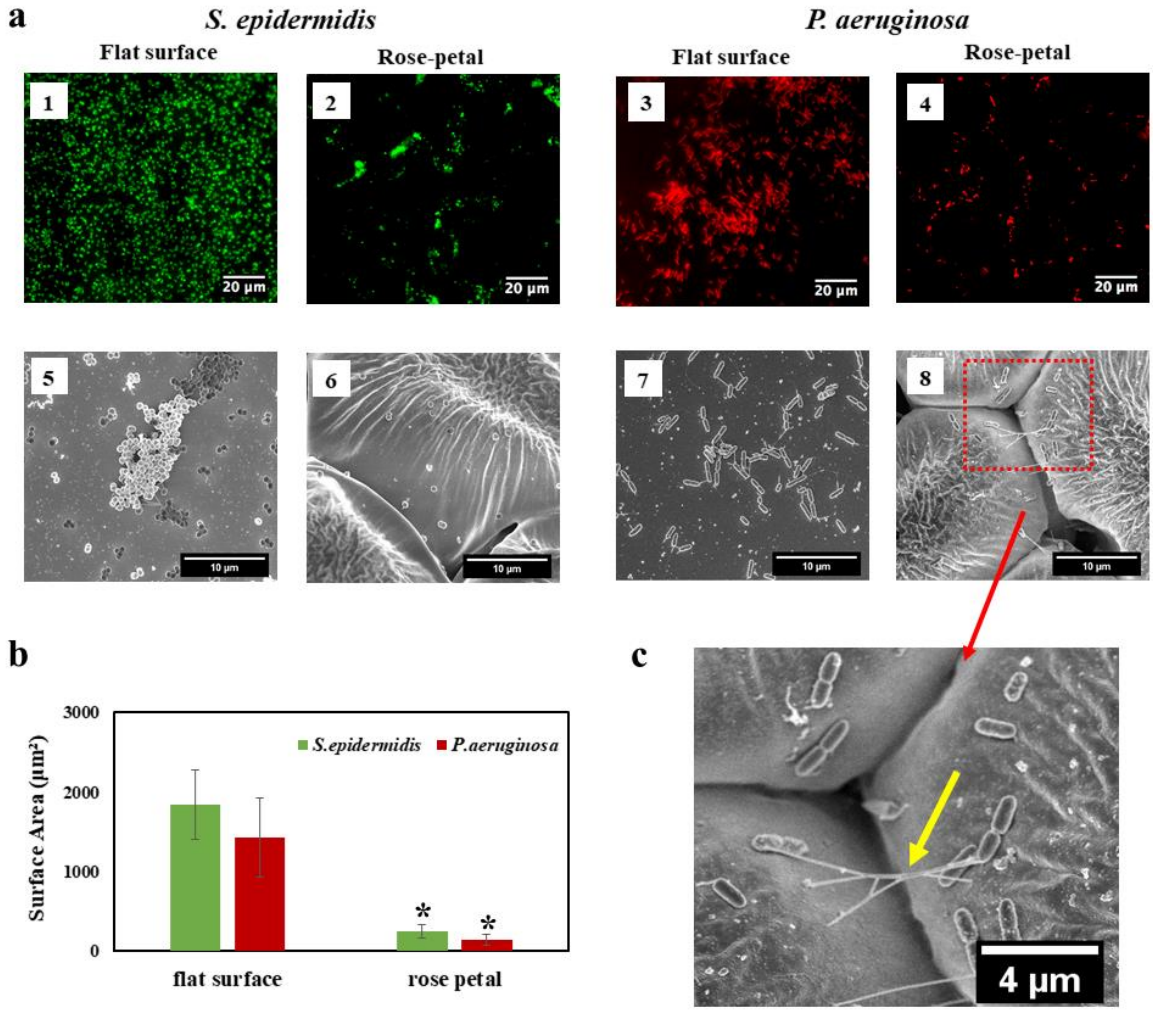

Figure 5. 4 Adherence of *S. epidermidis* and *P. aeruginosa* on different surfaces after 2 hours' incubation. **(a)** Fluorescent microscopy (1-4) and SEM (5-8) images of *S. epidermidis* and *P. aeruginosa* on flat and rose-petal structured surfaces. **(b)** The surface area coverage of each type of bacteria in the field of view (121.25 × 108.75 µm^2) for each surface was determined by ImageJ. Values are mean ± standard deviation of three independent experiments. **(c)** A zoomed in view of the cross-section in a8 showed the existence of cellular appendages (yellow arrow), which might mediate bacterial attachment of *P. aeruginosa*, by connecting isolated cells.

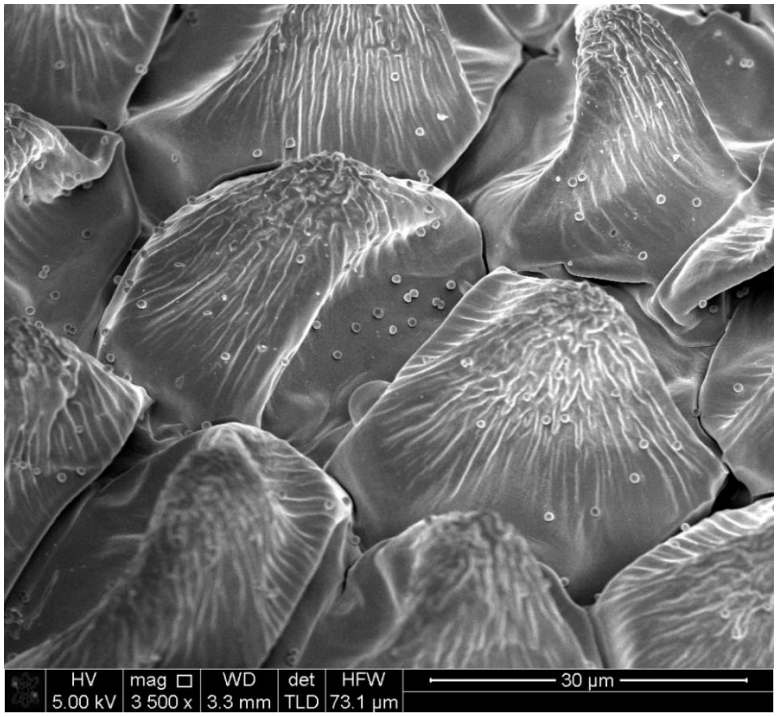

Figure 5. 5 *S. epidermidis* preferred to attach into the valleys or recessed crevices between micro-papillae, instead of attaching onto the cuticular folds. Most *S. epidermidis* cells were isolated on the surface.

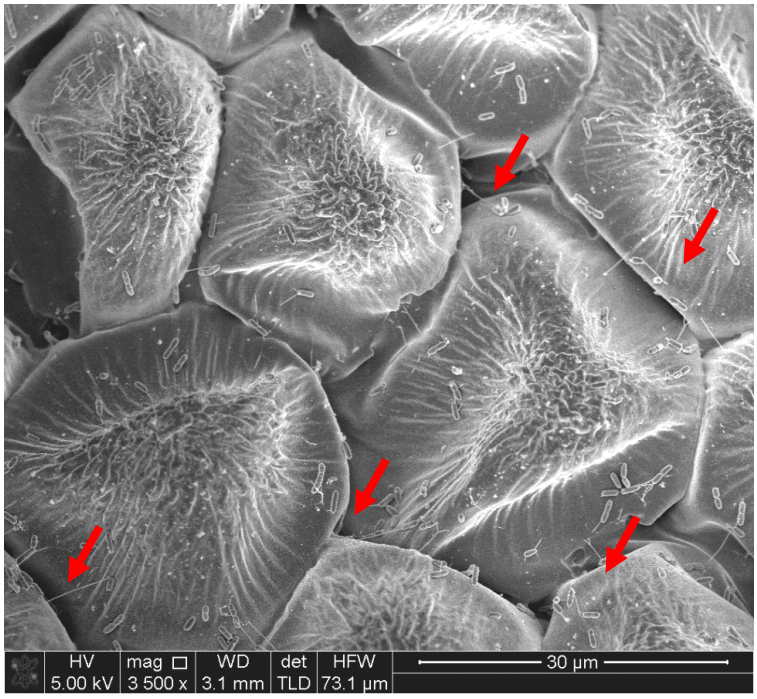

Figure 5. 6 *P. aeruginosa* preferred to attach into the valleys or recessed crevices between micro-papillae, instead of attaching onto the cuticular folds. Some cells appeared to make small aggregates via cell appendages (red arrows).

To investigate the interactions at a higher spatial resolution, SEM was used to visualize *S. epidermidis/ P. aeruginosa* on different surfaces. On flat surfaces, *S. epidermidis* tended to cluster into small aggregates (Figure 5.4 a5). By contrast, on the rose-petal surfaces, which comprised of hierarchically arranged micro- (i.e. arrays of papillae) and nanostructures (i.e. cuticular folds), 85.6 ±5.8% of *S. epidermidis* cells (based on analyzing nine SEM images) were localized in the valleys or crevices between micro-papillae (Figure 5.4 a6 & 5.5). Cells were not commonly seen at the top of the micro-papillae. These observations were consistent with the acquired fluorescent images (Figure 5.4 a2&4), where large areas without fluorescent cells were seen and presumably represented the sites of nano-folds. We did not observe cell aggregates of *S. epidermidis* on rose-petal surface and found that most of the attached cells were isolated (Figure 5.4 a6 & 5.5). Similar observations were also found for *P. aeruginosa*, as shown in Figure 5.4 a7-8 & 5.6. In this case, 90.4 ±3.1% of cells (based on the analysis of nine SEM images) were present in the valleys. The major difference between the cell types was that *P. aeruginosa* cells were connected by long tube-like appendages, which may have mediated cellular attachment by connecting the isolated cells together (Figure 5.4c).

5.3.3 Biofilm growth is delayed by the rose-petal structured surfaces

5.3.3.1 Biofilm growth of S. epidermidis on different surfaces

To investigate whether the rose-petal structures are effective in delaying biofilm growth, *S. epidermidis* biofilms were cultured for 2 days and then analyzed using fluorescent microscopy as well as SEM (Figure 5.7). Maximum intensity projections through the thickness of *S. epidermidis* biofilms showed bright patches on the flat surface (Figure 5.7 a1), indicating a typical biofilm growth comprising multiple layers of cells. Few smaller green patches were observed on the rose-petal structured surface, which appeared as circular or oval structures with centrally located dark regions that lacked fluorescence (Figure 5.7 a2). The diameter of these circular regions was measured to be 21 ± 4 μm, which is similar to the dimensions of hemispherical micro-papillae (i.e. 23 ± 3 μm in diameter) on the rose-petal structures. This indicates that *S. epidermidis* clusters/biofilms preferentially form around the micro-papillae. The total biomass on the rose-petal surface was significantly lower (63.2 ±9.4% less) compared with the biomass on the flat surface (see Figure 5.7c), indicating that rose-petal structure can delay the biofilm growth. A dense biofilm network

was observed on the flat surface, and string-like structures consisting of filamentous fibrils appeared to bridge *S. epidermidis* cells together (Figure 5.7 b1&2). These filamentous fibrils are known to be part of EPS structure of *S. epidermidis* biofilms (Takahashi *et al.*, 2015) which indicates a more mature biofilm growth. By contrast, no filamentous fibrils were observed on the rose-petal surfaces (Figure 5.7 b3&4). A few cellular clusters were sparsely scattered on the rose-petal structure and the majority of cells occupied the valleys between the micro-papillae (Figure 5.7 b3 & 5.8), consistent with the findings of fluorescent imaging (Figure 5.7 a2) which revealed cells preferentially surrounding the micro-papillae. Small aggregates of around ~20 cells were observed on the cuticular folds (Figure 5.7 b4); however, 3D clusters or aggregates on the cuticular folds at the top of micro-papillae were relatively rare. The diameter of *S. epidermidis* cells were measured to be 700 ±70 nm in this study, which is of similar dimensions compared to the feature size of folds (width ~700 ±100 nm, gap ~500 ±150 nm). *S. epidermidis* cells can deposit into these fold gaps thereby forming small aggregates at the top of micro-papillae over time (Figure 5.8).

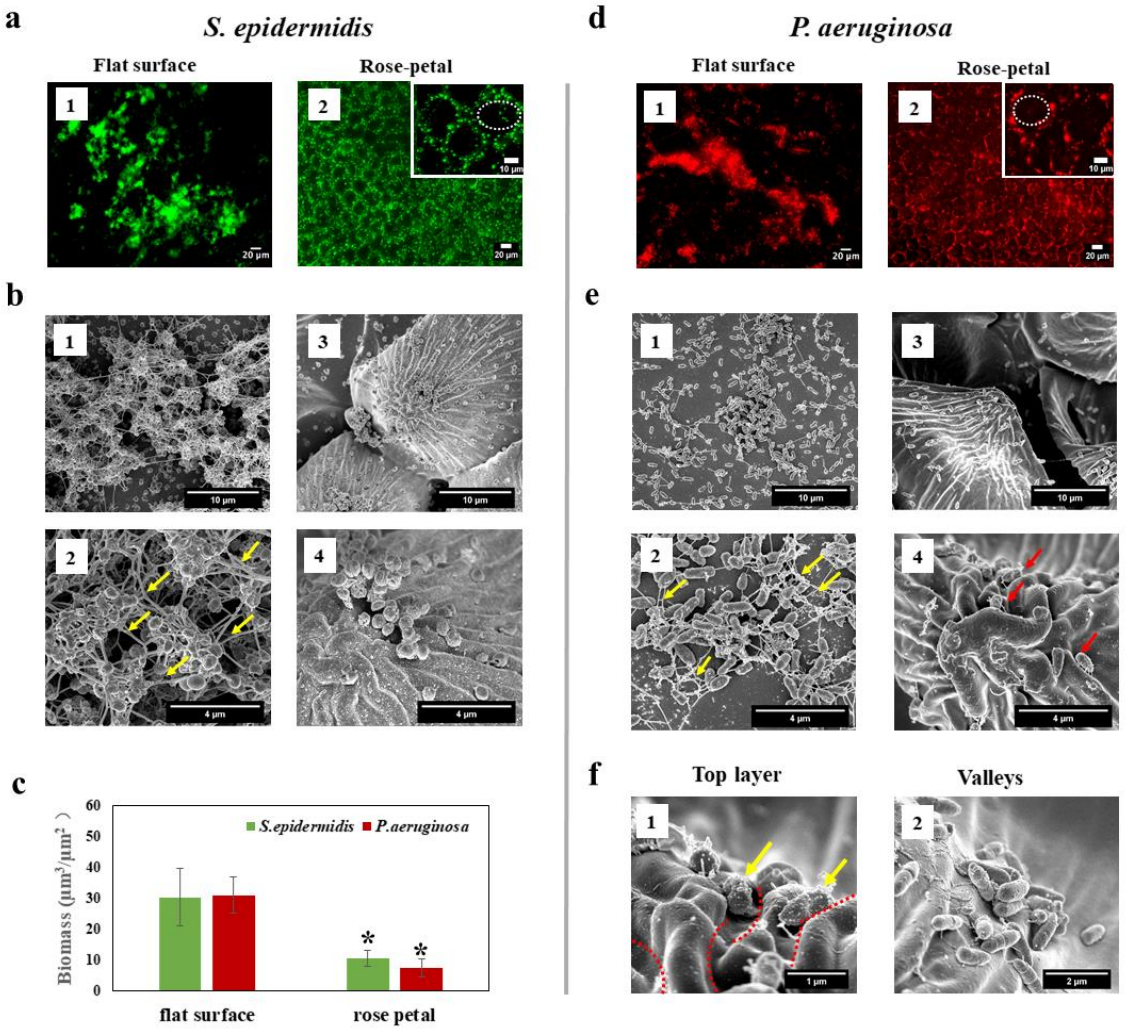

Figure 5. 7 Biofilm formation (2 days) on the flat and rose-petal structured surfaces. **(a)** Fluorescent images of *S. epidermidis* biofilms on different surfaces. The cells on the rose-petal surfaces are distributed in oval shaped patterns which is highlighted by a dashed white line in a2. **(b)** SEM images of *S. epidermidis* biofilms on different surfaces. b1 and b3 are lower magnification images; b2 and b4 are high magnifications. Yellow arrows indicate the filamentous fibrils from the EPS of biofilms. **(c)** Biomass volume per unit area on the different surfaces calculated from ImageJ Comstat2. Values are mean ± standard deviation of three independent experiments. **(d)** Fluorescent images showing *P. aeruginosa* biofilms on different surfaces. The dashed white line highlights a cuticular region, with cells distributed in a circular pattern around the edge of micro-papillae. **(e)** SEM images of *P. aeruginosa* biofilms on different surfaces at lower magnifications (e1 and e3) and higher magnifications (e2 and e4). Yellow arrows indicate the filamentous fibrils from the EPS of biofilms and red arrows indicate the isolated bacterial cells within the cuticular folds. **(f)** High-magnification SEM images of *P. aeruginosa* biofilms on rose-petal surface, yellow arrows indicate the bacterial alignment within the cuticular nano-folds, and red dash lines indicate the boundary of folds, as shown in f1. *P. aeruginosa* aggregates can form in the valleys of micro-papillae, as shown in f2.

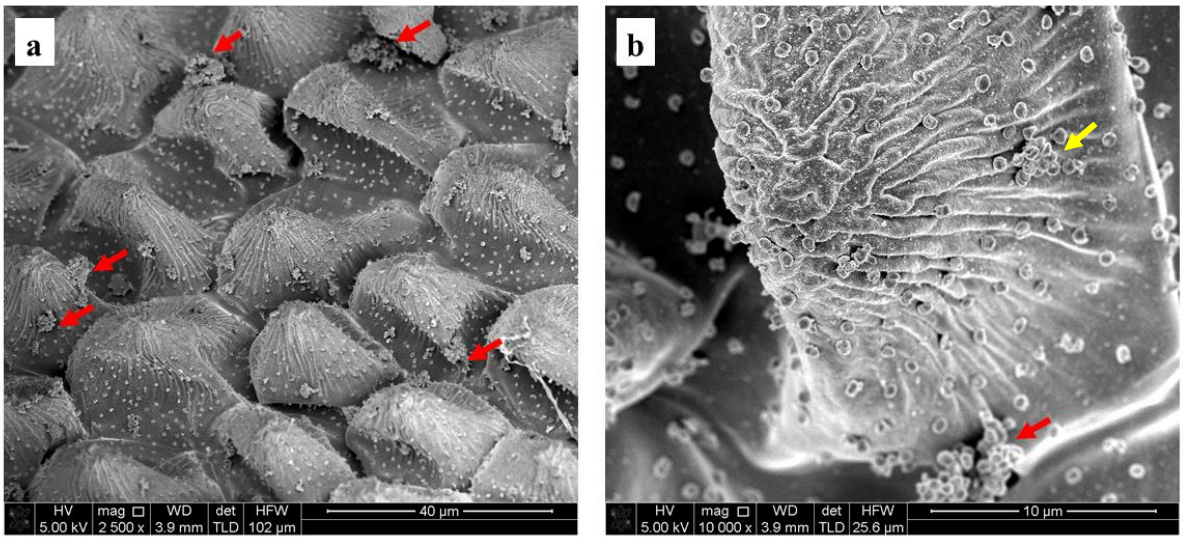

Figure 5. 8 Biofilm growth of *S. epidermidis* on rose-petal surfaces. **(a)** SEM image with a 20° tilt showing that the majority of cells selectively occupied the valley sites between the micropapillae (red arrows). (b) *S. epidermidis* cells can deposit into the folders thereby dispersing around the cuticular folds, or only forming smaller aggregation aligning with the folds (yellow arrows), as compared with the big aggregations formed in the valley sites of the micropapillae (red arrows).

5.3.3.2 Biofilm growth of P. aeruginosa on different surfaces

Maximum intensity projections through the thickness of *P. aeruginosa* biofilms and the corresponding SEM images of the different surfaces are shown in Figure 5.7 d-e. Circular or oval shaped structures were observed in the fluorescent images of rose-petal surface (Figure 5.7 d2). This indicates that *P. aeruginosa* biofilm preferentially grew in between micro-papillae, akin to the growth mechanism of *S. epidermidis*. The total biomass of *P. aeruginosa* biofilms was significantly reduced on the rose-petal structured surfaces (76.0 ±10.0% less), comparing to the biomass on the flat surface (see Figure 5.7c). Figure 5.7e (1&2) shows the existence of *P. aeruginosa* clusters with a developed network of filamentous fibrils surrounding the cell bodies on the flat surface. In contrast to *S. epidermidis*, *P. aeruginosa* biofilms did not contain significant aggregates or clusters on the rose-petal surface, possibly due to the lower initial bacterial density and the nutrient-limited conditions arising from rapid cellular growth (Figure 5.7e 3 & 5.9). Most cells were found to be isolated on structured surfaces, in contrast to the flat surface (Figure 5.7e). At a higher magnification, small bacterial aggregates were observed, comprising ~10 cells in the valleys of micro-papillae on the rose-petal surface (Figure 5.7f 2 & 5.9 b), without showing the long filamentous fibrils. *P. aeruginosa* cells were also occasionally found attached within the cuticular nano-folds at the top of micro-papillae (Figure 5.7 e4& f1). We measured the gap between folds to be 500 ±150 nm (Figure 2 a3) which is similar to the diameter of *P. aeruginosa* and found that a single *P. aeruginosa* cell was capable of settling into these gaps over time. The cells tended to align with the folds (Figure 5.7 f1 & 5.9 c-d) and the preference for alignment along the nano-folds was strong even though the fold structure was irregular. The crowns of the cuticular folds were visible after the long-term bacterial growth (i.e. 24 hours), as the bacteria tended to remain confined in the ridges between the nano-folds (Figure 5.7 f1 & 5.9 c-d). To further assess *P. aeruginosa* biofilm growth, the period of biofilm development was extended to 48 hours - the same incubation time of *S. epidermidis* biofilms. In these experiments, the biomass on rose-petal structured surface was also found to be significantly lower (68.7 ± 13.4% less) in comparison of the biomass on the flat surface (Figure 5.10). The observations confirm that the rose-petal structure was able to delay the early stage biofilm growth of *P. aeruginosa*.

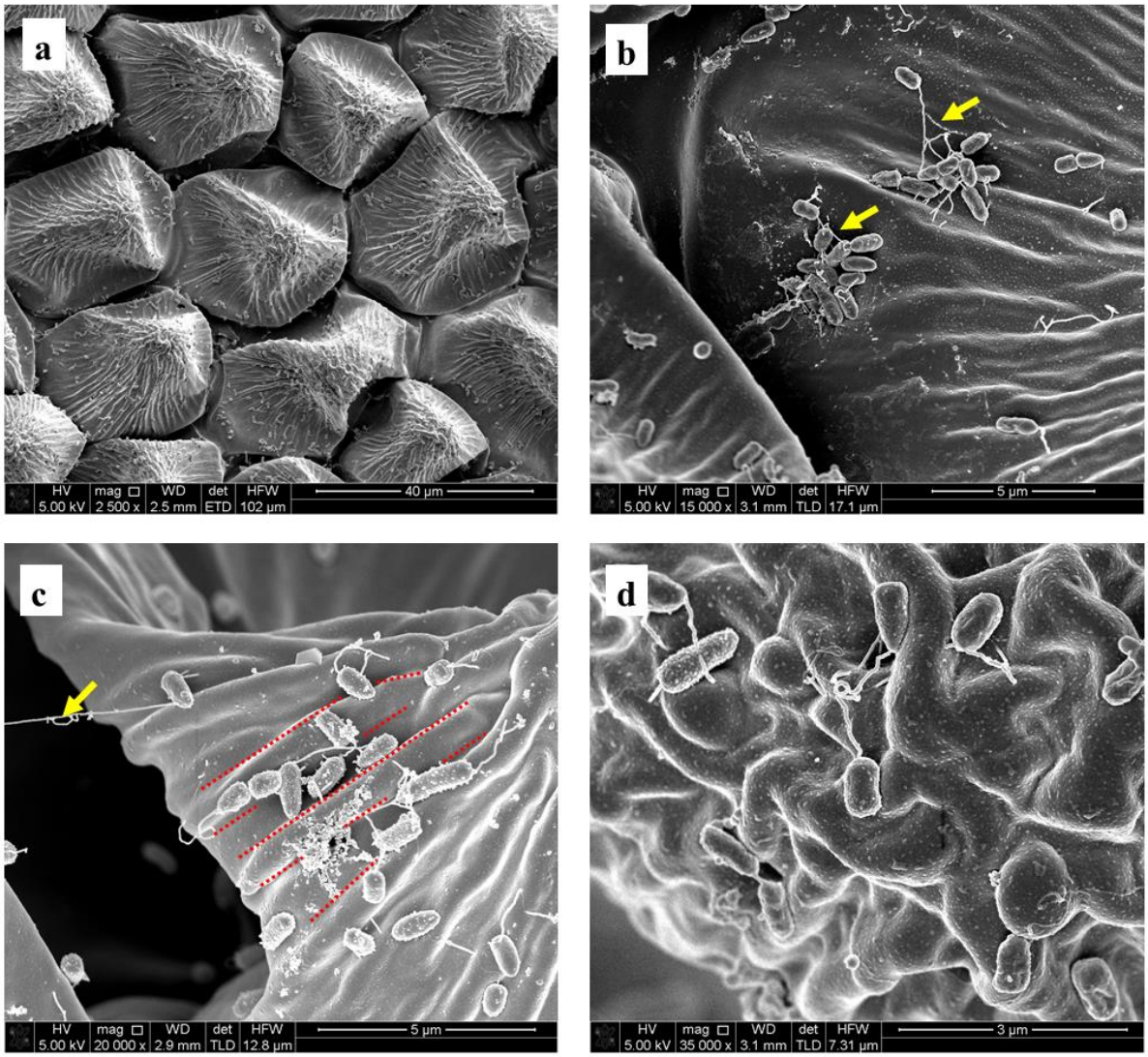

Figure 5. 9 SEM images of *P. aeruginosa* biofilm growth on the rose-petal structured surfaces. (a): *P. aeruginosa* cells didn't form significant aggregates or clusters on the rose-petal surface. Most cells were isolated rather than clustered into aggregates. (b): Bacterial aggregation comprising ~ 10 cells in the valleys of micro-papillae on the rose-petal surface. Yellow arrows indicate fibrils observed nears small clusters of cells. (c): Bacterial alignment within the cuticular folds, red dashed lines indicate the boundary of cuticular folds, and yellow arrows indicate cell appendages or fibrils. (d): The preference for alignment with the cuticular folds is sufficiently strong that even when the fold structure is irregular and the crowns of the cuticular folds are still visible, the bacteria still tend to remain in the confined spaces between them.

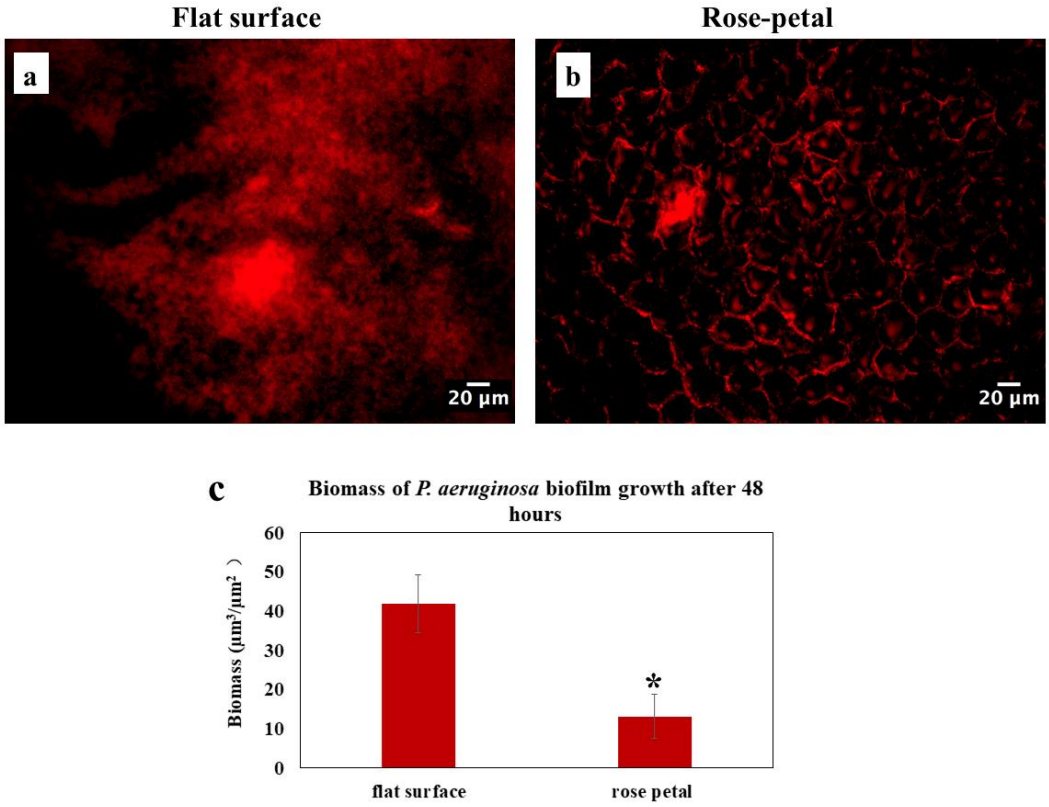

Figure 5. 10 Biofilm growth of *P. aeruginosa* on the flat and rose-petal structured surfaces after 48 hours. (a-b): Representative fluorescent images of *P. aeruginosa* biofilms on different surfaces. Porous structures were observed in the fluorescent images of rose-petal surface, indicating that *P. aeruginosa* biofilm still preferred to grow in between micro-papillae even after 48 hours. (c) Biomass volume per area on the different surfaces. *$p <$ 0.05 was considered statistically significant. Values are mean ± standard deviation of three independent experiments.

5.3.4 Bacterial growth of *P. aeruginosa* on unitary nano-pillars

We used a simpler surface pattern containing unitary nano-pillars to examine the alignment of *P. aeruginosa* and evaluate anti-microbial performance against the hierarchical rose-petal structures. These nano-pillars have a diameter of 500 nm, pitch of 1 µm and height of 2 µm, which is same as the nano-pillar structured surfaces as discussed in Chapter 4. The unitary nano-pillar structured surface was moderately hydrophobic (CA of 94.8°±3.7°) and the dimensions of the topographical features was similar to the nano-folds on rose-petals and comparable to the size of *P. aeruginosa* cells. Figure 5.5 a-b showed that bacterial cells aligned with gaps between the nano-pillars after 2 hours, consistent with previous investigations (Hochbaum and Aizenberg, 2010). Results in Chapter 4 have shown the

similar results and bacterial nanotubes tended to connect pillars. The total surface area covered by bacteria after 2 hours was significantly lower on the nano-pillar surface compared with the rose-petal surface (see Figure 5.11c&5.4b, 107.2 ±28.6 μm^2 vs 143.8 ±71.2 μm^2, p =0.012), possibly owing to the restricted area (pillar pitch) where bacteria can make the initial contacts to material surface. However, the biomass of *P. aeruginosa* after 24 hours (15.7 ±4.3 $\mu m^3/\mu m^2$, Figure 5.11c) on nano-pillars was significantly higher than on rose-petal replica surfaces (7.3 ±2.8 $\mu m^3/\mu m^2$, Figure 5.7c) (p =0.002). Bacteria continued to deposit into the nano-pillar pitches, and dense filamentous fibrils were observed surrounding the cells, similar to the flat surfaces (Figure 5.11d2). However, the biomass on nano-pillars after 24 hours is still significant lower comparing to that on the flat surfaces (31.1 ±6.0 $\mu m^3/\mu m^2$, Figure 5.7c) (p= 2.7×10^{-7}), indicating that unitary nanostructures can still isolate cells and delay biofilm growth.

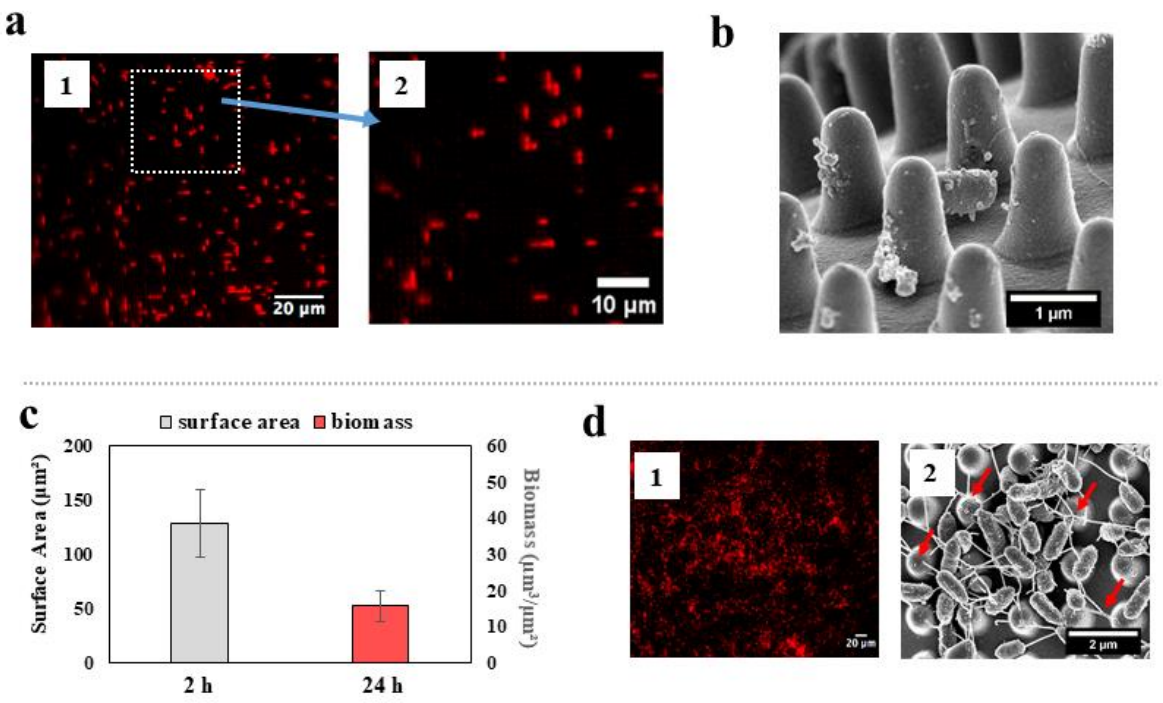

Figure 5. 11 (a) Fluorescent microscopy and **(b)** SEM images of *P. aeruginosa* on nano-pillar surfaces after 2 hours, showing the cell patterning/aligning behaviour. **(c)** The surface area coverage (2 hours) and biomass (24 hours) of *P. aeruginosa* on nano-pillar surfaces. Values are mean ± standard deviation of three independent experiments. **(d)** Fluorescent microscopy and SEM images of *P. aeruginosa* on nano-pillar surfaces after 24 hours, showing dense filamentous networks (red arrows).

5.3.5 The mechanism of inhibiting biofilm growth on rose-petal surface

The efficiency of bacterial attachment on surfaces is dictated by chemical and physical properties of surfaces (Berne *et al.*, 2018). We fabricated flat, rose-petal and nano-pillar structured surfaces using a nano-casting technique with UV-curable epoxy, so the surface chemistry in each case can be assumed to be the same. The major difference was the surface topographical features and this was a critical determinant of bacterial attachment and biofilm growth.

We hypothesized that hierarchical structures (i.e. micro-papillae and nano-folds) on rose-petal surfaces inhibit initial bacterial attachment after 2 hours. As a result of these structures, the rose petal surface exhibits as a modified state of hydrophobicity, termed as the Cassie-Baxter impregnating wetting state. The nanostructured cuticular folds can trap air within the folds, corresponding to the Cassie-state of lotus-leaf; thereby bacterial cells cannot penetrate the air-layer over short timeframes (Figure 5.12). This mechanism is similar to the lotus-leaf where the trapped air restricts the direct contact between bacteria and surfaces. However, unlike the lotus-leaf that has a low CAH, the papillae valleys can trap water thereby resulting in a high CAH. Visualizing the bacteria-material interfaces under the Cassie impregnating wetting state which combines wetting and non-wetting, is not an easy task. It may require sophisticated imaging such as high-resolution Cryo FIB-SEM instead of conventional microscopy (Rykaczewski *et al.*, 2012), especially down to the 1μm scale. However, as seen in Figure 5.4, cells only preferentially colonize the valleys surrounding the papillae and this region is also devoid of nano-folds. The hypothesis which describes the lack of bacterial attachment within nano-folds (Figure 5.12) is consistent with our observation of *S. epidermidis* and *P. aeruginosa* adherence behaviour on rose petal surfaces (~2 hours).

If the bacterial growth extends to 1-2 days (biofilm assay), bacterial cells still only accumulate surrounding the papillae forming ring/oval-like structures (Figure 5.12). The initial wetted micro-papillae valleys can harbor more bacterial cells as they tend to increase the overall surface area, thereby are more favorable for cell colonization if comparing to the nano-folds (Figure 5.12). However, unlike biofilms spreading on the flat or unitary nano-pillar surfaces, we found that either *S. epidermidis* or *P. aeruginosa* biofilms on rose-petal surfaces were isolated and overall biofilm growth was impaired (Figure 5.7). Notably, we found that the bacterial growth was lower on unitary nano-pillars after 2 hours, whilst biofilm formation was increased after 24 hours if comparing with the rose-petal surfaces. On unitary nano-pillars, the fibers produced by bacteria established connections between

isolated cells, and thus may mediate cell-cell communication. However, no large bacterial clusters or dense filamentous structures were found within micro-papillae on rose-petal surfaces (Figure 5.7). The papillae depth may play an important role as a physical barrier to hinder the development of fibrous network. Therefore, the communication between the neighboring cell aggregates/clusters that self-developed in each papillae valley may get blocked, and consequently retard biofilm development (Figure 5.12). Such a hindrance of biofilm development by specific topographically engineered surfaces has been observed previously (Hou *et al.*, 2011; Kargar *et al.*, 2016; Chang *et al.*, 2018). For example, colloidal crystals of a larger diameter (~1500 nm) can more effectively separate cell bodies than the ones in a diameter of 450 nm, thereby delaying biofilm growth (Kargar *et al.*, 2016). Other studies have tested biofilm growth on micro-posts (~20×20 μm, pitch~10 μm), similar to the dimension of micro-papillae on the rose-petals (Hou *et al.*, 2011). Decreased biofilm growth was observed within the valleys between the unitary micro-posts, while more biofilm was formed on the top of posts (i.e. protruding plateaus) (Hou *et al.*, 2011). This indicated that a larger scaled topography size helps to isolate cells while its larger contact area on the top may facilitate more bacterial growth.

However, no significant clusters within nano-folds were found, indicating that creating a secondary topography on the microstructure is more effective to delay bacterial growth compared with the bare microstructures. When submerged in water, the trapped air in nano-folds would vanish over time, similar to the lotus-leaf structures, resulting in the transition of Cassie to Wenzel state. Bacterial cells can eventually make contacts with the nano-folds after this region is completely wetted (Figure 5.12). The dimensions of nano-folds (width ~700 ±100 nm, gap ~500 ±150 nm) are similar to the bacterial size. Therefore, either *S. epidermidis* or *P. aeruginosa* cells can deposit into the folds and align with the fold structure, especially for *P. aeruginosa* (Figure 5.7& 5.12). *P. aeruginosa* cells also align within unitary nano-pillars (Figure 5.11), which maximizes the contact area with the material surfaces. Similar observations have been reported by other researchers, although the underpinning mechanism is not yet clear (Dubey and Ben-Yehuda, 2011; Friedlander *et al.*, 2013; Dubey *et al.*, 2016; Baidya *et al.*, 2018). Specific bacterial mutants could be a useful tool to investigate cell alignment and surface structure mediated cell-cell communication, and this will be a target for future work. However, the long and irregular fold ridges can isolate cells via the alignment on rose-petal (Figure 5.9c& 5.12), and such isolation behaviour is also identical on our nano-pillars with showing the lower biofilm biomass comparing to the flat

surfaces. This delayed the formation of cell-cell connections, thereby hindering their communication and constraining bacterial cluster development.

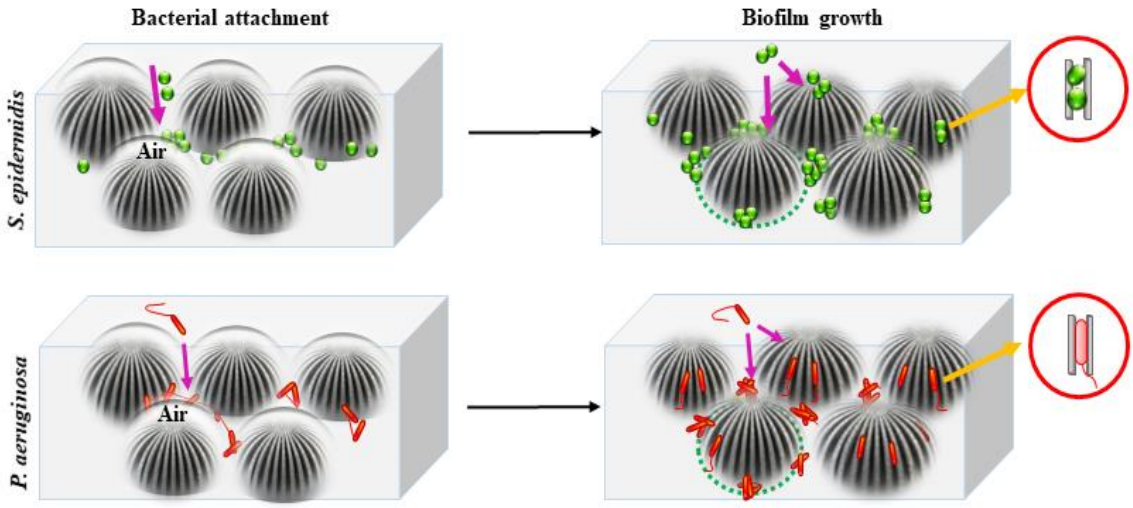

Figure 5. 12 Hypothesized anti-biofilm mechanisms for the transition from bacterial attachment to biofilm growth on rose petal structured surfaces.

5.4 CONCLUSIONS

In summary, our study has revealed that rose-petal structured surfaces can delay bacterial attachment and biofilm formation with clinically relevant strains of bacteria. We successfully demonstrated the fabrication of a hierarchical rose-petal structure via a simple UV-curable nano-casting technique, which is cost-effective when compared with fabrication methods like e-beam lithography and nanoimprinting lithography. The rose-petal replicas exhibit a high CA and CAH as a Cassie impregnating wetting state. Similar to superhydrophobic lotus-leaf, the trapped air within nano-folds may hinder the bacterial attachment. While bacteria preferentially form clusters within the valleys of micro-papillae, as they are preferentially wetted and offer more favorable colonization sites when comparing to the nano-folds. We specifically discussed the anti-biofilm mechanism of hierarchical structures under submerged conditions, and the different topography size influence biofilm formation via different mechanisms: micro-papillae blocked the bacterial clusters in between the valleys, limiting the potential for cell-cell communication via fibrous networks, thereby resulting in impaired biofilm growth. At the same time, having a secondary nanostructure (nano-folds) on microstructures can align bacterial cells within the constrained gaps, thereby

delaying in developing cell clusters during short term growth of biofilm.

Rose-petal surfaces have shown potential in parallel and multistep droplet manipulation owing to their high CAH. The hierarchical structures characterized here may be useful for the development of microfluidics and portable/wearable biosensors (Wong *et al.*, 2015). In addition, such hierarchical structures can capture and release circulating tumor cells (CTCs) for subsequent analysis (Dou *et al.*, 2017), exhibiting great potential in biomedical devices. Therefore, this study is a significant step toward the application of rose-petal surfaces where biofilm control is also important. Furthermore, hierarchical structures may be useful to study the roles of microbial cell-cell interactions in biofilm formation. Determining the most effective topography size for controlling biofilm development is an important next step for the development of antifouling surfaces. Future studies will also aim to investigate the anti-biofilm mechanisms in more detail, for example by comparing the anti-biofilm efficacy of rose-petal hierarchical structures with other artificial unitary or hierarchical structures with different scales, investigating bacterial patterning on rose-petal nano-folds and their effects on biofilm formation, and determining whether rose petal replica surfaces are capable of inhibiting growth of biofilms by different species of bacteria.

5.5 Appendix

The in-house Matlab code that extract the droplet edges:

```
close all; clear all; clc;
a = imread('0-11.tif');
b = imread('5-1.tif');
c = imread('10-1.tif');
d = imread('15-1.tif');
e = imread('20-1.tif');
f = imread('25-11.tif');
g = imread('30-11.tif');
I = rgb2gray(a);
j = rgb2gray(b);
k = rgb2gray(c);
l = rgb2gray(d);
m = rgb2gray(e);
n = rgb2gray(f);
o = rgb2gray(g);
BW1 = edge(I,'Prewitt',0.2,'nothinning');
%BW11 = imshow(BW1,'ColorMap', [1 1 1; 1 1 0]);
%BW8 = bwskel(BW1);
%imshow(BW11);
BW2 = edge(j,'Prewitt',0.2,'nothinning');
%BW22 = label2rgb(BW2,'ColorMap', [1 1 1; 1 1 0]);
BW3 = edge(k,'Prewitt',0.2,'nothinning');
BW4 = edge(l,'Prewitt',0.2,'nothinning');
BW5 = edge(m,'Prewitt',0.1,'nothinning');
BW6 = edge(n,'Prewitt',0.1,'nothinning');
BW7 = edge(o,'Prewitt',0.1,'nothinning');
BW = BW1+BW2+BW3+BW4+BW5+BW6+BW7;
%BW = imread(BW11)+imread(BW22);
imshow(BW)
```

Chapter 6

Anti-wetting and anti-fouling performances of different lubricant-infused slippery surfaces

6.1 INTRODUCTION

Inspired by Nepenthes pitcher plants, Aizenberg *et al.* firstly introduced slippery lubricant-infused surfaces to combat the long-term biofouling (Wong *et al.*, 2011; Epstein *et al.*, 2012; Kim *et al.*, 2013; Howell *et al.*, 2014; Amini *et al.*, 2017; Kovalenko *et al.*, 2017; Howell *et al.*, 2018). Thus far, it has been proposed two different methods (2D versus 3D lubricant infusion), to design stable lubricant-infused surfaces (Wei *et al.*, 2016; Amini *et al.*, 2017). The first method involves the 2D impregnation of lubricant into the chemically functionalized micro/nano-structures, preferentially facilitating the lubricant spreading and retention/blocking via van der Waals and capillary forces to form a stable immiscible over-layer (Wong *et al.*, 2011; Epstein *et al.*, 2012; Solomon *et al.*, 2016; Amini *et al.*, 2017). The second method involves the 3D encapsulation and adsorption of lubricant within the cross-linked polymer networks, forming an organogel-like surface (Howell *et al.*, 2014; MacCallum *et al.*, 2014; Solomon *et al.*, 2016; Amini *et al.*, 2017; Jiang *et al.*, 2017). These surfaces restrict the direct contact with the liquid droplets, which are immiscible with and float on the lubricant over-layer (Wei *et al.*, 2016; Amini *et al.*, 2017). In addition, the droplet above the lubricant moves remarkable ease with an extremely low contact angle hysteresis (<5°) (Wong *et al.*, 2011; Smith *et al.*, 2013; Daniel *et al.*, 2018), thereby either 2D or 3D slippery lubricant-infused surface can repel a variety of contaminated liquids with self-cleaning properties. Recent studies also demonstrated that slippery surfaces showed exceptional biofouling-repellence against *P. aeruginosa*, *S. aureus*, and *E. coli* biofilm-forming strains, owing the weak bacterial adhesion on the lubricant-liquid interfaces (Epstein *et al.*, 2012; Howell *et al.*, 2014; MacCallum *et al.*, 2014). Also, slippery lubricant-infused surfaces have the advantages in self-healing, withstanding high external pressure, anti-icing, water harvesting, and thermal management, showing the promising potentials in the industrial applications (Lee *et al.*, 2014; Wang *et al.*, 2016a).

Although the potential of either 2D or 3D lubricant-infused surfaces have been demonstrated separately, several questions remained unanswered. One important question is understanding the droplet dynamics on these surfaces, for example, droplet motility, whether rolling or sliding, the velocities of shedding away, and if the droplet can bounce off from surfaces upon impacting. Droplets with contaminates coming from rains, dews, or other bulk fluids can cause fouling if getting pinned on surfaces. Additionally, dried contaminated droplets can cause another surface fouling with leaving behind patterned stains (Solomon *et al.*, 2016; McBride *et al.*, 2018). Therefore, understanding the droplet dynamics on lubricant

layer is non-trivial, which governs the contact line pinning of droplets and can anticipate the surface anti-fouling performances.

In the present study, we fabricated 2D and 3D lubricant-infused surfaces as model slippery surfaces: (1) 2D lubricant-impregnated surfaces (referred as LIS) after the retention/blocking of silicone oil within the porous epoxy nano-pillars, and (2) 3D swollen polydimethylsiloxane (referred as S-PDMS) after the diffusion of the same lubricant into the polymer network. In other words, the PDMS is swelling owing to the diffusion of silicone oil into the cross-linked matrix (Howell *et al.*, 2014; MacCallum *et al.*, 2014; Solomon *et al.*, 2016; Amini *et al.*, 2017; Jiang *et al.*, 2017). The anti-wetting performances of both slippery surfaces were evaluated via evaluating droplet impact and droplet motility dynamics. The anti-fouling performances of slippery surfaces were initially tested against the particle dusts and the dried stains. The typical biofilm-forming strain *P. aeruginosa* was further utilized as a model for the evaluation of anti-biofouling performances. The anti-wetting and anti-fouling performances of the LIS, S-PDMS and the unmodified PDMS (as control) surfaces were systematically compared. These analyses will be useful for designing smarter or more efficient anti-fouling surfaces.

6.2 MATERIALS AND METHODS

6.2.1 Fabrication of slippery surfaces:

For the preparation of LIS, the epoxy nano-pillar arrays were made from silicon masters ($1\times1cm^2$ and around ~ 1mm thick) as described elsewhere (Pokroy *et al.*, 2009; Hochbaum and Aizenberg, 2010; Kim *et al.*, 2012; Friedlander *et al.*, 2013), and have been detailed described in Chapter 4. In this study, UV-curable epoxy (OG 142-87, Epoxy Technology, Inc.) was used to get the final imprints of pillars. The epoxy was cured under a UV-lamp, with the luminous intensity of 100 mW/cm^2 and the wavelength of 365 nm, for 20–25 minutes until fully cured. The epoxy-pillars were checked under the microscope to ensure there was no collapse of pillars before use. Finally, the epoxy-pillars were further rendered hydrophobic with 0.2 mL (tridecafluoro-1, 1, 2, 2-tetrahydrooctyl)-trichlorosilane (Gelest Inc.) by exposure in a desiccator under vacuum overnight.

For the preparation of S-PDMS, a mixture of Poly (dimethylsiloxane) (PDMS) and its curing agent was prepared from SYLGARD 184 Elastomer Kit (Dow Corning Corporation, Midland, MI) with a ratio of 10:1 (wt/wt). The solution was thoroughly mixed and degassed

in a vacuum chamber for 30 minutes to eliminate air bubbles. After that, around 14.4 ml of the mixture was poured into a 120mm square petri dish (Gosselin™), with forming around a 1 mm-thickness PDMS layer. The PDMS was cured at the room temperature for 2 days. Finally, we gently cut the cured PDMS sheet into small pieces ($1\times1cm^2$).

For the infusion of lubricant, either silinized epoxy-pillars or cured PDMS surfaces were completely immersed in a silicone oil (10 cSt, 0.93 g/mL, Sigma-Aldrich) bath and left for 24 hours to allow the lubricant to fully infiltrate into the porous structures of epoxy-pillars or the PDMS polymer networks (Figure 6.1). The excess lubricant was gently removed from the surface by filter papers, in order to eliminate the effects of excess lubricant-layer (i.e. wetting ridge) on the following tests (Schellenberger *et al.*, 2015; Semprebon *et al.*, 2017; Sadullah *et al.*, 2018).

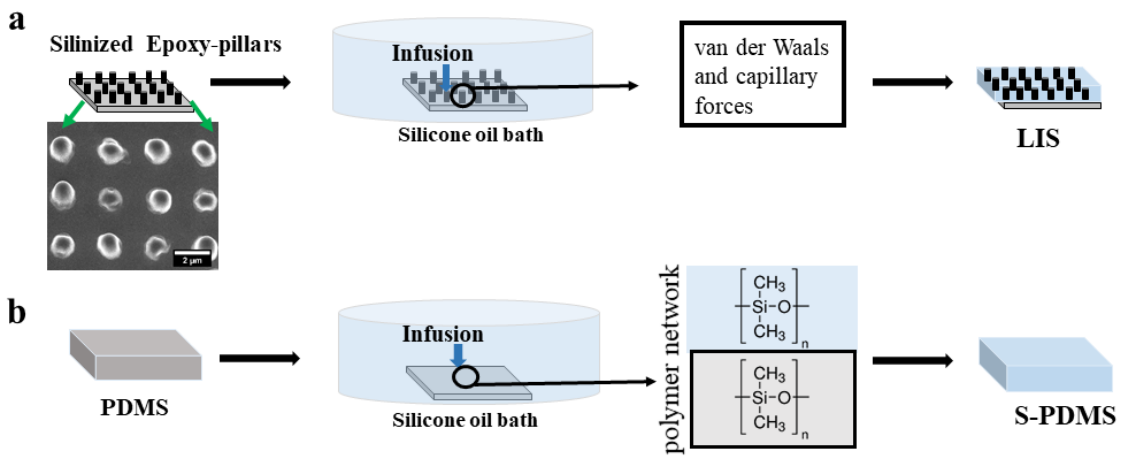

Figure 6. 1 Schematic of the process to make either LIS or S-PDMS slippery surfaces.

6.2.2 Characterization of slippery surfaces

The epoxy-pillars were imaged by scanning electron microscopy (SEM) using an FEI Helios NanoLab 600 DualBeam system, operated at 5 KV. By using a milligram-balance (OHAUS analytical balance) with a sensitivity of 0.1 mg, the sample weight before and after lubricant-infusion were measured. Also, the thickness of the surface layer having lubricant was estimated based on the measured weight, wetting area and the lubricant density. An in-house goniometer as described in (Gart *et al.*, 2015; Huhtamäki *et al.*, 2018) was set-up to measure the static and dynamic water contact angles under an ambient condition. The advancing angles of slippery surfaces was measured via a syringe-pump system (needle gauge size ~25,

water droplet ~10 μl, dispersion rate~ 0.2 ml/minute); and receding angles were measured as the liquid was withdrawn via the same method. At least five droplet measurements were taken, and the results were presented as the mean contact angles with standard deviations.

6.2.3 Droplet dynamics tests

10 μL of deionized water droplets were dispersed via a syringe-pump system (needle gauge size ~25, dispersion rate~ 0.2 ml/minute) and used in the following measurements. All the droplet dynamics was recorded by a high-speed camera (Photron FASTCAM Mini UX50) at 2000 fps. For the drop impact test, the Weber number *We* was controlled by the falling height of the drop dispense, thereby resulting in the impact velocity of U_0 =1 m/s and U_0 =4.5 m/s, corresponding to *We* = 21 and *We* = 422, respectively. Here, the *We* number is defined as $We = \rho_w U_0^2 R_0/\gamma_{wa}$, where ρ_w, U_0, R_0, and γ_{wa} are the water density (≈1000 kg/m^3), impact velocity, drop radius, and water−air surface tension at room temperature (≈72.4 mN/m) (Wong *et al.*, 2011), respectively. For the droplet mobility test, all the surfaces were tilted by 15°; and a lower *We* =2 was chosen to better observe the droplet bounce off.

6.2.4 "Self-cleaning" effect tests

The surface fouling was generated by randomly spreading the ground coffee particles or by the stains after evaporating 3 μl of a stardust aqueous solution (3mg/ml, Waitrose Cooks' Homebaking stardust) on surfaces. The dried stains were visualized by a camera with a TV lens (50 mm) mounted with an extension tube (40 mm). Deionized water droplets were dispersed as described above and all the washing process was recorded by the high-speed camera at 2000 fps (Photron FASTCAM Mini UX50).

6.2.5 Bacteria culture and biofouling tests

Bacteria culture, bacterial adhesion and biofilm growth: Biofilm-forming strain *P. aeruginosa* PAO1-mCherry (Nottingham subline) (Sidorenko *et al.*, 2017) was used in this study and was routinely cultured in Tryptic Soy Broth (TSB, Melford Laboratories Ltd, UK), in a shaker at 180 rpm, 37℃ for 16 hours prior to the assay of bacterial adhesion/biofilm formation. *P. aeruginosa* PAO1-mCherry was further diluted to OD_{600}= 0.30 with a spectrophotometer (Biochrom Libra S11, Biochrom Ltd., Cambridge, UK). 3 ml of the diluted bacterial culture was incubated with the PDMS (as control), LIS and S-PDMS surfaces in 12-well culture plates at 37℃, for 2 hours (bacterial adhesion assay), 2 days and 6 days (biofilm assay) respectively. For the biofilms developed up to 6 days, half of the TSB medium was changed every 2 days. At the least three independent experiments were

performed for each surface type.

Fluorescent Microscope Analysis: The surfaces after either bacterial adhesion or biofilm formation assay, were gently rinsed three times with Phosphate Buffered Saline (PBS, pH=7.4) to remove loosely adhered bacteria. After that, samples were directly visualized by Olympus BX61 upright fluorescent microscope with a 20x objective lens. The bacterial cells after 2 hours' incubation were visualized by acquiring 2D fluorescent images in a single focal plane (121.25 × 108.75 μm^2). For biofilms, z-stacks were performed through the thickness of biofilm from 5 random locations on the surfaces. The biomass under each field of view (430.00 × 324.38 μm^2) was determined using the COMSTAT2 plugin (Lyngby, Denmark) in ImageJ.

Toxicity Tests: Shaken cultures of *P. aeruginosa* (OD_{600}=0.01) in 20 mL TSB were grown with and without the silicone oil (10% by volume) as described elsewhere (Epstein *et al.*, 2012; Howell *et al.*, 2014). Then the bacterial cultures were further incubated in a shaker at 37 °C at 180 rpm. Optical density measurements at 600 nm were taken at 3, 6, and 24 hours with the spectrometer.

6.2.6 Statistical Analysis

Data are represented as mean values with standard error. Student's t-test assuming unequal variations was applied and $*p < 0.05$ was considered statistically significant in this study.

6.3 RESULTS AND DISCUSSION

6.3.1 Fabrication of different lubricant-based slippery surfaces

Two different lubricant-based slippery surfaces (LIS vs S-PDMS) were fabricated with the same lubricating fluids – silicone oil (10 cSt, 0.93 g/mL, Sigma-Aldrich), as schematically depicted in Figure 6.1. The main criteria to fabricate LIS surfaces is that the surface is preferentially wetted by the lubricant, while the liquid which wants to repel is floating on the lubricant layer instead of displacing or penetrating it (Wong *et al.*, 2011). In order to assess this, it has been proposed that a stable lubricant layer needs to satisfy the following equations (Wong *et al.*, 2011):

$$\Delta E_1 = r_w(\gamma_{oil}\cos\theta_{oil} - \gamma_{water}\cos\theta_{water}) - \gamma_{ow} > 0 \quad (1)$$

$$\Delta E_2 = r_w(\gamma_{oil}\cos\theta_{oil} - \gamma_{water}\cos\theta_{water}) + \gamma_{water} - \gamma_{oil} > 0 \quad (2)$$

Where r_w is the roughness factor (the ratio between the actual and projected surface areas of the textured solid surface); γ_{oil} and γ_{water} are the surface tension of the infused lubricant oil and the water, γ_{ow} is the interfacial tension of the oil-water interface; θ_{water} and θ_{oil} are their corresponding contact angles (CA) on the solid surface (with air around) (See detailed calculation in Table S6.1 in Appendix). Herein, we generated the ordered pillars (diameter ~1 μm, space ~2 μm and height~ 2 μm, see inset SEM image, Figure 6.1a) on surfaces to provide rough textures for the immobilization of lubricant. After rendering hydrophobic via silinization, we confirmed that our LIS can have a stable lubricant layer (ΔE_1= 31.99 mN/m, ΔE_2=130.99 mN/m). In this study, the sample size of LIS and S-PDMS is 1×1 cm^2 and around ~1mm thick, thereby the surface volume for lubricant infusion is the same for either surface. We checked the weight difference of samples before and after lubricant infusion with a milligram-balance, and found that the lubricant can fully infuse into either surface after 24 hours, as the sample weight didn't increase after that time. The infused lubricant on LIS was weighted to be 1.13 ±0.21 mg, and the surface layer having lubricant was estimated to be 12.2 ± 2.2 μm. LIS is strongly depending on the surface texture for the immobilization of lubricant and can only generate a thin lubricant oil layer over the texture (i.e. 2 μm height for epoxy-pillars). However, PDMS can adsorb more lubricant via diffusion, and we determined the adsorbed lubricant was 79.73 ±2.55 mg and the diffused matrix thickness was estimated to be 857.3 ± 27.5 μm. This indicated that silicone oil can be adsorbed or diffused into the nearly whole PDMS matrix (i.e. 1 mm thickness). The investigation above indicated that S-PDMS has more lubricant via diffusion as compared with LIS in this study.

Table 6. 1 The key surface features of the surfaces used in this study.

	Substrate volume (area ×thickness)	Sub-feature dimension	Infused lubricant weight(mg)	Lubricant-layer (μm)	Static contact angle (deg)	Contact angle hysteresis (deg)
PDMS(control)	1cm^2×1mm	n.a.[a]	n.a.[a]	n.a.[a]	113.0 ± 3.2°	45.2± 4.8°
LIS	1cm^2×1mm	Pillars (diameter~1 μm, pitch~2 μm, height~ 2 μm)	1.13 ±0.21	12.2 ± 2.2	110.7 ± 5.1°	5.5± 2.7°
S-PDMS	1cm^2×1mm	n.a.[a]	79.73 ±2.55	857.3 ± 27.5	104.5 ± 4.9°	3.3± 2.1°

[a]N.a., not applicable.

6.3.2 Droplet dynamics on slippery surface

The static contact angle (CA), and the contact angle hysteresis (CAH) of water droplets on the control PDMS, LIS and S-PDMS were investigated (Table 6.1). In contrast to both slippery lubricant-infused surfaces, the control PDMS without lubricant showed typical hydrophobic properties, with a water CA of 113.0 ± 3.2° and a high CAH (45.2± 4.8°). Following infusion with silicon oil, either LIS or S-PDMS surfaces retained a similar water CA, while the CAH decreased significantly. LIS has a CAH of 5.5± 2.7° and S-PDMS has a CAH of 3.3± 2.1°, showing ultralow CAH values and indicating a lack of pinning on both surfaces. However, we questioned that if S-PDMS is more slippery than LIS since its CAH is lower.

Firstly, we tested if our surfaces can repel water droplets upon impact. Anti-wetting surfaces are required to have a reliable performance against falling droplets, for example rain and dew drops in nature. Herein, we did the drop impact tests at different Weber number (We~ 21 and 422) with the same water droplet volume (10 µl), via fast-imaging analysis. A series of time-resolved images of spreading and retraction dynamics of droplets on the control PDMS, LIS and S-PDMS surfaces were shown in Figure 6.2 a-b. At either low or high Weber number, there was no noticeable difference during the water drop spreading (0~3.5 ms) among the surfaces. The droplets all deformed into a pancake shape on all surfaces, reaching the maximum diameter (R_{max}) upon impacting after 3.5 ms, which is independent of Weber numbers as previously investigated (Muschi *et al.*, 2018). We quantitatively examined the ratio R/R_0 of the impacting water drop diameter (R) with respect to the initial drop diameter (R_0) at the different Weber numbers, as shown in Figure 6.2b. For each case, the plots of R/R_0 against time of different surfaces were nearly collapsing onto a single curve during the spreading, while R_{max}/R_0 increases with the Weber number, indicating that a higher impact velocity results in a fast spreading as the impact time is the same (3.5 ms). For the droplet retraction (3.5~30 ms) at the lower Weber number, the droplets cannot bounce off from the control PDMS or LIS surfaces, in contrast to S-PDMS where enabled a partial rebound of droplets after 30 ms with a tiny residue of water remained (Figure 6.2a). This indicated that S-PDMS has a superior slipperiness even at a lower Weber number with a lower impacting speed. The water droplet still got pinned on the control PDMS at a higher Weber number, and cannot bounce off (Figure 6.2b). However, the water droplets can bounce off the LIS and S-PDMS surfaces after 30 ms with emission of a water jet (Figure 6.2b). During the droplet retraction at both Weber numbers, the R/R_0 of either LIS or S-PDMS decreased

quickly as compared with the control PDMS surfaces (Figure 6.2c), indicating that water droplet finds easy to recede on slippery surfaces until which can bounce off. For either slippery surface, the CAH is very low, thereby the energy dissipation caused by the drop deformation during spreading and receding is weak (Muschi *et al.*, 2018). Therefore, after receding, the drop still has enough energy to fully bounce off at a higher Weber number, which is not the case on the control PDMS having a high CAH.

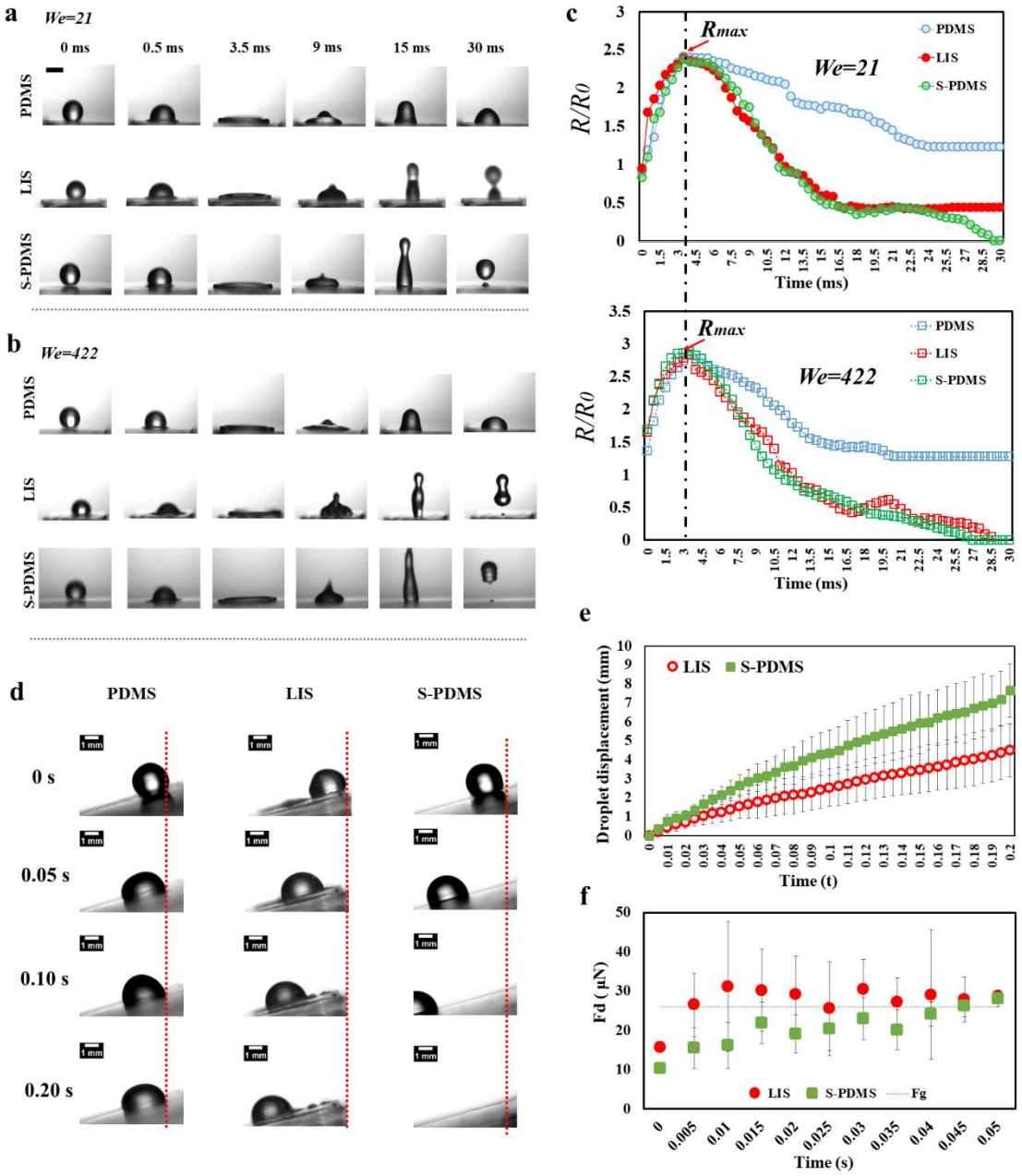

Figure 6. 2 (a-b): Time evolution of a water drop (~10 µl) impacting different surfaces at an impact velocity of (a) U_0 =1 m/s and (b) U_0 =4.5 m/s, corresponding to Weber numbers of We = 21 and We = 422, respectively. The time scale is the same on both figures. Scale bar is 2 mm. **(c):** Time evolution of the diameter of the impacting water drop normalized by the initial drop diameter at different Weber numbers of on different surfaces. **(d):** Time evolution

of a water drop (~10 µl) moving on the inclined surfaces (tilt angle~15°). **(e):** The droplet contact line displacement with time for LIS and S-PDMS surfaces, the displacement varies linearly with time, indicating the droplet is moving with a nearly constant speed. Values are mean ± standard deviation of three independent experiments. **(f):** The calculated dissipative force F_d by using equation (3), when droplets moving over the slippery surfaces overtime (0~ 0.05s). Values are mean ± standard deviation of three independent experiments.

Next, we sought to investigate the water-shielding ability on inclined surfaces (tilt angle~15°), as in the practice gravity is a common driving force to facilitate the spontaneous water detachment (Cao *et al.*, 2015). The droplet is always getting pinned on the control PDMS surface, corresponding to its high CAH (Figure 6.2d). However, the droplets can shed away on either LIS or S-PDMS surfaces within seconds, showing their superior slippery properties (Figure 6.2d). Notably, the droplet can shed away from S-PDMS surface within 0.2 s, quicker than the one moving on the LIS surface. To account for this, we quantified the droplet contact line displacement with time for LIS and S-PDMS surfaces as shown in Figure 6.2e. The droplet moved nearly at a velocity *U*~ 20.6 ±4.9 mm/s on LIS surface, closing to the value as previously investigated (Daniel *et al.*, 2018). By contrast, the droplet velocity on S-PDMS is *U* ~ 36.1±7.1 mm/s, which is nearly twice of the droplet speed on LIS. This may indicate that S-PDMS has a more effective water-shielding ability.

When a droplet is placed on an inclined surface, the mobility of droplets are governed by the gravitational forces ($F_g = mg \sin \Theta_{tilt}$) and dissipative forces (Furmidge, 1962). F_g was calculated to be about 25.9 µN for control PDMS, LIS and S-PDMS. Where, the dissipative force (F_d) was given by

$$F_d = k * 2R_b\gamma_{water}(\cos \Theta_{Rear} - \cos \Theta_{Front}) \qquad (3)$$

where m, g and θ_{tilt} represent the droplet mass, the gravitational acceleration and the inclined angle respectively, θ_{Rear} and θ_{Front} are the apparent rear and front contact angles of the droplet (see Appendix Figure S6.1), R_b is the droplet base radius and γ_{water} is the water/air surface tension(Smith *et al.*, 2013; Jiang *et al.*, 2017; Gao *et al.*, 2018). Here, the dimensionless parameter k is related to the actual shape of the drop, which ranged between $4/\pi$ and $\pi/2$ according to analytical models (Extrand and Gent, 1990; ElSherbini and Jacobi, 2006) and numerical simulations(Brown *et al.*, 1980). A few recent experimental measurements reported that k can be 1.1-1.48 for various droplet on solid surfaces (Gao *et al.*, 2018). Here, we also assume that the initial base shape is circle with k=1, which has been widely adopted for estimating the dissipative forces on slippery surfaces (Semprebon *et al.*, 2017; Daniel *et*

al., 2018; Gao *et al.*, 2018).

We measured the dynamic R_b, θ_{Rear} and θ_{Front} when droplets moving over the slippery surfaces and calculated F_d by using equation (3) (Figure 6.2f). 0~ 0.05s was chosen because the droplet moved out of field of view during the recording process thereafter. The initial $F_{d\ (initial)}$ (t~0 s) of control PDMS was 133.5 ±1.6 μN > F_g (~25.9 μN), thereby the droplets always get pinned on the surface as the gravitational force cannot overcome the dissipative force, as seen in Figure 2d. By contrast, $F_{d\ (initial)}$ (t~0 s) of LIS and S-PDMS were 15.8±1.0 μN and 9.7±0.8 μN, which were only around 7-12% of the control PDMS ($Fd_{\ (initial)}$ ~133.5 ±1.6 μN) and significantly lower than F_g (~25.9 μN). If we estimated the droplet driving force (F_{drive}) by using the equation $F_{drive} = F_g - F_d = ma$, where a is the acceleration of the droplet, then F_{drive} is estimated to be ~10.1±1.0 μN for LIS and 16.2±0.8 μN for S-PDMS. Then apparently S-PDMS can have a higher $a_{initial}$ at this transient state, thereby expect to have a higher speed afterwards if assuming the initial droplet moving speed is the same. However, we noted that F_d of either surface increased overtime to eventually reach an equilibrium state, where $F_d \approx F_g$ and $F_{drive} \approx 0$, and LIS can reach this state quicker than S-PDMS (Figure 6.2f). It has been reported that the dissipative force F_d of a moving droplet on lubricated surfaces is also depending on the viscous stress $\eta U/h$, and $F_d \propto \eta U/h$, where η is the oil viscosity, U is the droplet moving speed, and h is lubricant film thickness(Daniel *et al.*, 2017; Daniel *et al.*, 2018). The stable lubricant layer can prevent pinning thereby giving rise to velocity-dependent, viscous dissipative force(Daniel *et al.*, 2017; Daniel *et al.*, 2018). Therefore, F_d can increase with U overtime, and finally attain the equilibrium, $F_d \approx F_g$ and $F_{drive} \approx 0$. This possibly explained the droplet moving at a nearly constant speed on slippery surfaces afterwards (Figure 6.2e). Notably, $F_{d(initial)}$ of S-PDMS is lower than LIS, which leads to a higher U as shown in Figure 6.2e.

Our investigation above demonstrated that water droplets can bounce off S-PDMS surfaces possessing a lower CAH even at a lower Weber number, and droplets can move quicker on the inclined surface. A large difference between LIS and S-PDMS surfaces is that their construction mechanism is different. S-PDMS can adsorb more lubricant volume within the surface, which possibly results in its stronger slipperiness. Researchers have shown that the CAH of a water drop on a lubricant-infused surface is lower if more lubricant is absorbed, thereby its dissipative force is lower, which significantly improved its mobility speed(Kim *et al.*, 2013; Zhang *et al.*, 2014; Solomon *et al.*, 2016). In this study, we investigated the droplet dynamics at the macro-scale. Literature reports of the water-lubricant interfaces

suggest there is an effective slip length (micro-or nano-scale) of the lubricant layer for the surface slipperiness(Amini *et al.*, 2017; Daniel *et al.*, 2017; Scarratt *et al.*, 2019). It has been reported that S-PDMS can have a thicker effective slip length as compared with similar LIS surfaces, thereby reflecting its greater slipperiness(Amini *et al.*, 2017). Other studies have also demonstrated that different lubricant volumes can lead to different morphologies of the wetting ridge owing to the existence of air-oil-water interfaces (Smith *et al.*, 2013; Solomon *et al.*, 2016; Semprebon *et al.*, 2017; McHale *et al.*, 2019). Therefore, the different size/shape of wetting ridge can affect droplet dynamics significantly(Smith *et al.*, 2013; Sadullah *et al.*, 2018). After removing the excessive lubricant on either LIS or S-PDMS, the effects of wetting ridge are expected to be eliminated in this study and we did not observe the apparent wetting ridge when investigating the droplet in transient state. However, further studies will be conducted to investigate the effects of slip length and wetting ridge on droplet dynamics in more details.

6.3.3 Self-cleaning effects of slippery surfaces

A self-cleaning surface is referred as the one from which contaminants such as dusts or stains can easily be removed by a liquid (Solomon *et al.*, 2016). The water droplets always become pinned on the control PDMS as investigated above. While for either LIS or S-PDMS having a low CAH, we expected that small water droplets can be easily shed from surfaces and take contaminants with them. Firstly, we confirmed the droplet rolling by adding fine ground coffee particles to the water droplet and used the high-speed camera to track the particle motion relative to the droplet when moving across the slippery surfaces. By using an in-house Matlab code, the particle trajectories were generated and are shown in Figure 6.3. The trajectories of these coffee particles clearly showed that droplets roll across the surface, showing the anti-fouling potentials in practical applications as gravity is a common driving force for the detachment of contaminated water detachment (Cao *et al.*, 2015). Then we spread ground coffee particles on inclined LIS and S-PDMS surfaces (tilt angle~15°), and a 10 μl water droplet can still roll away the coffee particles on either surface (Figure 6.4a). Notably, as the spreading coffee particles were not uniform on surfaces thereby may cause different pinning points, we do not aim to compare the effectiveness of cleaning in this case. While the investigation above showed that either slippery surface has the ability to roll off the surface dusts by water droplets.

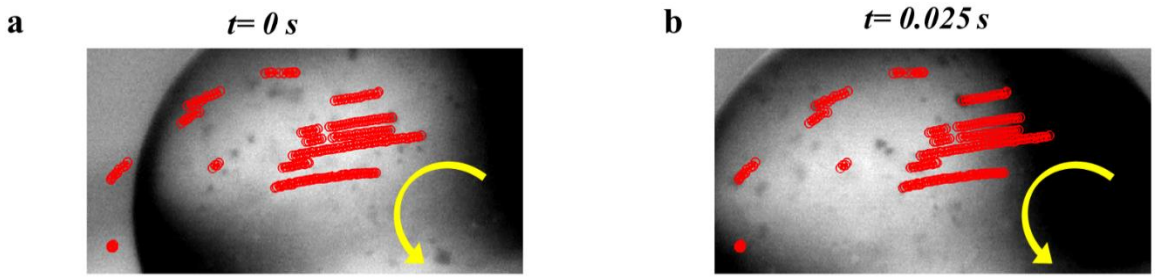

Figure 6. 3 Droplet rolling across the slippery surfaces, captured via fast-imaging camera at 2000 fps. Red circles denote the trajectory of particles as the droplets execute rolling motion between time t=0 to t=0.025 s. Yellow arrows indicate the rolling direction.

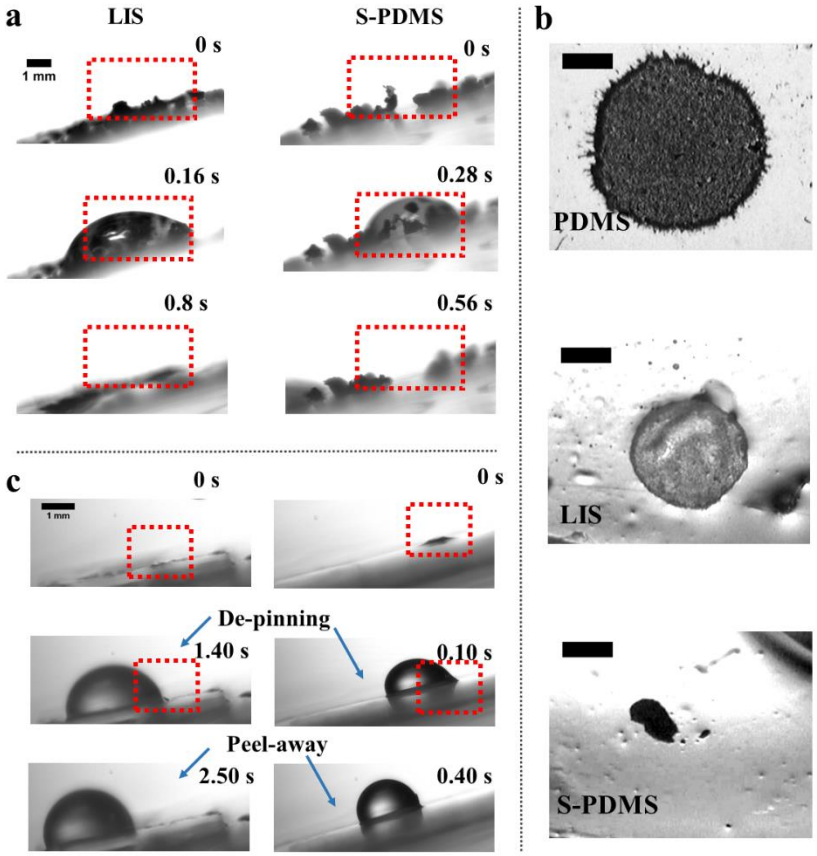

Figure 6. 4 (a): Either LIS or S-PDMS can roll off the spreading coffee particles by water droplets. **(b):** The left stains after evaporating 3 µl droplet of a stardust aqueous solution on the surfaces of control PDMS, LIS and S-PDMS, respectively (scale bar 500 µm). **(c):** The dried dust stains on LIS and S-PDMS can be peeled away by small water droplets.

Next, we sought to investigate whether slippery surfaces can remove stains easily as the evaporation of contaminated water droplet can leave stains on surfaces (i.e. coffee ring effect), which is difficult to remove (Yunker *et al.*, 2011; Cao *et al.*, 2015; McBride *et al.*, 2018). The process depends on the receding of droplet contact line (CL), and we investigated this through evaporation of 3 µl of a stardust aqueous solution. The initial CL of droplets were measured to be 1.70 ±0.02 mm for PDMS, 1.85 ±0.07 mm for LIS, and 1.90 ±0.04 mm for S-PDMS, respectively (Figure 6.5a). The evaporated droplet remained a coffee-ring-like porous dust stain on the PDMS surface in the diameter of 1.68 ±0.06 mm, similar to the scale of its initial CL indicting its difficulty to recede (Figure 6.4b). The stain on LIS was condensed and smaller in the diameter of 1.14 ±0.02 mm (61.6% of its initial CL), implying its easy receding of CL comparing to the PDMS (Figure 6.4b). The size of the stain on S-PDMS shrank significantly to 0.41 ±0.11 mm (21.6% of its initial CL), indicating this stain is more condensed and S-PDMS surface can more easily recede the CL (Figure 6.4b). This is consistent to our investigation showing S-PDMS has superior slipperiness comparing to another two. The dried stains on either LIS or S-PDMS can be easily removed by tissue papers, while the one on the PDMS collapsed into small particles and contaminated the whole surfaces (Figure 6.5b). The dust stain on S-PDMS can also be de-pinned and peeled away by a 10 µl water droplet after 0.40 s, in contrast to that a 20 µl water droplet was used for peeling away the stain on LIS after 2.50 s (Figure 6.4c). The time difference may be attributed to that the stain on LIS is bigger than the one on S-PDMS thereby more energy should be charged to the LIS to release the fresh air-lubricant interface (Cao *et al.*, 2015). However, the investigation above demonstrated the dried dust droplets may adsorb to the lubricant layer with easy “peeling-away” via tissue papers or small water droplets, owing to the low adhesion between stain and lubricant interfaces. This indicated the potential of slippery surfaces to inhibit the coffee ring effect by overcoming pinning problems.

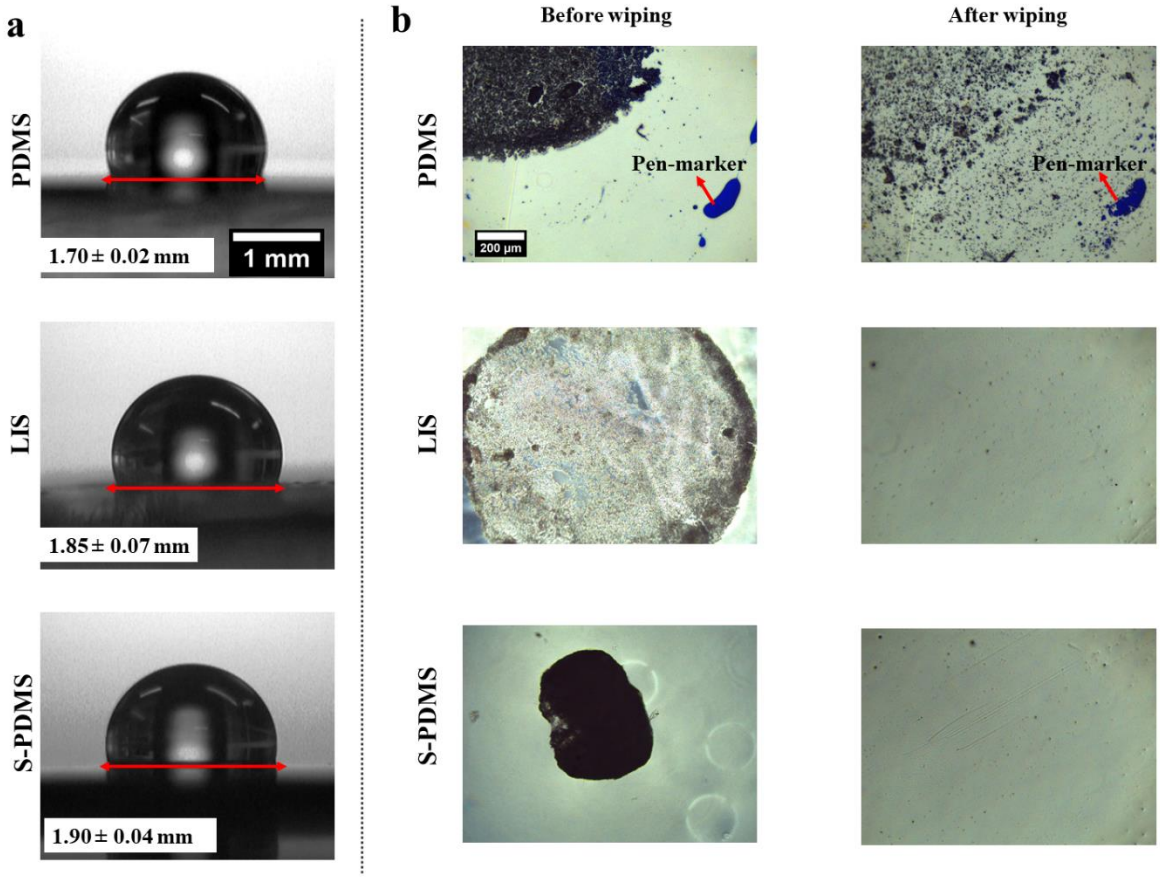

Figure 6. 5 (a): The initial CL of 3 µl droplet of a stardust aqueous solution on the surfaces of control PDMS, LIS and S-PDMS, respectively. **(b):** The dried stains on either LIS or S-PDMS can be easily removed by tissue papers, while the one on the PDMS collapsed into small particles and contaminated the whole surfaces.

6.3.4 Anti-biofilm performances of slippery surfaces

Firstly, we investigated the evaporation of 2-days *P. aeruginosa* biofilm culture droplets (Figure 6.6a &6.7 a) as well as the dried stains left on the surfaces. Similar to the star dusts investigated above, the evaporated biofilm droplet remained a coffee-ring-like stain on the PDMS surface, similar to the initial CL of biofilm culture droplet (Figure 6.7 a). The dried biofilm stain cannot be wiped or collapsed via the tissue papers, indicating its highly adhesion after drying on the PDMS surfaces (Figure 6.7 b). However, the biofilm stains on either LIS or S-PDMS were much smaller as compared with their initial biofilm droplet CLs (Figure S6.3a), and the dried biofilm stains were still easily removed by tissue papers from either surface (Figure 6.6a & 6.7 b). Also, the biofilm stain on S-PDMS can be peeled away by a 10 µl water droplet after 0.6 s (Figure 6.6b). A 20 µl water droplet cannot peel away the stain on LIS easily with leaving water residues; however, the biofilm stains can still be

peeled away after 2-3 times washing with a 20 µl water droplet (Figure 6.8). The biofilm culture droplets are very viscous and composed of glue-like extracellular polymeric substances (EPS), thereby can strongly adhere onto solid surfaces comparing to the aqueous solution. This possibly explained the more difficulty of de-pinning and peeling biofilm stains on surfaces. However, the investigations above still indicate that slippery surfaces can also anti-fouling against dried biological contaminant stains (i.e. dried biofilms).

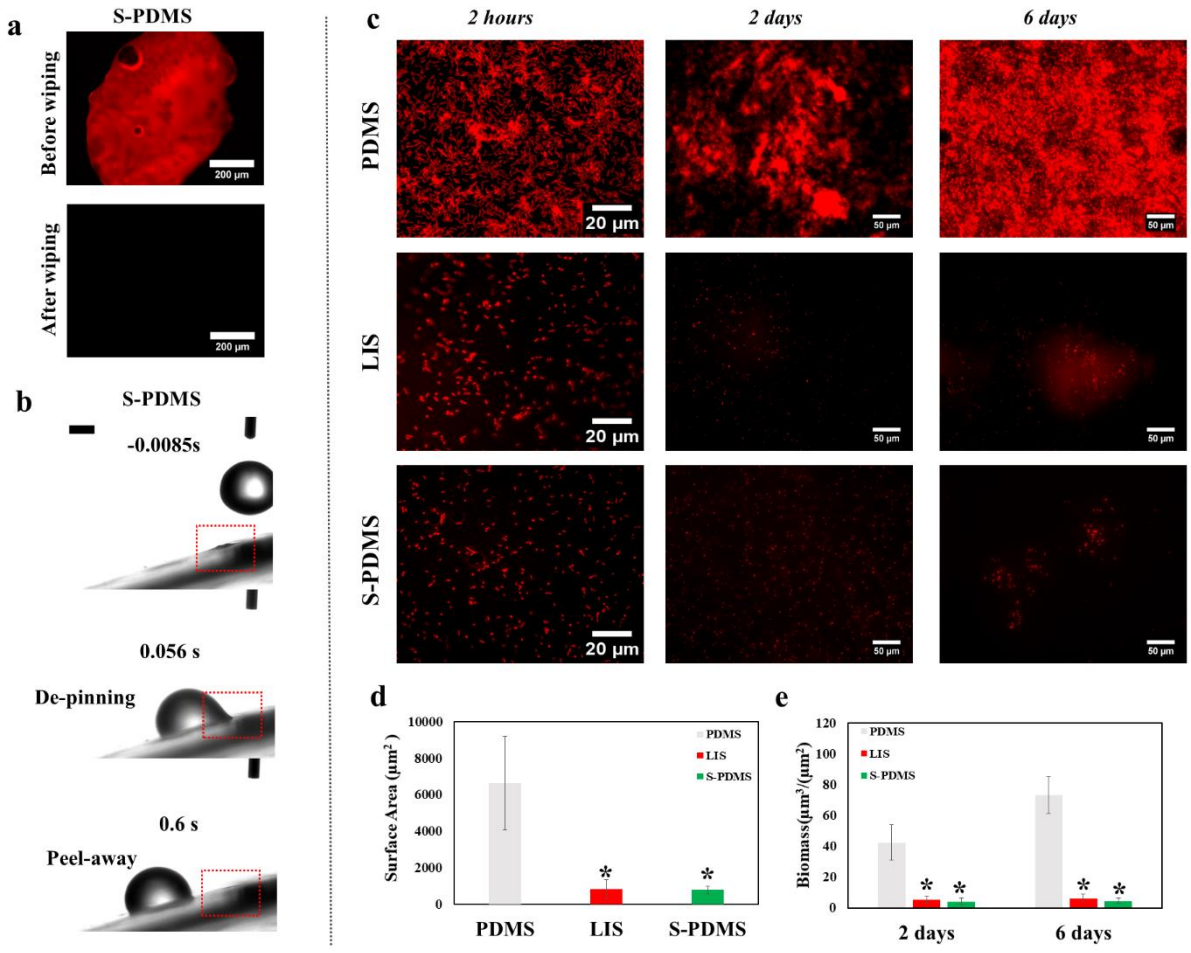

Figure 6. 6 (a): The fluorescent images of dried biofilm stains on S-PDMS showing that they can be easily removed by tissue papers; **(b):** The biofilm stain on S-PDMS can be peeled away by a 10 µl water droplet after 0.6 s. **(c):** Fluorescent images of the growth of *P. aeruginosa* after different timescales. **(d):** The surface area coverage of *P. aeruginosa* in the field of view (121.25 × 108.75 µm^2) for each surface was determined by ImageJ. *$p<0.05$ was considered as significant. **(e):** Biomass volume per unit area on the different surfaces calculated from ImageJ Comstat2. *$p<0.05$ was considered as significant. Values in (d-e) are mean ± standard deviation of three independent experiments.

To further evaluate the anti-biofouling properties of slippery surfaces, the growth of *P. aeruginosa* was examined after different timescales (Figure 6.6c). We firstly examined that if the slippery surface can inhibit the initial bacterial attachment after 2 hours. As shown in Figure 6.6c, uniform bacterial attachment was happened on the control PDMS surfaces with locally forming bacterial aggregates or clusters. However, only sparse and isolated cells were seen on either LIS or S-PDMS. Additionally, the quantification of the surface area covered by bacteria (Figure 6.6d) showed that either LIS or S-PDMS significantly reduced the initial bacterial attachment; by 85.9 ±10.8% or 86.7 ±5.9% less compared to the control PDMS, respectively. After this, we grew the *P. aeruginosa* biofilms on different surfaces after 2 and 6 days, as shown in the images of maximum intensity projections through the thickness of biofilms (Figure 6.6c). The control PDMS surfaces showed intense fluorescent patches, indicating a typical biofilm growth comprising multiple layers of cells after 2 and 6 days. *P. aeruginosa* biofilms after 6 days showed a denser and robust biofilm network after the extended culture period with fully covering the surface. In contrast, the slippery surfaces (LIS and S-PDMS) after either 2 days or 6 days, showed no visible adherent biofilms upon being removed from the culture medium, and only had some sparse cells similar to the bacterial attachment after 2 hours (Figure 6.6c). The total biomass of the LIS and S-PDMS surface after 2 days were significantly lower (86.6 ±7.1% and 90.0 ±6.1% less), as compared with the biomass of the control PDMS surfaces (see Figure 6.6e). Additionally, we found that the total biomass of the LIS and S-PDMS surface after 6 days were also significantly reduced (91.3 ±3.0% and 93.1 ±3.7 % less), comparing to the biomass of the control PDMS surfaces (Figure 6.6e). Notably, there appeared more biofilm reduction on slippery surfaces after 6 days if comparing the biofilms after 2 days. We evaluated the biomass of slippery surfaces after different days, showing as 5.3 ±2.7 $\mu m^3/\ \mu m^2$ of LIS and 4.0 ±2.4 $\mu m^3/\ \mu m^2$ of S-PDMS after 2days, 6.3 ±2.7 $\mu m^3/\ \mu m^2$ of LIS and 4.7 ±1.7 $\mu m^3/\ \mu m^2$ of S-PDMS after 6 days (Figure 6.6e). This implied that there was no significant biomass increase during 2-6 days on slippery surfaces, in contrast to the control PDMS where its biofilm biomass after 6 days was nearly twice of the one after 2 days (Figure 6.6e). Our experimental results were consistent with the previous investigations (Epstein *et al.*, 2012; Kovalenko *et al.*, 2017) showing that bacteria have poor ability to anchor a lubricant-liquid "surface" to grow biofilms.

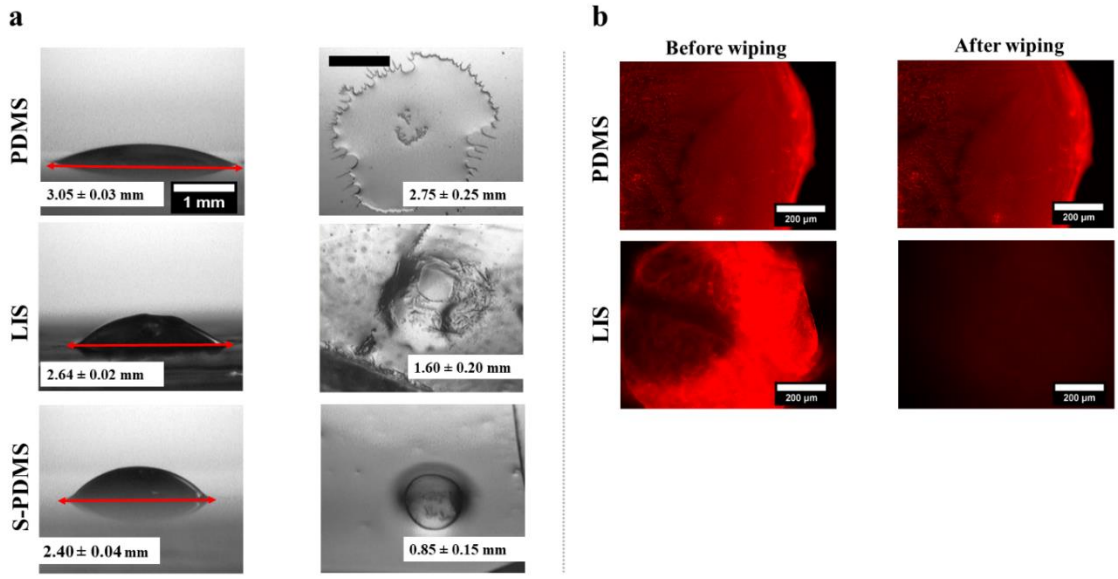

Figure 6. 7 The evaporated biofilm droplet remained a coffee-ring-like stain on the PDMS surface, similar to the initial CL of biofilm culture droplet. The dried biofilm stain cannot be wiped or collapsed via the tissue papers, indicating its highly adhesion after drying on the PDMS surfaces. However, the biofilm stains on either LIS or S-PDMS were much smaller as compared to their initial biofilm droplet CLs, and the dried biofilm stains were still easily removed by tissue papers from either surface. Scale bar in (a) are all set as 1mm. Scale bar in (b) are all set as 200 μm.

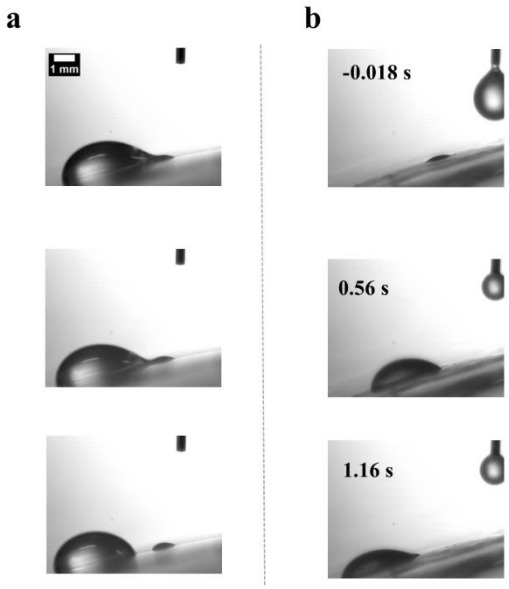

Figure 6. 8 A 20 μl water droplet cannot peel away the stain on LIS easily with leaving water residues as shown in (a); however, the biofilm stains can still be peeled away after 2-3 times washing with a 20 μl water droplet as shown in (b).

The growth curves of *P. aeruginosa* culture with and without the lubricant (i.e. silicone oil) were shown in Figure 6.9, and confirmed that the lubricant is nontoxic to the model microorganism used in this study. Silicone oil is non-fluorinated biocompatible liquid and has been widely used in biomedical applications (Howell *et al.*, 2018). Therefore, we can confirm that the anti-biofouling performance of our slippery surfaces does not result from the lubricant toxicity, but its special surface properties. The exceptional ability of our slippery surfaces to resist the biofilm growth of *P. aeruginosa* excited us to find out if they have the potential to inhibit other biofilm growth. We studied the clinically biofilm-forming pathogen, *Staphylococcus epidermidis* (FH-8) (Shields *et al.*, 2013), for the incubation of 2 hour, 2 days and 6 days (Figure 6.10). *S. epidermidis* attachment (2 hours) was significantly reduced by 94.4 ±4.9% on LIS and by 95.5 ±3.5% on S-PDMS versus the control PDMS, based on the surface area covered by the adhered bacteria (Figure 6.10 b). The biomass of *S. epidermidis* biofilms (6 days) on the control PDMS was also nearly the twice of the ones after 2 days, showing the continuous biofilm growth (Figure 6.10 c). However, there was also no significant biomass increase of biofilms on slippery surfaces during 2-6 days. *S. epidermidis* biomass of 2 days was significantly reduced by 82.3 ±4.8% on LIS and by 86.1 ±6.6% on S-PDMS versus the control PDMS (Figure 6.10 c). In addition, *S. epidermidis* biomass of the LIS and S-PDMS surface after 6 days were also significantly reduced (85.0 ±8.7% and 90.8 ±3.9 % less), comparing to the biomass of the control PDMS surfaces (Figure 6.10 c). This indicated that the anti-biofilm properties of either LIS or S-PDMS is nonspecific and is general to pathogenic biofilm-forming bacteria.

The ease of removing dried biofilm stains and the poor biofilm growth on lubricated slippery surfaces (LIS and S-PDMS) indicate their special mechanism different from solid surfaces. It has been reported that the lubricant layer on surfaces can impair the mechanical triggers of bacterial biofilm formation (Wong *et al.*, 2011; MacCallum *et al.*, 2014). Owing to low contact hysteresis, bacteria may slide along the lubricant interface with much lower friction-resistance than experienced in the control PDMS (MacCallum *et al.*, 2014). When bacteria are in contact with a lubricant interface, they are not able to anchor to the mobile interface via flagella/pili or other cellular mechanisms as would be possible on a solid surface (Epstein *et al.*, 2012). This also explained the shrinkage of biofilm stains on slippery surfaces as bacteria cells were sliding/moving along the lubricant with the CL receding. Additionally, the cells still cannot strongly adhere on the lubricant interface after drying, thereby which can be easily removed by tissue papers or small water droplets.

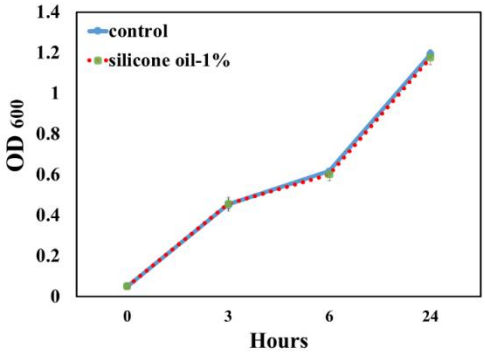

Figure 6. 9 Indistinguishable growth curves of *P. aeruginosa* cultured in shaken TSB media containing 1% of silicon oil at 0, 3, 6 and 24 h suggests no toxicity and biocompatibility of the lubricant.

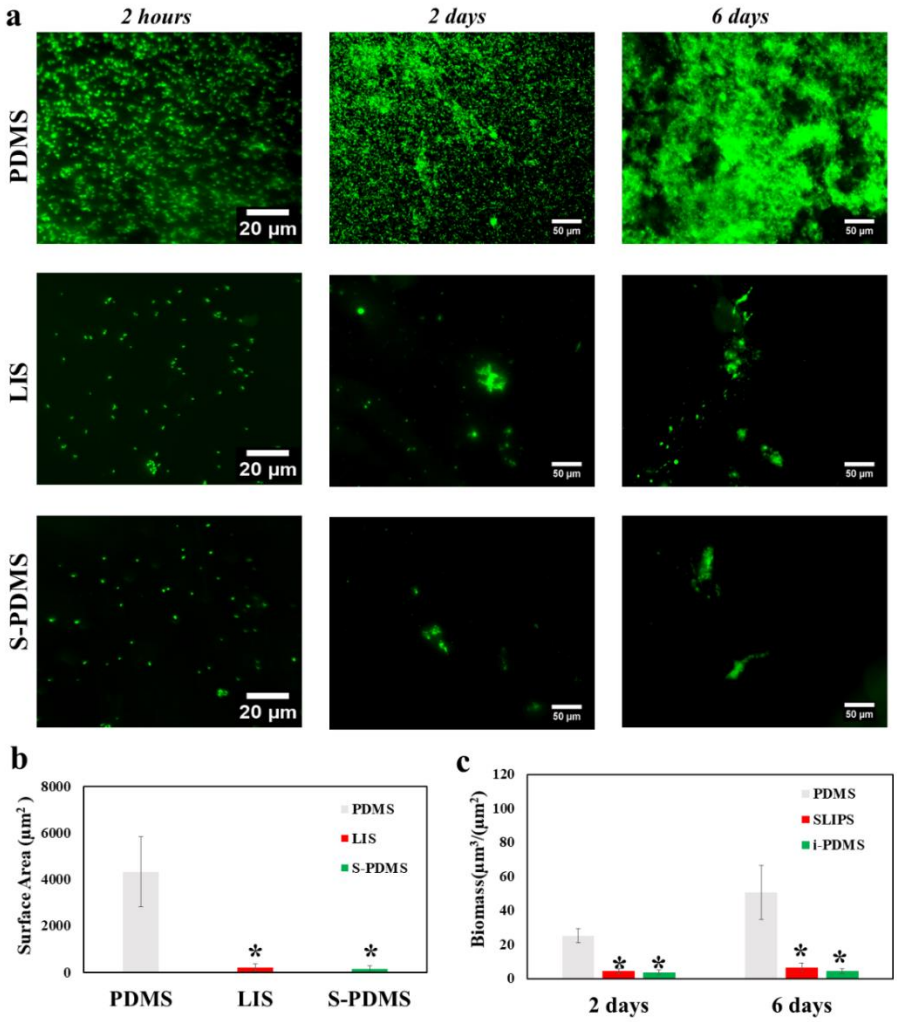

Figure 6. 10 (a): Fluorescent images of the growth of *S. epidermidis* after different timescales. **(b):** The surface area coverage of *S. epidermidis* in the field of view (121.25 × 108.75 µm^2) for each surface was determined by ImageJ. *$p<0.05$ was considered as significant. **(c):** Biomass volume per unit area on the different surfaces calculated from ImageJ Comstat2. *$p<0.05$ was considered as significant. Values in (b-c) are mean ± standard deviation of three independent experiments.

6.4 CONCLUSIONS

In summary, we have created two different slippery surfaces (i.e. LIS and S-PDMS) and studied their physical properties in terms of anti-wetting, surface energy dissipation and antifouling. The stable immiscible lubricant-layer enables these slippery surfaces to repel water droplets compared to the PDMS control surface. S-PDMS showed even smaller contact angle hysteresis (~3.3°) than LIS (~5.5°) possibly due to more lubricant adsorbed within the polymer chains of PDMS. As a result, the contact line of the water droplet shrinks quickest among those three surfaces. Our quantitative analysis has demonstrated that the dissipative forces for the slippery surface are a fraction (7-12%) of the PDMS surface when tilted at 15°. As a result, the difference between the contribution of gravity force and dissipative force on the droplet is capable to easily remove the coffee stain from both slippery surfaces, which makes them self-cleaning surfaces. Both slippery surfaces have exhibited strong anti-fouling characteristics against *P. aeruginosa* and *S. epidermidis* biofilms under static conditions even after 6 days. After the evaporation, either artificial dust dissolved in liquid or the biofilm slime can be easily removed from both slippery surfaces. The droplet dynamics tests have shown that the water droplet is more likely to bounce back in those slippery surfaces at both low and high Weber numbers, particularly for S-PDMS. This implies the lower energy dissipation of these two slippery surfaces due to lower contact angle hysteresis. The further decrease of the contact angle hysteresis by only ~2.2° can significantly affect the droplet rebounding characteristics at low Weber number. Overall, both slippery surfaces have shown exceptional self-cleaning and antifouling performance compared to the PDMS.

Compared to LIS, S-PDMS is easier and cheaper to fabricate while exhibiting some improvement in terms of self-cleaning and antifouling. In principle, LIS can be created onto a variety of materials (e.g. polymers, titanium, steels, and glasses) with different surface textures (Li *et al.*, 2013; Wang *et al.*, 2016a; Doll *et al.*, 2017; Keller *et al.*, 2019). However, the costs of fabricating a large area of surface textures could be high. S-PDMS is cheaper and easier to fabricate, which relies on the cross-linked polymer network to absorb the lubricant, while, it is at least as effective as LIS in terms of preventing biofilm formation. Making polymer coatings or sprayable paints may allow for a large-scale application on arbitrary surfaces.

6.5 Appendix

Table S6. 1 Calculations based on equations (1&2). "Epoxy" and "S.epoxy" indicate the epoxy nano-pillars without and with the surface silinization. Θ_{water} and Θ_{oil} are the average values from the measured static contact angles on flat substrates from at least three individual measurements. r_w represents the roughness factor of the substrate, which is the ratio between the actual and projected surface areas of the textured solids. In the case of epoxy nano-pillars, with width a (~1 μm), edge-to-edge spacing b (~2 μm), and height h (~2 μm), $R=1+\pi ah/(a+b)^2$. γ_{water}, γ_{oil} represent the surface tensions of water and silicone oil, taken from reference (Wong *et al.*, 2011) and reference (Smith *et al.*, 2013), respectively. γ_{ow} represents the interfacial tension for water- oil interface, taken from reference(Smith *et al.*, 2013).

Solid	**r_w**	**γ_{water}(mN/m)**	**γ_{oil}(m N/m)**	**γ_{ow} (mN/m)**	**Θ_{water}**	**Θ_{oil}**	**ΔE_1**	**ΔE_2**	**Stable**
Epoxy	1.7	72.4	20.1	46.7	87	0	-18.97	80.03	no
S.Epoxy	1.7	72.4	20.1	46.7	120	60	31.99	130.99	yes

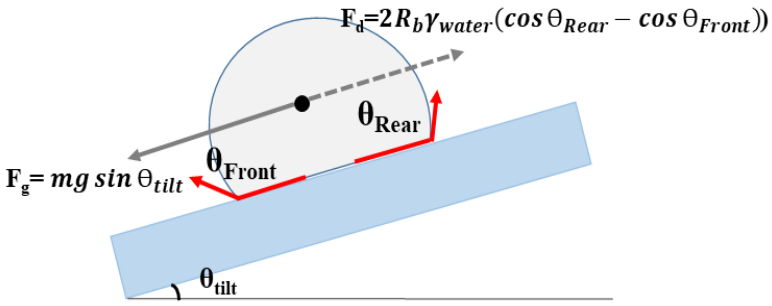

Figure S6. 1 Schematic for the calculation of F_g and F_d as described in the main text.

Chapter 7
Conclusions and Future work

7.1 Conclusions

In this study, nano-pillar, rose-petal and slippery lubricant-infused surfaces were designed and fabricated. Their anti-biofilm efficacies were evaluated against clinical bacterial strains (*S. epidermidis* or *P. aeruginosa*), as compared with their corresponding control surfaces. Overall, each surface showed resistance to bacterial biofilm growth, while the bacterial responses are significantly affected by surface architectures and physical properties. Based on the key results in this study, the following conclusions can be drawn:

- Bacteria aligns with regard to surface topography, in which case cells always try to maximum the contact areas with the solid surfaces. When pitch of pillars is much bigger than cell size, cell orientation is random. With the decrease of pitch, cell alignment is more likely to be parallel and perpendicular to pillar. Particularly, rod-shaped *P. aeruginosa* cells showed the extreme case that always attached and aligned in between 1 μm-spaced nano-pillars, which were parallel and perpendicular to pillars. This principle of alignment is applicable to bacterial mutants lacking flagella or pili, which showed the similar cell alignment within the 1 μm-spaced nano-pillars.
- Bacterial nanotubes were observed, where the extending nanotubes can contact the pillars and intercellular ones can connect the cells. Additionally, nanotubes also occurred in the bacteria mutants, indicating that the formation of bacterial nanotubes are prevalent to aid in cell-surface or cell-cell connections.
- Biofilm growth of *P. aeruginosa* after 24 hours were delayed on the nano-pillar surfaces compared with the control flat surfaces, indicating that unitary nanostructures can isolate cells and delay biofilm growth. While the 1μm-spacing nano-pillars showed the lowest bacterial attachment after 2 hours but it is not effective in delaying biofilm growth after 24 hours.
- Nano-pillars with smaller spacing facilitate the extension and elongation of bacterial nanotube networks. Therefore, nano-pillars of 1 μm space can be easily overcome by the nanotubes which connected the isolated bacterial aggregates far apart. Such nanotube networks can possibly aid in the cell-cell communications, thereby promoting the further biofilm development.
- Inspired with the above investigations, hierarchical rose-petal structured surfaces with micro-papillae and nano-folds were fabricated. The biofilm growth of *P. aeruginosa* after 24 hours was lower compared with the nanopillars (space ~1 μm),

indicating that a secondary nanostructure (nano-folds) on microstructures can improve the effectiveness in delaying biofilm growth.

- Similar to superhydrophobic lotus-leaf, the trapped air within nano-folds may hinder the bacterial attachment of *S. epidermidis* and *P. aeruginosa* after 2 hours. While bacteria preferentially form clusters within the valleys of micro-papillae, as they are preferentially wetted and offer more favourable colonization sites compared to the nano-folds.
- Micro-papillae isolated the bacterial clusters sitting in the valleys, inhibiting cell-cell communication. Therefore, within the first 24 hours, biofilm mainly formed between papillae. The secondary nanostructure (nano-folds) on microstructures enables bacterial cells along with the grooves on papillae, thereby delaying growth of early stage biofilm.
- Though either nano-pillar or rose-petal structured surfaces have shown promising in delaying the early-stage biofilm growth, however, in the long term these surfaces can still facilitate significant biofilms to grow. Even so, nano-pillar and rose-petal surfaces are still useful for us to study bacteria-material interactions. These two surfaces can be useful tools as model systems for investigating the multi dynamics of bacterial growth.
- In order to inhibit biofilm growth in long term, two kinds of slippery surfaces were fabricated via impregnating silicone oil into the porous surface nanostructures (referred as LIS) or diffusing into the polydimethylsiloxane (PDMS) matrix (referred as S-PDMS). Either slippery surface can prevent around 90% of bacterial biofilm growth of *S. epidermidis* and *P. aeruginosa* after 6 days, as compared with the unmodified control PDMS surfaces.
- S-PDMS showed stronger slipperiness against water droplets and more effective "self-cleaning" effects against the particle dusts or stains on the surface, possibly owing to the more lubricant adsorbed within the matrix. The slipperiness of these surfaces can effectively inhibit biofilm formation, as bacteria were unable to colonize on these slippery surfaces.
- Owing to much smaller contact angle hysteresis, bacteria may slide along the lubricant interface with much lower friction-resistance than experienced in the control PDMS. This also explained the shrinkage of biofilm stains on slippery surfaces as bacteria cells can easily slide along the lubricant with the contact line

receding. Due to weak adhesion, the dehydrated biofilms on these slippery surfaces can be easily removed by tissue papers or small water droplets.

7.2 Future work

The investigations of bacterial biofilm growth on different surfaces in this study complemented the findings of previous researches, and this study is a significant step toward a further understanding of bacteria-material interactions, regarding the surface topography and physical properties. Nevertheless, some suggestions can be drawn which can be valuable for future work.

- Further characterization of bacterial nanotubes and investigating its role in biofilm development

  In this study, we mainly adopted high-resolution SEM to visualize bacterial nanotubes. Critical point drying may cause artefacts of samples though our images corresponded to previous researches. Therefore, Cryogenic electron microscopy (Cryo-EM) may be a useful tool to visualize the bacterial nanotubes that will better preserve the microstructure of nanotubes, thereby it can determine detailed architectures and emanation site of these nanotubes. Furthermore, there is a lack of analysis regarding to the tube dynamics in this study. Total internal reflection fluorescence (TIRF) with super-resolution structured illumination microscopy (SIM) (Dubey *et al.*, 2016) can be adopted to visualize the emanating, growth of bacterial nanotubes, or even their connections between cells or biofilm cluster under a specific designed bacterial incubator chamber.

- Further characterization of Cassie impregnating wetting state on rose-petal surfaces

  Directly visualizing the Cassie impregnating wetting state that combines wetting and non-wetting is not an easy task, which may need the help of high-resolution Cryo Focused Ion Beam Scanning Electron Microscopy (Cryo-FIB/SEM). This approach has been used by Varanasi and co-workers to obtain images down to the 1µm scale (Rykaczewski *et al.*, 2012), and will be adopted for our future work.

- Further investigation of the anti-biofilm mechanisms of rose-petal surfaces

  This study only used unitary nano-pillar surfaces with similar dimension to nano-folds, to demonstrate the efficacy of hierarchical structures. Future work can be done by comparing the anti-biofilm efficacy of rose-petal hierarchical structures with other artificial unitary or hierarchical structures with different scales (e.g. lotus leaf), investigating whether rose petal replica surfaces are capable of inhibiting growth of biofilms by different species of bacteria and determining the most effective size of hierarchical structures that can delay biofilm growth.

- Further investigation of anti-wetting properties of slippery lubricant-infused surfaces

  For the future work, one can fabricate different surface topography for the oil infusion. The thickness of PDMS can also be varied and the silicone oil with different viscosity can be chosen to study how they may affect slipperiness of oil infused surfaces. In this case, the effects of surface topography, substrate thickness, oil viscosity on the surface slipperiness can be further investigated. Furthermore, AFM may be a useful tool to investigate the effective slip length of lubricant layer (Amini *et al.*, 2017; Scarratt *et al.*, 2019). The analysis of wetting ridges can also be done using confocal reflection interference contrast microscopy (Daniel *et al.*, 2017; Daniel *et al.*, 2018).

- Further investigation of anti-biofilm mechanisms of slippery lubricant-infused surfaces

  It would also be useful to study how bacteria motility may affect interactions between bacteria-lubricant layer using a wide range of bacterial mutants (e.g. lacking flagella or pili). Furthermore, designing a flow chamber with controlling the flow rate may help to understand the growth and detachment of biofilm on slippery surfaces, while the depletion of lubricant will be taken into considerations.

References

Altissimo, M. (2010) 'E-beam lithography for micro-/nanofabrication', *Biomicrofluidics*, 4(2), p. 026503.

Amini, S., Kolle, S., Petrone, L., Ahanotu, O., Sunny, S., Sutanto, C.N., Hoon, S., Cohen, L., Weaver, J.C. and Aizenberg, J. (2017) 'Preventing mussel adhesion using lubricant-infused materials', *Science*, 357(6352), pp. 668-673.

Ammar, Y., Swailes, D., Bridgens, B. and Chen, J. (2015) 'Influence of surface roughness on the initial formation of biofilm', *Surface and coatings technology*, 284, pp. 410-416.

An, Y.H., Dickinson, R.B. and Doyle, R.J. (2000) 'Mechanisms of bacterial adhesion and pathogenesis of implant and tissue infections', in *Handbook of Bacterial Adhesion*. Springer, pp. 1-27.

Araujo, J.C., Téran, F.C., Oliveira, R.A., Nour, E.A., Montenegro, M.A., Campos, J.R. and Vazoller, R.F. (2003) 'Comparison of hexamethyldisilazane and critical point drying treatments for SEM analysis of anaerobic biofilms and granular sludge', *Journal of electron microscopy*, 52(4), pp. 429-433.

Azeredo, J., Azevedo, N.F., Briandet, R., Cerca, N., Coenye, T., Costa, A.R., Desvaux, M., Di Bonaventura, G., Hébraud, M. and Jaglic, Z. (2017) 'Critical review on biofilm methods', *Critical reviews in microbiology*, 43(3), pp. 313-351.

Bagherifard, S., Hickey, D.J., de Luca, A.C., Malheiro, V.N., Markaki, A.E., Guagliano, M. and Webster, T.J. (2015) 'The influence of nanostructured features on bacterial adhesion and bone cell functions on severely shot peened 316L stainless steel', *Biomaterials*, 73, pp. 185-197.

Baidya, A.K., Bhattacharya, S., Dubey, G.P., Mamou, G. and Ben-Yehuda, S. (2018) 'Bacterial nanotubes: a conduit for intercellular molecular trade', *Current opinion in microbiology*, 42, pp. 1-6.

Bandara, C.D., Singh, S., Afara, I.O., Wolff, A., Tesfamichael, T., Ostrikov, K. and Oloyede, A. (2017) 'Bactericidal effects of natural nanotopography of dragonfly wing on *Escherichia coli*', *ACS applied materials & interfaces*, 9(8), pp. 6746-6760.

Banerjee, I., Pangule, R.C. and Kane, R.S. (2011) 'Antifouling coatings: recent developments in the design of surfaces that prevent fouling by proteins, bacteria, and marine organisms', *Advanced materials*, 23(6), pp. 690-718.

Beech, I.B., Sunner, J.A. and Hiraoka, K. (2010) 'Microbe-surface interactions in biofouling and biocorrosion processes', *International microbiology*, 8(3), pp. 157-168.

Berne, C., Ducret, A., Hardy, G.G. and Brun, Y.V. (2015) 'Adhesins involved in attachment to abiotic surfaces by Gram-negative bacteria', *Microbial biofilms*, pp. 163-199.

Berne, C., Ellison, C.K., Ducret, A. and Brun, Y.V. (2018) 'Bacterial adhesion at the single-cell level', *Nature reviews microbiology*, 16, pp. 616-27.

Bhadra, C.M., Truong, V.K., Pham, V.T., Al Kobaisi, M., Seniutinas, G., Wang, J.Y., Juodkazis, S., Crawford, R.J. and Ivanova, E.P. (2015) 'Antibacterial titanium nano-patterned arrays inspired by dragonfly wings', *Scientific Reports*, 5, p. 16817.

Bhattacharjee, S., Ko, C.-H. and Elimelech, M. (1998) 'DLVO interaction between rough surfaces', *Langmuir*, 14(12), pp. 3365-3375.

Bhattacharya, S., Baidya, A.K., Pal, R.R., Mamou, G., Gatt, Y.E., Margalit, H., Rosenshine, I. and Ben-Yehuda, S. (2019) 'A ubiquitous platform for bacterial nanotube biogenesis', *Cell reports*, 27(2), pp. 334-342. e10.

Bhushan, B., Jung, Y.C. and Koch, K. (2009) 'Micro-, nano-and hierarchical structures for superhydrophobicity, self-cleaning and low adhesion', *Philosophical Transactions of the Royal Society A: Mathematical, Physical and Engineering Sciences*, 367(1894), pp. 1631-1672.

Bixler, G.D., Theiss, A., Bhushan, B. and Lee, S.C. (2014) 'Anti-fouling properties of microstructured surfaces bio-inspired by rice leaves and butterfly wings', *Journal of colloid and interface science*, 419, pp. 114-133.

Bos, R., Van der Mei, H.C. and Busscher, H.J. (1999) 'Physico-chemistry of initial microbial adhesive interactions–its mechanisms and methods for study', *FEMS microbiology reviews*, 23(2), pp. 179-230.

Brown, R.A., Orr, F.M. and Scriven, L.E. (1980) ' Static drop on an inclined plate: analysis by the finite element method ', *Journal of colloid and interface science*, 73(1), pp. 76-87.

Bruzaud, J., Tarrade, J., Coudreuse, A., Canette, A., Herry, J.-M., de Givenchy, E.T., Darmanin, T., Guittard, F., Guilbaud, M. and Bellon-Fontaine, M.-N. (2015) 'Flagella but not type IV pili are involved in the initial adhesion of *Pseudomonas aeruginosa* PAO1 to hydrophobic or superhydrophobic surfaces', *Colloids and Surfaces B: Biointerfaces*, 131, pp. 59-66.

Bryers, J.D. (2008) 'Medical biofilms', *Biotechnology and bioengineering*, 100(1), pp. 1-18.

Busscher, H.J. and van der Mei, H.C. (2006) 'Microbial adhesion in flow displacement systems', *Clinical microbiology reviews*, 19(1), pp. 127-141.

Campoccia, D., Montanaro, L. and Arciola, C.R. (2013) 'A review of the biomaterials technologies for infection-resistant surfaces', *Biomaterials*, 34(34), pp. 8533-8554.

Cao, M., Guo, D., Yu, C., Li, K., Liu, M. and Jiang, L. (2015) 'Water-repellent properties of superhydrophobic and lubricant-infused "slippery" surfaces: a brief study on the functions and applications', *ACS applied materials & interfaces*, 8(6), pp. 3615-3623.

Cao, Y., Su, B., Chinnaraj, S., Jana, S., Bowen, L., Charlton, S., Duan, P., Jakubovics, N.S. and Chen, J. (2018) 'Nanostructured titanium surfaces exhibit recalcitrance towards *Staphylococcus epidermidis* biofilm formation', *Scientific Reports*, 8(1), p. 1071.

Chandki, R., Banthia, P. and Banthia, R. (2011) 'Biofilms: A microbial home', *Journal of Indian Society of Periodontology*, 15(2), p. 111.

Chandra, D. and Yang, S. (2010) 'Stability of high-aspect-ratio micropillar arrays against adhesive and capillary forces', *Accounts of chemical research*, 43(8), pp. 1080-1091.

Chang, Y.-R., Weeks, E.R. and Ducker, W.A. (2018) 'Surface topography hinders bacterial surface motility', *ACS applied materials & interfaces*, 10(11), pp. 9225-9234.

Chapman, R.G., Ostuni, E., Liang, M.N., Meluleni, G., Kim, E., Yan, L., Pier, G., Warren, H.S. and Whitesides, G.M. (2001) 'Polymeric thin films that resist the adsorption of proteins and the adhesion of bacteria', *Langmuir*, 17(4), pp. 1225-1233.

Chen, J. (2016) 'Thin film coatings and the biological interface 7', *Thin Film Coatings for Biomaterials and Biomedical Applications*, p. 143.

Chen, L., Geissler, A., Bonaccurso, E. and Zhang, K. (2014) 'Transparent slippery surfaces made with sustainable porous cellulose lauroyl ester films', *ACS applied materials & interfaces*, 6(9), pp. 6969-6976.

Chen, S., Li, L., Zhao, C. and Zheng, J. (2010) 'Surface hydration: Principles and applications toward low-fouling/nonfouling biomaterials', *Polymer*, 51(23), pp. 5283-5293.

Cheng, G., Li, G., Xue, H., Chen, S., Bryers, J.D. and Jiang, S. (2009) 'Zwitterionic carboxybetaine polymer surfaces and their resistance to long-term biofilm formation', *Biomaterials*, 30(28), pp. 5234-5240.

Cheng, G., Zhang, Z., Chen, S., Bryers, J.D. and Jiang, S. (2007) 'Inhibition of bacterial adhesion and biofilm formation on zwitterionic surfaces', *Biomaterials*, 28(29), pp. 4192-4199.

Chiu, G.-T. and Shaw, J.M. (1997) 'Optical lithography: introduction', *IBM Journal of Research and Development*, 41(1.2), pp. 3-6.

Choi, M., Lim, J., Choi, W., Kim, W. and Yong, K. (2017) 'Investigating the unrevealed photocatalytic activity and stability of nanostructured brookite TiO_2 film as an environmental photocatalyst', *ACS applied materials & interfaces*, 9(19), pp. 16252-16260.

Chuang, Y.-C., Chu, C.-K., Lin, S.-Y. and Chen, L.-J. (2014) 'Evaporation of water droplets on soft patterned surfaces', *Soft matter*, 10(19), pp. 3394-3403.

Chung, E. (2015) 'Effect of superhydrophobic titanium surface on initial salivary pellicle acquisition and oral biofilm formation', PhD thesis, University of Toronto, Ontario, Canada.

Chung, K.K., Schumacher, J.F., Sampson, E.M., Burne, R.A., Antonelli, P.J. and Brennan, A.B. (2007) 'Impact of engineered surface microtopography on biofilm formation of *Staphylococcus aureus*', *Biointerphases*, 2(2), pp. 89-94.

Cirelli, R., Watson, G. and Nalamasu, O. (2001) 'Optical Lithography', *Encyclopedia of Materials: Science and Technology*, pp. 6441-6448.

Conrad, J.C., Gibiansky, M.L., Jin, F., Gordon, V.D., Motto, D.A., Mathewson, M.A., Stopka, W.G., Zelasko, D.C., Shrout, J.D. and Wong, G.C. (2011) 'Flagella and pili-mediated near-surface single-cell motility mechanisms in *P. aeruginosa*', *Biophysical journal*, 100(7), pp. 1608-1616.

Costerton, J.W. (1999) 'Introduction to biofilm', *International journal of antimicrobial agents*, 11(3), pp. 217-221.

Costerton, J.W., Cheng, K.J., Geesey, G.G., Ladd, T.I., Nickel, J.C., Dasgupta, M. and Marrie, T.J. (1987) 'Bacterial biofilms in nature and disease', *Annual Reviews in Microbiology*, 41(1), pp. 435-464.

Crick, C.R., Ismail, S., Pratten, J. and Parkin, I.P. (2011) 'An investigation into bacterial attachment to an elastomeric superhydrophobic surface prepared via aerosol assisted deposition', *Thin Solid Films*, 519(11), pp. 3722-3727.

Czarnecki, J. and Warszyński, P. (1987) 'The evaluation of tangential forces due to surface inhomogeneties in the particle deposition process', *Colloids and surfaces*, 22(2), pp. 187-205.

Dai, S., Zhang, D., Shi, Q., Han, X., Wang, S. and Du, Z. (2013) 'Biomimetic fabrication and tunable wetting properties of three-dimensional hierarchical ZnO structures by combining soft lithography templated with lotus leaf and hydrothermal treatments', *CrystEngComm*, 15(27), pp. 5417-5424.

Daniel, D., Timonen, J.V., Li, R., Velling, S.J., Kreder, M.J., Tetreault, A. and Aizenberg, J. (2018) 'Origins of extreme liquid repellency on structured, flat, and lubricated hydrophobic surfaces', *Physical review letters*, 120(24), p. 244503.

Daniel, D., Timonen, J.V.I., Li, R., Velling, S.J. and Aizenberg, J. (2017) 'Oleoplaning droplets on lubricated surfaces', *Nature Physics*, 13(10), p. 1020.

Dawson, L.F., Valiente, E., Faulds-Pain, A., Donahue, E.H. and Wren, B.W. (2012) 'Characterisation of *Clostridium difficile* biofilm formation, a role for Spo0A', *PloS one*, 7(12), p. e50527.

Decker, E., Frank, B., Suo, Y. and Garoff, S. (1999) 'Physics of contact angle measurement', *Colloids and Surfaces A: Physicochemical and Engineering Aspects*, 156(1-3), pp. 177-189.

Di Bonaventura, G., Pompilio, A., Picciani, C., Iezzi, M., D'Antonio, D. and Piccolomini, R. (2006) 'Biofilm formation by the emerging fungal pathogen *Trichosporon asahii*: development, architecture, and antifungal resistance', *Antimicrobial agents and chemotherapy*, 50(10), pp. 3269-3276.

Di Bonaventura, G., Spedicato, I., D'Antonio, D., Robuffo, I. and Piccolomini, R. (2004) 'Biofilm formation by *Stenotrophomonas maltophilia*: modulation by quinolones, trimethoprim-sulfamethoxazole, and ceftazidime', *Antimicrobial agents and chemotherapy*, 48(1), pp. 151-160.

Díaz, C., Schilardi, P.L., Salvarezza, R.C. and De Mele, M.F.L. (2011) 'Have flagella a preferred orientation during early stages of biofilm formation? AFM study using patterned substrates', *Colloids and Surfaces B: Biointerfaces*, 82(2), pp. 536-542.

Dickson, M.N., Liang, E.I., Rodriguez, L.A., Vollereaux, N. and Yee, A.F. (2015) 'Nanopatterned polymer surfaces with bactericidal properties', *Biointerphases*, 10(2), p. 021010.

Diu, T., Faruqui, N., Sjostrom, T., Lamarre, B., Jenkinson, H.F., Su, B. and Ryadnov, M.G. (2014) 'Cicada-inspired cell-instructive nanopatterned arrays', *Scientific Reports*, 4, p. 7122.

Doll, K., Fadeeva, E., Schaeske, J., Ehmke, T., Winkel, A., Heisterkamp, A., Chichkov, B.N., Stiesch, M. and Stumpp, N.S. (2017) 'Development of laser-structured liquid-infused titanium with strong biofilm-repellent properties', *ACS applied materials & interfaces*, 9(11), pp. 9359-9368.

Doll, P., Al-Ahmad, A., Bacher, A., Muslija, A., Thelen, R., Hahn, L., Ahrens, R., Spindler, B. and Guber, A. (2019) 'Fabrication of silicon nanopillar arrays by electron beam lithography and reactive ion etching for advanced bacterial adhesion studies', *Materials Research Express*, 6(6), p. 065402.

Donlan, R.M. (2002) 'Biofilms: microbial life on surfaces', *Emerging infectious diseases*, 8(9), p.881.

Dou, X.-Q., Zhang, D., Feng, C. and Jiang, L. (2015) 'Bioinspired hierarchical surface structures with tunable wettability for regulating bacteria adhesion', *ACS nano*, 9(11), pp. 10664-10672.

Dou, X., Li, P., Jiang, S., Bayat, H. and Schönherr, H. (2017) 'Bioinspired hierarchically structured surfaces for efficient capture and release of circulating tumor cells', *ACS applied materials & interfaces*, 9(10), pp. 8508-8518.

Dubey, G.P. and Ben-Yehuda, S. (2011) 'Intercellular nanotubes mediate bacterial communication', *Cell*, 144(4), pp. 590-600.

Dubey, G.P., Mohan, G.B.M., Dubrovsky, A., Amen, T., Tsipshtein, S., Rouvinski, A., Rosenberg, A., Kaganovich, D., Sherman, E. and Medalia, O. (2016) 'Architecture and characteristics of bacterial nanotubes', *Developmental cell*, 36(4), pp. 453-461.

Dufour, D., Leung, V. and Lévesque, C.M. (2010) 'Bacterial biofilm: structure, function, and antimicrobial resistance', *Endodontic Topics*, 22(1), pp. 2-16.

Dufrêne, Y.F., Martínez-Martín, D., Medalsy, I., Alsteens, D. and Müller, D.J. (2013) 'Multiparametric imaging of biological systems by force-distance curve–based AFM', *Nature methods*, 10(9), p. 847.

Dundar Arisoy, F., Kolewe, K.W., Homyak, B., Kurtz, I.S., Schiffman, J.D. and Watkins, J.J. (2018) 'Bioinspired photocatalytic shark skin surfaces with antibacterial and antifouling activity via nanoimprint lithography', *ACS applied materials & interfaces*, 10(23), pp. 20055-20063.

ElSherbini, A. and Jacobi, A.M. (2006) 'Retention forces and contact angles for critical liquid drops on non-horizontal surfaces', *Journal of colloid and interface science*, 299(2), pp. 841-849.

Epstein, A.K., Wong, T.-S., Belisle, R.A., Boggs, E.M. and Aizenberg, J. (2012) 'Liquid-infused structured surfaces with exceptional anti-biofouling performance', *Proceedings of the National Academy of Sciences*, 109(33), pp. 13182-13187.

Eral, H. and Oh, J. (2013) 'Contact angle hysteresis: a review of fundamentals and applications', *Colloid and polymer science*, 291(2), pp. 247-260.

Extrand, C.W. and Gent, A.N. (1990) 'Retention of liquid drops by solid surfaces', *Journal of colloid and interface science*, 138(2), pp. 431-442.

Fadeeva, E., Truong, V.K., Stiesch, M., Chichkov, B.N., Crawford, R.J., Wang, J. and Ivanova, E.P. (2011) 'Bacterial retention on superhydrophobic titanium surfaces fabricated by femtosecond laser ablation', *Langmuir*, 27(6), pp. 3012-3019.

Feng, G., Cheng, Y., Wang, S.-Y., Borca-Tasciuc, D.A., Worobo, R.W. and Moraru, C.I. (2015) 'Bacterial attachment and biofilm formation on surfaces are reduced by small-diameter nanoscale pores: how small is small enough?', *npj Biofilms and Microbiomes*, 1, p. 15022.

Feng, L., Zhang, Y., Xi, J., Zhu, Y., Wang, N., Xia, F. and Jiang, L. (2008) 'Petal effect: a superhydrophobic state with high adhesive force', *Langmuir*, 24(8), pp. 4114-4119.

Flemming, H.C., Neu, T.R. and Wozniak, D.J. (2007) 'The EPS matrix: the "house of biofilm cells"', *Journal of bacteriology*, 189(22), pp. 7945-7.

Flemming, H.C. and Wingender, J. (2010) 'The biofilm matrix', *Nature reviews microbiology*, 8(9), pp. 623-33.

Freschauf, L.R., McLane, J., Sharma, H. and Khine, M. (2012) 'Shrink-induced superhydrophobic and antibacterial surfaces in consumer plastics', *PLoS One*, 7(8), p. e40987.

Friedlander, R.S., Vlamakis, H., Kim, P., Khan, M., Kolter, R. and Aizenberg, J. (2013) 'Bacterial flagella explore microscale hummocks and hollows to increase adhesion', *Proceedings of the National Academy of Sciences*, 110(14), pp. 5624-5629.

Friedlander, R.S., Vogel, N. and Aizenberg, J. (2015) 'Role of flagella in adhesion of *Escherichia coli* to abiotic surfaces', *Langmuir*, 31(22), pp. 6137-6144.

Furmidge, C. (1962) 'Studies at phase interfaces. I. The sliding of liquid drops on solid surfaces and a theory for spray retention', *Journal of colloid science*, 17(4), pp. 309-324.

Gao, L. and McCarthy, T.J. (2006) 'Contact angle hysteresis explained', *Langmuir*, 22(14), pp. 6234-6237.

Gao, N., Geyer, F., Pilat, D.W., Wooh, S., Vollmer, D., Butt, H.-J. and Berger, R. (2018) 'How drops start sliding over solid surfaces', *Nature Physics*, 14(2), p. 191.

Garrett, T.R., Bhakoo, M. and Zhang, Z. (2008) 'Bacterial adhesion and biofilms on surfaces', *Progress in Natural Science*, 18(9), pp. 1049-1056.

Gart, S., Mates, J.E., Megaridis, C.M. and Jung, S. (2015) 'Droplet impacting a cantilever: A leaf-raindrop system', *Physical Review Applied*, 3(4), p. 044019.

Goulter, R.M., Gentle, I.R. and Dykes, G.A. (2009) 'Issues in determining factors influencing bacterial attachment: a review using the attachment of *Escherichia coli* to abiotic surfaces as an example', *Letters in applied microbiology*, 49(1), pp. 1-7.

Green, D.W., Lee, K.K.-H., Watson, J.A., Kim, H.-Y., Yoon, K.-S., Kim, E.-J., Lee, J.-M., Watson, G.S. and Jung, H.-S. (2017) 'High quality bioreplication of intricate nanostructures from a fragile gecko skin surface with bactericidal properties', *Scientific Reports*, 7(1), pp. 1-12.

Gu, H., Chen, A., Song, X., Brasch, M.E., Henderson, J.H. and Ren, D. (2016) 'How *Escherichia coli* lands and forms cell clusters on a surface: A new role of surface topography', *Scientific Reports*, 6, p. 29516.

Guo, J., Fang, W., Welle, A., Feng, W., Filpponen, I., Rojas, O.J. and Levkin, P.A. (2016) 'Superhydrophobic and slippery lubricant-infused flexible transparent nanocellulose films by photoinduced thiol–ene functionalization', *ACS applied materials & interfaces*, 8(49), pp. 34115-34122.

Harding, J.L. and Reynolds, M.M. (2014) 'Combating medical device fouling', *Trends in biotechnology*, 32(3), pp. 140-146.

Harris, L.G., Tosatti, S., Wieland, M., Textor, M. and Richards, R.G. (2004) '*Staphylococcus aureus* adhesion to titanium oxide surfaces coated with non-functionalized and peptide-functionalized poly (L-lysine)-grafted-poly (ethylene glycol) copolymers', *Biomaterials*, 25(18), pp. 4135-4148.

Hasan, J. and Chatterjee, K. (2015) 'Recent advances in engineering topography mediated antibacterial surfaces', *Nanoscale*, 7(38), pp. 15568-15575.

Hasan, J., Crawford, R.J. and Ivanova, E.P. (2013a) 'Antibacterial surfaces: the quest for a new generation of biomaterials', *Trends in biotechnology*, 31(5), pp. 295-304.

Hasan, J., Webb, H.K., Truong, V.K., Pogodin, S., Baulin, V.A., Watson, G.S., Watson, J.A., Crawford, R.J. and Ivanova, E.P. (2013b) 'Selective bactericidal activity of nanopatterned superhydrophobic cicada *Psaltoda claripennis* wing surfaces', *Applied microbiology and biotechnology*, 97(20), pp. 9257-9262.

Hasan, S., Danishuddin, M. and Khan, A.U. (2015) 'Inhibitory effect of zingiber officinale towards *Streptococcus mutans* virulence and caries development: *in vitro* and *in vivo* studies', *BMC microbiology*, 15(1), p. 1.

Helbig, R., Günther, D., Friedrichs, J., Rößler, F., Lasagni, A. and Werner, C. (2016) 'The impact of structure dimensions on initial bacterial adhesion', *Biomaterials science*, 4(7), pp. 1074-1078.

Hermansson, M. (1999) 'The DLVO theory in microbial adhesion', *Colloids and Surfaces B: Biointerfaces*, 14(1), pp. 105-119.

Hizal, F., Choi, C.-H., Busscher, H.J. and van der Mei, H.C. (2016) '*Staphylococcal* adhesion, detachment and transmission on nanopillared Si surfaces', *ACS applied materials & interfaces*, 8(44), pp. 30430-30439.

Hizal, F., Rungraeng, N., Lee, J., Jun, S., Busscher, H.J., Van Der Mei, H.C. and Choi, C.-H. (2017) 'Nanoengineered superhydrophobic surfaces of aluminum with extremely low bacterial adhesivity', *ACS applied materials & interfaces*, 9(13), pp. 12118-12129.

Hochbaum, A.I. and Aizenberg, J. (2010) 'Bacteria pattern spontaneously on periodic nanostructure arrays'. *Nano letters*, 10(9), 3717-3721.

Hori, K. and Matsumoto, S. (2010) 'Bacterial adhesion: From mechanism to control', *Biochemical Engineering Journal*, 48(3), pp. 424-434.

Hou, S., Gu, H., Smith, C. and Ren, D. (2011) 'Microtopographic patterns affect *Escherichia coli* biofilm formation on poly (dimethylsiloxane) surfaces', *Langmuir*, 27(6), pp. 2686-2691.

Howell, C., Grinthal, A., Sunny, S., Aizenberg, M. and Aizenberg, J. (2018) 'Designing liquid‐infused surfaces for medical applications: a review', *Advanced Materials*, 30(50), p. 1802724.

Howell, C., Vu, T.L., Lin, J.J., Kolle, S., Juthani, N., Watson, E., Weaver, J.C., Alvarenga, J. and Aizenberg, J. (2014) 'Self-replenishing vascularized fouling-release surfaces', *ACS applied materials & interfaces*, 6(15), pp. 13299-13307.

Hsu, L., Fang, J., Borca-Tasciuc, D., Worobo, R. and Moraru, C.I. (2013) 'The effect of micro-and nanoscale topography on the adhesion of bacterial cells to solid surfaces', *Applied and environmental microbiology*, 79(8), pp. 2703-2712.

Huhtamäki, T., Tian, X., Korhonen, J.T. and Ras, R.H. (2018) 'Surface-wetting characterization using contact-angle measurements', *Nature protocols*, 13(7), p. 1521.

Ista, L.K., Fan, H., Baca, O. and López, G.P. (1996) 'Attachment of bacteria to model solid surfaces: oligo (ethylene glycol) surfaces inhibit bacterial attachment', *FEMS microbiology letters*, 142(1), pp. 59-63.

Ista, L.K. and López, G.P. (2012) 'Interfacial tension analysis of oligo (ethylene glycol)-terminated self-assembled monolayers and their resistance to bacterial attachment', *Langmuir*, 28(35), pp. 12844-12850.

Ivanova, E.P., Hasan, J., Webb, H.K., Gervinskas, G., Juodkazis, S., Truong, V.K., Wu, A.H.F., Lamb, R.N., Baulin, V.A. and Watson, G.S. (2013a) 'Bactericidal activity of black silicon', *Nature communications*, 4(1), pp. 1-7.

Ivanova, E.P., Hasan, J., Webb, H.K., Truong, V.K., Watson, G.S., Watson, J.A., Baulin, V.A., Pogodin, S., Wang, J.Y., Tobin, M.J., Lobbe, C. and Crawford, R.J. (2012) 'Natural bactericidal surfaces: mechanical rupture of *Pseudomonas aeruginosa* cells by cicada wings', *Small*, 8(16), pp. 2489-94.

Ivanova, E.P., Nguyen, S.H., Webb, H.K., Hasan, J., Truong, V.K., Lamb, R.N., Duan, X., Tobin, M.J., Mahon, P.J. and Crawford, R.J. (2013b) 'Molecular organization of the nanoscale surface structures of the dragonfly *Hemianax papuensis* wing epicuticle', *PLoS One*, 8(7), p. e67893.

Ivanova, E.P., Truong, V.K., Webb, H.K., Baulin, V.A., Wang, J.Y., Mohammodi, N., Wang, F., Fluke, C. and Crawford, R.J. (2011) 'Differential attraction and repulsion of *Staphylococcus aureus* and *Pseudomonas aeruginosa* on molecularly smooth titanium films', *Scientific Reports*, 1, p. 165.

Izano, E.A., Amarante, M.A., Kher, W.B. and Kaplan, J.B. (2008) 'Differential roles of poly-N-acetylglucosamine surface polysaccharide and extracellular DNA in *Staphylococcus aureus* and *Staphylococcus epidermidis* biofilms', *Applied and environmental microbiology*, 74(2), pp. 470-476.

Jayathilake, P.G., Li, B., Zuliani, P., Curtis, T. and Chen, J. (2019) 'Modelling bacterial twitching in fluid flows: a CFD-DEM approach', *bioRxiv*, p. 648915.

Jeong, H.E., Kim, I., Karam, P., Choi, H.-J. and Yang, P. (2013) 'Bacterial recognition of silicon nanowire arrays', *Nano letters*, 13(6), pp. 2864-2869.

Jiang, J., Zhang, H., He, W., Li, T., Li, H., Liu, P., Liu, M., Wang, Z., Wang, Z. and Yao, X. (2017) 'Adhesion of microdroplets on water-repellent surfaces toward the prevention of surface fouling and pathogen spreading by respiratory droplets', *ACS applied materials & interfaces*, 9(7), pp. 6599-6608.

Jiang, W., Wang, L., Liu, H., Ma, H., Tian, H., Chen, B., Shi, Y., Yin, L. and Ding, Y. (2014) 'Bio-inspired directional high-aspect-ratio nanopillars: fabrication and actuation', *RSC Advances*, 4(79), pp. 42002-42008.

Jin, F., Conrad, J.C., Gibiansky, M.L. and Wong, G.C. (2011) 'Bacteria use type-IV pili to slingshot on surfaces', *Proceedings of the National Academy of Sciences*, 108(31), pp. 12617-12622.

Joo, H.-S. and Otto, M. (2012) 'Molecular basis of *in vivo* biofilm formation by bacterial pathogens', *Chemistry & biology*, 19(12), pp. 1503-1513.

Kanematsu, H. and Barry, D.M. (2015) 'Conditioning Films', In: Kanematsu, H., Barry, D. M. (eds) *Biofilm and materials science*. Springer, Berlin, pp. 9-15.

Kaplan, J.B., Ragunath, C., Ramasubbu, N. and Fine, D.H. (2003) 'Detachment of *Actinobacillus actinomycetemcomitans* biofilm cells by an endogenous β-hexosaminidase activity', *Journal of bacteriology*, 185(16), pp. 4693-4698.

Kargar, M., Chang, Y.-R., Khalili Hosseinabad, H., Pruden, A. and Ducker, W.A. (2016) 'Colloidal crystals delay formation of early stage bacterial biofilms', *ACS Biomaterials Science & Engineering*, 2(6), pp. 1039-1048.

Kaur, R. and Liu, S. (2016) 'Antibacterial surface design–contact kill', *Progress in Surface Science*, 91(3), pp. 136-153.

Keller, N., Bruchmann, J., Sollich, T., Richter, C., Thelen, R., Kotz, F., Schwartz, T., Helmer, D. and Rapp, B.E. (2019) 'Study of biofilm growth on slippery liquid-infused porous surfaces made from fluoropor', *ACS applied materials & interfaces*, 11(4), pp. 4480-4487.

Khedir, K.R., Kannarpady, G.K., Ishihara, H., Woo, J., Trigwell, S., Ryerson, C. and Biris, A.S. (2011) 'Advanced studies of water evaporation kinetics over teflon-coated tungsten nanorod surfaces with variable hydrophobicity and morphology', *The Journal of Physical Chemistry C*, 115(28), pp. 13804-13812.

Kim, P., Adorno-Martinez, W.E., Khan, M. and Aizenberg, J. (2012) 'Enriching libraries of high-aspect-ratio micro-or nanostructures by rapid, low-cost, benchtop nanofabrication', *Nature protocols*, 7(2), p. 311.

Kim, P., Epstein, A.K., Khan, M., Zarzar, L.D., Lipomi, D.J., Whitesides, G.M. and Aizenberg, J. (2011) 'Structural transformation by electrodeposition on patterned substrates (STEPS): a new versatile nanofabrication method', *Nano letters*, 12(2), pp. 527-533.

Kim, P., Kreder, M.J., Alvarenga, J. and Aizenberg, J. (2013) 'Hierarchical or not? Effect of the length scale and hierarchy of the surface roughness on omniphobicity of lubricant-infused substrates', *Nano letters*, 13(4), pp. 1793-1799.

Knetsch, M.L.W. and Koole, L.H. (2011) 'New strategies in the development of antimicrobial coatings: the example of increasing usage of silver and silver nanoparticles', *Polymers*, 3(1), pp. 340-366.

Koch, K., Bhushan, B. and Barthlott, W. (2008) 'Diversity of structure, morphology and wetting of plant surfaces', *Soft Matter*, 4(10), pp. 1943-1963.

Koch, K., Bhushan, B., Jung, Y.C. and Barthlott, W. (2009) 'Fabrication of artificial Lotus leaves and significance of hierarchical structure for superhydrophobicity and low adhesion', *Soft Matter*, 5(7), pp. 1386-1393.

Konradi, R., Acikgoz, C. and Textor, M. (2012) 'Polyoxazolines for nonfouling surface coatings—a direct comparison to the gold standard PEG', *Macromolecular rapid communications*, 33(19), pp. 1663-1676.

Kovalenko, Y., Sotiri, I., Timonen, J.V., Overton, J.C., Holmes, G., Aizenberg, J. and Howell, C. (2017) 'Bacterial interactions with immobilized liquid layers', *Advanced healthcare materials*, 6(15), p. 1600948.

Kulinich, S. and Farzaneh, M. (2009) 'Effect of contact angle hysteresis on water droplet evaporation from super-hydrophobic surfaces', *Applied Surface Science*, 255(7), pp. 4056-4060.

Kumar, C., Le Houérou, V., Speck, T. and Bohn, H.F. (2018) 'Straightforward and precise approach to replicate complex hierarchical structures from plant surfaces onto soft matter polymer', *Royal Society open science*, 5(4), p. 172132.

Kumar, C.G. and Anand, S.K. (1998) 'Significance of microbial biofilms in food industry: a review', *International journal of food microbiology*, 42(1), pp. 9-27.

Kwok, D.Y. and Neumann, A.W. (1999) 'Contact angle measurement and contact angle interpretation', *Advances in colloid and interface science*, 81(3), pp. 167-249.

Lai, C.Q. (2018) 'Bacterial attachment, aggregation, and alignment on subcellular nanogratings', *Langmuir*, 34(13), pp. 4059-4070.

Lee, C. and Kim, C.-J.C. (2009) 'Maximizing the giant liquid slip on superhydrophobic microstructures by nanostructuring their sidewalls', *Langmuir*, 25(21), pp. 12812-12818.

Lee, C., Kim, H. and Nam, Y. (2014) 'Drop impact dynamics on oil-infused nanostructured surfaces', *Langmuir*, 30(28), pp. 8400-8407.

Lemon, K.P., Higgins, D.E. and Kolter, R. (2007) 'Flagellar motility is critical for *Listeria monocytogenes* biofilm formation', *Journal of bacteriology*, 189(12), pp. 4418-4424.

Li, J., Kleintschek, T., Rieder, A., Cheng, Y., Baumbach, T., Obst, U., Schwartz, T. and Levkin, P.A. (2013) 'Hydrophobic liquid-infused porous polymer surfaces for antibacterial applications', *ACS applied materials & interfaces*, 5(14), pp. 6704-6711.

Li, J., Ueda, E., Paulssen, D. and Levkin, P.A. (2019) 'Slippery lubricant-infused surfaces: properties and emerging applications', *Advanced Functional Materials*, 29(4), p. 1802317.

Li, X. (2016) 'Bactericidal mechanism of nanopatterned surfaces', *Physical Chemistry Chemical Physics*, 18(2), pp. 1311-1316.

Li, X., Cheung, G.S., Watson, G.S., Watson, J.A., Lin, S., Schwarzkopf, L. and Green, D.W. (2016) 'The nanotipped hairs of gecko skin and biotemplated replicas impair and/or kill pathogenic bacteria with high efficiency', *Nanoscale*, 8(45): 18860-18869.

Li, Y.F., Sun, H.W., Gao, R., Liu, K.Y., Zhang, H.Q., Fu, Q.H., Qing, S.L., Guo, G. and Zou, Q.M. (2015) 'Inhibited biofilm formation and improved antibacterial activity of a novel nanoemulsion against cariogenic *Streptococcus mutans in vitro* and *in vivo*', *International journal of nanomedicine*, 10, p. 447.

Li, Z., Lee, D., Sheng, X., Cohen, R.E. and Rubner, M.F. (2006) 'Two-level antibacterial coating with both release-killing and contact-killing capabilities', *Langmuir*, 22(24), pp. 9820-9823.

Lin, X., Li, J., Ma, S., Liu, G., Yang, K., Tong, M. and Lin, D. (2014) 'Toxicity of TiO_2 nanoparticles to *Escherichia coli*: effects of particle size, crystal phase and water chemistry', *PloS one*, 9(10), p. e110247.

Liu, Y. and Choi, C.-H. (2013) 'Condensation-induced wetting state and contact angle hysteresis on superhydrophobic lotus leaves', *Colloid and polymer science*, 291(2), pp. 437-445.

Lo, J.C., Horsley, D.A. and Skinner, J.L. (2012) 'Fabrication of large arrays of plasmonic nanostructures via double casting', *Advanced Fabrication Technologies for Micro/Nano Optics and Photonics V*. International Society for Optics and Photonics, 8249, p. 824915.

Loeb, G.I. and Neihof, R.A. (1975) 'Marine conditioning films', *Applied chemistry at protein interfaces*, 145(16), pp. 319-335.

Lorenzetti, M., Dogša, I., Stošicki, T.a., Stopar, D., Kalin, M., Kobe, S. and Novak, S.a. (2015) 'The influence of surface modification on bacterial adhesion to titanium-based substrates', *ACS applied materials & interfaces*, 7(3), pp. 1644-1651.

Lorite, G.S., Rodrigues, C.M., De Souza, A.A., Kranz, C., Mizaikoff, B. and Cotta, M.A. (2011) 'The role of conditioning film formation and surface chemical changes on *Xylella fastidiosa* adhesion and biofilm evolution', *Journal of colloid and interface science*, 359(1), pp. 289-295.

Lu, N., Zhang, W., Weng, Y., Chen, X., Cheng, Y. and Zhou, P. (2016) 'Fabrication of PDMS surfaces with micro patterns and the effect of pattern sizes on bacteria adhesion', *Food Control*, 68, pp. 344-351.

Ma, J., Sun, Y., Gleichauf, K., Lou, J. and Li, Q. (2011) 'Nanostructure on taro leaves resists fouling by colloids and bacteria under submerged conditions', *Langmuir*, 27(16), pp. 10035-10040.

Mabboux, F., Ponsonnet, L., Morrier, J.-J., Jaffrezic, N. and Barsotti, O. (2004) 'Surface free energy and bacterial retention to saliva-coated dental implant materials—an *in vitro* study', *Colloids and Surfaces B: Biointerfaces*, 39(4), pp. 199-205.

MacCallum, N., Howell, C., Kim, P., Sun, D., Friedlander, R., Ranisau, J., Ahanotu, O., Lin, J.J., Vena, A. and Hatton, B. (2014) 'Liquid-infused silicone as a biofouling-free medical material', *ACS Biomaterials Science & Engineering*, 1(1), pp. 43-51.

Maier, B. and Wong, G.C. (2015) 'How bacteria use type IV pili machinery on surfaces', *Trends in microbiology*, 23(12), pp. 775-788.

Mainwaring, D.E., Nguyen, S.H., Webb, H., Jakubov, T., Tobin, M., Lamb, R.N., Wu, A.H.F., Marchant, R., Crawford, R.J. and Ivanova, E.P. (2016) 'The nature of inherent bactericidal activity: insights from the nanotopology of three species of dragonfly', *Nanoscale*, 8(12), pp. 6527-6534.

Malvankar, N.S. and Lovley, D.R. (2012) 'Microbial nanowires: a new paradigm for biological electron transfer and bioelectronics', *ChemSusChem*, 5(6), pp. 1039-1046.

Manna, U., Raman, N., Welsh, M.A., Zayas-Gonzalez, Y.M., Blackwell, H.E., Palecek, S.P. and Lynn, D.M. (2016) 'Slippery liquid-infused porous surfaces that prevent microbial surface fouling and kill non-adherent pathogens in surrounding media: a controlled release approach', *Advanced functional materials*, 26(21), pp. 3599-3611.

Mantle, S. and England, N.H.S. (2015) 'Reducing HCAI-what the commissioner needs to know', *NHS England*, 8.

Marmur, A. (2004) 'The lotus effect: superhydrophobicity and metastability', *Langmuir*, 20(9), pp. 3517-3519.

Maruthupandy, M., Anand, M., Maduraiveeran, G., Beevi, A.S.H. and Priya, R.J. (2015) 'Electrical conductivity measurements of bacterial nanowires from *Pseudomonas aeruginosa'*, *Advances in natural sciences: Nanoscience and Nanotechnology*, 6(4), p. 045007.

McBride, S.A., Dash, S. and Varanasi, K.K. (2018) 'Evaporative crystallization in drops on superhydrophobic and liquid-impregnated surfaces', *Langmuir*, 34(41), pp. 12350-12358.

McClaine, J.W. and Ford, R.M. (2002) 'Reversal of flagellar rotation is important in initial attachment of *Escherichia coli* to glass in a dynamic system with high-and low-ionic-strength buffers', *Appl. Environ. Microbiol.*, 68(3), pp. 1280-1289.

McCord, M.A. and Rooks, M.J. (2000) "SPIE handbook of microlithography, micromachining and microfabrication." SPIE, Bellingham.

McFarland, K.A., Dolben, E.L., LeRoux, M., Kambara, T.K., Ramsey, K.M., Kirkpatrick, R.L., Mougous, J.D., Hogan, D.A. and Dove, S.L. (2015) 'A self-lysis pathway that enhances the virulence of a pathogenic bacterium', *Proceedings of the National Academy of Sciences*, 112(27), pp. 8433-8438.

McHale, G., Orme, B.V., Wells, G.G. and Ledesma-Aguilar, R. (2019) 'Apparent contact angles on lubricant-impregnated surfaces/SLIPS: from superhydrophobicity to electrowetting', *Langmuir*, 35(11), pp. 4197-4204.

Meng, X., Wang, Z., Wang, L., Heng, L. and Jiang, L. (2018) 'A stable solid slippery surface with thermally assisted self-healing ability', *Journal of Materials Chemistry A*, 6(34), pp. 16355-16360.

Mittelman, M.W. (1996) 'Adhesion to biomaterials', In: Fletcher, M. (ed.) *Bacterial adhesion: molecular and ecological diversity.* Wiley-Liss, Inc, New York, pp. 89-127.

Mohammad M.A., Muhammad M., Dew S.K., Stepanova M. (2012) 'Fundamentals of electron beam exposure and development', In: Stepanova M., Dew S. (eds) *Nanofabrication*. Springer, Vienna, pp. 11-41.

Molino, P.J., Yang, D., Penna, M., Miyazawa, K., Knowles, B.R., MacLaughlin, S., Fukuma, T., Yarovsky, I. and Higgins, M.J. (2018) 'Hydration layer structure of biofouling-resistant nanoparticles', *ACS nano*, 12(11), pp. 11610-11624.

Mon, H., Chang, Y.-R., Ritter, A.L., Falkinham Iii, J.O. and Ducker, W.A. (2017) 'Effects of colloidal crystals, antibiotics, and surface-bound antimicrobials on *Pseudomonas aeruginosa* surface density', *ACS Biomaterials Science & Engineering*, 4(1), pp. 257-265.

Monroe, D. (2007) 'Looking for chinks in the armor of bacterial biofilms', *PLoS Biol*, 5(11), p. e307.

Moradali, M.F., Ghods, S. and Rehm, B.H.A. (2017) '*Pseudomonas aeruginosa* lifestyle: a paradigm for adaptation, survival, and persistence', *Frontiers in cellular and infection microbiology*, 7, p. 39.

Muschi, M., Brudieu, B., Teisseire, J. and Sauret, A. (2018) 'Drop impact dynamics on slippery liquid-infused porous surfaces: influence of oil thickness', *Soft matter*, 14(7), pp. 1100-1107.

Nel, A., Xia, T., Mädler, L. and Li, N. (2006) 'Toxic potential of materials at the nanolevel', *Science*, 311(5761), pp. 622-627.

Nowlin, K., Boseman, A., Covell, A. and LaJeunesse, D. (2015) 'Adhesion-dependent rupturing of *Saccharomyces cerevisiae* on biological antimicrobial nanostructured surfaces', *Journal of the royal society interface*, 12(102), p. 20140999.

Odom, T.W., Love, J.C., Wolfe, D.B., Paul, K.E. and Whitesides, G.M. (2002) 'Improved pattern transfer in soft lithography using composite stamps', *Langmuir*, 18(13), pp. 5314-5320.

Ostuni, E., Chapman, R.G., Liang, M.N., Meluleni, G., Pier, G., Ingber, D.E. and Whitesides, G.M. (2001) 'Self-assembled monolayers that resist the adsorption of proteins and the adhesion of bacterial and mammalian cells', *Langmuir*, 17(20), pp. 6336-6343.

Pal, R.R., Baidya, A.K., Mamou, G., Bhattacharya, S., Socol, Y., Kobi, S., Katsowich, N., Ben-Yehuda, S. and Rosenshine, I. (2019) 'Pathogenic *E. coli* extracts nutrients from infected host cells utilizing injectisome components', *Cell*, 177(3), pp. 683-696. e18.

Palmer, J., Flint, S. and Brooks, J. (2007) 'Bacterial cell attachment, the beginning of a biofilm', *Journal of industrial microbiology & biotechnology*, 34(9), pp. 577-588.

Palmer, R.J. and White, D.C. (1997) 'Developmental biology of biofilms: implications for treatment and control', *Trends in microbiology*, 5(11), pp. 435-440.

Parker, N.W., Brodie, A.D. and McCoy, J.H. (2000) 'High-throughput NGL electron-beam direct-write lithography system', *Emerging lithographic technologies*, International Society for Optics and Photonics, 3997, pp. 713-720.

Peterson, B.W., He, Y., Ren, Y., Zerdoum, A., Libera, M.R., Sharma, P.K., van Winkelhoff, A.J., Neut, D., Stoodley, P., van der Mei, H.C. and Busscher, H.J. (2015) 'Viscoelasticity of biofilms and their recalcitrance to mechanical and chemical challenges', *FEMS microbiology reviews*, 39(2), pp. 234-45.

Petrova, O.E. and Sauer, K. (2012) 'Sticky situations: key components that control bacterial surface attachment', *Journal of bacteriology*, 194(10), pp. 2413-2425.

Pirbadian, S., Barchinger, S.E., Leung, K.M., Byun, H.S., Jangir, Y., Bouhenni, R.A., Reed, S.B., Romine, M.F., Saffarini, D.A. and Shi, L. (2014) '*Shewanella oneidensis* MR-1 nanowires are outer membrane and periplasmic extensions of the extracellular electron transport components', *Proceedings of the National Academy of Sciences*, 111(35), pp. 12883-12888.

Pirbadian, S., Barchinger, S.E., Leung, K.M., Byun, H.S., Jangir, Y., Bouhenni, R.A., Reed, S.B., Romine, M.F., Saffarini, D.A. and Shi, L. (2015) 'Bacterial nanowires of *Shewanella oneidensis* MR-1 are outer membrane and periplasmic extensions of the extracellular electron transport components', *Biophysical Journal*, 108(2), p. 368a.

Pogodin, S., Hasan, J., Baulin, V.A., Webb, H.K., Truong, V.K., Nguyen, T.H.P., Boshkovikj, V., Fluke, C.J., Watson, G.S. and Watson, J.A. (2013) 'Biophysical model of bacterial cell interactions with nanopatterned cicada wing surfaces', *Biophysical journal*, 104(4), pp. 835-840.

Pokroy, B., Epstein, A.K., Persson-Gulda, M. and Aizenberg, J. (2009) 'Fabrication of bioinspired actuated nanostructures with arbitrary geometry and stiffness', *Advanced Materials*, 21(4), pp. 463-469.

Poulsen, L.V. (1999) 'Microbial biofilm in food processing', *LWT-Food Science and Technology*, 32(6), pp. 321-326.

Prabhu, S. and Poulose, E.K. (2012) 'Silver nanoparticles: mechanism of antimicrobial action, synthesis, medical applications, and toxicity effects', *International Nano Letters*, 2(1), p. 32.

Pratt, L.A. and Kolter, R. (1998) 'Genetic analysis of *Escherichia coli* biofilm formation: roles of flagella, motility, chemotaxis and type I pili', *Molecular microbiology*, 30(2), pp. 285-293.

Preston, D.J., Song, Y., Lu, Z., Antao, D.S. and Wang, E.N. (2017) 'Design of lubricant infused surfaces', *ACS applied materials & interfaces*, 9(48), pp. 42383-42392.

Privett, B.J., Youn, J., Hong, S.A., Lee, J., Han, J., Shin, J.H. and Schoenfisch, M.H. (2011) 'Antibacterial fluorinated silica colloid superhydrophobic surfaces', *Langmuir*, 27(15), pp. 9597-9601.

Quirynen, M. and Bollen, C.M.L. (1995) 'The influence of surface roughness and surface-free energy on supra-and subgingival plaque formation in man', *Journal of clinical periodontology*, 22(1), pp. 1-14.

Rai-Choudhury, P. (ed.) (1997) *Handbook of microlithography, micromachining, and microfabrication: microlithography*. SPIE Optical Engineering Press, Bellingham.

Rasamiravaka, T., Labtani, Q., Duez, P. and El Jaziri, M. (2015) 'The formation of biofilms by *Pseudomonas aeruginosa*: a review of the natural and synthetic compounds interfering with control mechanisms', *BioMed research international*, 2015.

Reddy, S.T., Chung, K.K., McDaniel, C.J., Darouiche, R.O., Landman, J. and Brennan, A.B. (2011) 'Micropatterned surfaces for reducing the risk of catheter-associated urinary tract infection: an *in vitro* study on the effect of sharklet micropatterned surfaces to inhibit bacterial colonization and migration of uropathogenic *Escherichia coli*', *Journal of endourology*, 25(9), pp. 1547-1552.

Reguera, G., McCarthy, K.D., Mehta, T., Nicoll, J.S., Tuominen, M.T. and Lovley, D.R. (2005) 'Extracellular electron transfer via microbial nanowires', *Nature*, 435(7045), p. 1098.

Remis, J.P., Wei, D., Gorur, A., Zemla, M., Haraga, J., Allen, S., Witkowska, H.E., Costerton, J.W., Berleman, J.E. and Auer, M. (2014) 'Bacterial social networks: structure and composition of *Myxococcus xanthus* outer membrane vesicle chains', *Environmental microbiology*, 16(2), pp. 598-610.

Renner, L.D. and Weibel, D.B. (2011) 'Physicochemical regulation of biofilm formation', *MRS bulletin*, 36(5), pp. 347-355.

Rykaczewski, K., Anand, S., Subramanyam, S.B. and Varanasi, K.K. (2013) 'Mechanism of frost formation on lubricant-impregnated surfaces', *Langmuir*, 29(17), pp. 5230-5238.

Rykaczewski, K., Landin, T., Walker, M.L., Scott, J.H.J. and Varanasi, K.K. (2012) 'Direct imaging of complex nano-to microscale interfaces involving solid, liquid, and gas phases', *ACS nano*, 6(10), pp. 9326-9334.

Sadullah, M.S., Semprebon, C. and Kusumaatmaja, H. (2018) 'Drop dynamics on liquid-infused surfaces: The role of the lubricant ridge', *Langmuir*, 34(27), pp. 8112-8118.

Saison, T., Peroz, C., Chauveau, V., Berthier, S., Sondergard, E. and Arribart, H. (2008) 'Replication of butterfly wing and natural lotus leaf structures by nanoimprint on silica sol–gel films', *Bioinspiration & biomimetics*, 3(4), p. 046004.

Scarratt, L.R., Zhu, L. and Neto, C. (2019) 'How slippery are SLIPS? measuring effective slip on lubricated surfaces with colloidal probe atmoc force microscopy', *Langmuir*, 35(8), pp. 2976-2982.

Schellenberger, F., Xie, J., Encinas, N., Hardy, A., Klapper, M., Papadopoulos, P., Butt, H.-J. and Vollmer, D. (2015) 'Direct observation of drops on slippery lubricant-infused surfaces', *Soft Matter*, 11(38), pp. 7617-7626.

Scheuerman, T.R., Camper, A.K. and Hamilton, M.A. (1998) 'Effects of substratum topography on bacterial adhesion', *Journal of colloid and interface science*, 208(1), pp. 23-33.

Seddiki, O., Harnagea, C., Levesque, L., Mantovani, D. and Rosei, F. (2014) 'Evidence of antibacterial activity on titanium surfaces through nanotextures', *Applied Surface Science*, 308, pp. 275-284.

Semprebon, C., McHale, G. and Kusumaatmaja, H. (2017) 'Apparent contact angle and contact angle hysteresis on liquid infused surfaces', *Soft matter*, 13(1), pp. 101-110.

Shields, R.C., Mokhtar, N., Ford, M., Hall, M.J., Burgess, J.G., ElBadawey, M.R. and Jakubovics, N.S. (2013) 'Efficacy of a marine bacterial nuclease against biofilm forming microorganisms isolated from chronic rhinosinusitis', *PLoS One*, 8(2), p. e55339.

Shin, S., Seo, J., Han, H., Kang, S., Kim, H. and Lee, T. (2016) 'Bio-inspired extreme wetting surfaces for biomedical applications', *Materials*, 9(2), p. 116.

Shrivastava, S., Bera, T., Roy, A., Singh, G., Ramachandrarao, P. and Dash, D. (2007) 'Characterization of enhanced antibacterial effects of novel silver nanoparticles', *Nanotechnology*, 18(22), p. 225103.

Sidorenko, J., Jatsenko, T. and Kivisaar, M. (2017) 'Ongoing evolution of *Pseudomonas aeruginosa* PAO1 sublines complicates studies of DNA damage repair and tolerance', *Mutation Research/Fundamental and Molecular Mechanisms of Mutagenesis*, 797, pp. 26-37.

Sjöström, T., Nobbs, A.H. and Su, B. (2016) 'Bactericidal nanospike surfaces via thermal oxidation of Ti alloy substrates', *Materials Letters*, 167, pp. 22-26.

Smith, J.D., Dhiman, R., Anand, S., Reza-Garduno, E., Cohen, R.E., McKinley, G.H. and Varanasi, K.K. (2013) 'Droplet mobility on lubricant-impregnated surfaces', *Soft Matter*, 9(6), pp. 1772-1780.

Smith, R. and Coast, J. (2013) 'The true cost of antimicrobial resistance', *BMJ: British Medical Journal*, 346, p. 1493.

Solomon, B.R., Subramanyam, S.B., Farnham, T.A., Khalil, K.S., Anand, S. and Varanasi, K.K. (2016) 'Lubricant-impregnated surfaces', in *Non-wettable Surfaces*. pp. 285-318.

Song, F., Brasch, M.E., Wang, H., Henderson, J.H., Sauer, K. and Ren, D. (2017) 'How bacteria respond to material stiffness during attachment: a role of *Escherichia coli* flagellar motility', *ACS applied materials & interfaces*, 9(27), pp. 22176-22184.

Song, F., Koo, H. and Ren, D. (2015) 'Effects of material properties on bacterial adhesion and biofilm formation', *Journal of dental research*, 94(8), pp. 1027-1034.

Song, F. and Ren, D. (2014) 'Stiffness of cross-linked poly (dimethylsiloxane) affects bacterial adhesion and antibiotic susceptibility of attached cells', *Langmuir*, 30(34), pp. 10354-10362.

Steidl, R.J., Lampa-Pastirk, S. and Reguera, G. (2016) 'Mechanistic stratification in electroactive biofilms of *Geobacter sulfurreducens* mediated by pilus nanowires', *Nature communications*, 7, p. 12217.

Stiefel, P., Schmidt-Emrich, S., Maniura-Weber, K. and Ren, Q. (2015) 'Critical aspects of using bacterial cell viability assays with the fluorophores SYTO9 and propidium iodide', *BMC microbiology*, 15(1), p. 36.

Stover, C.K., Pham, X.Q., Erwin, A.L., Mizoguchi, S.D., Warrener, P., Hickey, M.J., Brinkman, F.S.L., Hufnagle, W.O., Kowalik, D.J. and Lagrou, M. (2000) 'Complete genome sequence of *Pseudomonas aeruginosa* PAO1, an opportunistic pathogen', *Nature*, 406(6799), p. 959.

Sure, S., Ackland, M.L., Torriero, A.A.J., Adholeya, A. and Kochar, M. (2016) 'Microbial nanowires: an electrifying tale', *Microbiology*, 162(12), pp. 2017-2028.

Takahashi, C., Kalita, G., Ogawa, N., Moriguchi, K., Tanemura, M., Kawashima, Y. and Yamamoto, H. (2015) 'Electron microscopy of *Staphylococcus epidermidis* fibril and biofilm formation using image-enhancing ionic liquid', *Analytical and bioanalytical chemistry*, 407(6), pp. 1607-1613.

Tang, H., Cao, T., Liang, X., Wang, A., Salley, S.O., McAllister, J. and Ng, K.Y. (2009) 'Influence of silicone surface roughness and hydrophobicity on adhesion and colonization of *Staphylococcus epidermidis*', *Journal of Biomedical Materials Research Part A*, 88(2), pp. 454-463.

Tang, P., Zhang, W., Wang, Y., Zhang, B., Wang, H., Lin, C. and Zhang, L. (2011) 'Effect of superhydrophobic surface of titanium on *Staphylococcus aureus* adhesion', *Journal of Nanomaterials*, 2011, p. 2.

Taylor, R.L., Verran, J., Lees, G.C. and Ward, A.P. (1998) 'The influence of substratum topography on bacterial adhesion to polymethyl methacrylate', *Journal of materials science: materials in medicine*, 9(1), pp. 17-22.

Thallinger, B., Prasetyo, E.N., Nyanhongo, G.S. and Guebitz, G.M. (2013) 'Antimicrobial enzymes: an emerging strategy to fight microbes and microbial biofilms', *Biotechnology journal*, 8(1), pp. 97-109.

Thomas, J.G. and Nakaishi, L.A. (2006) 'Managing the complexity of a dynamic biofilm', *The journal of the American dental association*, 137, pp. S10-S15.

Tripathy, A., Sen, P., Su, B. and Briscoe, W.H. (2017) 'Natural and bioinspired nanostructured bactericidal surfaces', *Advances in colloid and interface science*, 248, pp. 85-104.

Truong, V.K., Webb, H.K., Fadeeva, E., Chichkov, B.N., Wu, A.H.F., Lamb, R., Wang, J.Y., Crawford, R.J. and Ivanova, E.P. (2012) 'Air-directed attachment of coccoid bacteria to the surface of superhydrophobic lotus-like titanium', *Biofouling*, 28(6), pp. 539-550.

Uyama, Y., Inoue, H., Ito, K., Kishida, A. and Ikada, Y. (1991) 'Comparison of different methods for contact angle measurement', *Journal of colloid and interface science*, 141(1), pp. 275-279.

Vogel, N., Belisle, R.A., Hatton, B., Wong, T.-S. and Aizenberg, J. (2013) 'Transparency and damage tolerance of patternable omniphobic lubricated surfaces based on inverse colloidal monolayers', *Nature communications*, 4, p. 2176.

Wang, P., Zhang, D., Sun, S., Li, T. and Sun, Y. (2016a) 'Fabrication of slippery lubricant-infused porous surface with high underwater transparency for the control of marine biofouling', *ACS applied materials & interfaces*, 9(1), pp. 972-982.

Wang, Y., Zhang, H., Liu, X. and Zhou, Z. (2016b) 'Slippery liquid-infused substrates: a versatile preparation, unique anti-wetting and drag-reduction effect on water', *Journal of Materials Chemistry A*, 4(7), pp. 2524-2529.

Watson, G.S., Green, D.W., Cribb, B.W., Brown, C.L., Meritt, C.R., Tobin, M.J., Vongsvivut, J., Sun, M., Liang, A.-P. and Watson, J.A. (2017) 'Insect analogue to the Lotus leaf: a planthopper wing membrane incorporating a low-adhesion, nonwetting, superhydrophobic, bactericidal, and biocompatible surface', *ACS applied materials & interfaces*, 9(28), pp. 24381-24392.

Watson, G.S., Green, D.W., Schwarzkopf, L., Li, X., Cribb, B.W., Myhra, S. and Watson, J.A. (2015) 'A gecko skin micro/nano structure–A low adhesion, superhydrophobic, anti-wetting, self-cleaning, biocompatible, antibacterial surface', *Acta biomaterialia*, 21, pp. 109-122.

Wei, C., Zhang, G., Zhang, Q., Zhan, X. and Chen, F. (2016) 'Silicone oil-infused slippery surfaces based on Sol–Gel process-induced nanocomposite coatings: A facile approach to highly stable bioinspired surface for biofouling resistance', *ACS applied materials & interfaces*, 8(50), pp. 34810-34819.

Wei, Q., Schlaich, C., Prévost, S., Schulz, A., Böttcher, C., Gradzielski, M., Qi, Z., Haag, R. and Schalley, C.A. (2014) 'Supramolecular polymers as surface coatings: Rapid fabrication of healable superhydrophobic and slippery surfaces', *Advanced Materials*, 26(43), pp. 7358-7364.

Weigert, M., Ross-Gillespie, A., Leinweber, A., Pessi, G., Brown, S.P. and Kümmerli, R. (2017) 'Manipulating virulence factor availability can have complex consequences for infections', *Evolutionary applications*, 10(1), pp. 91-101.

Wolfe, D.B., Love, J.C. and Whitesides, G.M. (2004) 'Nanostructures replicated by polymer molding', In: Hari N.(ed) *Encyclopedia of Nanoscience and Nanotechnology*. American scientific publishers, California, pp. 2657-2666.

Wong, T.-S., Kang, S.H., Tang, S.K., Smythe, E.J., Hatton, B.D., Grinthal, A. and Aizenberg, J. (2011) 'Bioinspired self-repairing slippery surfaces with pressure-stable omniphobicity', *Nature*, 477(7365), p. 443.

Wong, W.S., Nasiri, N., Liu, G., Rumsey-Hill, N., Craig, V.S., Nisbet, D.R. and Tricoli, A. (2015) 'Flexible transparent hierarchical nanomesh for rose petal-like droplet manipulation and lossless transfer', *Advanced Materials Interfaces*, 2(9), p. 1500071.

Xiao, L., Li, J., Mieszkin, S., Di Fino, A., Clare, A.S., Callow, M.E., Callow, J.A., Grunze, M., Rosenhahn, A. and Levkin, P.A. (2013) 'Slippery liquid-infused porous surfaces showing marine antibiofouling properties', *ACS applied materials & interfaces*, 5(20), pp. 10074-10080.

Xu, L.-C. and Siedlecki, C.A. (2014) '*Staphylococcus epidermidis* adhesion on hydrophobic and hydrophilic textured biomaterial surfaces', *Biomedical Materials*, 9(3), p. 035003.

Xu, L.-C., Wo, Y., Meyerhoff, M.E. and Siedlecki, C.A. (2017) 'Inhibition of bacterial adhesion and biofilm formation by dual functional textured and nitric oxide releasing surfaces', *Acta biomaterialia*, 51, pp. 53-65.

Xu, L.C. and Siedlecki, C.A. (2017) 'Protein adsorption, platelet adhesion, and bacterial adhesion to polyethylene-glycol-textured polyurethane biomaterial surfaces', *Journal of Biomedical Materials Research Part B: Applied Biomaterials*, 105(3), pp. 668-678.

Xue, F., Liu, J., Guo, L., Zhang, L. and Li, Q. (2015) 'Theoretical study on the bactericidal nature of nanopatterned surfaces', *Journal of theoretical biology*, 385, pp. 1-7.

Yoda, I., Koseki, H., Tomita, M., Shida, T., Horiuchi, H., Sakoda, H. and Osaki, M. (2014) 'Effect of surface roughness of biomaterials on *Staphylococcus epidermidis* adhesion', *BMC microbiology*, 14(1), p. 234.

Young, T. (1805) 'An essay on the cohesion of fluids', *Philosophical Transactions of the Royal Society of London*, 95, pp. 65-87.

Yu, Q., Wu, Z. and Chen, H. (2015) 'Dual-function antibacterial surfaces for biomedical applications', *Acta biomaterialia*, 16, pp. 1-13.

Yunker, P.J., Still, T., Lohr, M.A. and Yodh, A. (2011) 'Suppression of the coffee-ring effect by shape-dependent capillary interactions', *Nature*, 476(7360), p. 308.

Zhang, J., Wang, A. and Seeger, S. (2014) 'Nepenthes pitcher inspired anti-wetting silicone nanofilaments coatings: preparation, unique anti-wetting and self-cleaning behaviors', *Advanced Functional Materials*, 24(8), pp. 1074-1080.

Zhang, X., Wang, L. and Levänen, E. (2013) 'Superhydrophobic surfaces for the reduction of bacterial adhesion', *RSC Advances*, 3(30), pp. 12003-12020.

Zhukova, L.V. (2015) 'Evidence for compression of *Escherichia coli* K12 cells under the effect of TiO_2 nanoparticles', *ACS applied materials & interfaces*, 7(49), pp. 27197-27205.